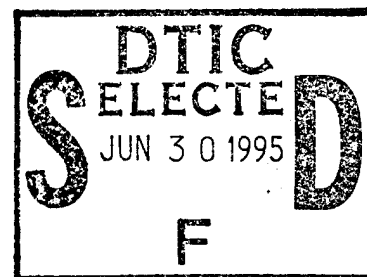


OPTICAL
PHASE CONJUGATION,
BEAM COUPLING,
AND
EFFECTS OF COLOR CENTERS
IN
PHOTOREFRACTIVE CRYSTALS



Putchu Venkateswarlu, Mehdi Moghbel,
Medury D. Sastry and Michael Curley

Department of Physics
Center for Nonlinear Optics & Materials
Alabama A. & M. University
Post Office Box 1268
4900 North Meridian Street
Normal Alabama 35762-1268

December 1994

FINAL REPORT FOR 07/16/90-11/30/94

APPROVED FOR PUBLIC RELEASE; DISTRIBUTION IS UNLIMITED

Solid State Electronics Directorate
Wright Laboratory
Air Force Materiel Command
Wright-Patterson Air Force Base, OH 45433-7331

19950628 014

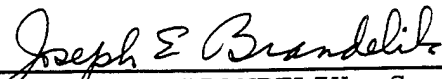
DTIC QUALITY ASSURED 1


NOTICE

WHEN GOVERNMENT DRAWINGS, SPECIFICATIONS, OR OTHER DATA ARE USED FOR ANY PURPOSE OTHER THAN IN CONNECTION WITH A DEFINITELY GOVERNMENT-RELATED PROCUREMENT, THE UNITED STATES GOVERNMENT INCURS NO RESPONSIBILITY OR ANY OBLIGATION WHATSOEVER. THE FACT THAT THE GOVERNMENT MAY HAVE FORMULATED OR IN ANY WAY SUPPLIED THE SAID DRAWINGS, SPECIFICATIONS, OR OTHER DATA, IS NOT TO BE REGARDED BY IMPLICATION, OR OTHERWISE IN ANY MANNER CONSTRUED, AS LICENSING THE HOLDER, OR ANY OTHER PERSON OR CORPORATION; OR AS CONVEYING ANY RIGHTS OR PERMISSION TO MANUFACTURE, USE, OR SELL ANY PATENTED INVENTION THAT MAY IN ANY WAY BE RELATED THERETO.

This report is releasable to the National Technical Information Service (NTIS). At NTIS, it will be available to the general public, including foreign nations.

This technical report has been reviewed and is approved for publication.


JOSEPH E. BRANDELIK, Sr. EE
E-O Techniques & Appl. Branch
Electro-Optics Division


JOHN O. CRIST, Actg. Chief
E-O Techniques & Appl. Branch
Electro-Optics Division


C. RICHARD LANE, Actg. Chief
Electro-Optics Division
S. S. Electronics Directorate

If your address has changed, if you wish to be removed from our mailing list, or if the addressee is no longer employed by your organization please notify WL/ELOT, WPAFB, OH 45433-7405 to help us maintain a current mailing list.

Copies of this report should not be returned unless return is required by security considerations, contractual obligations, or notice on a specific document.

REPORT DOCUMENTATION PAGE

Form Approved
OMB No. 0704-0188

Public reporting burden for this collection of information is estimated to average 1 hour per response, including the time for reviewing instructions, searching existing data sources, gathering and maintaining the data needed, and completing and reviewing the collection of information. Send comments regarding this burden estimate or any other aspect of this collection of information, including suggestions for reducing this burden, to Washington Headquarters Services, Directorate for Information Operations and Reports, 1215 Jefferson Davis Highway, Suite 1204, Arlington, VA 22202-4302, and to the Office of Management and Budget, Paperwork Reduction Project (0704-0188), Washington, DC 20503.

1. AGENCY USE ONLY (Leave blank)		2. REPORT DATE DEC 94	3. REPORT TYPE AND DATES COVERED 07/16/90 - 11/30/94	
4. TITLE AND SUBTITLE Optical Phase Conjugation, Beam Coupling, and Effects of Color Centers in Photorefractive Crystals			5. FUNDING NUMBERS C: F33615-90-C-1445 PE: 62204F PR: 2001 TA: 02 WU: AL	
6. AUTHOR(S) Putcha Venkaterswarlu, Mehdi Moghbel, Medury D. Sastry, and Michael Curley				
7. PERFORMING ORGANIZATION NAME(S) AND ADDRESS(ES) Department of Physics Center for Nonlinear Optics & Materials Alabama A & M University Post Office Box 1268 Normal, Alabama 35762			8. PERFORMING ORGANIZATION REPORT NUMBER	
9. SPONSORING/MONITORING AGENCY NAME(S) AND ADDRESS(ES) Solid State Electronics Directorate Wright Laboratory Air Force Materiel Command Wright-Patterson AFB OH 45433-7331			10. SPONSORING/MONITORING AGENCY REPORT NUMBER WL-TR-94-5050	
11. SUPPLEMENTARY NOTES Effort was part of BAA 89-03-PMRE, 100% set aside for Historically Black Colleges and Universities or Minority Institutions as defined in DOD FAR Sup. 26.7002				
12a. DISTRIBUTION/AVAILABILITY STATEMENT Approved for public release; distribution unlimited			12b. DISTRIBUTION CODE	
13. ABSTRACT (Maximum 200 words) This effort was a research program to investigate the (coherent and incoherent) nonlinear optical properties as a function of color centers. The investigation included multiwave mixing (four wave mixing and phase conjugation), spectral, and electron paramagnetic resonance properties of gamma-ray induced color centers. Investigations on BaTiO ₃ include EPR measurements, parametric dependence of energy transfer for two coherent beams, influence of Fe ³⁺ and Cu ²⁺ impurities on the origin of photorefractive effects, resonance phase conjugation, and other beam coupling. SBN and BSO were studied.				
14. SUBJECT TERMS Phase conjugation, multiwave mixing, color centers, electron paramagnetic resonance, BaTiO ₃ , SBN, BSO			15. NUMBER OF PAGES 185	
			16. PRICE CODE	
17. SECURITY CLASSIFICATION OF REPORT UNCLASSIFIED	18. SECURITY CLASSIFICATION OF THIS PAGE UNCLASSIFIED	19. SECURITY CLASSIFICATION OF ABSTRACT UNCLASSIFIED	20. LIMITATION OF ABSTRACT UNLIMITED	

TABLE OF CONTENTS

		Page
1	Introduction	1
	1.1 Background	1
	1.2 Degenerate Four-wave Mixing	2
	1.3 Self-Pumped Phase Conjugation	3
	1.4 Incoherent Beam couplings	4
	1.5 Coherent Beam Couplings	5
	1.6 Optical Phase Conjugation in Resonant/Saturable Absorptive Systems with Color Centers	6
	1.7 The Present Work	8
2	Optically Induced Grating Erasure Studies and Determination of Charge Carrier Densities in $\text{Sr}_{0.75}\text{Ba}_{0.25}\text{Nb}_2\text{O}_6$: Effects of Gamma Irradiation and Ce and Cr Doping	16
	2.0 Introduction	16
	2.1 Some "Facts About $\text{Sr}_{0.75}\text{Ba}_{0.25}\text{Nb}_2\text{O}_6$ and the Problems Addressed	16
	2.2 Sample Preparation	18
	2.3 Experimental Procedures	19
	2.4 Experimental Results	20
	2.4.1 Electronic Absorption	20
	2.4.2 Optically Induced Erasure Measurements	21
	2.4.3 Charge Density Measurements	23
	2.5 Discussion	25
	2.6 Wavelength Dependence of Degenerate Four-Wave Mixing/Phase Conjugation in SBN Crystal	27
	2.7 Acknowledgement	28
3	Enhancement of Phase Conjugate Signal in Gamma Irradiated BaTiO_3: Possible Role of Color Centers and Resonance Phase Conjugation	46
	3.1 Introduction	46
	3.2 Experimental	47
4	Parametric Dependence of Energy Transfer and Coherent Two Beam coupling in BaTiO_3	59
	4.1 Introduction	59
	4.2 Experimental Procedure	59
	4.2.1 Experimental Setup	59
	4.2.2 Method of Parametric Study	60
	4.2.3 Method of Recording Experimental Data	60
	4.2.4 Method of Data Presentation	61
	4.3 Results and Discussion	61
	4.3.1 Angular Dependence	61
	4.3.2 Dependence on Points of Entry of Beam	62

4.3.3	Dependence on x(Points of Beam Entry) when the Beam falls on the c Face	63
4.3.4	Dependence on Angle of Incidence when beams Fall on c Face	64
4.3.5	Results when Horixontally Polarized Beam Interacts with Vertically orientated c Axis	64
4.3.6	Dependence of Energy Transfer on Points of Entry	64
4.3.7	Exchange of Energy in Two Beam Coupling in Photorefractive Crystals	65
4.3.7.1	For Orientations where there is no Self-Pump Phase Conjugation	65
4.3.7.2	For the Orientation where there is Phase Conjugation	66
5	New Beam Coupling in BaTiO₃	86
5.1	Introduction	86
5.2	Experiment	86
5.3	Results and Discussion	87
5.3.1	Coherent Beams	87
5.3.2	Incoherent Beams	91
5.3.3	Growth of Phase Conjugates when the Beams 1 and 2 are Incoherent	91
5.3.4	Growth of Phase Conjugates 1* and 2* for Coherent Beams	92
6	Role of Iron Group Impurities in the Microscopic Origin of Photorefractive Effects in BaTiO₃:EPR Investigations on Fe³⁺ and Cu²⁺ Under Laser Illumination	112
6.1	Introduction	112
6.2	Experimental Procedure	114
6.3	Characterizion of Impurity Centers in Barium Titanate	114
6.3.1	Fe ³⁺ Center in BaTiO ₃	115
6.3.2	EPR of Cu ²⁺ in BaTiO ₃	117
6.4	Effect of "In Situ" Laser Illumination	119
6.4.1	Mechanically Poled Crystal M1	120
6.4.2	Electrically Poled Crystal E1	121
6.4.3	Analysis of Time Dependence of Growth and Decay of Fe ³⁺	122
6.5	Discussion	123
6.5.1	Photo-Induced Valence Change and its Temperature Dependence	124
6.5.2	Decay and Growth Behavior	124
6.5.3	Surge in Fe ³⁺ Under Depleted Pump Condition and Mechanism of Growth of Transient Grating	125
6.6	Conclusions	127
7	Study of Photorefraction and EPR Experiments in BSO Single Crystal and Photoinduced Charge Transfer	146
7.1	Introduction	146
7.2	Optical Work with Phase Conjugation	146
7.2.1	Absorption	147
7.2.2	Optical Phase Conjugation	147

7.3 Study of the EPR of BSO:Fe ³⁺ under the He-Ne Laser Illumination and Photoinduced Charge Transfer	149
7.3.1 Background	149
7.3.2 Experimental	150
7.3.3 He-Ne Laser Illumination on EPR Lines and Charge Transfer on Fe ³⁺	150
7.3.4 Conclusion	153

Accession For	
NTIS CRA&I	<input checked="" type="checkbox"/>
DTIC TAB	<input type="checkbox"/>
Unannounced	<input type="checkbox"/>
Justification	
By	
Distribution /	
Availability Codes	
Dist	Avail and/or Special
A-1	

LIST OF FIGURES

Figure	Page
1.1 Experimental arrangement to study optical phase conjugation in photorefractive crystals through degenerate four-wave mixing.....	10
1.2 Schematic for self-pumping.	10
1.3 Experimental arrangement for incoherent beam coupling.	11
1.4 Signals at the detectors D_1 (full line) and D_2 (dashed line) vs time. $A_1 = 16.5$ mW and $A_2 = 4$ mW.....	11
1.5 Signals at the detectors D_1 (full line) and D_2 (dashed line) vs time. $A_1 = 9.5$ mW and $A_2 = 9$ mW.....	12
1.6 Parallelogram configuration for phase conjugation.....	13
1.7 Self-pumped phase conjugate signals: D_1 and D_2 are signals at detectors D_1 and D_2 in Fig. 1.6.....	14
1.8 Self-pumped phase conjugate signals at detectors D_2 in full line and those at detector D_1 in dashed line.....	15
2.1 Formation of a photorefractive index grating when two coherent beams interfere inside the crystal.....	31
2.2 Schematic experimental setup showing two writing beams 1 and 2, and expanded collimated beam.....	32
2.3 Absorption spectrum of pure SBN crystal in the spectral region 340 nm - 700 nm before gamma irradiation.....	33
2.4 Absorption spectrum of Ce:SBN crystal (0.1% Ce) in the spectral region 340 nm - 700 nm before gamma irradiation.....	34
2.5 Absorption spectrum of Cr:SBN crystal (1% Cr) in the spectral region 340 nm - 700 nm before gamma irradiation.....	35
2.6 Absorption spectrum of pure SBN crystal in the spectral region 185 nm - 905 nm after gamma irradiation.....	36

2.7	Absorption spectrum of Ce:SBN crystal (0.1% Ce) in the spectral region 185 nm - 905 nm after gamma irradiation.....	37
2.8	Absorption spectrum of Cr:SBN crystal (1% Cr) in the spectral region 185 nm - 905 nm after gamma irradiation.....	38
2.9	Decay time constant as a function of erasure beam intensity at various crossing angles for pure SBN crystal before gamma irradiation.....	39
2.10	Decay time constant as a function of erasure beam intensity at various crossing angles for pure SBN crystal after gamma irradiation.....	40
2.11	Decay constant rate per unit erasure intensity as a function of k^2 for Cr:SBN crystal before gamma irradiation.....	41
2.12	Decay constant rate per unit erasure intensity as a function of k^2 for Cr:SBN crystal after gamma irradiation.....	42
2.13	Schematic experimental setup of four-wave mixing.....	43
2.14	The normalized phase conjugate intensities for gamma irradiated pure SBN crystal at different wavelength from an Ar^+ laser.....	44
2.15	The plot of decay time of phase conjugate signal as a function of wavelengths for pure gamma irradiated SBN crystal.....	45
3.1	The plot of the PMT response as a function of time, using different wavelengths from an Ar^+ laser.....	51
3.2	The phase conjugate signal as a function of time at different wavelengths using a gamma irradiated mechanically poled $BaTiO_3$ crystal.....	52
3.3	The phase conjugate signal as a function of time at different wavelengths from an Ar^+ laser, using unirradiated electrically poled $BaTiO_3$ crystal #1.....	53
3.4	The phase conjugate signal as a function of time at different wavelengths, using an unirradiated $BaTiO_3$ crystal #2.....	54
3.5	The normalized phase conjugate intensity for the three crystals at different wavelengths.....	55
3.6	The plot of decay time constant of phase conjugate as a function of wavelengths.....	56

3.7 The optical absorption spectrum of unirradiated and gamma irradiated BaTiO ₃ crystal.....	57
3.8 Optical absorption of O ⁻ -trapped holes in low temperature (10K) x-irradiated undoped LiNbO ₃	58
4.1 Schematic of experimental setup.....	73
4.2 Free hand tracing of four-pen strip chart record output of four simultaneously recorded signals.	74
4.3 Change in transmitted intensities $\Delta A_{1t}=A_{1s}-A_{1i}$ and $\Delta A_{2t}=A_{2s}-A_{2i}$ in BaTiO ₃ crystal as the angle of incidence at the point of entry is changed. The point of entry is at x = 2.5 mm	75
4.3a Change in transmitted intensities in BaTiO ₃ crystal before γ -irradiation as the angle of incidence at the point of entry is changed. The point of entry is at x = 2.5 mm.....	76
4.4 Change in transmitted intensities $\Delta A_{1t}=A_{1s}-A_{1i}$ and $\Delta A_{2t}=A_{2s}-A_{2i}$ in γ -irradiated BaTiO ₃ crystal as the point of entry is changed. The angle of entry is 20°	77
4.4a Change in transmitted intensities in BaTiO ₃ crystal before gamma irradiation as the point of entry is changed.....	78
4.5 Change in transmitted intensities $\Delta A_{1t}=A_{1s}-A_{1i}$ and $\Delta A_{2t}=A_{2s}-A_{2i}$ in γ -irradiated BaTiO ₃ crystal as the point of entry is changed. The angle of entry is 10°.....	79
4.5a Change in transmitted intensities in BaTiO ₃ crystal before γ -irradiation as the point of entry is changed.....	80
4.6 Change in transmitted intensities $\Delta A_{1t}=A_{1s}-A_{1i}$ and $\Delta A_{2t}=A_{2s}-A_{2i}$ in γ -irradiated BaTiO ₃ crystal as the point of entry is changed. The angle of entry is 10°.....	81
4.6a Change in transmitted intensities in BaTiO ₃ crystal before γ -irradiation as the point of entry is changed.....	82

4.6b	Change in transmitted intensities in BaTiO ₃ crystal as the point of entry is changed.....	83
4.7	Change in transmitted intensities $\Delta A_{1t}=A_{1s}-A_{1i}$ and $\Delta A_{2t}=A_{2s}-A_{2i}$ in γ -irradiated BaTiO ₃ crystal as the angle of incidence at the point of entry is changed. The point of entry is 2.5 mm.....	84
4.7a	Change in transmitted intensities $\Delta A_{1t}=A_{1s}-A_{1i}$ and $\Delta A_{2t}=A_{2s}-A_{2i}$ in BaTiO ₃ crystal before g-irradiation as the point of entry is changed.....	85
5.1	Schematic of experimental setup for the pincushion effect using both coherent and incoherent light.....	97
5.2	Two beam coupling showing development of the fanned beam inside the crystal when two beams 1 and 2 are incident at the surface.	98
5.3	The simultaneous growth of the phase conjugates 1* and 2* of the coherent beams 1 and 2.....	99
5.4	Phase conjugate signal 1* (dashed line) and 2* (solid line) of two incoherent beams under two beam coupling. (Set I).....	100
5.5	Phase conjugate signal 1* (dashed line) and 2* (solid line) of two coherent beams when beam 2 is put off, (set 1).	101
5.5a	Fitted curve of phase conjugate signal 2* using equation 5.9 involving two exponential decays and one growth when beam 2 is put off, (set 1)....	102
5.5b	Fitted curve of phase conjugate signal 1* using equation 5.10 involving two exponential decays and one growth when beam 2 is put off, (set 1)....	103
5.6	Phase conjugate signal 1* (dashed line) and 2* (solid line) of two coherent beams when beam 2 is put off, (set II)..	104
5.6a	Fitted curve of phase conjugate signal 2* using equation 5.9 involving two exponential decays and one growth when beam 2 is put off, (set II).....	105
5.6b	Fitted curve of phase conjugate signal 1* using equation 5.10 involving two exponential decays and one growth when beam 2 is put off, (set II)..	106
5.7	Phase conjugate signal 1* (dashed line) and 2* (solid line) of two coherent beams when beam 1 is put off, (set III).....	107

5.8	Phase conjugate signal 1* (dashed line) and 2* (solid line) of two coherent beams when beam 1 is put off, (set IV).....	108
5.9a	Fitted curve of phase conjugate signal 1* using equation 5.11 involving one exponential growth when incoherent two beam coupling takes place. (Set I).	109
5.9b	Fitted curve of phase conjugate signal 2* using equation 5.12 involving one exponential growth when incoherent two beam coupling takes place. (Set I).	110
5.10	The simultaneous growth of the phase conjugates 1* and 2* of the coherent beams 1 and 2. because of vibrations, the growth curves do not show any fluctuations.	111
6.1(a)	EPR of Mechanically poled BaTiO ₃ crystal (M1), when H c-axis.....	130
6.1(b)	EPR of Mechanically poled BaTiO ₃ crystal (M1), when H ⊥ c-axis.....	131
6.2	EPR of E1-BaTiO ₃ crystal, when H c-axis.....	132
6.3	EPR of E1-BaTiO ₃ crystal, when H ⊥ c-axis.....	133
6.4	Angular variation of the EPR spectrum of Fe ³⁺ in (a,c) plane of Barium Titanate (E1).....	134
6.5	Angular variation of the EPR spectrum of Cu ²⁺ in (a,b) plane of Barium Titanate (M1).....	135
6.6	Angular dependence of g value in (a,c) plane.....	136
6.7	The effect of laser light on the EPR spectrum of Fe ³⁺ in M1 for H ⊥ c-axis....	137
6.8	Time dependence of the detector current under the condition of half bright and half dark illumination of mechanically poled crystal (M1).....	138
6.9	Recovery and decay of Fe ³⁺ signal under the condition of laser OFF and laser ON for M1-BaTiO ₃	139
6.10.(a)	Decay and (b) growth characteristic of Cu ²⁺ signal in M1-BaTiO ₃ when H ⊥ c-axis.....	140
6.11	The effect of half bright-half dark illumination on the line shape of 1/2 → -1/2 transition of Fe ³⁺ in E1-BaTiO ₃ crystal.....	141
6.12	Decay and growth of Fe ³⁺ intensity (1/2 → -1/2 line) in E1-BaTiO ₃ at room temperature with and without laser illumination respectively.....	142

6.13	The temperature dependence of the laser illumination effects on the intensity of $1/2 \rightarrow -1/2$ transition of Fe^{3+} in E1-BaTiO_3 crystal.....	143
6.14	Time dependence of the transmitted beam intensity of writing beam A_{10} after the second beam was switched OFF.....	144
7.1	Absorption spectrum of crystal C_1 in region 350 - 700 nm.....	156
7.2	Absorption spectrum of crystal C_1 in region 700 - 2600 nm.....	157
7.3	Schematic experimental setup of four wave mixing in BSO.....	158
7.4	Variation of signal intensity of Optical Phase Conjugation (arbitrary units) with wavelength in crystal C_1	159
7.5	Intensity of OPC signal for a "home grown" doped BSO crystal C_2 at different wavelengths.....	160
7.6	Decay time constants of OPC signal for a commercial BSO crystals C_3 at different wavelengths.....	161
7.7	Decay time constants of OPC signal for a "home grown" iron doped BSO crystal C_2 at different wavelengths.....	162
7.8	Intensity of Fe^{3+} cubic spectrum at room temperature with uniform laser illumination.....	163
7.9	Intensity of Fe^{3+} cubic spectrum at room temperature with nonuniform laser illumination.....	164
7.10	Intensity of Fe^{3+} noncubic spectrum of "home grown" BSO, with nonuniform illumination.....	165
7.11	Decay and growth of EPR signal intensity of Fe^{3+} at cubic site.....	166
7.12	Decay and decay time constants of EPR signal intensity at cubic site.....	167
7.13	Decay and decay time constant of EPR signal at noncubic site.....	168
7.14	EPR cubic spectrum of "home grown" iron doped BSO crystal C_2 at 77 K, without and with laser illumination.....	169

LIST OF TABLES

Table	Page
2.1 Dark Decay Times Obtained using Optically Induced Erasure Technique in Samples: Pure SBN, Ce:SBN and Cr:SBN, before and after Gamma Irradiation.....	22
2.2 The Values of k_{02} (in nw/c Units) and [pwo] Number per c.c. Values Obtained Using the Corresponding Values Reported for BaTiO ₃ as Reference Values...	25
4.1 Change in intensity vs angle of incidence at $x = 2.5$ mm.	69
4.1a Change in intensity vs angle of incidence at $x = 2.5$ mm at angles where there is self-pumped phase conjugation.....	69
4.2 Change in intensity vs point of entry at 20°	70
4.2a Change in intensity vs point of entry at 20° at x values where there is self-pumped phase conjugation	70
4.3 Change in intensity vs point of entry at 10°	70
4.4 Change in intensity vs point of entry at 10°	71
4.5 Change in intensity vs angle of incidence at $x = 2.5$ mm.....	71
4.6 Typical basic observed data used in Table 4.1 representing change in intensity vs angle of incidence at $x = 2.5$ mm.....	72
5.1 Decay time constants and magnitudes of equations 5.7 for coherent two beam coupling in BaTiO ₃ . Beam 1* at D1 is shown with beam 2 off	93
5.2 Decay time constants and magnitudes of equations 5.8 for coherent two beam coupling in BaTiO ₃ . Beam 2* at D2 is shown with beam 2 off.	93

5.3	Decay time constants and magnitudes of equations 5.7 for coherent two beam coupling in BaTiO ₃ . Beam 1* at D1 is shown with beam 1 off.	93
5.4	Decay time constants and magnitudes of equations 5.8 for coherent two beam coupling in BaTiO ₃ . Beam 2* at D2 is shown with beam 1 off.	94
5.5	Decay time constants and magnitudes of equations 5.7 for incoherent two beam coupling in BaTiO ₃ . Beam 1* at D1 is shown with beam 1 off.	94
5.6	Decay time constants and magnitudes of equations 5.8 for incoherent two beam coupling in BaTiO ₃ . Beam 2* at D2 is shown with beam 1 off.	94
5.7	Shows growth time constants and magnitudes for incoherent beams for signal 1* when two beam coupling takes place	95
5.8	Shows growth constants and magnitudes for incoherent beams for signal 2* when two beam coupling takes place	95
5.9	Shows growth constants and magnitudes for coherent beams for signal 1* when two beam coupling takes place	95
5.10	Shows growth constants and magnitudes for coherent beams for signal 1* when two beam coupling takes place when table is vibrated.	96
6.1	Time constant characterizing the decay of and growth of Fe ³⁺ signal on switching on/off laser light.....	145
7.1	Variation of phase conjugate signal intensity with wavelength in the undoped crystal C ₁	148
7.2	OPC signal in (a.u.) of "home grown" iron doped BSO crystal C ₂ at different wavelengths.....	155
7.3	Decay time constant (in seconds) of OPC signal for a commercial BSO at different wavelengths.....	155
7.4	Decay time constant (in seconds) of OPC signal for a "home grown" iron doped BSO crystal C ₂ at different wavelengths.....	155

Scientific Collaborators

Putchu Venkateswarlu Professor, Principal Investigator

V. K. Mago Research Assistant Professor 1990-92

N. Kukhterev Research Assistant Research Professor, Research Associate 1991-92

(Part Time)

M. D. Sastry Research Assistant Professor, Research Associate 1992-93

Mehdi Moghbel - Graduate Student (Ph. D.)

Michael Curley - Graduate Student (M. S.)

Garfield M. Percey - Graduate Student (M. S.) Part-time 1993-1994

Preface

This final performance report presents the results of the work carried out on the project on optical phase conjugation, beam couplings and effects of color centers in photorefractive crystals Barium Titanate (BaTiO_3), Strontium Barium niobate (SBN) and Bismuth Silicon Oxide (BSO). Color centers in crystals could be produced by doping the crystals with impurities or by irradiating them by radiation. The impurities could be also present inherently in the crystal. γ -irradiation has been used initially at the University of West Virginia with the help of Dr. N. S. Dalal and later at the University of North Carolina, Chapel Hill, NC with the help of Dr. S. Kalachandra. Absorption Spectra of the irradiated crystals immediately after irradiation were recorded in Chapel Hill by Dr. Laurie, E. McNeil. The BSO crystals were grown by Dr. M. D. Aggarwal and Dr. W. S. Wang in the Minority Research Center of Excellence in our University. We are thankful to these scientists for their help.

Electron Paramagnetic Resonance (EPR) Spectroscopy has been used in BaTiO_3 where Fe and Cu were inherently present and BSO which was doped with Fe. These experiments, under He-Ne laser illumination, gave useful information on photoinduced charge transfer in these crystals. SBN, SBN:Ce and SBN:Cu did not show EPR signals at room temperature, but they all gave good information on optical phase conjugation and the effects of γ -irradiation and impurities. The report contains seven chapters, the first one being an introduction.

Chapter 1

Introduction

1.1 Background

When a macroscopic material medium is subjected to electromagnetic radiation, the medium tends to be polarized. This effect characterized by induced polarization can be expanded in a power series given by [1.1],

$$P(E) = E\chi(E) = \chi^{(1)}(E) + \chi^{(2)}EE + \chi^{(3)}EEE + \dots \quad 1.1$$

where χ represents electric susceptibility, and E , the electric field. The linear susceptibility $\chi^{(1)}$ is a second rank tensor and is a complex quantity responsible for the optical phenomena of absorption, emission, reflection or refraction. The nonlinear susceptibility $\chi^{(2)}$ is a third rank tensor while $\chi^{(3)}$ is a fourth rank tensor with $3^{r+1} = 81$ elements, r being the order of the process [1.2].

The second order susceptibility $\chi^{(2)}$ is responsible for processes like second harmonic generation, while the third order susceptibility $\chi^{(3)}$ is responsible for the processes like optical phase conjugation, third harmonic generation, two photon absorption, stimulated Raman scattering, stimulated Brillouin scattering [1.1], etc. In centrally symmetric systems $\chi^{(2)}$ is zero, but $\chi^{(3)}$ is not.

Optical phase conjugation has been receiving increased attention because of its promise for application in many areas like coherent image amplification, optical filtering, pointing and tracking of moving objects, image processing and high resolution spectroscopy.[1.3,1.4]

One class of materials useful for the generation of phase conjugate beams is photorefractive crystals [1.5] like BaTiO_3 , $\text{Ba}_2\text{NaNb}_5\text{O}_{15}$ (BANANA), BSO, $\text{Sr}_{1-x}\text{Ba}_x\text{Nb}_2\text{O}_6$ (SBN) etc. In these materials, the index of refraction changes with the intensity of the incident light.

The efficiency of the grating depends on the photorefractive sensitivity of the material which in turn depends on the energy levels, the densities of the donors or traps, and on the charge migration in the material. Several theoretical and experimental investigations have been conducted on the effects of impurities in different photorefractive materials. Theoretical models have also been proposed for the light induced migration of charges, migration by diffusion and "hopping" of carriers to adjacent sites [1.6,1.7]. Both the models predict that grating formation and grating decay are exponential in time. These models have been applied to the study of phase gratings in poled and unpoled crystals and estimates of trap densities have been obtained. This is discussed in Chapter 2 for SBN crystals.

1.2 Degenerate Four-Wave Mixing

A popular method of generating optical phase conjugation is by degenerate four-wave mixing (DFWM) first proposed by Hellwarth [1.8] and used later by other workers [1.9,1.10]. It involves the interference of four light beams in a nonlinear medium. Three of the beams A_1 , A_2 , and A_3 of the same wavelength (Fig. 1.1) are input beams. One of them A_3 is the object beam whose conjugate is sought and the other two (A_1 and A_2) are reference beams which travel in opposite directions. The fourth beam A_4 is the phase conjugate beam of the object beam A_3 and emerges along the same line as A_3 but in the opposite direction. A_4 represents the Bragg diffraction of A_2 in the spatial grating (stationary in time) formed by A_1 and A_3 . Similarly, it represents the Bragg diffraction of A_1 in the spatial grating formed by A_2 and A_3 . A_1 and A_2 may be considered to form a temporally modulated grating [1.11] stationary in space. The probe beam A_3 scatters off this breathing grating which leads to the conjugate wave A_4 . An experimental arrangement to study optical phase conjugation by DFWM is shown in Fig. 1.1.

1.3 Self-Pumped Phase Conjugation

Feinberg [1.12] demonstrated self-pumped phase conjugation in a single domain crystal of BaTiO_3 in which the incident laser beam creates a fan of light that illuminates one of the edges of the crystal. The device operates by four-wave mixing using the photorefractive effect but without any external pumping beam or external mirror. The pumping beams are derived from the incident beam and are internally reflected inside the crystal adjacent to its edge. Fig. 1.2 explains the development of four-wave mixing and self-pumped phase conjugation [1.2]. It is predicted [1.12,1.13] that a beam can self-pump its own phase conjugate beam only if $\gamma L > 2.34$ where L is the interaction length and γ is a coupling parameter that depends on the electro-optic coefficients and the charge density of the crystal, and on the geometry of the optical beams relative to the crystal. From the sample used, γ is appreciable only for positive angles of incidence ϕ in the range $0 < \phi < 90^\circ$, so a beam incident from the left of the normal ($\phi < 0$) in Fig. 1.2 will not self-pump its own phase conjugate beam. However, we observed [1.14,1.15], in our sample of BaTiO_3 , that it is possible to self-pump even with $\phi < 0$ though with much lower efficiency than with $\phi > 0$. Feinberg [1.16] showed that a beam incident at $\phi > 0$ self-pumps itself and provides also the necessary pumping beams for other beams incident at any angle including negative ones. Phase conjugation of these beams occurs when they overlap the first beam (or its phase conjugate) in the crystal or when they overlap any of the stimulated filaments of fanned beam inside, that the first beam generated. The first beam and its phase conjugate act as counter propagating pumping beams for other incident beams. We discuss phase conjugation in Chapters 4 and 5 of this report.

Gunter et al.[1.17] observed sinusoidal intensity oscillations of the phase conjugate wave reflected from a self-pumped BaTiO_3 crystal. Experiments in our laboratory [1.18] showed that the frequency of oscillations decreased with decreasing wavelength and decreasing power of the laser.

Smout et al.[1.19] observed that the period of oscillations or self-pulsations in the output intensity from a self-pumped phase conjugate mirror varies not only with the incident laser intensity but also with the specific position and orientation of the crystal with respect to the input beam. By changing the displacement (x) of the incident beam from $x = 0$ mm to $x = 1$ mm, and keeping the angle of incidence at $\phi = 5^\circ$, the pulsating behavior and reflections changed drastically reaching a steady state at $x = 1$ mm and beyond. The pulsations were recorded [1.17] for the range $0^\circ \leq \theta \leq 15^\circ$ and no pulsations could be observed for $\theta > 40^\circ$ for any value of x . Other phase conjugations like double phase conjugation (DPC) by Sternklar et al.[1.20] and Weiss et al.[1.21] and Birdwing phase conjugation (BWPC) by Ewbank [1.22] have been reported by using a pair of incoherent beams. In BWPC as well as in DPC the resultant cross coupling of the two incident incoherent beams A_1 and A_2 produce a pair of phase conjugate beams, phase conjugate to A_2 and A_1 respectively without any image cross talk.

1.4 Incoherent Beam Couplings

Eason and Smout [1.23,1.24] carried out an analysis of mutually incoherent beam couplings in BaTiO_3 when they are incident on a single face of the crystal with incident angles of 15° and 16° in the quadrant favorable for self-pumping. They reported observations of a loop of light which provided a coupling mechanism between the two input beams resulting in two phase conjugate outputs. Results on beam couplings in BaTiO_3 self-pumped at 5145, 4880, 4765 and 4580 Å by two incoherent beams A_1 and A_2 with variable power ratios have been reported briefly from our laboratory [1.25]. Fig. 1.3 shows the experimental arrangement which is similar to the one used by Eason and Smout [1.23]. With a ratio of about 4:1 in powers of A_1 (16.5 mW) and A_2 (4 mW), the signal $A_1^*(t)$ at D_1 shows self-oscillations while $A_2^*(t)$ at D_2 remains steady when individually pumped (Fig. 1.4). Here $A_1^*(t)$ and $A_2^*(t)$ represent phase conjugates of A_1

and A_2 respectively. The frequency of oscillations at D_1 increases with the wavelength of the laser and its power. With simultaneous pumping, the signal at D_1 becomes stable and the one at D_2 goes to zero (see Fig. 1.4).

With the beam powers nearly equal, in the range, 6 - 17 mW $A_1^*(t)$ and $A_2^*(t)$ show up well under individual pumping, but do not coexist and each beam effectively erases the other beams grating under simultaneous pumping (Fig. 1.5).

1.5 Coherent Beam Couplings

Venkateswarlu et al.[1.14] used different configurations to study coherent beam couplings. In the first case which is a parallelogram configuration, two coherent beams A_1 (3.9 mW) and A_2 (4.4 mW) from an Ar⁺ laser (4580 Å) cross (with $\theta = 40^\circ$) in an electrically poled BaTiO₃ crystal with the horizontal laser polarization parallel to the c axis (Fig. 1.6). If the crystal is individually exposed to A_1 (or A_2), one observes self-pumped beam $A_1^*(t)$ [or $A_2^*(t)$]. When A_1 is allowed to enter the crystal after the self-pumped phase conjugate signal $A_2^*(t)$ levels off, there is a sudden increase in the signal at detector D_2 (see Fig. 1.7). The signals at D_2 and D_1 are represented in the same manner as in the earlier section. One can see from Fig. 1.7 that the steady-state values of $A_2^*(t)$, $\hat{A}_1(t)$ and $\Delta_2(t)$ are in the approximate ratio 9:36:7. One can see in a similar manner that $A_1^*(t)$, $\hat{A}_2(t)$ and $\Delta_1(t)$ are in the ratio 8:175:6. A_1 and A_2 both self-pump but $A_1^*(t) \ll A_2^*(t)$ and $\hat{A}_2(t) > \hat{A}_1(t)$. Here $\hat{A}_1(t)$ and $\hat{A}_2(t)$ represent the beams A_1 and A_2 getting Bragg diffracted due to fanning into the reverse direction of A_2 and A_1 respectively. $\Delta A_1(t)$ and $\Delta A_2(t)$ represent the grating erasure effects on $A_1^*(t)$ and $A_2^*(t)$ by the beams A_2 and A_1 respectively.

In a separate parallelogram experiment, the self-pump of the beams A_1 and A_2 and their beam couplings are studied at different points of entrance on the crystal surface, at different excitation wavelengths and at different powers. The beam crossing angle is 48°

and the angle of incidence of A_2 is 20° . If the point of entry is 1.5 mm from the edge nearest to A_2 , A_2 shows systematic oscillations whose frequency increases with wavelength and power while A_1 continues to be steady (see Fig. 1.8). If both beams A_1 and A_2 pump simultaneously, the detectors at D_1 and D_2 both show about 16-fold increase in intensities (Fig. 1.8). Thus, the signal at D_2 under simultaneous pumping represented by $[A_2^*(t) + \hat{A}_1(t) - \Delta_2(t)]$ is about 16 times more than the signal $A_2^*(t)$ under individual pumping. Similar observations are made with the signals at D_1 . This is because due to significant mutual fanning, A_1 and A_2 Bragg diffract considerably into the reverse directions of each other to D_2 and D_1 respectively making $\hat{A}_2(t) \gg A_1^*(t)$ and $\hat{A}_1(t) \gg A_2^*(t)$. The self-pump of A_1 is found to be better with 4580 Å and 4765 Å excitations than with other wavelengths.

1.6 Optical Phase Conjugation in Resonant/Saturable Absorptive Systems with Color Centers

In addition to systems which show nonresonant nonlinearity and nonresonant optical phase conjugation discussed so far, there are systems where resonant energy levels exist because of color centers due to radiation effects or because of inherent or doped impurities. Saturable absorptive/resonant systems generate optical phase conjugation because of population modulation and resonant third order nonlinear susceptibility at resonant wavelengths or at those wavelengths where saturable absorption is possible.

Four-wave mixing and optical phase conjugation have been demonstrated by Basiev et al.[1.26] with F_2^- center in LiF using high power pulsed excitation by Nd^{3+} YAG radiation at 1.06 μm . Rand [1.27] recently reported cw four-wave mixing and phase conjugation using F_2 color centers in LiF crystal. The resonance in γ -irradiated LiF at room temperature was shown to arise from saturated absorption involving intersystem crossing of F_2 centers and has a width that reveals the excited triplet to ground state decay

rate. Rand demonstrated the elimination of aberration in these optical phase conjugation experiments with LiF having F_2 centers.

Volume holographic grating formation and optical phase conjugation was obtained through resonant nonlinearity in Ruby crystal [1.28-1.32], KCl doped with ReO_4 [1.31] Na vapour [1.32] etc.

The theory of conjugate reflection via resonant saturation was first developed by Abrams and Lind [1.33]. They utilized the well known nonlinear susceptibility of a homogeneously broadened two level absorber, which upon resonance sets up an amplitude grating that couples counter propagating waves and the probe wave, to generate a conjugate wave. In other words, spatial modulation of the susceptibility due to local gain saturation (spatial hole burning) acts as a volume hologram with the result that the counter propagating pump wave gets diffracted and generates the conjugate wave. The nonlinear susceptibility involved in the resonance interaction in a saturable absorber depends not only on E^2 but also on higher order terms.

The first transitory hologram by saturable absorption involving Ruby was reported by Hill [1.28]. Liao and Bloom [1.29] demonstrated a wave from conjugation by degenerate four wave mixing in ruby crystal using a 5145 Å cw Ar^+ laser, which in the bright regions of the illuminated space takes some of the Cr^{3+} ions in the ground 4A_2 state to 2E state via the continuum of states 4T etc. This produces $Cr^{3+} (^2E)$ ion in the bright regions of the grating while the $Cr^{3+} (^4A_2)$ ions in the dark regions remain unaffected. this situation leads to a spatial modulation of the Cr^{3+} ground state population resulting in a refractive index grating because of the difference in absorption coefficients of the two kinds of ions. Conversion efficiency of 3% in the conjugate wave front generation was obtained in these studies. Catunda et al. [1.30] measured the nonlinear index of refraction n_2 of $Al_2O_3:Cr^{3+}$ (ruby) and $GdAlO_3:Cr^{3+}$ and showed that the crystals are nonlinear at Ar^+ laser wavelengths. Shand [1.31] demonstrated the enhancement of third order susceptibility due to electronic transition in Tb^{3+} in terbium aluminum garnet ($TbAlG$).

1.7 The Present Work

The present work is aimed at understanding the basic mechanism of photorefraction, particularly the possible role of impurities and radiation induced color centers, and to understand the factors influencing energy transfer between the beams causing the interference pattern.

The crystals investigated are BaTiO_3 , SBN, SBN doped with cerium and chromium and BSO.

The techniques used are (i) two beam coupling (ii) degenerate four-wave mixing and phase conjugation and (iii) Electron Paramagnetic Resonance (EPR) Spectroscopy.

Parametric dependence of beam coupling and phase conjugation forms an important part of this report and is given in Chapter 4. In this process a new beam coupling and phase conjugation have been found and the results are reported in Chapter 5. The effects of impurities and radiation on optical phase conjugation characteristics in SBN are discussed in Chapter 2. These effects on BaTiO_3 are discussed in Chapter 3 while those in BSO are given in Chapter 7.

The effects He-Ne laser illumination on the EPR lines of iron and copper in BaTiO_3 and the photoinduced charge transfer on these ions in this crystal are presented in Chapter 6. Similar work on BSO is discussed in Chapter 7.

References

- 1.1 R. A. Fisher, Optical Phase Conjugation, Academic Press, New York (1983).
- 1.2 P. Venkateswarlu, M. Moghbel, P. Chandra Sekhar, M. C. George and A. Miahnahri, Beam coupling in BaTiO_3 and Phase Conjugation Effects in Laser Spectroscopy and Nonlinear Effects in Solids, edited by S. Radhakrishna and B. C. Tan, Narosea Publishing House, New Delli, 1990.
- 1.3 D. M. Pepper, Scientific American 254, 74, (1986).
- 1.4 P. Venkateswarlu, M. C. George, H. Jagannath, R. G. Mitchell and A. Miahnahri, Volume Holographic Gratings and Optical Phase Conjugation in Nonresonant and Resonant Systems in Proceedings of the Second Asia-Pacific Physics Conference, Bangalore, 1986, editor, S. Chandrasekhar, World Scientific Publishing Co., Singapore (1987).

- 1.5 D. L. Staebler, Holographic Recording Materials, editor H. H. Smith, Springer-Verlag, Berlin (1977).
- 1.6 J. Feinberg, D. Heiman, A. R. Tanguay Jr., and R. W. Hellwarth, J. Appl. Phys., 51,1297, (1980).
- 1.7 R. J. Townsend and J. T. Lamanchia, Appl. Phys. 41, 5188, (1970).
- 1.8 R. W. Hellwarth, J. Opt. Soc. Am., 67,1,(1977)
- 1.9 J. Feinberg, Optical Phase Conjugation in Photorefractive Materials in reference 1.1.
- 1.10 H. Jagannath, R. G. Mitchell, M. C. George and P. Venkateswarlu, Ind. J. Phys. 60b, 99, (1986).
- 1.11 D. M. Pepper and A. Yariv, Conjugation by Parametric Mixing in Transparent Media in reference 3.
- 1.12 J. Feinberg, Opt. Lett., 7,486, (1986).
- 1.13 K. R. McDonald and J. Feinberg, J. Opt. Soc. Am., 73, 548, (1983)
- 1.14 P. Venkateswarlu, P. Chandra Sekhar, H. Jagannath, M. C. George and M. Moghbel, Coherent Beam Coupling and Pulsations in Self-Pumped BaTiO₃ in Conference on Lasers and Electro Optics Technical Digest Series, 7, 220-221, Opt. Soc. Am., Washington, DC, (1988).
- 1.15 M. Moghbel, Coherent Beam Coupling in BaTiO₃ and the Effects of Self-Pumping in Reflection and Transmission, M. S. thesis, Alabama A&M University, Huntsville, AL (1989).
- 1.16 J. Feinberg, Opt. Lett., 8, 480 (1983)
- 1.17 P. Gunter, E. Voit and M. Z. Zha, Opt. Comm.,55, 210 (1985).
- 1.18 P. Venkaswarlu, P. Chandra Sekhar, M. Dokhanian and A. Miahnahri, Coherent Beam Couplings and Self-Oscillations in BaTiO₃, OSA Annual Meeting, Technical Digest Series, 11, 169, Opt. Soc. Am. Washington, DC, (1988).
- 1.19 A. M. C. Smout and R. W. Eason, Opt. Comm., 59, 77, (1986).
- 1.20 S. Sternklar, S. Weiss, M. Sergev and B. Fisher, Opt. Lett., 11, 528, (1986).
- 1.21 S. Weiss, S. Sternklar and B. Fisher, Opt. Lett., 12, 114, (1987).
- 1.22 M. D. Ewbank, Opt. Lett., 13, 47, (1988).
- 1.23 R. W. Eason and A. M. C. Smout, Opt. Lett., 51, (1987).
- 1.24 A. M. C. Smout and R. W. Eason, Opt. Lett., 12, (1987).
- 1.25 P. Venkateswarlu, H. Jagannath, M. C. George and A. Miahnahri, Beam Coupling and Self-Pulsation, International Laser Science Conference (ILS III), Atlantic City, Optics News 73, 62, (1987) Opt. Soc. Am., Washington, DC ,(1987).
- 1.26 T. T. Basiev, Yu K. Voronko, P. G. Zverev, S. B. Mirov and A. M. Prokhorov, Sov. Tech. Phys. Lett., 8, 658, (1982).
- 1.27 S. C. Rand, Opt. Lett., 135, (1986).
- 1.28 K. O. Hill, appl. Opt., 10, 1965, (1971).
- 1.29 P. F. Liao and D. M. Bloom, Opt. Lett., 3, 4, (1978).
- 1.30 T. Catunda, J. P. Andreeta and J. C. Castro, Appl. Opt., (1986) in publication
- 1.31 D. E. Watkins, J. F. figueria and S. J. Thonas, Opt. Lett., 2, 59, (1980).
- 1.32 D. M. Bloom, P. F. Liao and N. P. Economon, Opt. Lett.,2, 59, (1978).

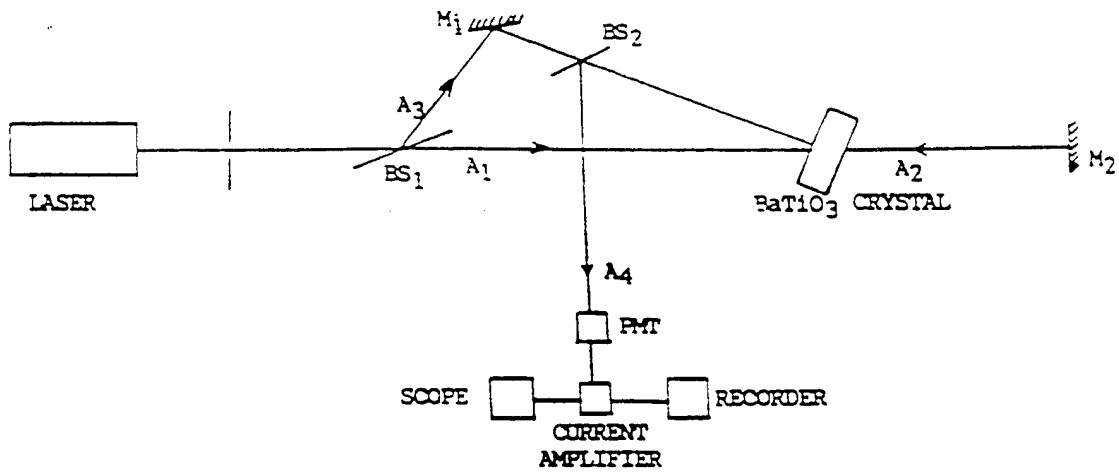


Fig. 1.1 Experimental arrangement to study optical phase conjugation in photorefractive crystals through degenerate four-wave mixing: M, mirrors; BS, beam splitters (Ref. 1.10).

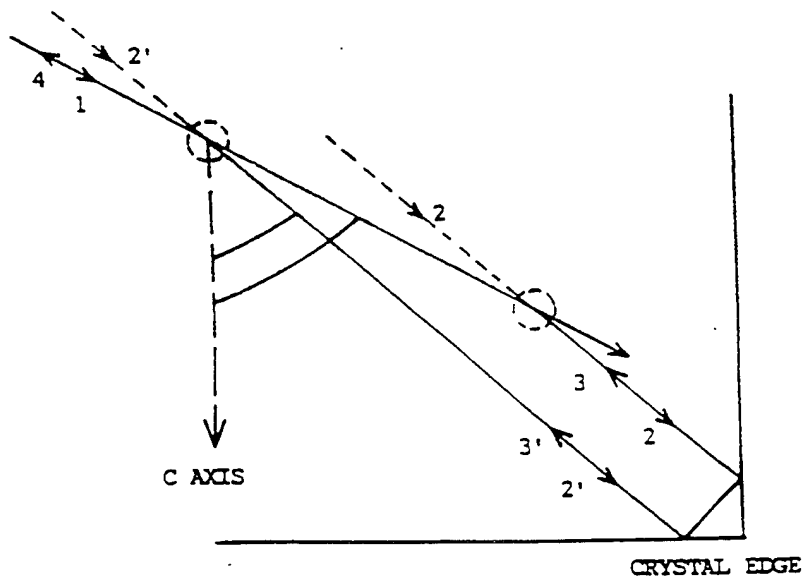


Fig. 1.2 Beam (1) enters the crystal from top left. Beam 2 splits off and is internally reflected twice near the crystal edge and becomes beam 3', which later intersects beam 1. Beam 2' has also split off from beam 1 and travels around the loop in the opposite direction. Beams 1', 2' and 3' also generate beam 4 in the interaction region circled on the left. Beam 4 is the phase-conjugate replica of beam 1, and it leaves the crystal in the direction opposite to that of the incident beam. [Feinberg, Ref. 1.12]. The dashed extensions of the beams 2 and 2' are only for clarity.

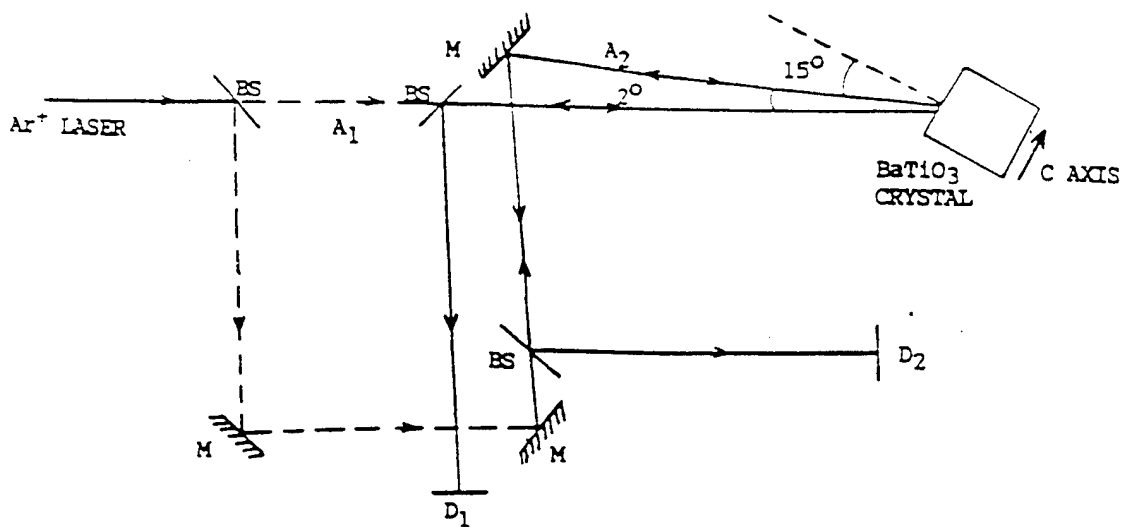


Fig. 1.3 Experimental arrangement for incoherent beam coupling. Beams A_1 and A_2 are incoherent. Path difference 150 cm. Multimode Ar^+ laser. M, mirrors; BS, beam splitters; D_1 detectors. [Ref 1.2].

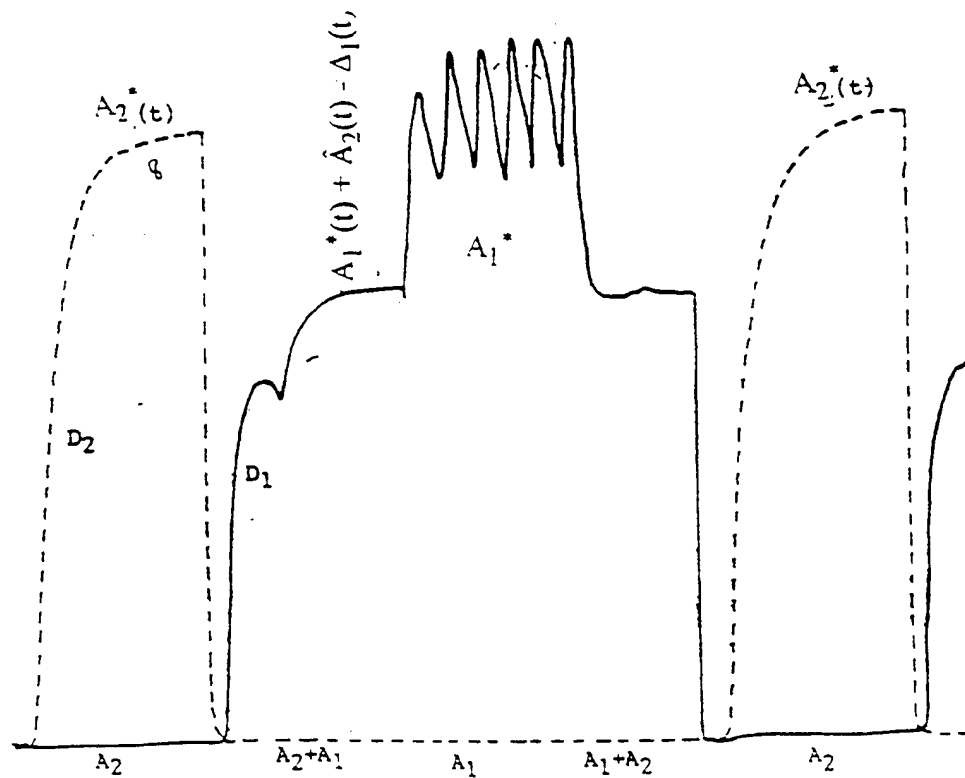


Fig. 1.4 Signals at the detectors D_1 (full line) and D_2 (dashed line) vs. time. $A_1 = 16.5 \text{ mW}$ and $A_2 = 4 \text{ mW}$ [Ref 1.2].

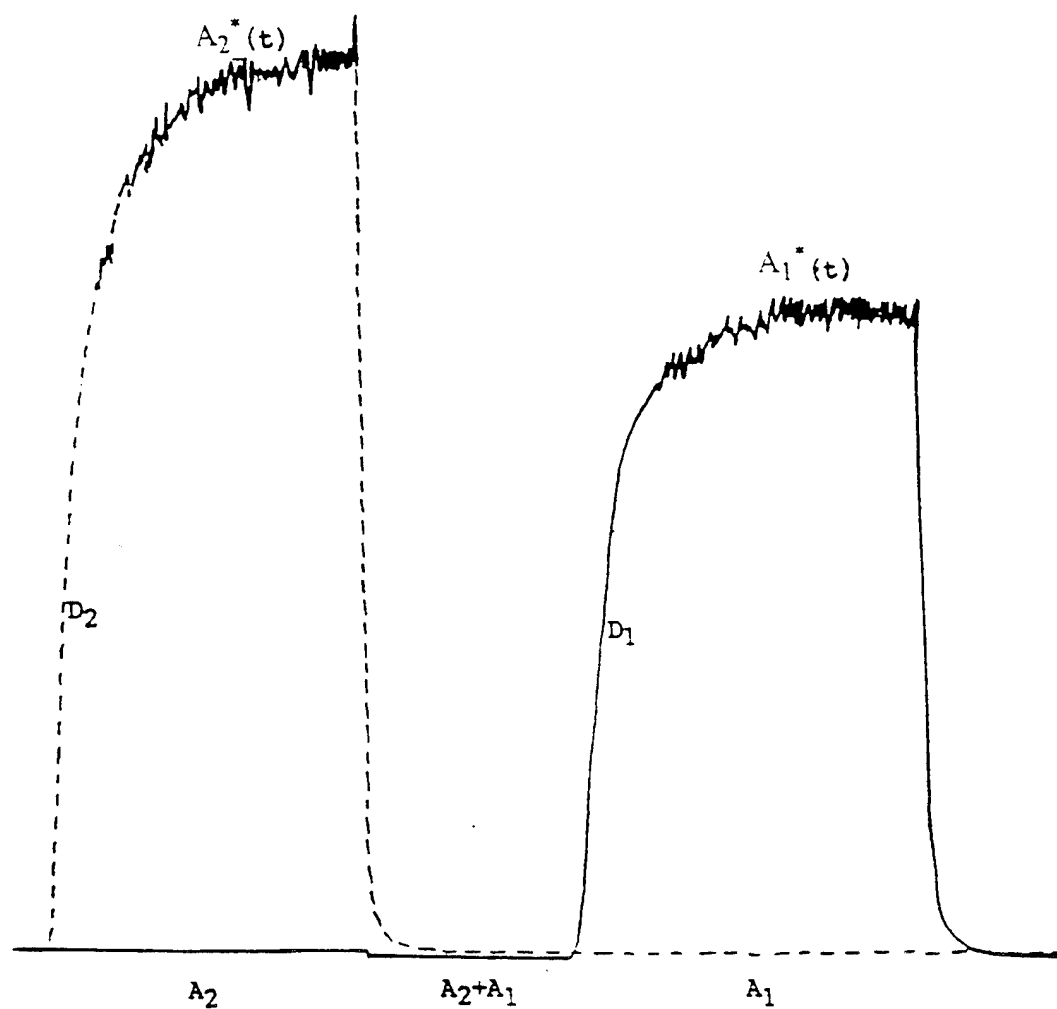


Fig. 1.5 Signals at the detectors D1 (full line) and D2 (dashed line) vs. time. $A_1 = 9.5$ mW, $A_2 = 9$ mW. Total time 12 min. [Ref. 1.2].

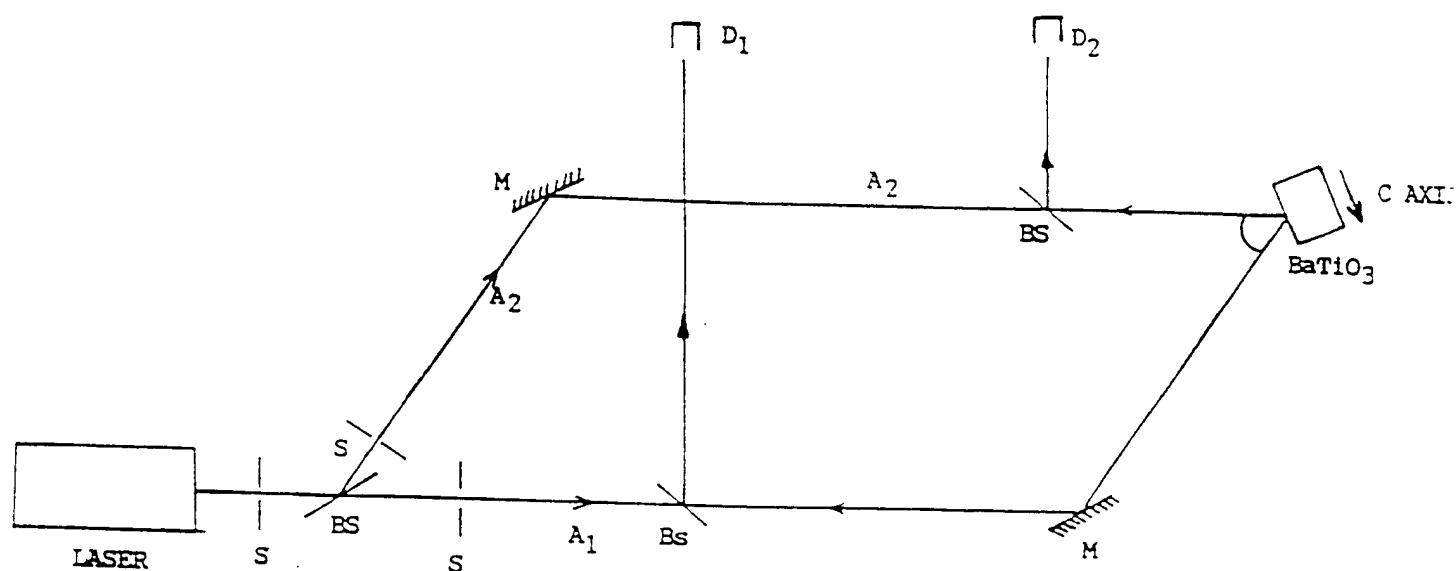


Fig. 1.6 Parallelogram configuration for phase conjugation: BS beam splitters; M, mirrors; S-slits; D_1 , D_2 , detectors; A_1, A_2 , input beams which meet at the center of the crystal; $A_1(t)$, $A_2(t)$, self-pumped phase conjugates of A_1 , A_2 ; $\hat{A}_1(t)$, $\hat{A}_2(t)$ cross-coupled beams of A_2 and A_1 respectively. Ref. (1.14).

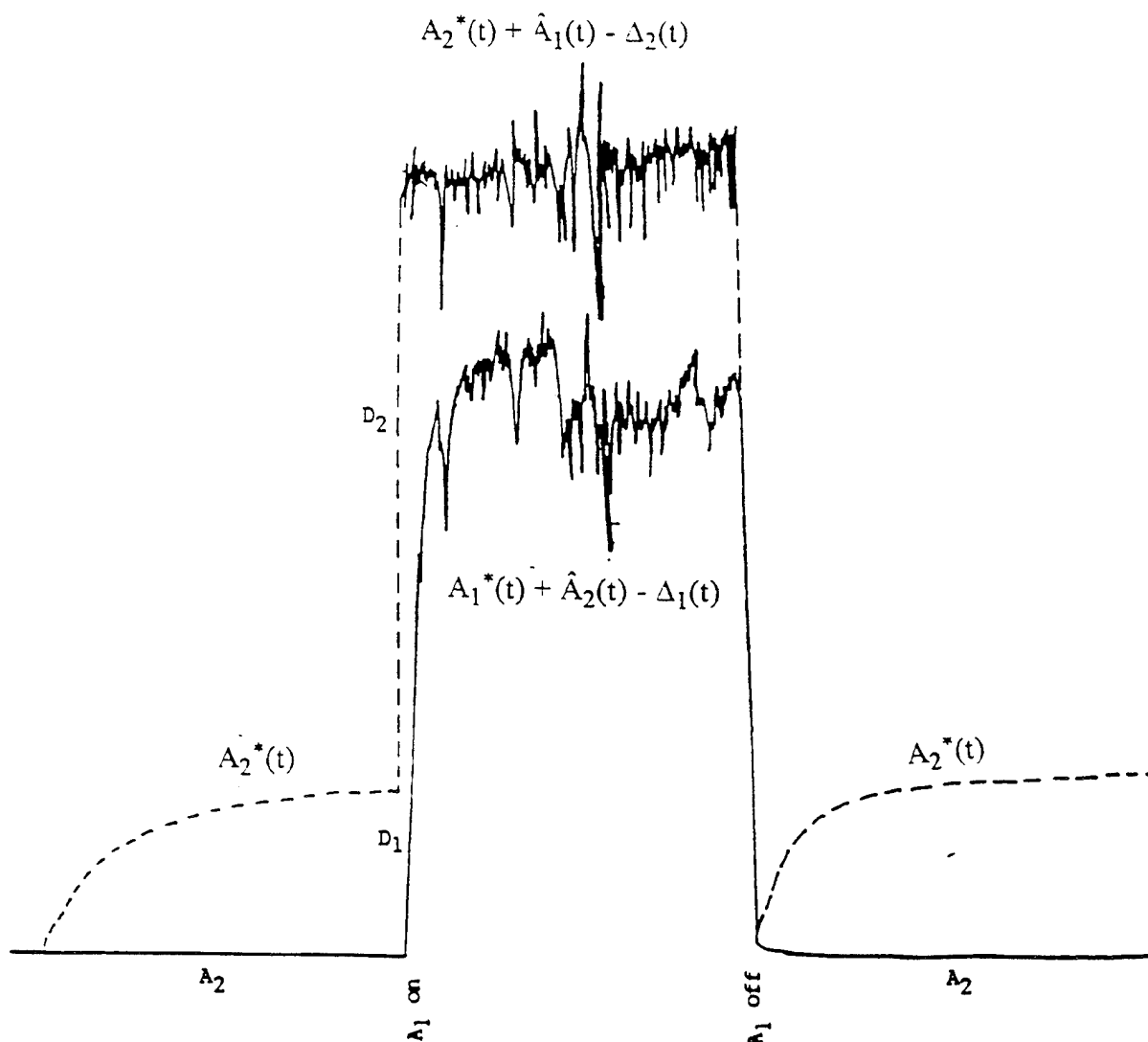


Fig. 1.7 Self-pumped phase conjugate signals: D_1 and D_2 are signals at detectors D_1 and D_2 in Fig. 1.6. $\Delta_1(t)$ and $\Delta_2(t)$ are erasure effects on $A_1^*(t)$ and $A_2^*(t)$ due to A_2 and A_1 respectively. Ar⁺ laser (4580 Å) has horizontal polarization; continuous line represents the signal at D_1 and dashed line the signal at D_2 . Total time: 5 min. (Ref. 1.14).

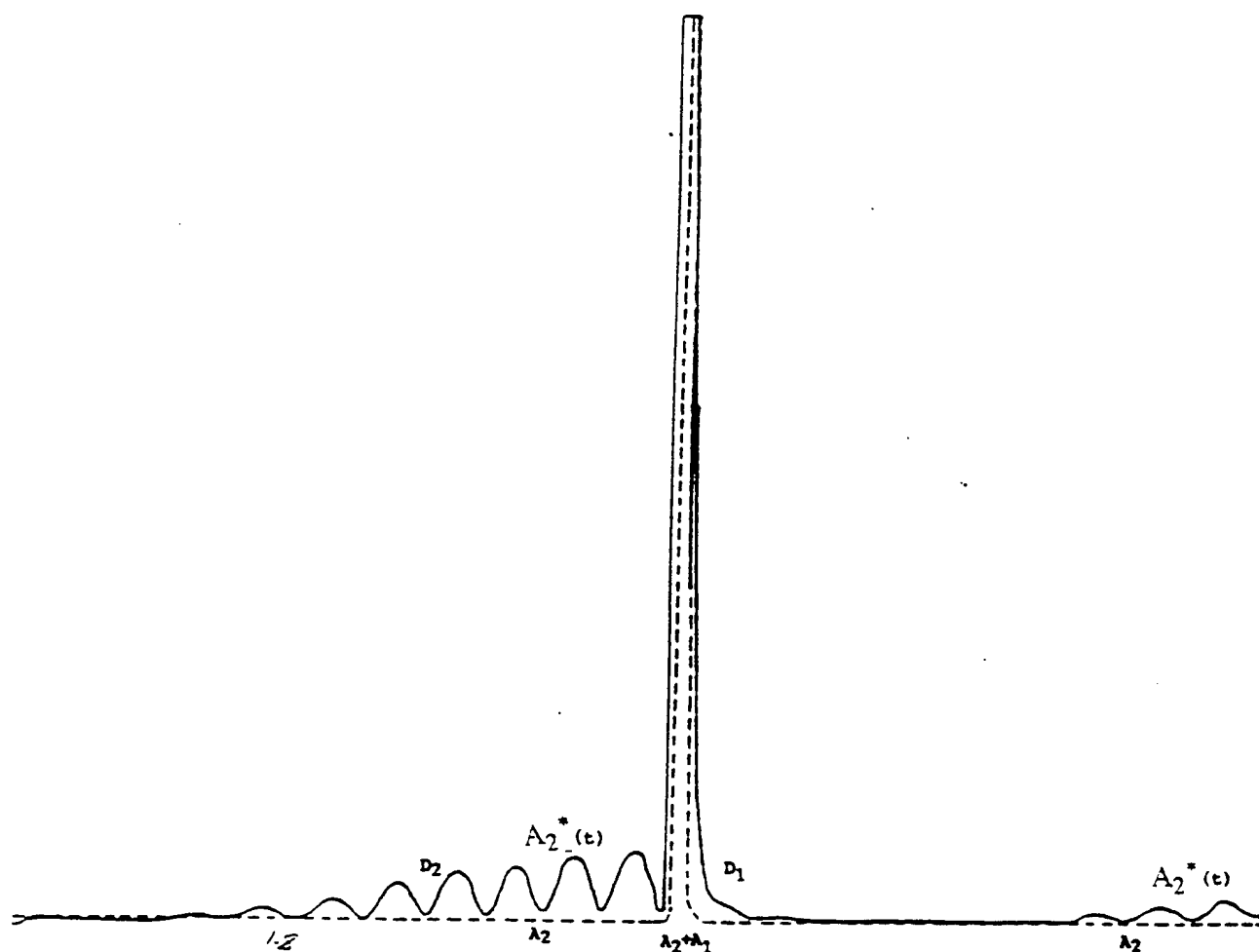


Fig. 1.8 Self-pumped phase conjugate signals at detectors D_2 in full line and those at detector D_1 in dashed line. Ar⁺ laser at 4765 Å. Parallelogram configuration with beam crossing angle as 48°. Beam A_2 enters at 1.5 mm from the nearest edge with 20° angle of incidence. Under individual pumping the signal at D_2 oscillates but not the one at D_1 . When A_1 is also opened, the signal at D_2 increases 16 times, and the signal at D_2 also shoots up. Total time 10 min. (Ref. 1.2).

CHAPTER 2

Optically Induced Grating Erasure Studies and Determination of Charge Carrier Densities in $\text{Sr}_{0.75}\text{Ba}_{0.25}\text{Nb}_2\text{O}_6$: Effects of Gamma Irradiation and Ce and Cr Doping

2.0 Introduction

Since the discovery of photorefractive effect (originally called optical damage) by Askin *et al.* [2.1], considerable work has been reported in LiNbO_3 , and subsequently in BaTiO_3 [2.2-2.5]. In view of the potential applications of the photorefractive effect in optical communications, etc., a number of investigations were directed to arrive at the materials having desired response times. Therefore, from the basic research point of view, the problem to be addressed is to find out and optimise the, controllable parameters which affect the response times.

2.1 Some "Facts" About $\text{Sr}_{0.75}\text{Ba}_{0.25}\text{Nb}_2\text{O}_6$ and the Problems Addressed

Photorefractive materials are usually electrical insulators with band gaps in the range 5 - 8 eV. These materials possess deep electron trapping centers containing photoexcitable charges. For materials such as SBN, electrons were

reported to be mobile charges on photoexcitation [2.6,2.7]. These traps in SBN are deeper and cannot be thermally ionized at room temperature, and can be detrapped only in the presence of light. Therefore when the light is turned off, charges remain localized in the "darker" regions of the crystal for a significant time, varying up to a few hours, unless the crystal is illuminated with a new pattern.

The light induced separation and migration of charges bring about an electrostatic field which, according to Kogelnik Theory [2.8], is 90° out of phase with the incident intensity pattern. Figure 2.1 shows the charge distribution is 180° out of phase with the incident intensity pattern, while the electrostatic field is phase shifted by 90° , also demonstrating the decay of a photorefractive index grating.

The practical applications of a photorefractive crystal depend upon the linear electro-optic coefficient. This can be both large and highly anisotropic in a photorefractive SBN crystal. The three electro-optic coefficients of interest in SBN [2.9] are: $r_{33} = 1340 \times 10^{-12}$ m/v, $r_{13} = 67 \times 10^{-12}$ m/v and $r_{51} = r_{42} = 42 \times 10^{-12}$ m/v.

The concern in this section is the characterization of SBN, SBN doped with 0.1% cerium, and SBN doped with 1% chromium (measuring $4.8 \times 5.5 \times 9.0$ mm³, $5.0 \times 5.4 \times 6.0$ mm³ and $4.4 \times 5.3 \times 4.7$ mm³ respectively) for their photorefractive properties by employing an optically induced-grating-erasure technique [2.6]. With the help of this technique, the photorefractive parameters, particularly the growth and decay constant of the photorefractive grating were determined, and their dependence on dopants Cr^{3+} and Ce^{3+} , and also the gamma irradiation were investigated at different intensities of the erasure beam. These

investigations were aimed at finding the conditions of improved photorefractive behavior of SBN.

Enhancing the photorefractive effect has been the goal of considerable materials research. In earlier times, workers [2.10] suggested that the photorefractive effect was caused by impurities or defects in photorefractive crystals. Subsequently, Peterson *et al.* [2.11] found that the magnitude of the photorefractive effect could be controlled by modifying the Fe impurity concentration in LiNbO_3 . Ewbank *et al.* [2.12] and Wood *et al.* [2.13] have examined extensively both undoped and Ce doped SBN crystals. The photorefractive SBN had an advantage over others in that its crystal structure contained a number of vacant lattice sites [2.14]. Therefore, these vacant sites could be filled by a number of dopants.

2.2 Sample Preparation

The crystals used in the present work were purchased commercially from JTT International in Orlando, Florida. One of the three was nominally pure and the concentration of impurities of the two others were 0.1% cerium and 1% chromium. These crystals were irradiated using a ^{137}Cs (caesium) source with dose rate of 0.8 Mrad h^{-1} [2.15]; ambient temperature = 35°C , to accumulative dose of 21 Mrad. The irradiation was done at the University of North Carolina at Chapel Hill.

2.3 Experimental Procedures

The absorption spectra of these crystals were recorded in the spectral region 185 nm - 905 nm using a Varian Spectrophotometer model Dms-200, after irradiation with gamma rays, and in the spectral region 340 nm - 700 nm using a Perkin Elmer Prism Spectrophotometer, before irradiation with gamma rays. This was done to understand the effects of impurities and the radiation induced centers on the optical properties.

In our two beam coupling experiments, schematically shown in Fig. 2.2, two coherent beams of light writing the index grating crossed each other inside the crystal. At the intersection of these two coherent beams inside the sample, a periodic modulation of a refractive index was created. The polarization of the incident beams was vertical, making a 90° angle with respect to the c-axis of the crystal. A third beam from the same laser source was expanded with a beam expander. Then, by placing a positive lens where a collimated beam of light was used to erase the index, grating formed inside the crystal. The power ratio of the writing beams and the erasure beam was around 1 to 4 (2.86 mW/cm^2 and 10.3 mW/cm^2 respectively). The erasure beam was incident on the crystal having a diameter of around 8 mm so that the crystal was flooded with a uniformly intense beam of light ($m=0$). To avoid a significant erasure effect by the writing beams, their intensities were kept lower than that of the erasure beams. To facilitate the recording of the decay of the grating, two shutters, one on the probe and the second on the erasure beam path length were positioned. By keeping the second shutter blocked and the first shutter open, enough time was given for the complete formation of the grating (at steady state). To record the decay of the index grating,

simultaneously, the shutter at the probe beam (first shutter) was closed and immediately after, the shutter at the erasure beam (second shutter) was opened. With this kind of arrangement, the PMT detector could only monitor the diffracted signal of the reading beam while the erasure beam was washing the index grating. The intensity of erasure beam was varied using neutral density filters. Using this method the dependence of grating erasure time on the erasure beam intensity was investigated. This essentially generated the data containing the dependence of charge relaxation time on the light intensity at a given wave vector or the beam crossing angle. Further, by repeating this experiment at different angles, the dependence of photoinduced charge relaxation on the grating wave vector was investigated.

Hence the decay rates as a function of erasure beam intensity at various grating wave vectors (crossing angles) could be evaluated. These measurements were carried out on six systems: pure SBN, SBN doped Cr^{3+} , SBN doped with Ce^{3+} and these three crystals after subjecting them to a gamma dose of 21 Mrad.

2.4 Experimental Results

2.4.1 Electronic Absorption

The electronic absorptions of pure SBN, Ce and Cr doped SBN before and after gamma irradiation are shown in Figs. 2.3-2.8.

It may be appropriate to mention here that the Cr doped sample showed the fastest photorefractive response among the systems investigated here. This may be because the Cr^{3+} absorption peak overlaps with the He-Ne excitation.

2.4.2 Optically Induced Grating Erasure Measurements

The optically induced grating erasure measurements were carried out to investigate the rate of grating erasure with light and deduce the dark decay time and charge carrier density [2.6]. This closely followed the methodology developed by Feinberg *et al.* [2.6], under the assumption of a single trap model. Feinberg, in a subsequent paper [2.16] revised this method to include a multitrap model. In case of SBN, as will be shown below, the charge carrier density did not substantially change with gamma irradiation and Cr and Ce doping suggesting that the single trap model is probably valid, particularly at $\lambda = 632 \text{ nm}$ (He-Ne laser).

The decay time of the grating was measured by two beam coupling at different intensities, obtained using neutral density filters. The decay time constants were obtained for different erasure beam intensities at a specific angle between the beam, i.e. for a fixed grating wavevector k . Similar measurements were made at different angles between 70° and 108° (measured externally). The reciprocal of decay time constant ($1/\tau$) as a function of erasure beam intensity for pure SBN, Cr:SBN, Ce:SBN and these crystals after gamma irradiation were drawn and those for pure SBN are shown in Figs. 2.9 and 2.10. These figures show that these were linearly related, with slopes increasing with the increase of angle of intersection of the beams. Further, we know that all these straight lines nearly converged for zero intensity of the erasure beam. This point gives the inverse of dark decay time. Table 2.1 lists the dark decay times for all the six cases. There was a spread in the value of dark decay constant (τ^{-1}) as the convergence of the erasure beam intensity I vs τ^{-1} lines was not too good in some cases. The probable spread in the

values of τ_{dark} is given in Table 2.1. However, this does not affect the general conclusions drawn from the comparative values of $(\tau_{\text{dark}})^{-1}$.

Table 2.1: Dark Decay Times Obtained using Optically Induced Erasure Technique in Samples: Pure SBN, Ce:SBN and Cr:SBN, before and after Gamma Irradiation.

τ_{dark} (in minutes)

Crystals	Before gamma irradiation	After gamma irradiation
Pure SBN	20 ± 8	0.65 ± 0.05
Ce : SBN	6 ± 1	1.5 ± 0.5
Cr : SBN	0.8 ± 0.3	0.15 ± 0.05

From the τ_{dark} values, given in Table 2.1, it could be inferred that the presence of impurities as well as γ -irradiation lower the dark decay at room temperature.

2.4.3 Charge Density Measurements

From Figures 2.11 and 2.12 the rate of decay of grating depends upon the grating wave vector . This is similar to what has been reported in the case of BaTiO₃ by Feinberg [2.6] who has shown that decay constant rate per unit erasure beam intensity varied linearly as k^2 in unit of $(n\omega/c)$, where n is the number density of carriers, ω is the frequency of excitation and c is the velocity of light. The variation of $(1/\tau)$ as a function of $k^2/(n\omega/c)^2 = 4\sin^2 \theta$, where θ is the angle of refraction has been drawn for the three crystals. This is shown in Figs. 2.11 and 2.12 for Cr:SBN before and after irradiation. From this, the value of k_0^2 which is the ratio of intercepts to slopes in Figures 2.11 and 2.12 was determined. The value of k_0^2 (characteristic wave vector) is related to the average density of migrating charges ($\rho\omega_0$) at a temperature "T" by the equation [2.6]

$$k_0^2 = \rho\omega_0 q^2 / \epsilon\epsilon_0 k_B T$$

where ω_0 = average charge distribution amplitude.

ρ = average density of mobile charges.

q = electronic charge.

ϵ = dielectric constant.

ϵ_0 = permittivity of the medium.

k_B = Boltzmann constant.

Feinberg calculated $\rho\omega_0 = 1.9(2) \times 10^{16} \text{ cm}^{-3}$ from the value of $k_0 = 0.32(2) n_0\omega/c$ (at 515 nm wavelength) for BaTiO₃ [2.6] . The value of $[\rho\omega_0]_{\text{SBN}}$ can be

obtained from the k_o^2 value calculated from Figures 2.11 and 2.12 and similar other form figures, and by taking the values obtained for BaTiO₃ as reference values.

$$\frac{[\rho\omega_o]_{\text{BaTiO}_3}}{[\rho\omega_o]_{\text{SBN}}} = \frac{[k_o^2]_{\text{BaTiO}_3}}{[k_o^2]_{\text{SBN}}} \cdot \frac{\epsilon_{\text{BaTiO}_3}}{\epsilon_{\text{SBN}}}$$

After correcting for the relative values of the refractive index, and also the frequencies of excitation, the values of k_o^2 obtained for the six cases of SBN investigated and also the corresponding $[\rho\omega_o]$ values are given in Table 2.2.

Table 2.2. The Values of k_0^2 (in $n\omega/c$ Units) and $[\rho\omega_0]$ Number per c.c. Values Obtained Using the Corresponding Values Reported for $BaTiO_3$ as Reference Values.

Sample	Before γ -irradiation		After γ -irradiation	
	k_0^2	$\rho\omega_0$ (cm^{-3})	k_0^2	$\rho\omega_0$ (cm^{-3})
Pure SBN	3.26	9.3×10^{18}	3.49	9.9×10^{18}
Ce : SBN	8.2	2.3×10^{19}	1.5	4.1×10^{18}
Cr : SBN	3.15	8.9×10^{18}	6.1	1.7×10^{19}

2.5 Discussion

The important aspects of the results obtained can be summarized as :

(i). The decay constant and also the dark decay times depended on the dopants, on the γ -radiation damage. With regard to these parameters, the radiation damage appeared to affect pure SBN more significantly than the doped SBN. Further, there was no order of magnitude change in the average charge carrier density.

The reduction in dark decay time under gamma irradiation appeared to suggest the creation of large number of shallower traps, and most likely oxygen vacancies, by gamma irradiation. Vazquez et al. [2.17] suggested in their study that trivalent Rh went substitutionally to the Nb^{5+} site. In our case of Cr^{3+} and Ce^{3+} , a similar situation existed, particularly with regard to Cr^{3+} , as it is a d-block element. In such a case for charge compensation, an equal number of $\text{O}^{\cdot\cdot}$ vacancies are to be produced. In these oxides, it is known that the electronic levels of oxygen vacancies filled with electrons lie close to conduction band. Therefore, they are easily ionizable at room temperature, thereby contributing to faster dark decay times. The lowering of dark decay time on gamma irradiation, suggested that creation and electron occupation of oxygen vacancies might have contributed to faster dark decay. In view of the presence of oxygen vacancies in doped samples even before gamma irradiation, these samples were relatively less affected by gamma irradiation. Rakuljic et al. [2.18] have reported time constants somewhat smaller than our values in their SBN samples double doped with Ce and Ca. This is probably due to much higher intensity of writing beams ($1\text{ W} / \text{cm}^2$) and / or due to the presence of Ca.

It is, therefore, possible that in the Cr doped sample the substantial reduction in the decay time constant can be associated with resonant effects at 630 nm, corresponding to Cr^{3+} electronic absorption. The decay time constant for the Cr doped sample decreased further only to a slightly lower value after gamma irradiation and essentially remained unaltered probably due to the presence of resonance absorption at 630 nm in both cases. In the Ce doped sample and pure SBN, however, there was substantial reduction in response time after gamma irradiation suggesting that the defects generated during gamma irradiation

effectively mediated a quick charge transfer during the erasure cycle. It may be commented that the order of magnitude of the time constant in all three crystals after the gamma irradiation was nearly the same and equal to that in the Cr doped sample before gamma irradiation, which appears to be due to resonant absorption by Cr^{3+} . This point may suggest that the gamma irradiation had essentially created centers facilitating resonant phase conjugation; however, the number density may not have been large enough to be observable in optical absorption.

(ii). At the wavelength used (632 nm), strong resonance absorption can occur in Cr doped SBN, and to a lesser extent in Ce doped SBN. (See the absorption spectra in Figs. 2.5 and 2.4 compared to Fig. 2.3.)

2.6 Wavelength Dependence Of Degenerate Four-wave Mixing/Phase Conjugation In SBN Crystal

The experimental sketch shown in Fig. 2.13 is used for the study of the wavelength dependence of phase conjugation in the undoped but gamma irradiated SBN crystal the details of which are given in the earlier sections. The different laser lines from a 6-W Ar^+ laser (series 2000, Spectra Physics) have been used. The probe and the pump beams which are vertically polarized are of 25 mW power while the reading beam was of 2.5 mW. The angle between the probe and pump beams was 15.3° . The c axis of the crystal was kept horizontal and the laser beams fall on the $9.0 \times 5 \text{ mm}^2$ face of the crystal $4.8 \times 5.5 \times 9.0 \text{ mm}^3$, 9 mm being the c axis direction. The wavelength dependence of the phase conjugate signal intensity is shown in Fig. 2.14 and that of the decay constant τ in Fig. 2.15. The maximum phase conjugate signal intensity is with laser line at 496 nm while decay time

constant at the wavelength is one of the two lowest. The other minimum of τ occurs at 472 nm where the phase conjugate signal intensity is also minimum. The general behavior of the wavelength dependence of the phase conjugate signal appears to indicate the resonant effects of the γ -irradiation which, as seen in Table 2.2, has increased the phase conjugate sensitivity. Further work is needed to understand the nature of the color center formed by irradiation. The SBN crystals studied here did not show any EPR signal at room temperature and probably a low temperature search and study of the EPR signal might give useful information in this connection.

2.7 Acknowledgment

The irradiation was done with the help of Dr. S Kalachandra and work on Varian Spectrometer was done by Dr. Laurie McNeil both at the University of North Carolina, Chapel Hill, N.C. We are thankful for their work.

REFERENCES

- 2.1. A. Askin , G. D. Boyd , J. M. Dziedzic , R.G. Smith, A. A. Ballman ,
H. J. Levenstein and K. Nassau , Appl. Phys. Lett., 9, 72 (1966).
- 2.2. J. J. Amodie, J. Appl. Phys. Letts., 18, 22, (1971).
- 2.3. L. Yong, W. K. Y. Wang, M. L. Thewalt, and W. D. Cornish, Appl.
Phys. Letts., 24, 264 (1974).
- 2.4. J. J. Amodei , RCA Rev., 32, 185-198 (1971).
- 2.5. W. D. Cornish, M. G. Moharam, and L. Yong, Appl. Phys. Lett., 4
1479 (1976).
- 2.6. J. Feinberg , D. Heiman , A. R. Tanguay and R. W. Heallwarth, J.
Appl. Phys., 51, 1297-1305 (1980).
- 2.7. I. P. Kaminow and E. H. Turner, "Handbook of Laser" Ed. by R. J.
Presly, The Chem. Rubber Co., 447 (1971).
- 2.8. H. Kogelnik, The Bell System Technical Journal 48, 2909 (1969).
- 2.9. Sanders Associates, Nashua, New Hampshire, U.S.A.
- 2.10. F. S. Chen, J. T. Lamanchia and D. B. Fraser, Appl. Phys.
Lett., 13, 223 (1968).
- 2.11. G. E. Peterson, A. M. Glass, and T. J. Negran, Appl. Phys. Lett.,
19, 130 (1971).
- 2.12. M. D. Ewbank, R. R. Neurgaonkar, W. K. Cory, and J. Feinberg, J.
Appl. Phys., 62, 374 (1987).

- 2.13. G. L. Wood, M. J. Miller, W. W. Clark III, E. J. Sharp, G. Salamo,
and R. R. Neurgaonkar, IEEE, J. Quant. Elect., 23, 2126 (1987).
- 2.14. R. R. Neurgaonkar, and W. K. Cory, J. Opt. Soc. Am. B 3, 274 (1986).
- 2.15. S. Kalachandra and D. T. Turner, Instr. J. Science Tech. Polymer,
28, 1749 (1987).
- 2.16. R. S. Cudney, R. M. Pierce, G. D. Bacher, and J. Feinberg, J. Opt.
Soc Am., 8, 1326 (1991).
- 2.17. R. A. Vazquez, R. R. Neurgaonkar, and M. D. Ewbank, J. Opt. Soc.
Am., B 9, 1416 (1992).
- 2.18. G. A. Rakuljic , K. Soyano , A. A. Agranat , A. Yariv and R.
R Neurgaonkar , Appl. Phys. Lett., 53, 1465 (1988).
- 2.19. J. Feinberg , in Optical Phase Conjugation, Ed. by Fisher R. A.,
Academic Press, 427 (1983).

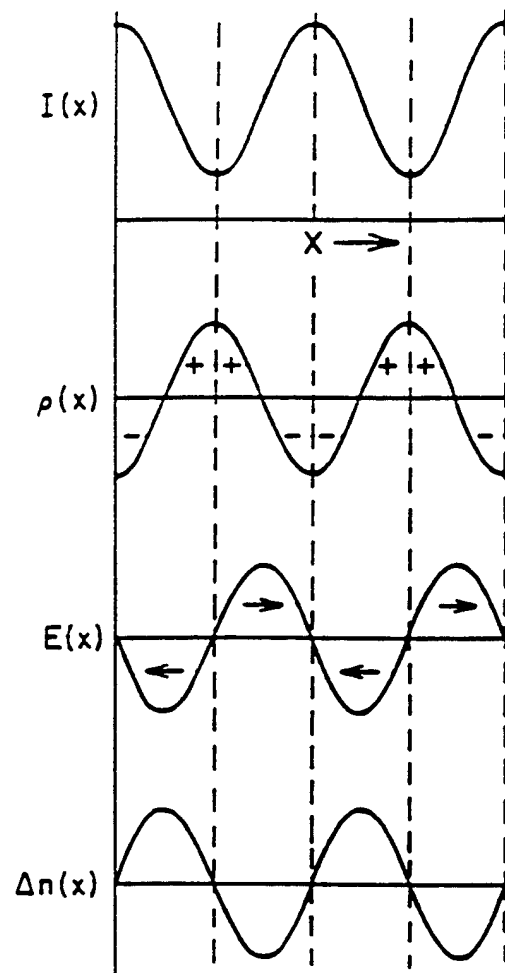


Figure 2.1. Formation of a photorefractive index grating when two coherent beams interfere inside the crystal, $I(x)$; Spatially periodic intensity of light, $\rho(x)$; Rearranged charge density, $E(x)$; Spatially periodic electrostatic field, $\Delta n(x)$; Change in refractive index by the linear electro-optic (Pockels effect), (ref. 2.19).

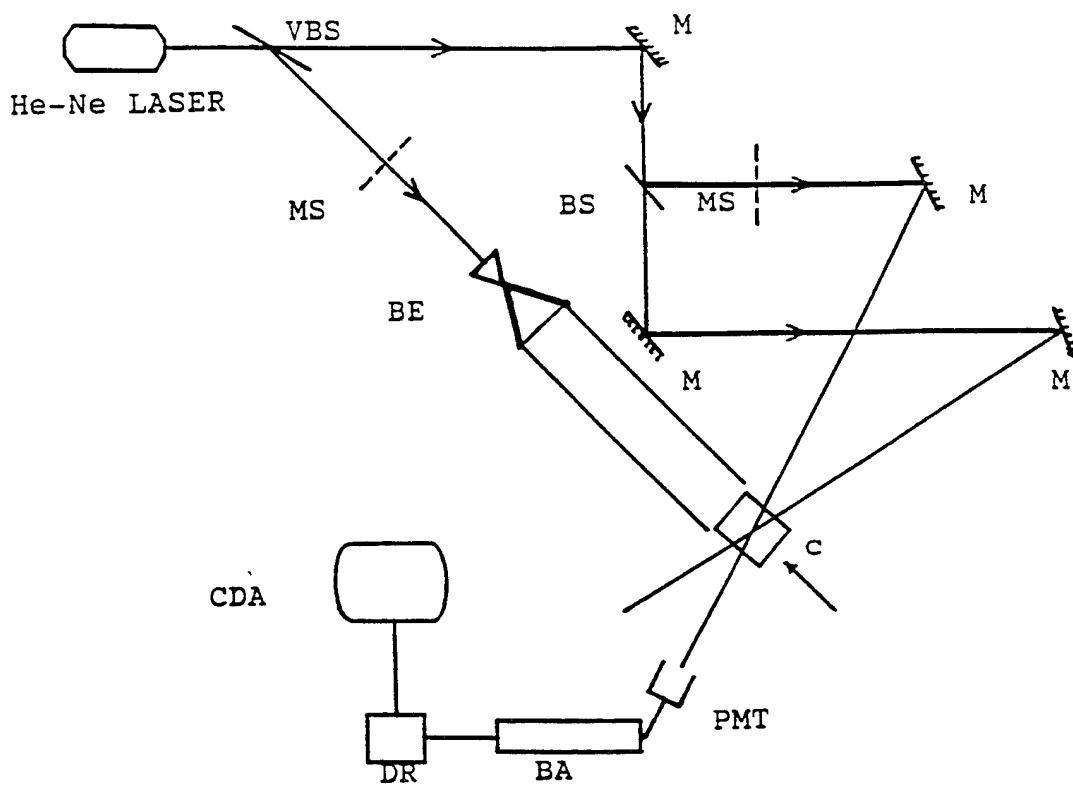


Figure 2.2. Schematic experimental setup showing two writing beams 1 and 2, and expanded collimated beam. For light induced erasure experiments, the intensity of transmitted writing beam 1 was detected as writing beam 2 was blocked while the erasure beam was suddenly unblocked. The decay of grating is detected using a PMT stored by digital recorder and analysed using computer.

VBS; variable beam plitter, M; mirror, BS; beam splitter, MS; mechanically shutter, BE; beam expander, BA; boxcar averager, DR; digital recorder, CDA; computer data acquisition.

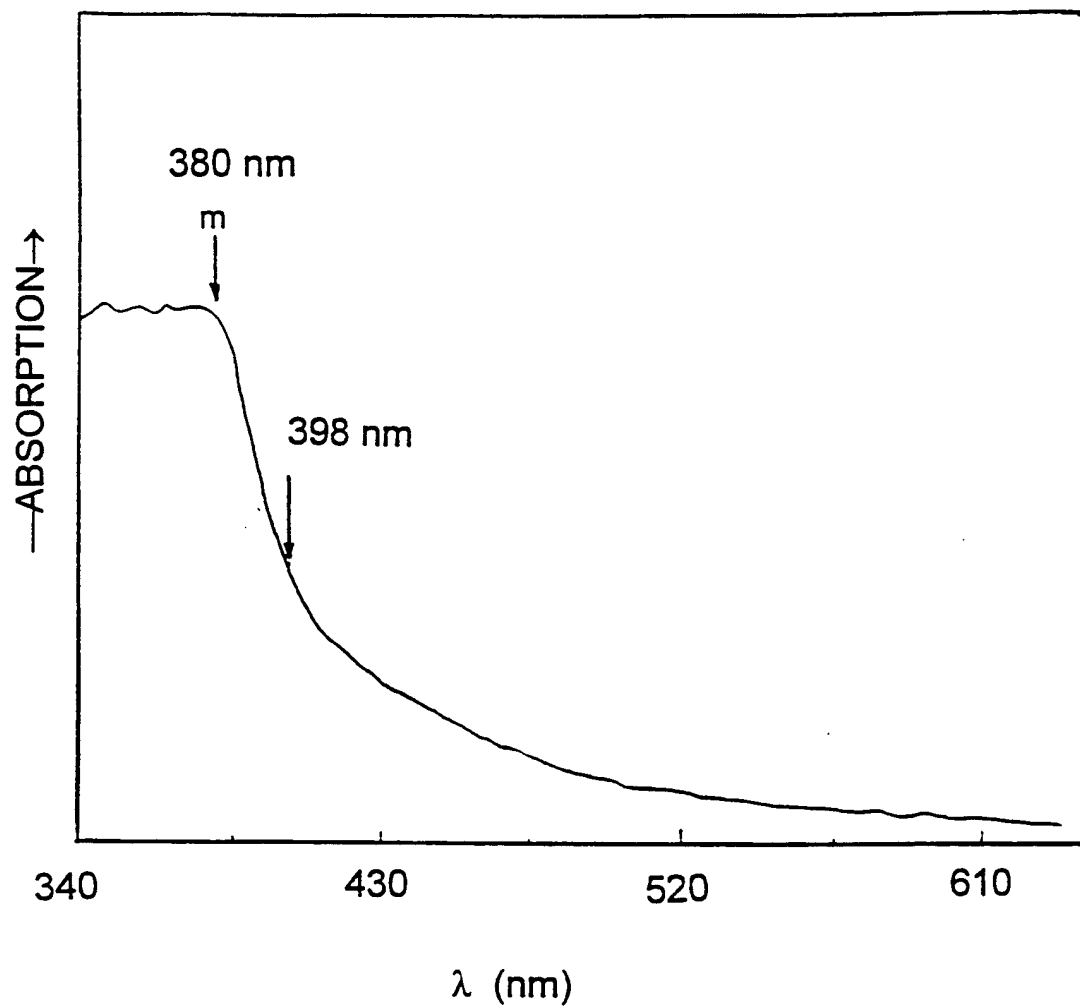


Figure 2.3. Absorption spectrum of pure SBN crystal in the spectral region 340 nm - 700 nm before gamma irradiation, using Perkin Elmer Prism Spectrophotometer .

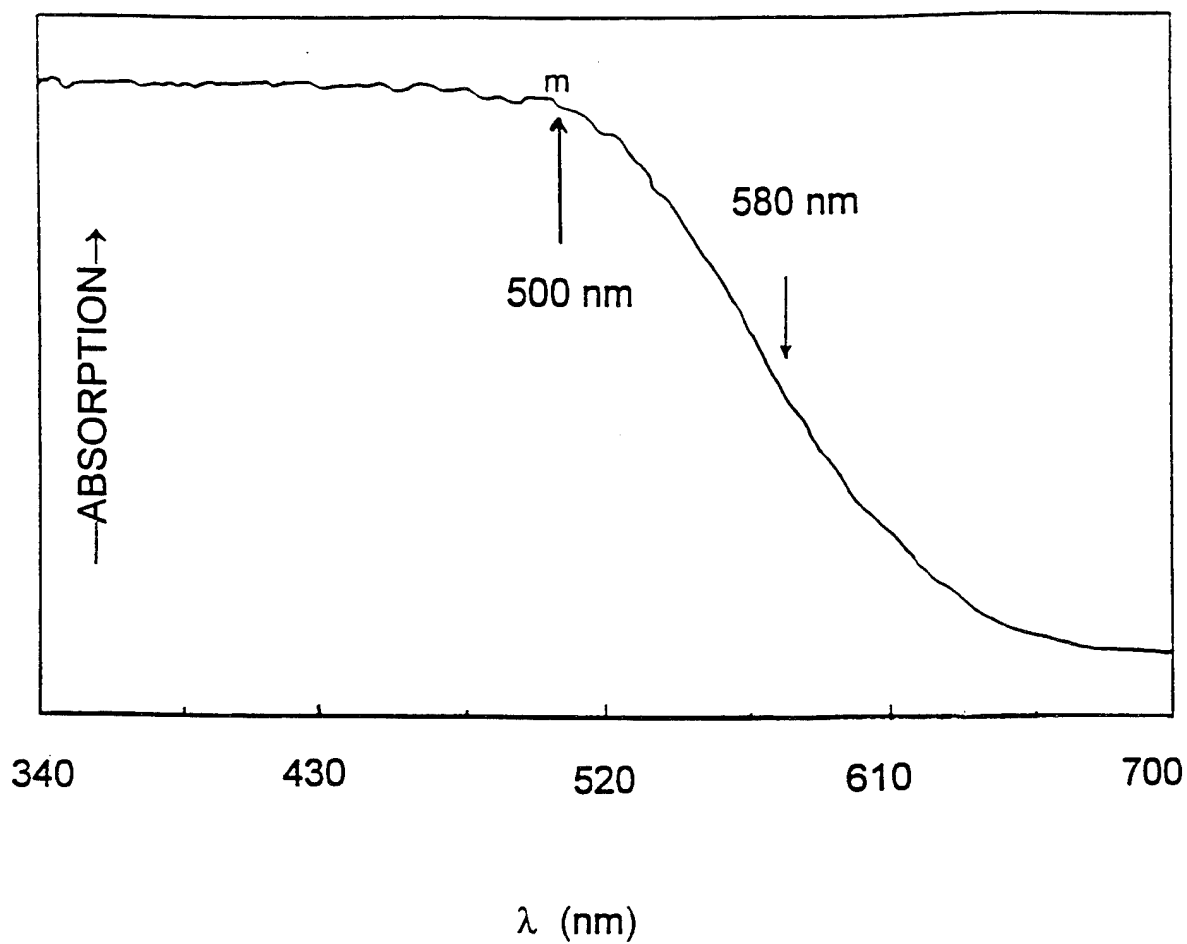


Figure 2.4. Absorption spectrum of Ce:SBN crystal (0.1% Ce) in the spectral region 340 nm - 700 nm before gamma irradiation, using Perkin Elmer Prism Spectrophotometer .

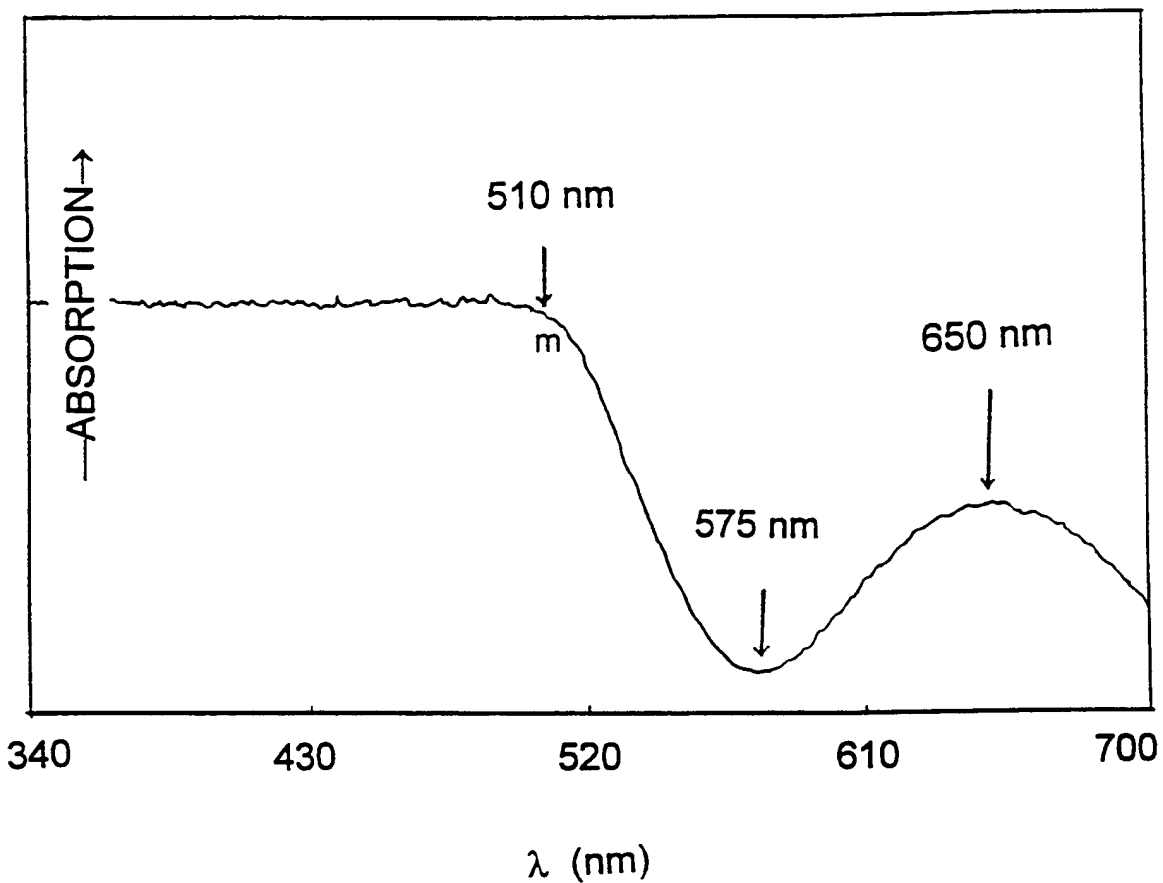


Figure 2.5. Absorption spectrum of Cr:SBN crystal (1% Cr) in the spectral region 340 nm - 700 nm before gamma irradiation, using Perkin Elmer Prism Spectrophotometer .

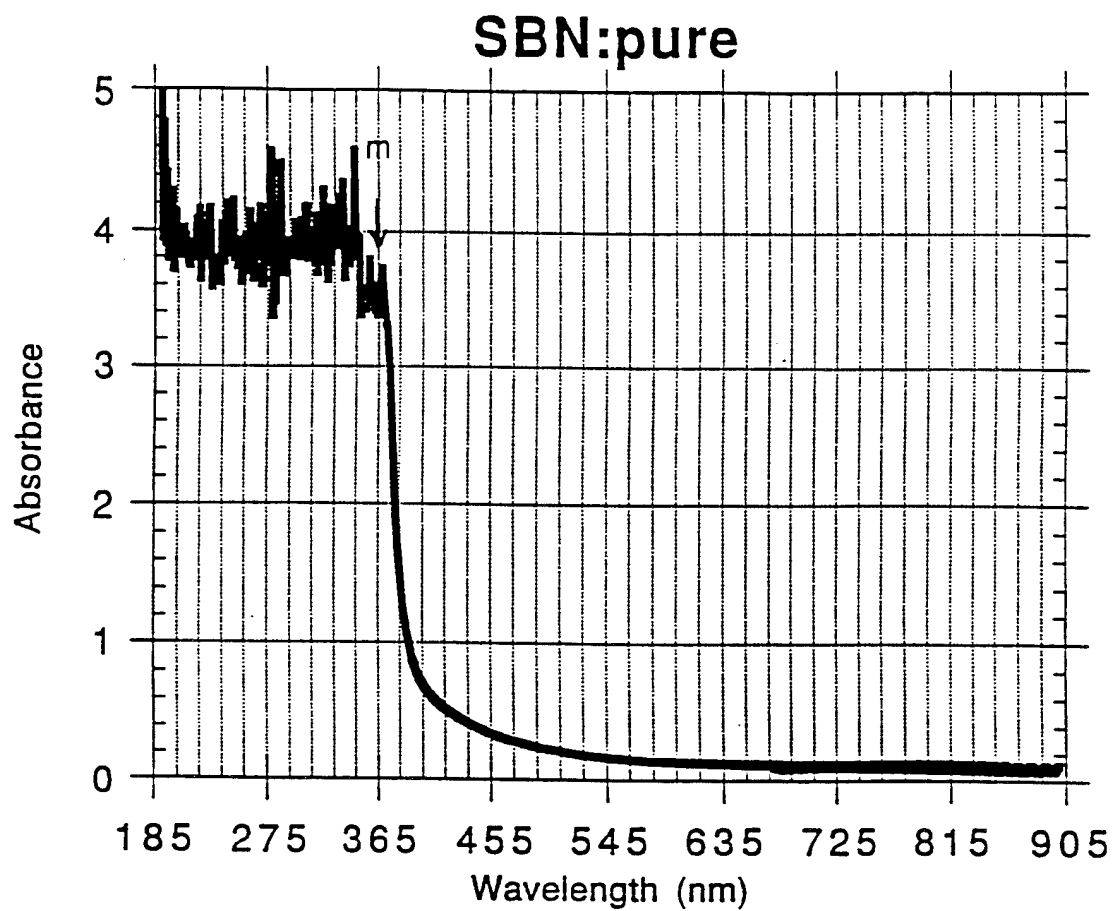


Figure 2.6. Absorption spectrum of pure SBN crystal in the spectral region 185 nm - 905 nm after gamma irradiation, using Varian spectrophotometer.

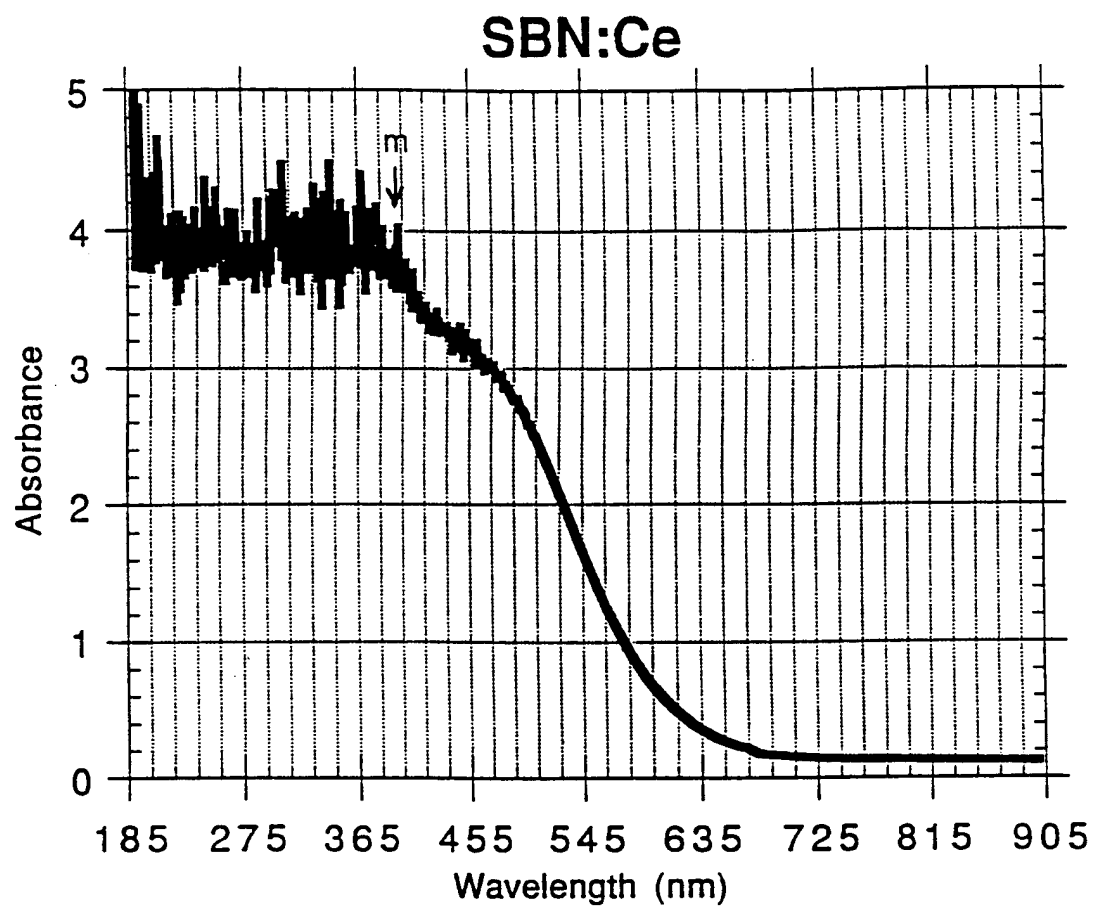


Figure 2.7. Absorption spectrum of Ce:SBN crystal (0.1% Ce) in the spectral region 185 nm - 905 nm after gamma irradiation, using Varian spectrophotometer.

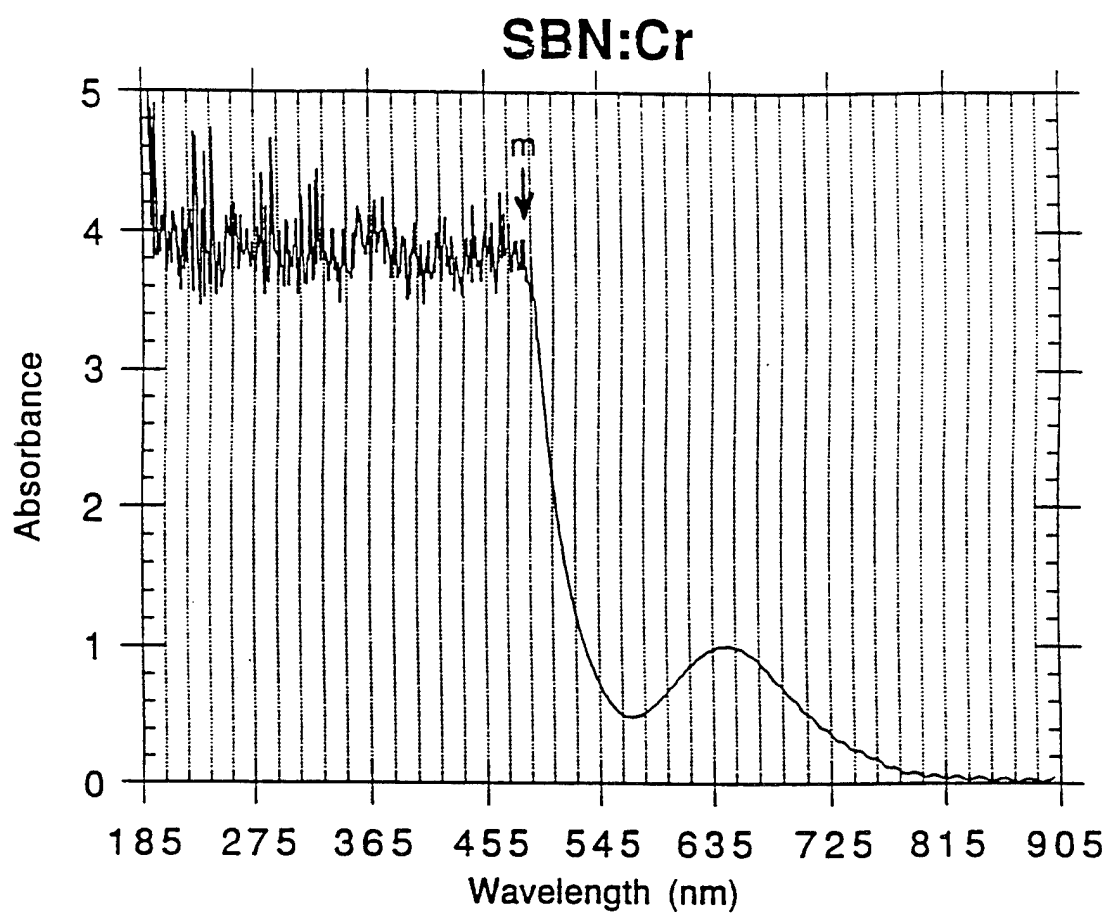


Figure 2.8. Absorption spectrum of Cr:SBN crystal (1% Cr) in the spectral region 185 nm - 905 nm after gamma irradiation, using Varian spectrophotometer.

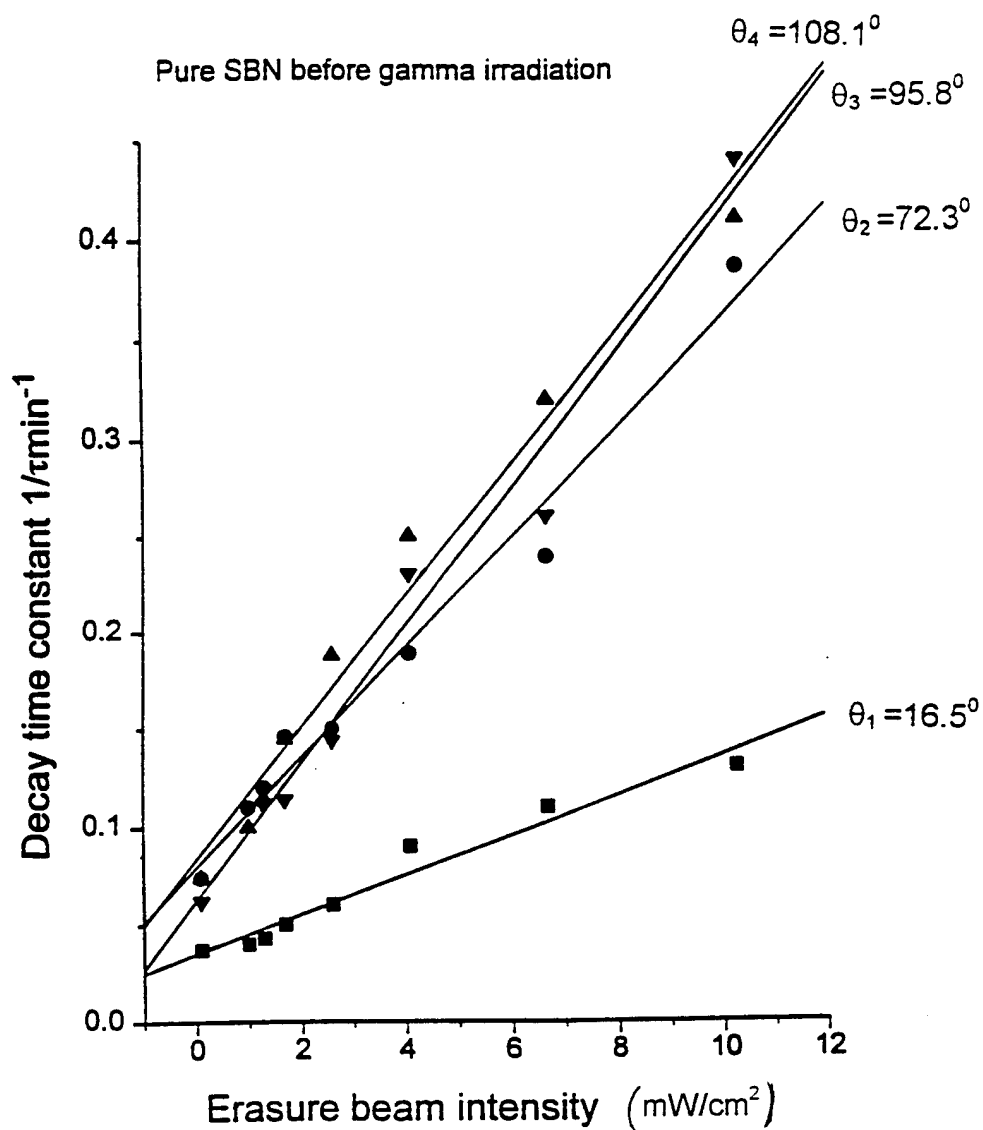


Figure 2.9. Decay time constant as a function of erasure beam intensity at various crossing angles (grating wave vectors), for pure SBN crystal before gamma irradiation.

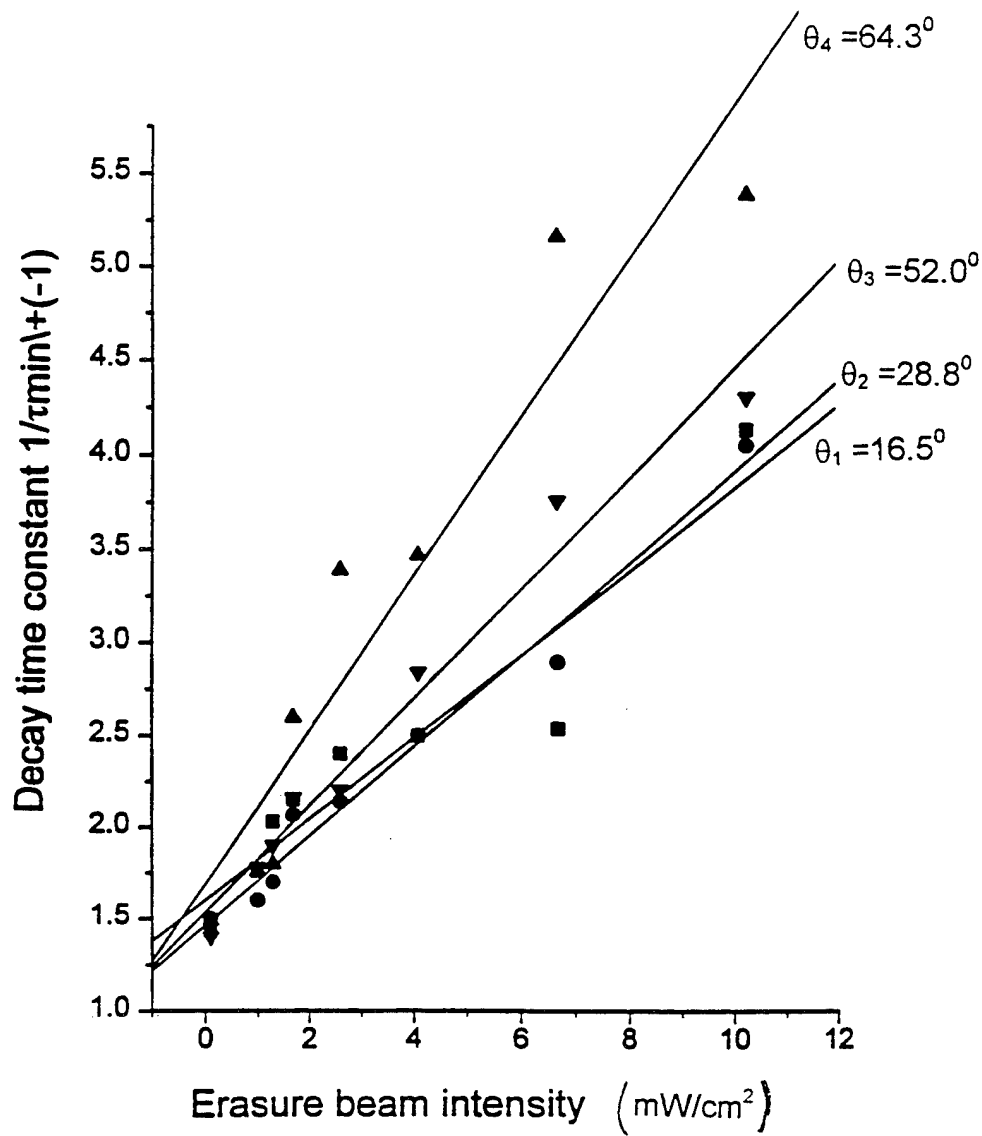


Figure 2.10. Decay time constant as a function of erasure beam intensity at various crossing angles (grating wave vectors), for pure SBN crystal after gamma irradiation.

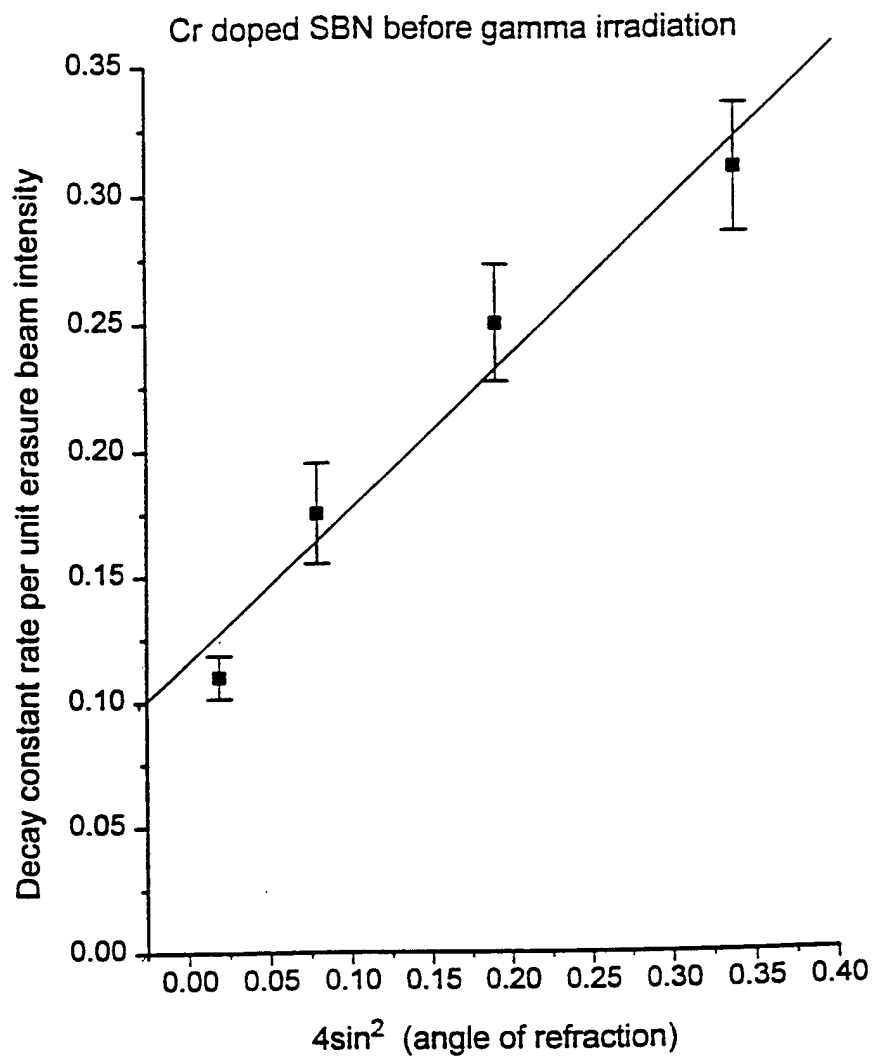


Figure 2.11. Decay constant rate per unit erasure intensity as a function of k^2 .

The squares are the experimentally measured data and the straight line is the best least square fit, for Cr:SBN crystal before gamma irradiation.

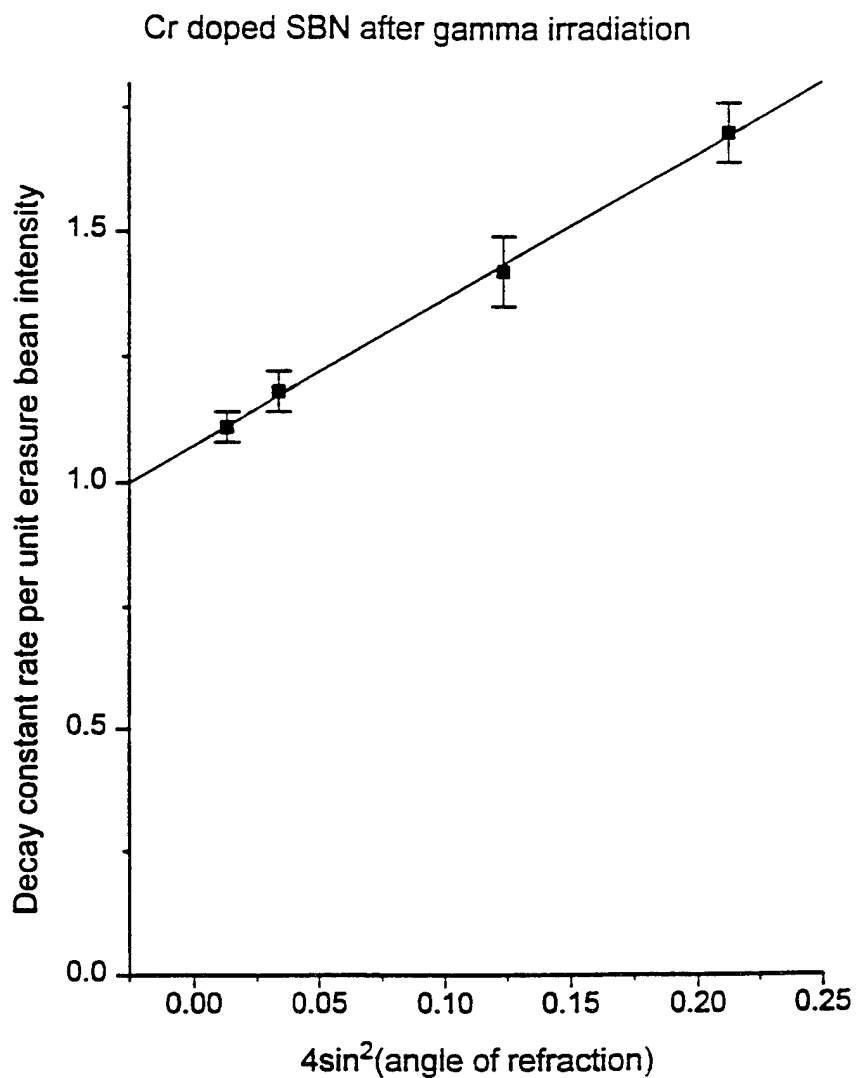


Figure 2.12. Decay constant rate per unit erasure intensity as a function of k^2 . The squares are the experimentally measured data and the straight line is the best least square fit, for Cr: SBN crystal after gamma irradiation.

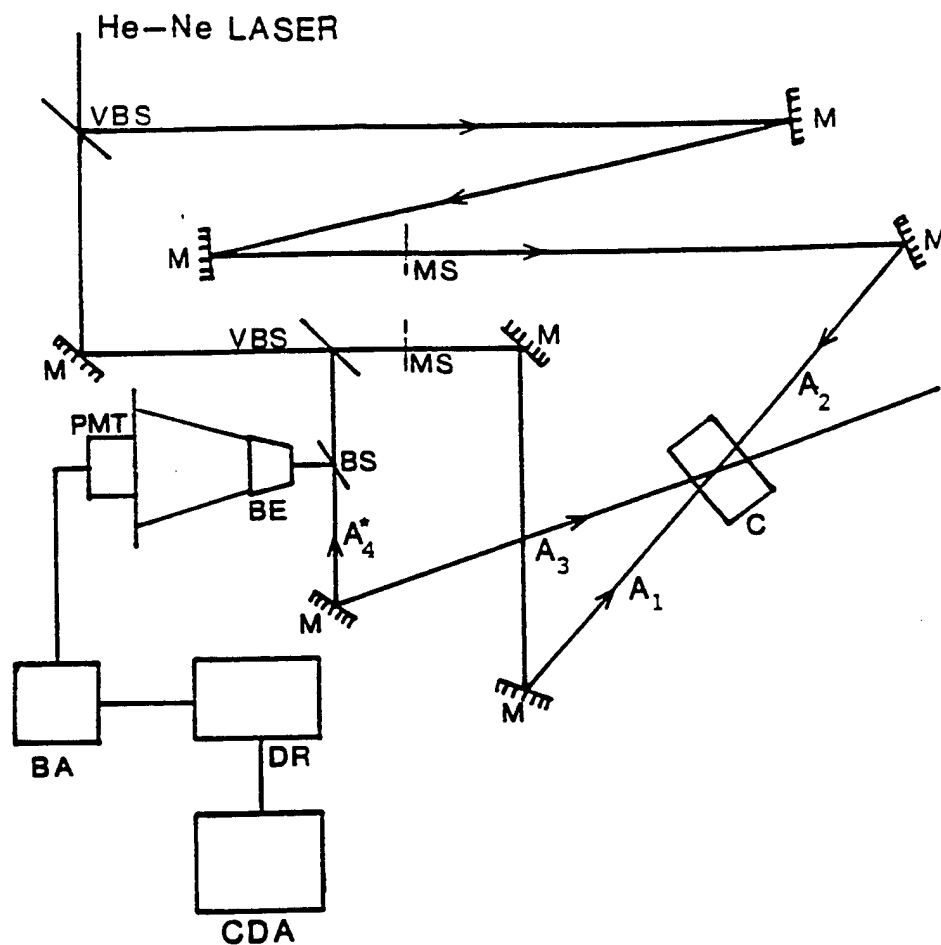


Figure 2.13. Schematic experimental setup of four-wave mixing. The phase conjugate beam is expanded and detected using a small pin hole following by a PMT. M; mirror, VBS; variable beam splitter, MS; mechanically shutter, BS; beam splitter, c; crystal, BE; beam expander, BA; boxcar averager, DR; digital recorder, CDA; computer data analyser.

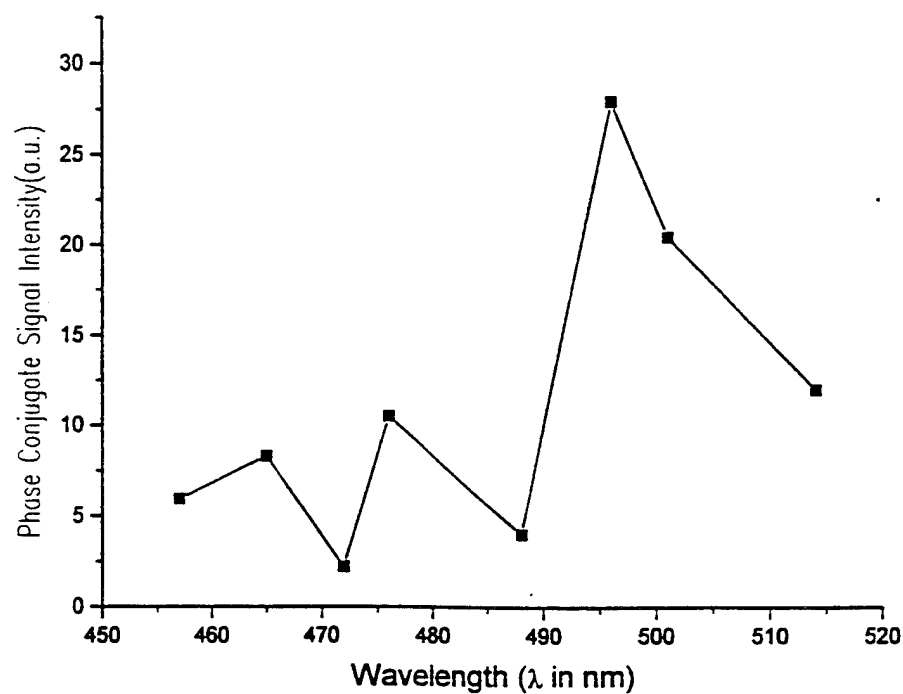


Figure 2.14. The normalized phase conjugate intensities for gamma irradiated pure SBN crystal at different wavelength from an Ar^+ laser. It indicates an order of magnitude enhancement of phase conjugate signal at 496 nm compared to lower wavelength.

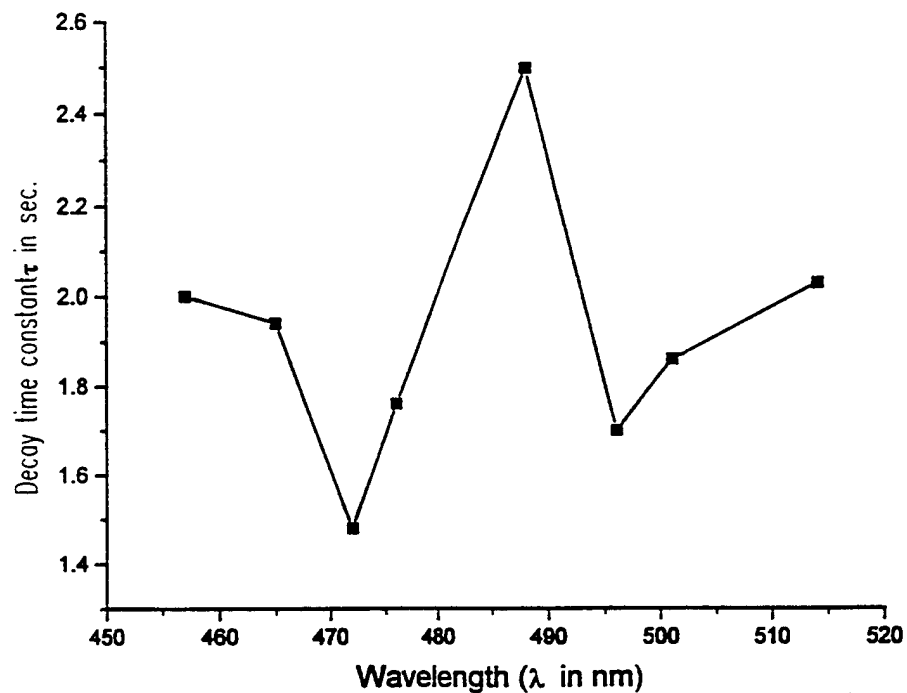


Figure 2.15. The plot of decay time constant of phase conjugate signal as a function of wavelengths, showing an anomalous decrease and increase of response time around 472 nm and 488 nm respectively, for pure gamma irradiated SBN crystal.

Chapter 3

Enhancement of Phase Conjugate Signal in Gamma Irradiated BaTiO₃: Possible Role of Color Centers and Resonance Phase Conjugation

3.1 Introduction

Atomic, molecular or solid-state crystal having quantized energy levels, will exhibit optical nonlinearity at the energies corresponding to resonantly enhanced excitation. Degenerate four-wave mixing provides a powerful tool to study the physical properties of atomic and molecular systems [3.1] using this resonant nonlinearity. Liao and Bloom [3.2] were the first to demonstrate the observation of cw conjugate wave generation by degenerate four-wave mixing in a solid. Cr³⁺ impurity energy levels in Ruby were used to create "population gratings" by resonant excitation, of $^4A \rightarrow ^2E$ transition of Cr³⁺ in Ruby. When an interference pattern was formed in the Ruby crystal, it resulted in the modulation of population in 2E state. Rand [3.3,3.4] has shown that radiation induced color centers can be very effectively used to produce population gratings and resonant phase conjugation in gamma irradiated LiF and diamond. In spite of extensive investigation on photorefractive crystals, no detailed published reports exist on the effect of radiation induced defects these crystals. In view of their possible

participation in the resonant nonlinearities, it was considered worthwhile to investigate the four-wave mixing on gamma irradiated SBN and BaTiO₃ at different wavelengths. The results obtained on SBN are described in Chapter 2. We have also investigated by four-wave mixing a mechanically poled BaTiO₃ crystal, subjected to a gamma dose of around 20 Mrad, three times, each in an interval of 6 months, at different lasing wavelengths of an Ar⁺ laser. Unirradiated electrically poled crystals were also studied for comparison. In this study we give evidence to suggest considerable enhancement in the phase conjugate signal around 495 nm in a gamma irradiated crystal, probably corresponding to the electronic excitation induced O⁻ ions.

3.2. Experimental

The experimental setup used for four-wave mixing, and phase conjugate detection is similar to the one described in Chapter 2, Figure 2.13. The measurements were done at the following wavelengths of Ar⁺ laser: 457, 472, 476, 488, 496, 501, and 515 nm. In these measurements the polarization of laser light was perpendicular to c axis to avoid fanning.

For meaningful comparison of the phase conjugate signals at all these wavelengths, the Ar⁺ laser was operated at all these wavelengths at the same power level (0.26 W). The wavelength selection was done after checking for the spectral purity of Ar⁺ ion output using a McPherson 218 Scanning Monocromator with a 788 stepper system. The PMT response at these wavelengths was checked, and found to be nearly wavelength independent in this range. (This is shown in Fig.

3.1.) It may be pointed out that the grating spacing at these wavelengths $L = \lambda / 2 \sin \theta$ does not vary by more than 10%. Therefore, L is taken as essentially unaltered.

The phase conjugate signal at different wavelengths was detected and its stability was ascertained by monitoring the phase conjugate signal as a function of time. The different wavelengths for the gamma irradiated mechanically poled crystal and two electrically poled unirradiated crystals are shown in Figures 3.2, 3.3 and 3.4. The phase conjugate signals at different wavelengths were normalized against the direct beam signals (Figure 3.1) of the same wavelength. The normalized phase conjugate intensities for the three crystals at different wavelengths are shown in Figure 3.5 which shows there was an order of magnitude enhancement of phase conjugate signal at 495 nm in the gamma irradiated crystal. It may be appropriate to mention that the gamma irradiated crystal was a mechanically poled crystal, unlike the electrically poled monodomain crystals used as reference unirradiated samples. Therefore, the enhancement in phase conjugate signal, at 495 nm, on gamma irradiation may be considered more than the extent shown in Figure 3.5. The increase may be taken as due to resonance effects created because of gamma irradiation like in SBN.

Lasher and Gooking [3.5] have investigated the wavelength dependence of photorefractive effect in an unirradiated BaTiO₃ crystal. They found it to exhibit weak $(1/\lambda)$ dependence as expected over a wide wavelength range. However, it was found to be nearly wavelength independent in the 450 - 520 nm region. They also studied photorefractive response time as a function of λ . They observed a strong λ - dependence of response time. We measured the decay time of the phase conjugate signal as a function of λ in a gamma irradiated crystal between 450 and 520 nm. An anomalous decrease of the response time was observed around 470

nm and 490 nm. (Fig. 3.6) It was probably a manifestation of the formation of population grating due to resonant effects/resonant absorption. Precise origin for this gamma irradiation / color center effect is still to be understood.

The next query naturally would be to identify whether any radiation induced species in BaTiO_3 would give an optical absorption around 495 nm. We have conducted the optical absorption before and after gamma irradiation. There was no prominent new peak observed in gamma irradiated samples. It may, however, be mentioned that a broad absorption around 500 nm got developed at the foot of the sharp band edge around 400 nm (Figure 3.7). Among the possible radiation induced defects in BaTiO_3 , the most probable one was an O^- ion, trapped near lattice / point defects. The absorption spectrum of O^- is well characterized in LiNbO_3 . It has a strong absorption around 500 nm [5.4] which is shown in Fig. 3.8. Therefore, the result discussed above suggested a possible resonance phase conjugation due to population grating formed by O^- ions in BaTiO_3 .

REFERENCES:

- 3.1. P. F. Liao, N. P. Economou and R. R. Freeman, Phys. Rev. Lett., 39, 1473 (1977).
- 3.2. P. F. Liao and D. M. Bloom, Opt. Lett., 3, 4 (1978).
- 3.3. S. C. Rand, Opt. Lett., 11, 135 (1986).
- 3.4. S. C. Rand, Opt. lett., 13, 140 (1988).
- 3.5. M. E. Lasher and D. M. Gookin, CLEO - 92, Paper # (CTUG5).
- 3.6. L. E. Halliburton, K. L. Sweeney and C. Y. Chen, Nuclear Instrument and Methods in Physics Research B, 344, (1989).

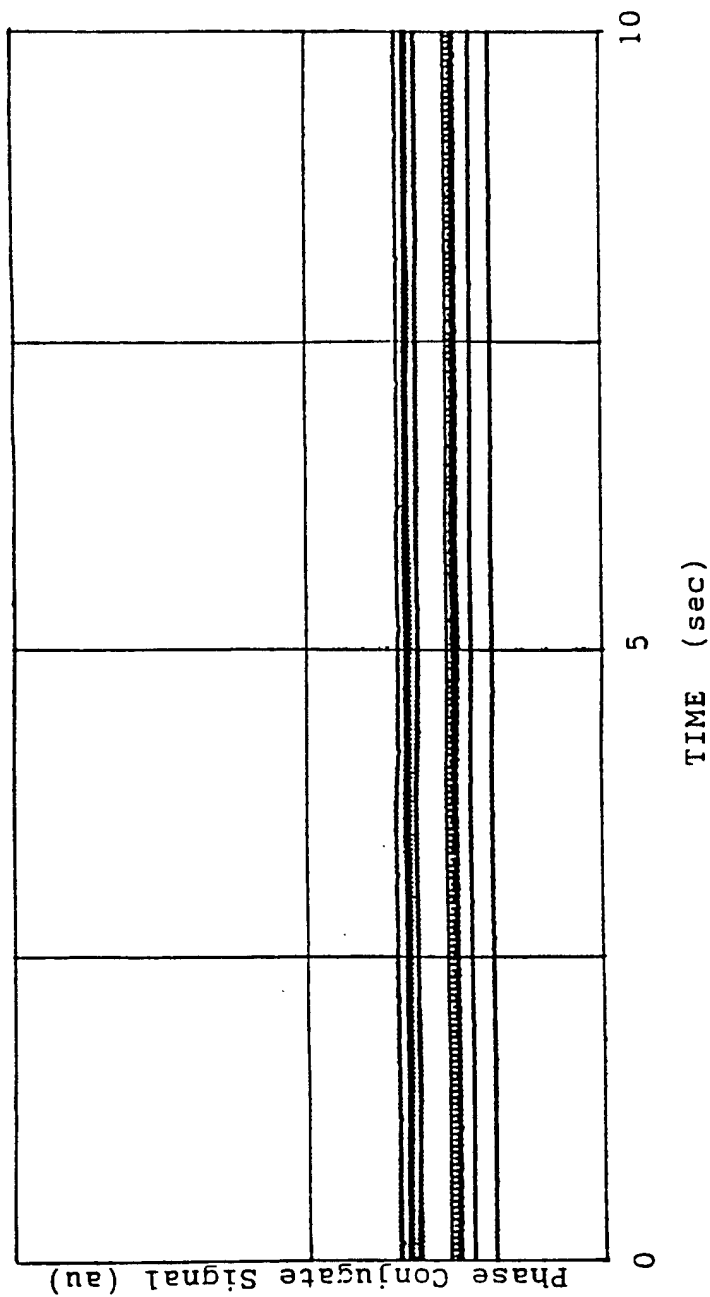


Figure 3.1 The plot of the PMT response as a function of time, using different wavelengths from an Ar^+ laser. It was found to be nearly wavelength independent in this range.

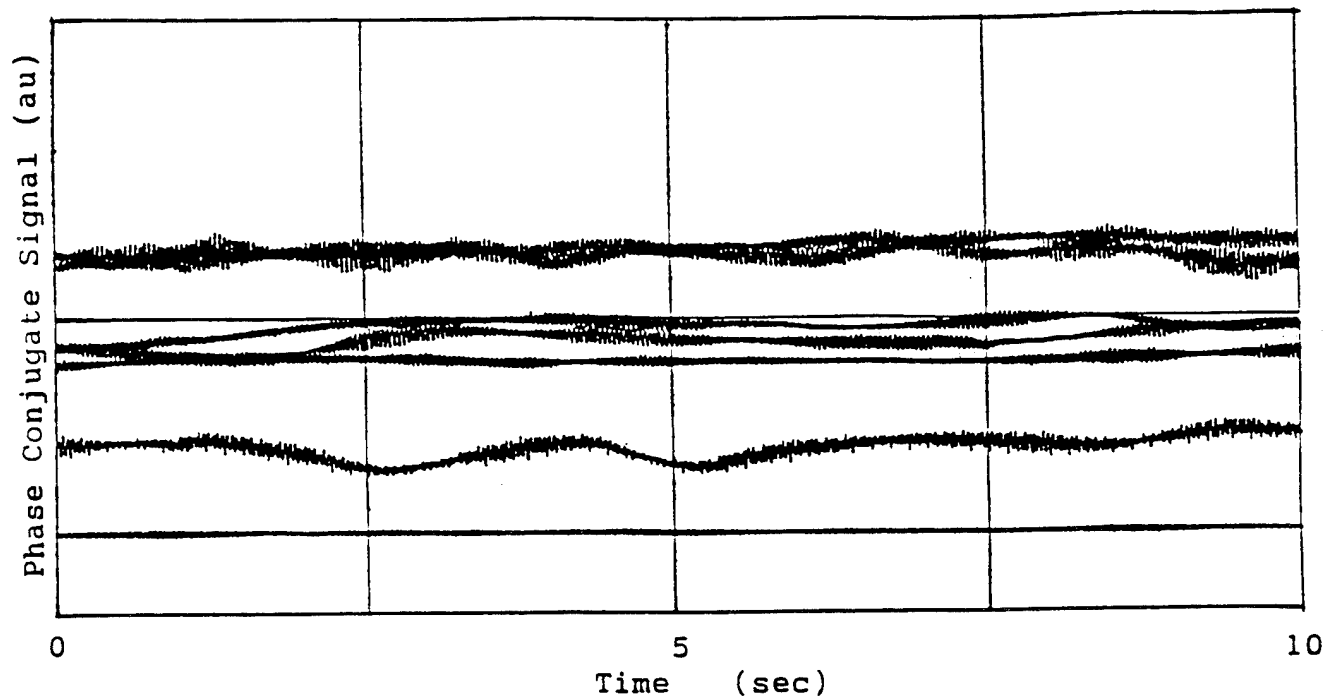


Figure 3.2 The phase conjugate signal as a function of time at different wavelengths from an Ar^+ laser, using a gamma irradiated mechanically poled BaTiO_3 crystal.

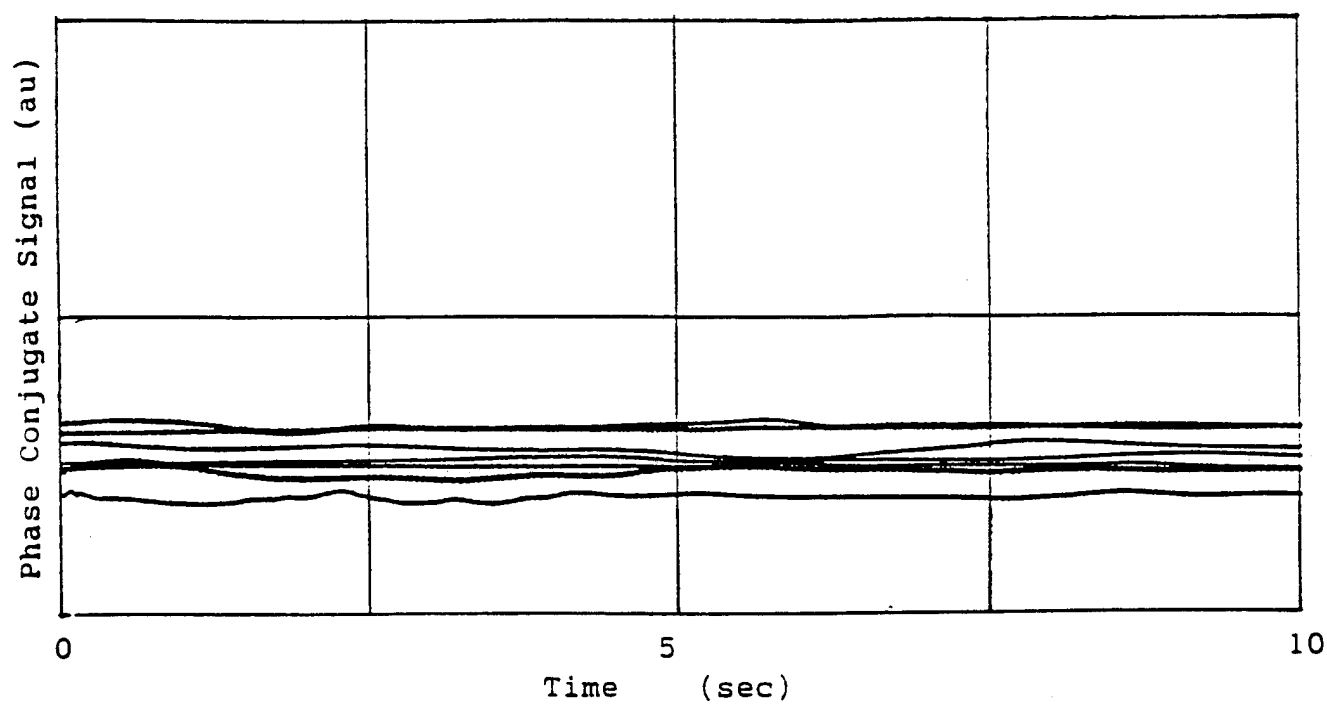


Figure 3.3 The phase conjugate signal as a function of time at different wavelengths from an Ar^+ laser, using an unirradiated electrically poled BaTiO_3 crystal #1.

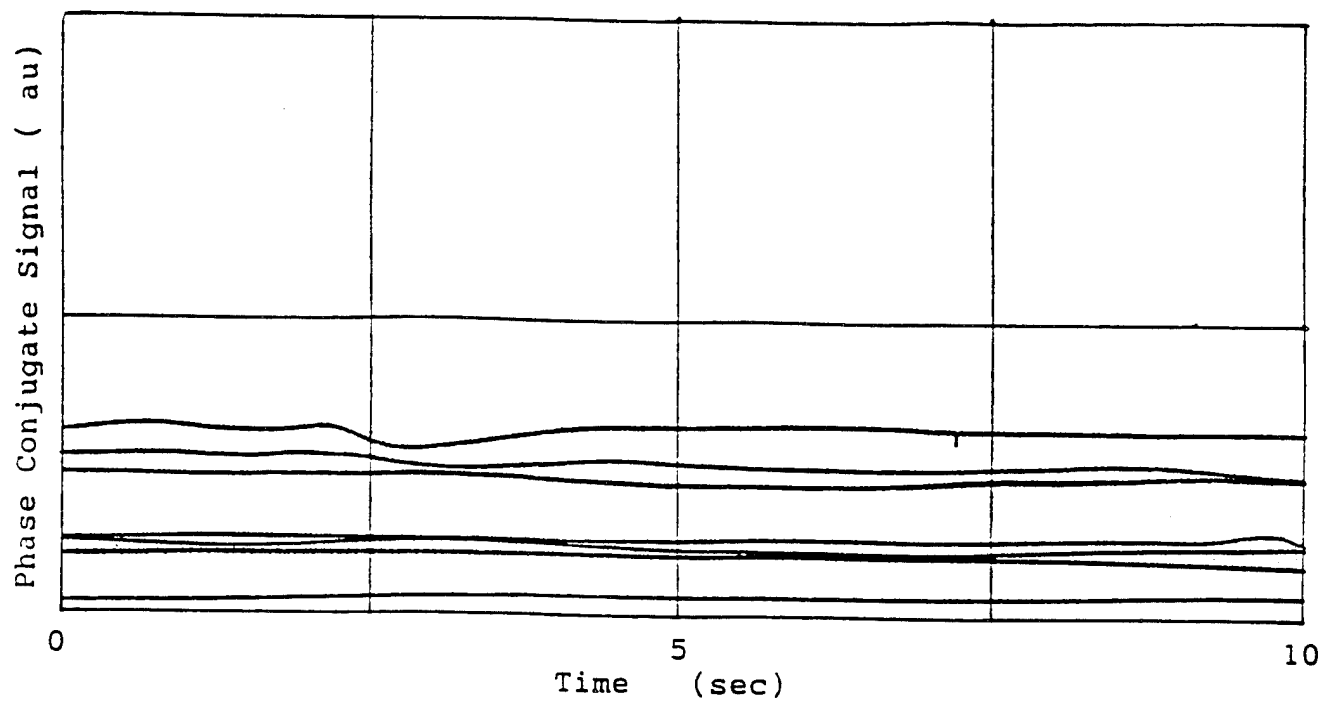


Figure 3.4 The phase conjugate signal as a function of time at different wavelengths, using an unirradiated BaTiO₃ crystal #2.

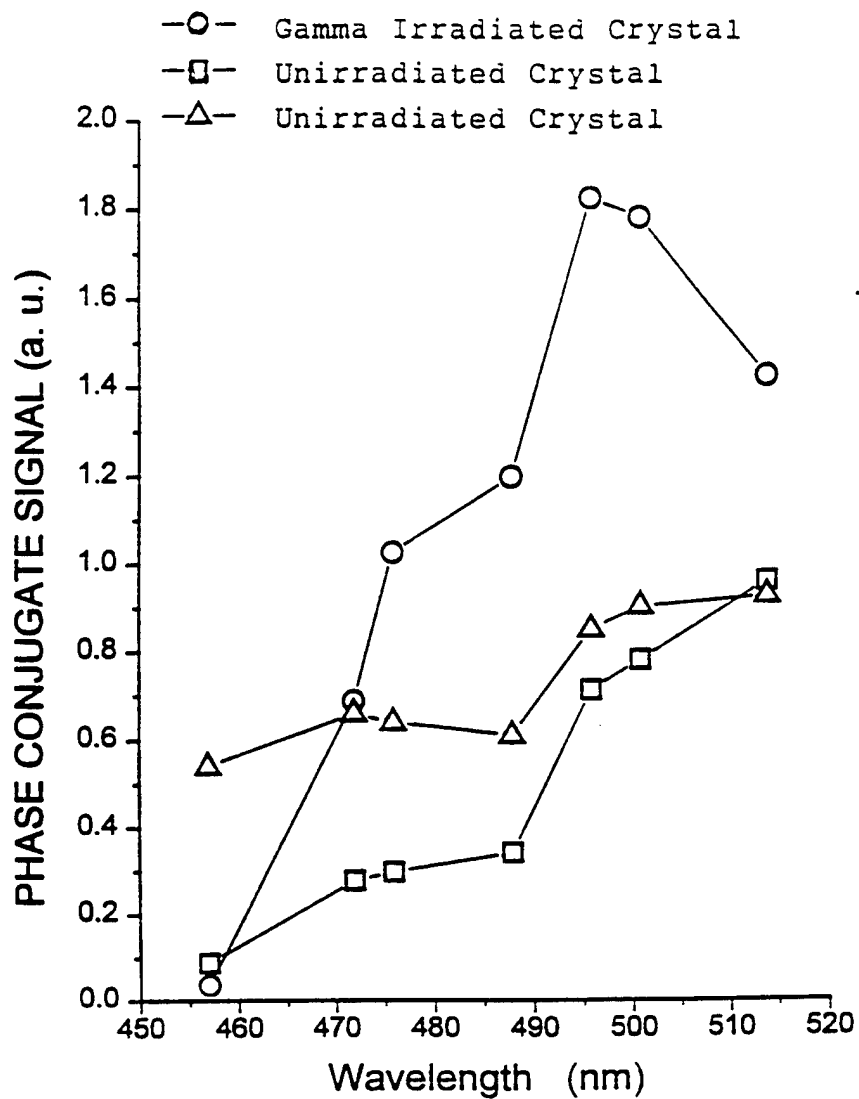


Figure 3.5 The normalized phase conjugate intensities for the three crystals at different wavelengths from an Ar^+ laser. It indicates an order of magnitude enhancement of phase conjugate signal at 495 nm in gamma irradiated crystal.

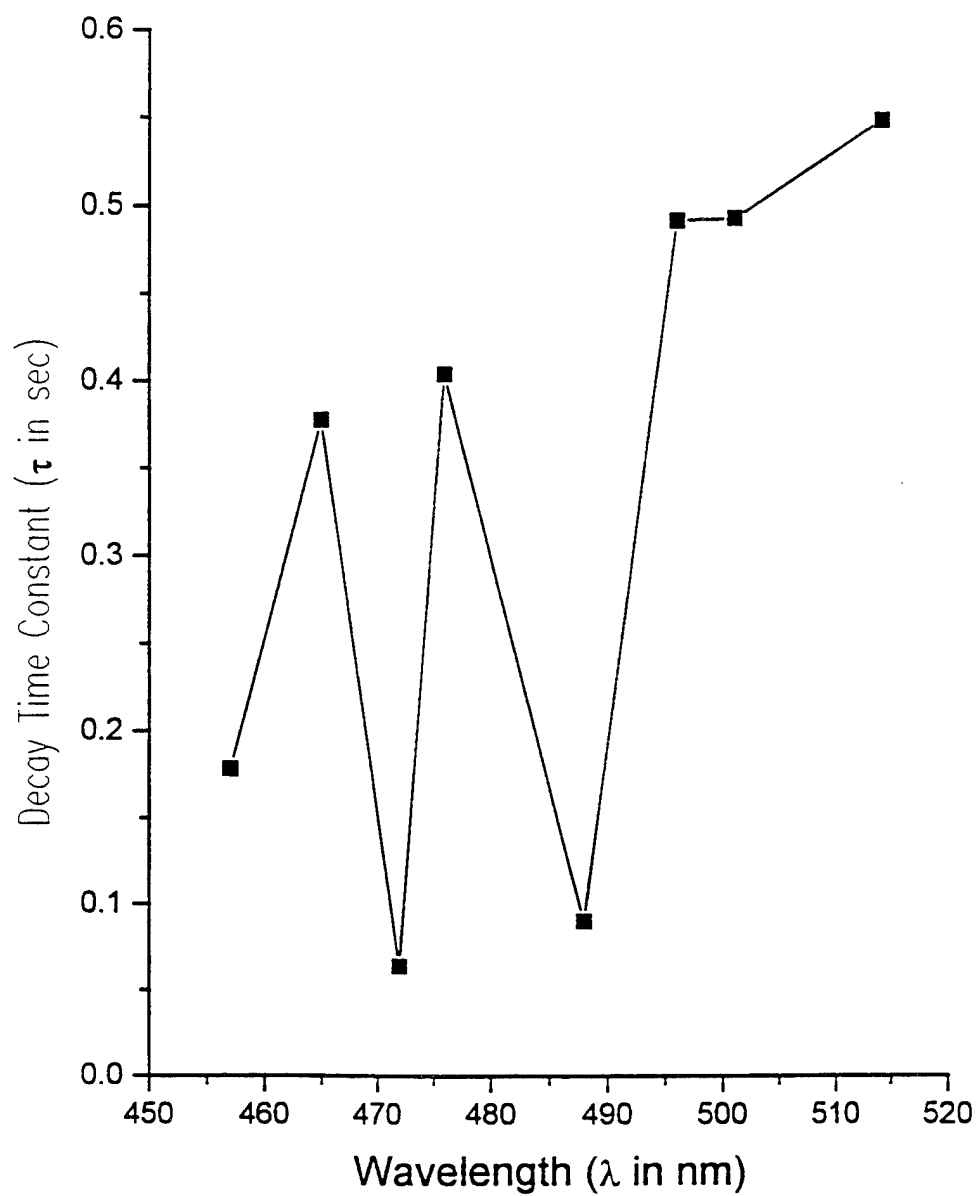


Figure 3.6 The plot of decay time constant of phase conjugate signal as a function of wavelengths, showing an anomalous decrease of response time around 490 nm.

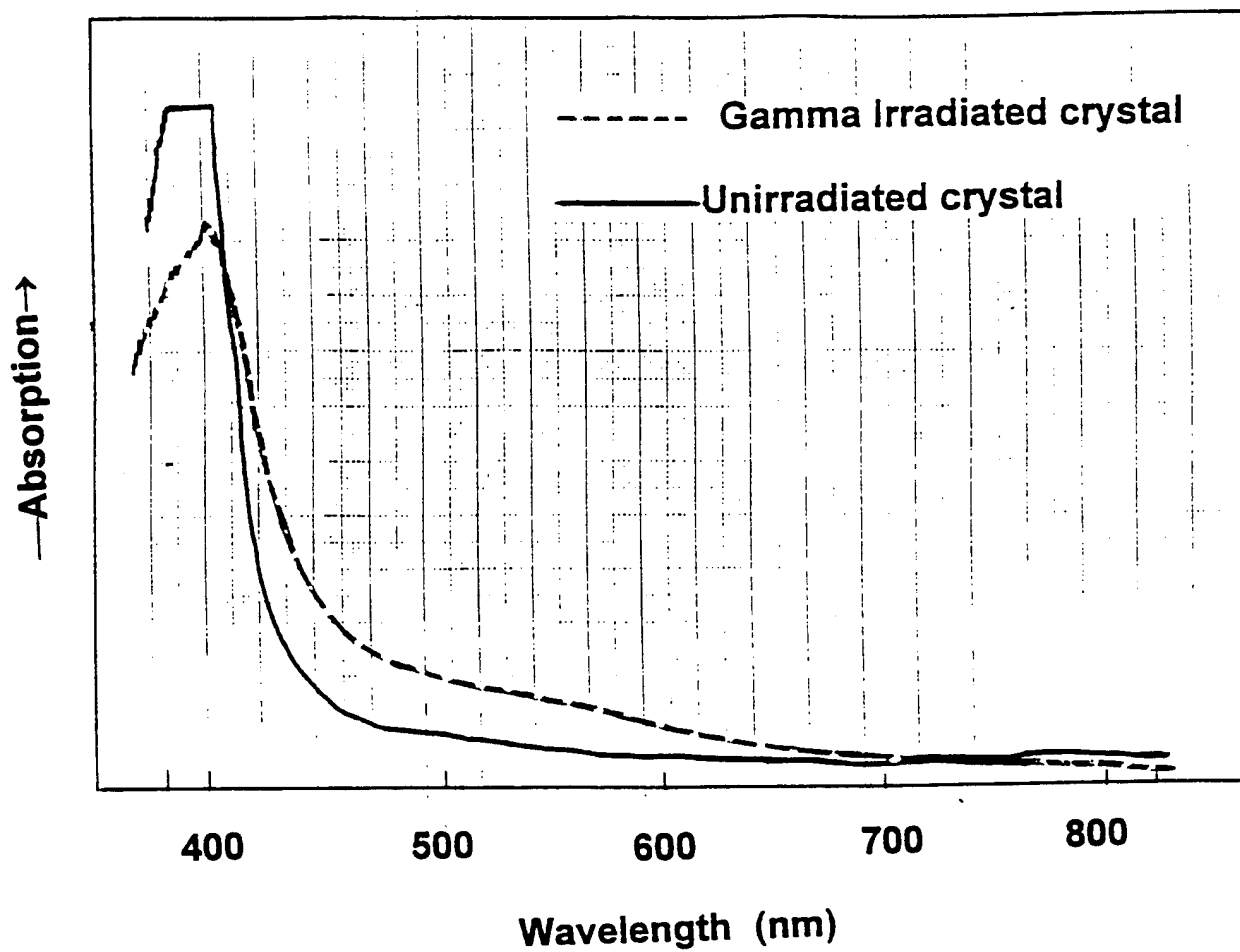


Figure 3.7 The optical absorption spectrum of unirradiated and gamma irradiated BaTiO₃ crystal.

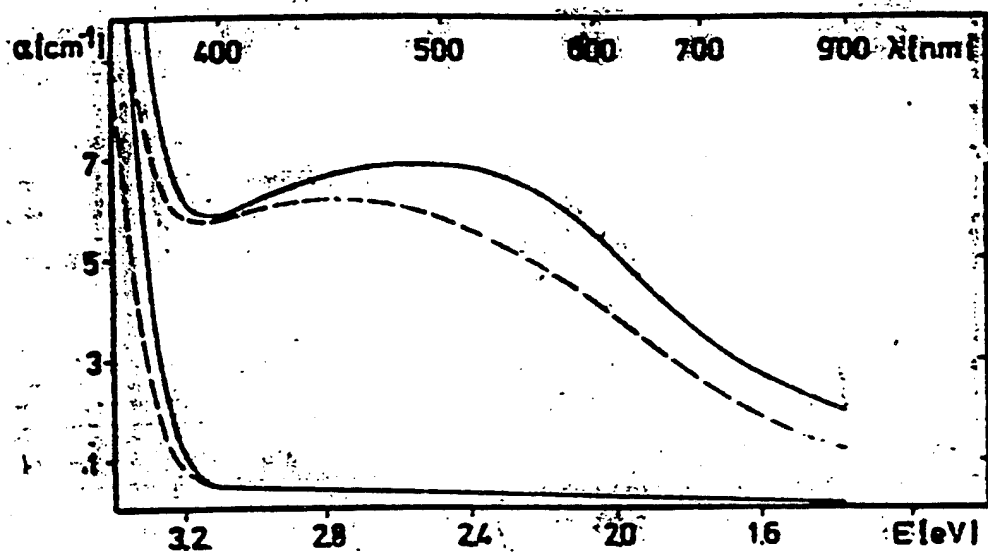


Figure 3.8 Optical absorption of O^{2-} -trapped holes in low temperature (10K) x-irradiated undoped $LiNbO_3$. The 1.6 eV Nb^{4+} band was not present in this crystal. Solid lines: σ -polarization; dashed lines : π -polarization (Ref. 3.1).

Chapter 4

PARAMETRIC DEPENDENCE OF ENERGY TRANSFER AND COHERENT TWO BEAM COUPLING IN BaTiO₃

4.1 Introduction

The energy transfer and beam coupling between two polarized coherent beams, interacting in an electrically poled BaTiO₃ crystal critically depend upon a number of experimental parameters due to the role of extent of beam overlap, and the role of internal reflection. The energy transfer in two beam coupling continues to be an interesting problem and has therefore been investigated in the present work as a function of the following parameters: angles of incidence, point of entry and orientation of optic axis.

4.2 Experimental Procedure

4.2.1 Experimental Setup

The experiments have been conducted on an electrically poled BaTiO₃ crystal obtained from Sanders Associates of Lockheed Corp. The dimensions of the crystal used are 5.42 x 5.18 x 5.08 mm³ with the optic axis along the 5.42 direction. The diameter of the beam is about 1 mm. Fig. 4.1 shows the schematic of experimental setup used. Two horizontally polarized coherent beams A₁ and A₂, (7.8 mW each, 1 mm diameter) from a He:Ne laser cross in BaTiO₃ crystal. The angle of incidence of beam A₁ is designated as ϕ and angle between the beams is 2θ . A Faraday isolator FI prevents the backward going phase conjugate beam from entering the He:Ne laser cavity. The energy transfer in the two beam coupling is analyzed by simultaneously monitoring four identical detector/amplifier signal detection systems D₁, D₂, D₃ and D₄ as shown in Figure 4.1.

They are operated in the linear region and are calibrated using standard techniques of placing varying neutral density filters in front of the detector and measuring the power as well the reading on the chart recorder.

4.2.2 Method of Parametric Study

The dependence of the beam couplings and energy transfer with respect to the angle of incidence have been studied by changing the angle of incidence of A_1 beam from -45° to $+45^\circ$ in steps of roughly 10° . The angle between the two beams is kept fixed at 10° , and also the direction of the optic axis is kept fixed in the laboratory frame. In all sets of experiments the point of entry, with the angle between the two beams fixed at 10° , is gradually changed in steps of 0.5 mm along the face of the crystal. It may be mentioned that all the data were taken after initial stabilization of the laser for 30 minutes, during which the crystal was blocked from the laser radiation.

4.2.3 Method of Recording Experimental Data

A typical procedure for recording the experimental data is as follows. Initially, only beam A_1 is switched on typically for 5 minutes. This is marked as region a in Fig. 4.2. The signal at the detector is recorded as a function of time to fix the base line in the absence of two beam coupling. This is expected to facilitate the delineation of two beam coupling effects. In this phase marked A₁ in Figure 4.2 the transmitted signal A_{1ti} (where subscript i stands for individual pumping, and t stands for transmitted beam) and the phase conjugate signal, A_{1i}^* if any are recorded. Then beam A_2 is also switched on and the two beam coupling is studied by simultaneously recording the intensities of the two transmitted beams with their phase conjugate signals. These intensities correspond to " $A_1 + A_2$ " phase of the experiment indicating the presence of A_1 and A_2 beams (region b of

Fig.4.2). The transmitted signals A_{1ts} , A_{2ts} , (where subscript s stands for simultaneous pumping) and phase conjugate signals A_{1s}^* and A_{2s}^* are recorded. Now A_1 is switched off to get the individual pumping signal of A_2 by recording both transmitted intensity A_{2ti} and the corresponding phase conjugate signal A_{2i}^* of the latter (region c of Fig. 4.2). Again A_1 is switched on for obtaining " $A_2 + A_1$ " phase of the experiment (region d of Fig. 4.2). A_2 beam is switched off to record the region e of Figure 4.2 where the beam A_1 only is on.

4.2.4 The Method of Data Presentation

Figure 4.2 represents a typical experimental record showing the simultaneous outputs of detectors D_1 , D_2 , D_3 and D_4 using a four pen chart recorder. The changes in intensities $\Delta A_{1t} = A_{1ts} - A_{1ti}$ and $\Delta A_{2t} = A_{2ts} - A_{2ti}$ are obtained from these experimental records. The gain in intensity in the two beam coupling experimentally manifests as positive ΔA_{jt} and the transfer of energy from the beam shows up as negative ΔA_{jt} ($j = 1, 2$). These experiments therefore, easily facilitate the investigation of energy transfer as a function of number of experimental parameters. Finally these changes ΔA_{1t} and ΔA_{2t} in the two beam coupling are studied as functions of various parameters.

4.3 Results and Discussion

4.3.1 Angular Dependence

Fig. 4.3 shows a summary of all the results when angles of incidence are changed while keeping angle between the two beams fixed at 10° and also the orientation of the optic axis is kept the same as shown in the inset in the Figure. The points marked O and \square in Figures represent ΔA_{1t} and ΔA_{2t} . \bullet and \blacksquare represent the cases where self-pump of

the incident beams takes place. Self-pump takes place when the angle of incidence ϕ of beam A_1 is the range $30^\circ - 50^\circ$. Qualitatively it is seen that both ΔA_{1t} and ΔA_{2t} undergo similar changes and ΔA_{2t} is about 0.8 times that of ΔA_{1t} . All the points in the Figure are normalized for equal intensities of the beams ΔA_{1t} or ΔA_{2t} . It can be seen that energy transfer is maximum at around $\pm 25^\circ$. Since the $\Delta A_{2t} < 0$ and $\Delta A_{1t} > 0$, it is clear that energy is transferred from beam A_2 to beam A_1 . The measurements on ΔA_{1t} and ΔA_{2t} corresponding to the points marked in Figure 4.3 are tabulated in Table 4.1. The corresponding values of ΔA^*_1 and ΔA^*_2 at those values of ϕ where self-pump shows up are also included in the table. Here $\Delta A^*_1 = A^*_{1s} - A^*_{1i}$ and $\Delta A^*_2 = A^*_{2s} - A^*_{2i}$ where A^*_{1i} and A^*_{2i} are the self-pump phase conjugate signals in intensities of the beams A_1 and A_2 at detectors D_1 and D_2 respectively under individual beam pumping. A^*_{1s} and A^*_{2s} are the signal intensities at D_1 and D_2 respectively under simultaneous pumping of $A_1 + A_2$. It is interesting to note that the values of ΔA_{1t} and ΔA_{2t} abruptly change when the phase conjugate of the beams develops. The observed points when there is no phase conjugation could be fitted to a sixth degree polynomial of ϕ while those when phase conjugation is observed by a two degree polynomial. These are shown by the smooth lines in the Figure. However, no physical significance could be attached to this variation at present.

The results on angular dependence using the above crystal before γ -irradiation are shown in Figure 4.3a and they are nearly similar in those in Figure 4.3.

4.3.2 Dependence on Points of Entry of the Beam

The dependence of the parameters ΔA_{1t} and ΔA_{2t} on the distance x (from 1.5 mm to 5.0 mm) of the point of entry of the beams from the c axis side of the crystal has been studied. The angle of incidence ϕ of A_1 is kept constant at angles of $+50^\circ$, $+45^\circ$, $+40^\circ$, $+30^\circ$, $+20^\circ$, $+10^\circ$, 0° , -10° , -20° , -30° and -40° respectively for the different experiments. The angle between the beams A_1 and A_2 is kept at 10° for all the experiments. There was

no self-pump at the values of $\phi = 0^\circ, -10^\circ, +10^\circ, -20^\circ, -30^\circ, -35^\circ$ and -40° . Self-pump phase conjugation was observed with $\phi = +20^\circ$ with $x = 3.5, 4.0$ and 4.5 mm, with $\phi = 30^\circ$ at $x = 2.0, 2.5$ and 3.0 mm, with $\phi = 40^\circ$ at $x = 2.5, 3.0$ and 3.5 mm, with $\phi = 45^\circ$ at $x = 2.5$ and 3.0 mm, with $\phi = 50^\circ$ at $x = 2.5$ and 3.0 mm respectively. Thus when $x = 2.5$ mm and 3.0 mm, self-pump phase conjugation was observed for ϕ values between 30° and 50° . With $x = 2.0$ mm at $\phi = 40^\circ$, phase conjugation was observed for beam A_2 only and not for A_1 . Under simultaneous pumping ΔA_2^* was negative. Typical results obtained for $\phi = 20^\circ$ and 10° are shown in Figures 4.4 and 4.5 respectively and the corresponding values of ΔA_{1t} and ΔA_{2t} are given in Tables 4.2 and 4.3 respectively. The corresponding results obtained with the crystal before γ -irradiation are shown in Figures 4.4a and 4.5a respectively.

4.3.3 Dependence on x (Points of Beam Entry) when the Beam Falls on the c Face.

The dependence of the parameters ΔA_{1t} and ΔA_{2t} on the distance x of the point of entry of the beams from the left edge of the crystal as in the above experiment is studied. There is no self-pump in these orientations. x changes from 1.5 mm to 5.0 mm. The angle of incidence ϕ of A_1 is kept constant at angles of $+20^\circ, +10^\circ, 0^\circ, -10^\circ$ and -20° respectively. The angle between the beams A_1 and A_2 is kept at 10° for all experiments. The ΔA_{1t} and ΔA_{2t} values reach a maximum at $x \approx 3$ mm and their dependence on x in all the Figures is similar. In experiments where $\phi = 20^\circ$ and 10° ΔA_{1t} is negative while ΔA_{2t} is positive. on the other hand in experiments where $\phi = 0^\circ, -10^\circ$ and -20° , ΔA_{1t} is positive and ΔA_{2t} is negative. The reason for this will be discussed later in Section 4.3.6. Typical results of an experiments when $\phi = 10^\circ$ are shown in Figure 4.6 and are tabulated in Table 4.4. The corresponding results obtained before the crystal was γ -irradiated are shown in Fig. 4.6a. The relative directions of the axis and of the beams A_1 and A_2 are shown in the

insets of the Figures. Figure 4.6b shows the results when the direction of the c axis is reversed. Here $\Delta A_1(t)$ and $\Delta A_2(t)$ reverse their sign.

4.3.4 Dependence on Angle of Incidence when Beams Fall on c Face

Figure 4.7 shows the dependence of ΔA_{1t} and ΔA_{2t} on the angle of incidence of the beams when the beams enter on the c face perpendicular to the c axis. The orientation of the crystal is shown in the inset of the Figure, and there is no self-pump in this orientation. Here as expected ΔA_{1t} and ΔA_{2t} change their signs as one passes from the minus value of ϕ to + value of ϕ . Table 4.5 gives ΔA_{1t} and ΔA_{2t} values of the different points marked.

4.3.5 Results when Horizontally Polarized Beam Interacts with Vertically Oriented c Axis

When the polarization of the beams and the orientation of the c axis are perpendicular, no significant interaction was observed between the beams. This was so at different angles between the beams as well as with different points of entrance of the beams in the crystal.

4.3.6 Dependence of Energy Transfer on the Points of Entry

The beam which has the larger component in the + c direction of the c axis gains energy from the other. In other words the beam which makes the smaller angle with the + c direction gains energy. This is an important point that has been noted in these experiments.

In Section 4.3.3 it has been noted that when the angles of incidence of beam A_1 are $+20^\circ$ and $+10^\circ$, the ΔA_{1t} values are negative and ΔA_{2t} values are positive. In these orientations A_1 loses energy to A_2 as A_2 makes smaller angle to the $+c$ direction of the c axis. The ΔA_{1t} values are positive and ΔA_{2t} values are negative when $\phi = 0^\circ, -10^\circ$ and -20° as beam A_1 makes the smaller angle with the positive direction of the c axis.

Fig. 4.3 shows the variation of ΔA_{1t} and ΔA_{2t} with the change in their angles of incidence. Here ΔA_{1t} values are positive and ΔA_{2t} values are negative showing that A_1 gains energy from A_2 for the orientation shown in the Figure for the reason indicated above. As indicated earlier there is an abrupt change in ΔA_{1t} and ΔA_{2t} in the region where self-pumped phase conjugation takes place. This is because part of the beams get phase conjugated instead of being transmitted.

4.3.7 Exchange of Energy in Two Beam Coupling in Photorefractive Crystals

4.3.7.1 For orientations where there is no self-pump phase conjugation

For these orientations in two beam coupling, there is a diffraction of one beam into the other and an energy transfer from one beam to the other. If the incidence beams are of the same intensity, the diffraction D and energy transfer E can be represented by the following equations:

$$A_{1ts} = A_{1ti} + \Delta A_{1ts} = A_{1ti} + D \text{ (from } A_2) + E \text{(1)}$$

$$A_{2ts} = A_{2ti} + \Delta A_{2ts} = A_{2ti} + D \text{ (from } A_1) + E \text{(2)}$$

Here A_{1ti} and A_{2ti} are the intensities of the beams A_1 and A_2 after individual transmissions through the crystals while A_{1ts} and A_{2ts} are the intensities of the transmitted signals when both beams ($A_1 + A_2$) are simultaneously put on. ΔA_{1ts} and ΔA_{2ts} are the changes in the transmitted signals because of simultaneous pumping. When the two coherent beams ($A_1 + A_2$) form a grating the crystal under simultaneous pumping, as A_1 and A_2 are of nearly

equal intensity, the diffracted signal component D will be the same in both A_{1ts} and A_{2ts} . However as the energy exchange takes place, assuming A_2 gives energy to A_1 , $\Delta A_{2ts} = D - E$ and $\Delta A_{1ts} = D + E$ as in equations 1 and 2. For the orientations where there is no phase conjugation, the values of D and E are calculated from the observed values of ΔA_{1ts} and ΔA_{2ts} and are given in Tables 4.1 to 4.5 corresponding to the Figures 4.3 to 4.7.

In Tables 4.1 to 4.5 the energy transfer component E is larger than the diffracted component D . Some of these aspects have been examined in detail using chopped beams by Kapoor et al.[4.1] from this lab. These experiments also lead to similar conclusions with regard to the relative magnitudes E and D .

4.3.7.2 For the orientation where there is phase conjugation

A separate representation of the case where there is self-pumped phase conjugation in individual and simultaneous pumping of two interacting beams in crystal is shown in Fig. 4.8. As indicated in Section 4.2.3 A_{1i}^* and A_{2i}^* represent the individual self-pumped phase conjugates of beams A_1 and A_2 respectively while A_{1s}^* and A_{2s}^* represent the corresponding phase conjugates under simultaneous pumping. A_{1ti} and A_{2ti} are individual transmitted beams intensities while A_{1ts} and A_{2ts} are transmitted intensities under simultaneous pumping. Thus $\Delta A_1^* = A_{1s}^* - A_{1i}^*$ and $\Delta A_2^* = A_{2s}^* - A_{2i}^*$ represent the changes in the phase conjugate intensities under simultaneous pumping. When there is individual self-pumped phase conjugation, part is spent in developing its phase conjugate so that part of the incident beam $A_{1ti} = A_1 - A_{1i}^*$ and $A_{2ti} = A_2 - A_{2i}^*$ neglecting crystal absorption for simplicity. The changes ΔA_2^* and ΔA_1^* come in because of mutual phase conjugation as explained by earlier workers where in the beam a part of beam A_2 gets diffracted in a separate grating into the opposite direction of A_1 in the direction of A_{1i}^* and simultaneously A_1 gets into the direction of A_{2i}^* . Along with mutual diffraction there will also be a transfer of energy from one beam to the other. The phenomenon leads to

the development of ΔA^*_2 and ΔA^*_1 . The values of ΔA^*_2 and ΔA^*_1 are included in Tables 4.1 and 4.5. Assuming ΔA^*_2 introduces a change in the transmitted intensity of A_{1ts} or affects the value of ΔA_{1ts} and similarly ΔA^*_1 affects the value of ΔA_{2ts} , the earlier equations involving the diffraction and energy transfer parameters will be revised when phase conjugation occurs as

$$\Delta A_{1ts} = D^* \pm E - \Delta A^*_2 \dots\dots\dots (3)$$

$$\Delta A_{2ts} = D^* \pm E - \Delta A^*_1 \dots\dots\dots (4)$$

As the two beams $A_1 + A_2$ are of nearly equal intensity D^* is the same in both equations. The sign of E is to be selected depending upon the direction of energy transfer. The values of D^* and E calculated from these formula are included in Tables 4.1 and 4.2 for the case where there is mutual phase conjugation. D^* is used instead of D to indicate that part of beams A_2 and A_1 are used in fanning F in the crystal and it is difficult at this stage to separate the parameters D and F . However D^* may be written as $D - F$. Because of this D^* may come out to have some times a negative value depending upon the extent of fanning value when there is phase conjugation. Tables 4.1 and 4.2 show that D^* is negative in some cases. Typical basic observed data used in Table 4.1 is given in Table 4.6 as an illustration.

As indicated earlier one expects diffraction and energy transfer in mutual phase conjugation. Thus

$$\Delta A^*_1 = d^* + e \dots\dots\dots (5)$$

$$\Delta A^*_2 = d^* - e \dots\dots\dots (6)$$

Here d^* indicates diffraction and e indicates energy transfer in mutual phase conjugation. The sign of e depends upon whether the change ΔA^*_2 is greater or less than the change ΔA^*_1 . In these equations d^* includes the effects of diffraction d and energy loss f due to fanning in mutual phase conjugation. Thus $d^* = d - f$. Here d^* could be negative sometimes as seen for example in Tables 4.1a and 4.2a, depending upon the extent of fanning.

The above analysis of the change ΔA^*_1 and ΔA^*_2 under simultaneous pumping suggests that both could be positive or both could be negative or one positive and the other negative (see Table 4.6). It is also possible that while A^*_{1i} and A^*_{2i} show up prominently under individual pumping, A^*_{1s} and A^*_{2s} under simultaneous pumping could be both zero, thus explaining the results obtained earlier by Venkateswarlu et al.[4.2, 4.3].

References;

- 4.1 R. Kapoor, M. Moghbel and P. Venkateswarlu, Opt. Lett.. 18, 696 (1993),
- 4.2 P. Venkateswarlu, H. Jagannath, M. C. George and A. Miahnahri, Beam Coupling and Self-pulsation, International Laser Science Conference (ILS III), Atlantic City, Optical Society of America, Washington DC (1987), Advances in Laser Science - III, P. 246, AIP Conference Proceedings no. 772.
- 4.3 P. Venkateswarlu, M. Moghbel, P. Chandra Sekhar, M. C. George and A. Miahnahri, in Laser Spectroscopy and Nonlinear Optics of Solids, edited by S. Radhakrishna and B. C. Tan, Narosa Publishing house, New Delhi, (1990).

Table 4.1 Change in intensity vs angle of incidence at $x = 2.5$ mm.

Angle °	ΔA_{1t}	ΔA_{2t}	D	E
-40	9.9	-8.9	0.5	9.4
-35	14.0	-10.8	0.2	13.8
-30	25.0	-19.0	3.0	22.0
-20	21.0	-18.1	1.45	19.55
-10	16.8	-13.2	1.8	15.0
0	13.7	-12.0	0.85	12.85
10	18.9	-12.7	3.1	15.8
20	20.9	-18.3	1.3	19.6

Table 4.1a Change in intensity vs angle of incidence at $x = 2.5$ mm at angles where there is self-pumped phase conjugation.

Angle °	ΔA_{1t}	ΔA_{2t}	ΔA_1^*	ΔA_2^*	D	E	d	e
30	7.4	-7.6	2.0	1.6	1.7	7.3	1.8	0.2
40	7.5	-5.5	3.0	-0.97	2.105	4.515	1.015	1.985
45	6.6	-4.7	-1.2	0.64	0.67	6.57	-0.28	0.92
50	4.2	-3.1	-6.4	3.49	-0.905	8.595	-1.455	4.945

Table 4.2 Change in intensity vs point of entry at 20°.

X	ΔA_{1t}	ΔA_{2t}	D	E
1.5	21.1	-18.6	1.25	19.85
2.0	20.8	-18.0	1.4	19.4
2.5	20.9	-18.3	1.3	19.6
3.0	18.7	-16.9	0.9	17.8
5.0	9.4	-21.1	-5.85	15.25

Table 4.2a Change in intensity vs point of entry at 20° at x values where there is self-pumped phase conjugation.

X	ΔA_{1t}	ΔA_{2t}	ΔA_1^*	ΔA_2^*	D	E	d	e
3.5	12.1	-15.1	-0.7	2.21	-0.745	15.055	0.755	1.405
4.0	9.4	-14.0	4.6	3.03	1.515	10.915	3.815	0.785
4.5	7.9	-12.3	3.9	1.4	0.45	8.85	2.65	1.25

Table 4.3 Change in intensity vs point of entry at +10°.

X	ΔA_{1t}	ΔA_{2t}	D	E
1.5	16.9	-10.5	3.1	13.7
2.0	12.3	-9.1	1.6	10.7
2.5	18.9	-12.7	3.2	15.8
3.0	19.3	-12.5	3.4	15.9
3.5	16.5	-11.1	2.7	13.8
4.0	16.1	-11.4	2.35	13.75
4.5	13.5	-10.8	1.35	12.15
5.0	3.6	-5.9	-1.15	4.75

Table 4.4 Change in intensity vs point of entry at $+10^\circ$.

X	ΔA_{1t}	ΔA_{2t}	D	E
1.5	-10.6	7.0	-1.8	8.8
2.0	-10.5	13.2	1.35	11.85
2.5	-14.1	13.8	-0.15	13.95
3.0	-15.2	16.4	0.6	15.8
3.5	-13.1	14.5	0.7	13.8
4.0	-9.8	11.2	0.7	10.5

Table 4.5 Change in intensity vs angle of incidence at $x = 2.5$ mm.

Angle $^\circ$	ΔA_{1t}	ΔA_{2t}	D	E
-30	31.4	-6.7	12.35	19.05
-20	36.1	-20.1	8.0	28.1
-10	27.4	-25.8	0.8	26.6
0	10.3	-14.4	-2.05	12.35
10	-14.1	13.8	-0.15	-13.95
20	-20.8	27.0	3.1	-23.9
30	-9.3	32.4	11.55	-20.85
40	-5.1	13.6	4.25	-9.35
45	0.0	6.3	3.15	3.15

Table 4.6 Typical basic observed data used in Table 4.1 representing change in intensity vs angle of incidence at $x = 2.5$ mm.

Angle °	A _{1ti}	A _{1ts}	ΔA_{1t}	A _{2ti}	A _{2ts}	ΔA_{2t}	A _{1i} *	A _{1s} *	ΔA_1 *	A _{2i} *	A _{2s} *	ΔA_2 *
-40	10.6	20.5	9.9	12.5	3.6	-8.9						
-35	14.5	28.5	14.0	14.7	3.9	-10.8						
-30	24.3	49.3	25.0	23.2	4.2	-19.0						
-20	24.6	45.6	21.0	25.0	6.9	-18.1						
-10	27.6	44.3	16.8	25.2	12.0	-13.2						
0	25.5	39.2	13.7	27.5	15.5	-12.0						
10	29.6	48.5	18.9	25.9	13.2	-12.7						
20	19.5	28.9	9.4	25.7	11.7	-14.0						
30	9.6	17.0	7.4	11.7	4.1	-7.6	3.0	5.0	2.0	1.6	3.2	1.6
40	8.6	16.1	7.5	9.6	4.1	-5.5	2.0	5.0	3.0	2.82	1.85	-0.97
45	7.8	14.4	6.6	8.7	4.0	-4.7	6.1	4.9	-1.2	2.68	3.32	6.4
50	4.2	8.4	4.2	7.0	3.9	-3.1	19.4	13.0	-6.4	4.27	7.76	3.49

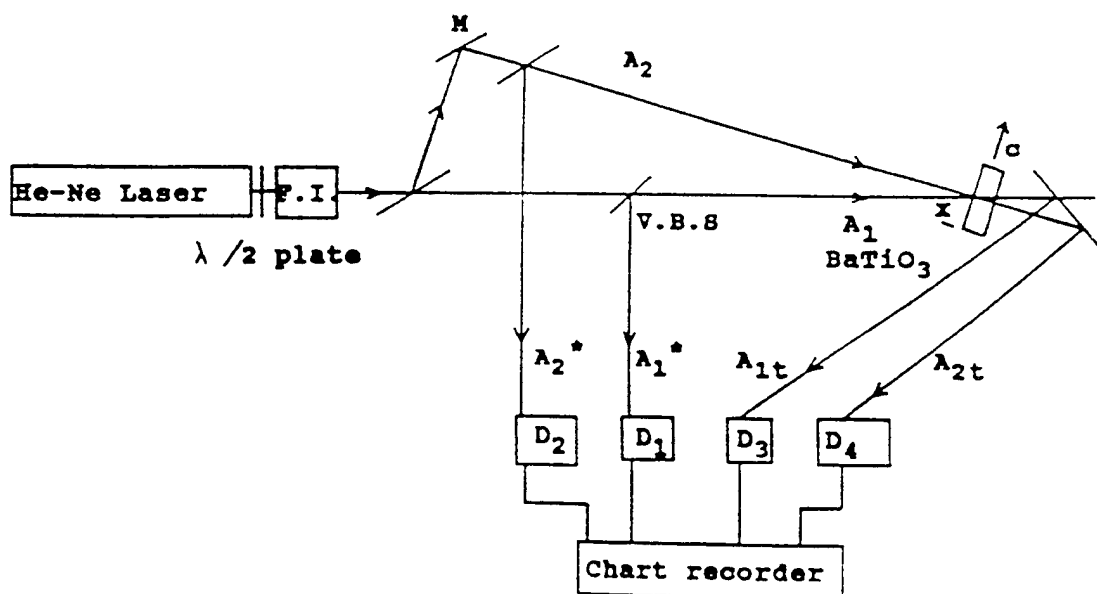


Fig. 4.1 Schematic of experimental setup, F. I. Faraday isolator, V.B.S. Variable beam splitter, D_j ($j = 1 - 4$) Detectors/Amplifiers.

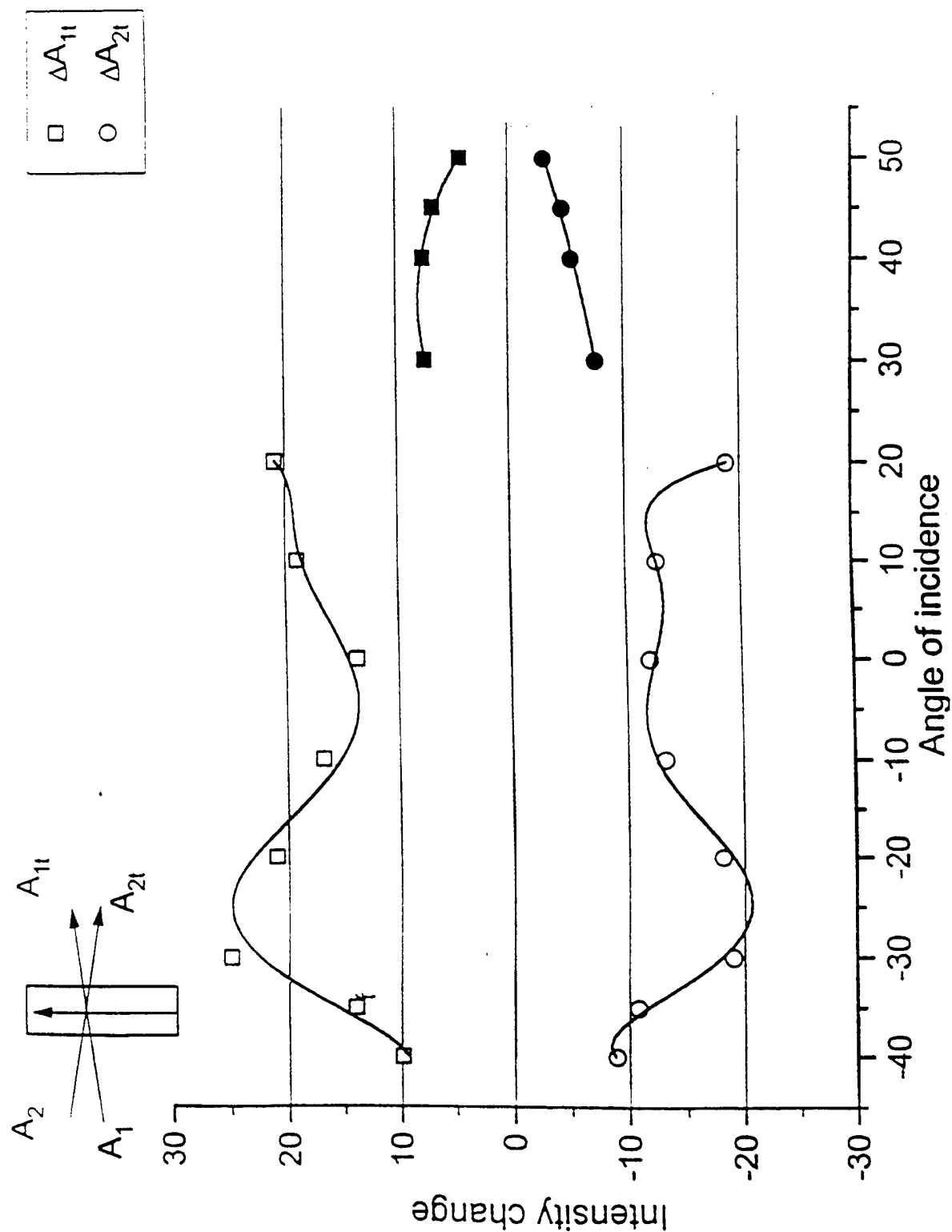
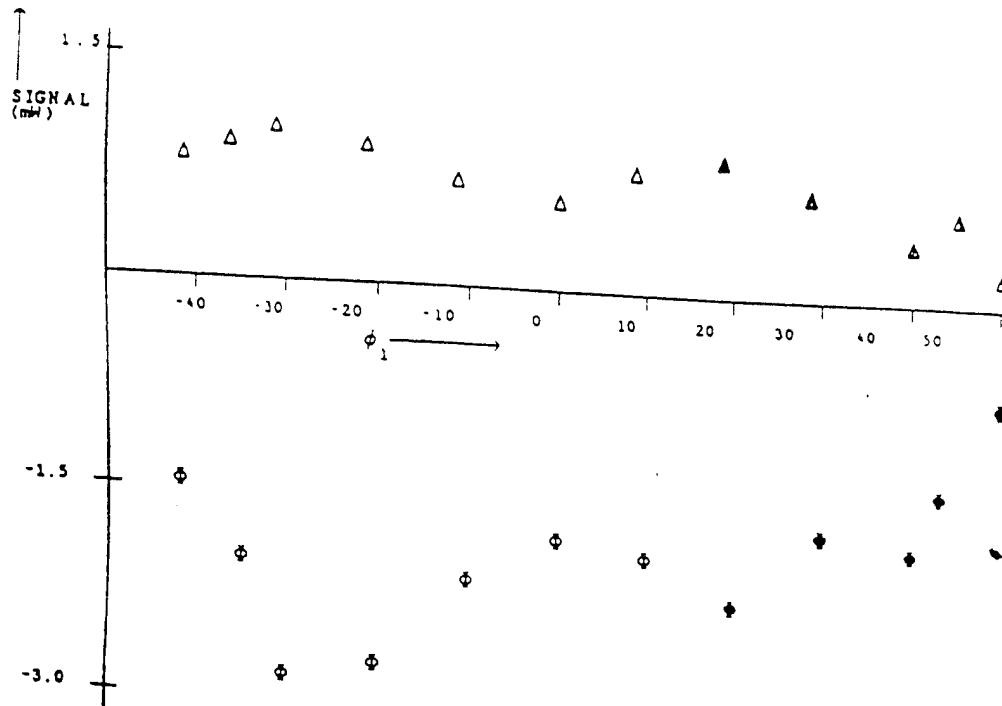
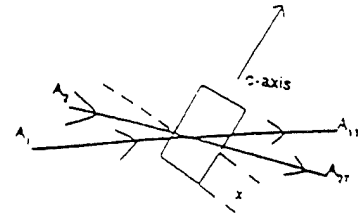


Fig.4.3 Change in transmitted intensities $\Delta A_{1t}=A_{1s}-A_{1i}$ and $\Delta A_{2t}=A_{2s}-A_{2i}$ in γ -irradiated BaTiO_3 crystal in two beam coupling as the angle of incidence at the point of entry is changed. Here A_{1i} and A_{2i} are transmitted intensities of individual beams, while A_{1s} and A_{2s} are transmitted intensities under two beam coupling. ■ and ● represent the cases when self-pumped phase conjugation takes place. The point of entry is at $x = 2.5$ mm.

Δ - Corresponds to $\Delta A_{1t} = A_{1ts} - A_{1ti}$
 ϕ - Corresponds to $\Delta A_{2t} = A_{2ts} - A_{2ti}$
 $x = 2.5 \text{ mm}$



Solid symbols correspond to points where phase conjugate signal is observed in individual pumping.

Fig.4.3a Change in transmitted intensities in BaTiO₃ crystal before γ -irradiation in two beam coupling as the angle of incidence at the point of entry is changed. Here A_{1i} and A_{2i} are transmitted intensities of individual beams, while A_{1s} and A_{2s} are transmitted intensities under two beam coupling. The point of entry is at $x = 2.5 \text{ mm}$.

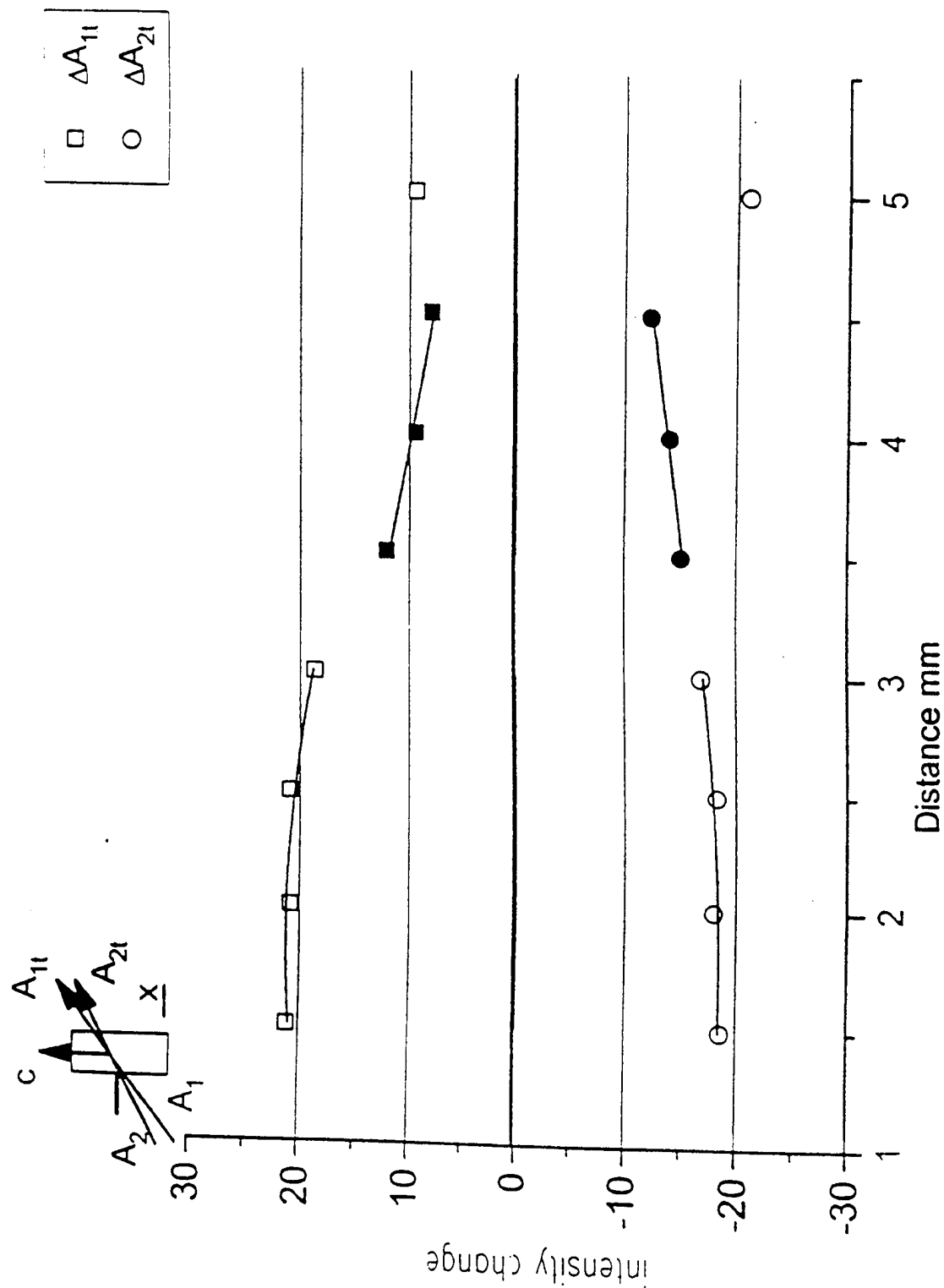
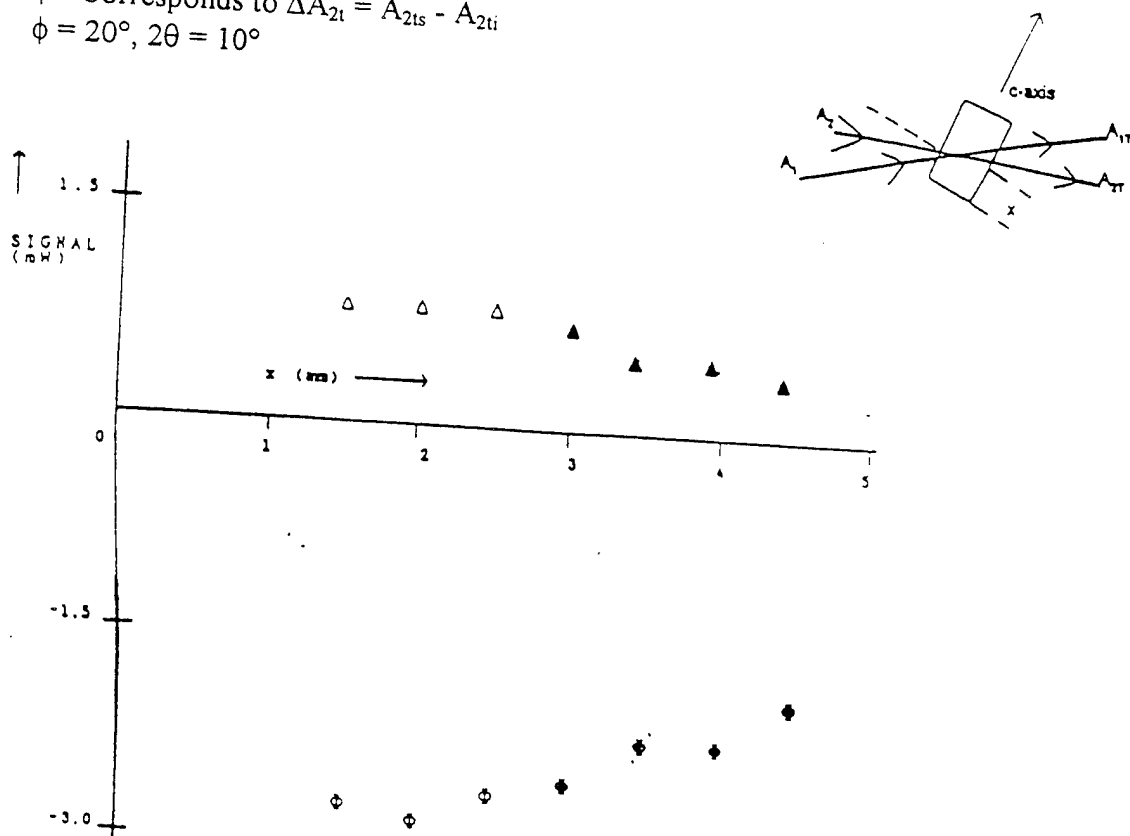


Fig. 4.4 Change in transmitted intensities $\Delta A_{1t} = A_{1s} - A_{1i}$ and $\Delta A_{2t} = A_{2s} - A_{2i}$ in γ -irradiated BaTiO_3 crystal in two beam coupling as the point of entry is changed. Here A_{1i} and A_{2i} are transmitted intensities of individual beams, while A_{1s} and A_{2s} are transmitted intensities under two beam coupling. \blacksquare and \bullet represent the cases when self-pumped phase conjugation takes place. The angle of entry is 20° .

Δ - Corresponds to $\Delta A_{1t} = A_{1ts} - A_{1ti}$
 ϕ - Corresponds to $\Delta A_{2t} = A_{2ts} - A_{2ti}$
 $\phi = 20^\circ, 2\theta = 10^\circ$



Solid symbols correspond to points where phase conjugate signal is observed in individual pumping.

Fig. 4.4a Change in transmitted intensities in BaTiO₃ crystal before γ -irradiation in two beam coupling as the point of entry is changed. Here A_{1i} and A_{2i} are transmitted intensities of individual beams, while A_{1s} and A_{2s} are transmitted intensities under two beam coupling.

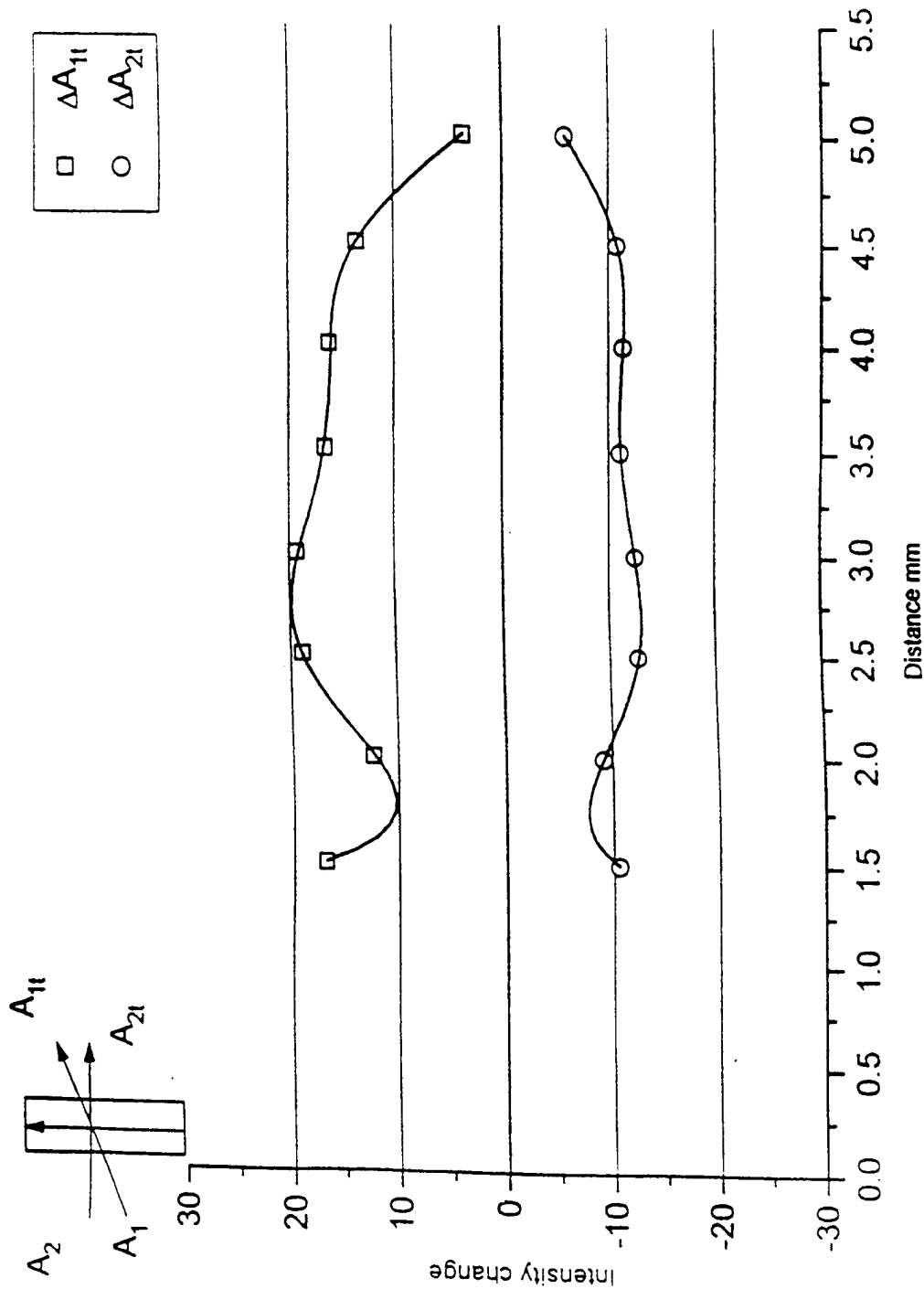


Fig. 4.5 Change in transmitted intensities $\Delta A_{1t}=A_{1s}-A_{1i}$ and $\Delta A_{2t}=A_{2s}-A_{2i}$ in γ -irradiated BaTiO₃ crystal in two beam coupling as the point of entry is changed. Here A_{1i} and A_{2i} are transmitted intensities of individual beams, while A_{1s} and A_{2s} are transmitted intensities under two beam coupling. ■ and ● represent the cases when self-pumped phase conjugation takes place. The angle of entry is 10°.

Δ - Corresponds to $\Delta A_{1t} = A_{1ts} - A_{1ti}$
 ϕ - Corresponds to $\Delta A_{2t} = A_{2ts} - A_{2ti}$
 $\phi = 10^\circ, 2\theta = 10^\circ$

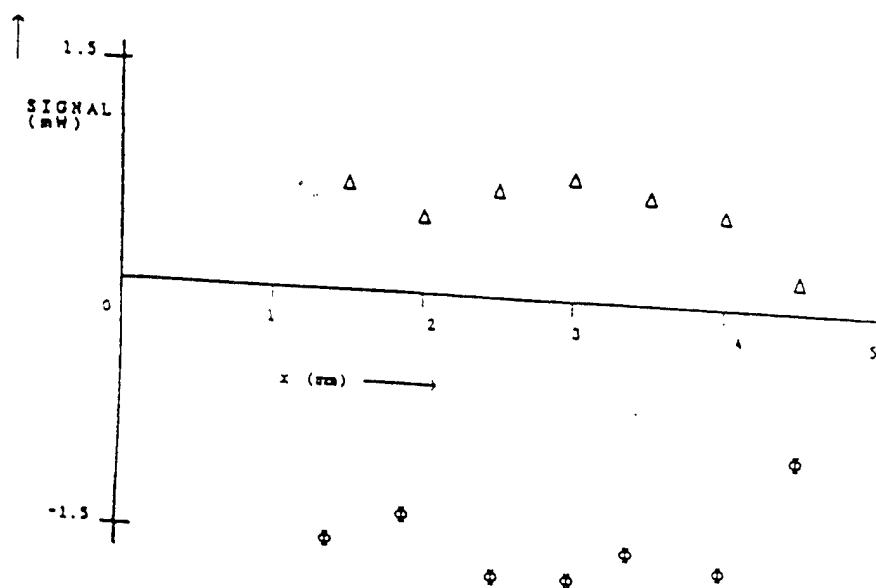
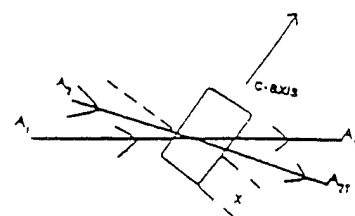


Fig. 4.5a Change in transmitted intensities in BaTiO₃ crystal before γ -irradiation in two beam coupling as the point of entry is changed. Here A_{1i} and A_{2i} are transmitted intensities of individual beams, while A_{1s} and A_{2s} are transmitted intensities under two beam coupling.

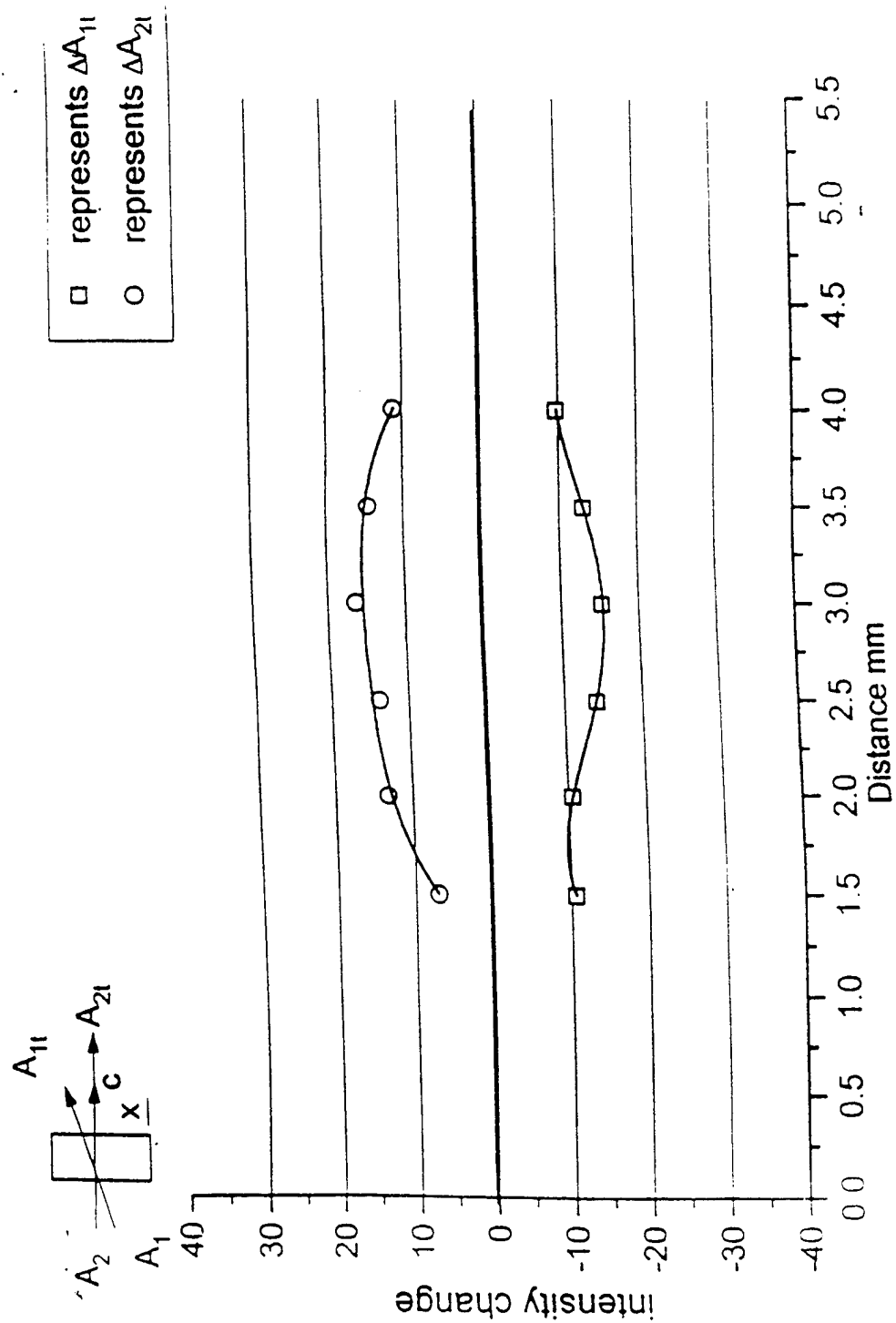


Fig. 4.6 Change in transmitted intensities $\Delta A_{1t} = A_{1s} - A_{1i}$ and $\Delta A_{2t} = A_{2s} - A_{2i}$ in γ -irradiated BaTiO_3 crystal in two beam coupling as the point of entry is changed. Here A_{1i} and A_{2i} are transmitted intensities of individual beams, while A_{1s} and A_{2s} are transmitted intensities under two beam coupling. The angle of entry is 10° .

Δ - Corresponds to $\Delta A_{1t} = A_{1ts} - A_{1ti}$
 ϕ - Corresponds to $\Delta A_{2t} = A_{2ts} - A_{2ti}$
 $\phi = 10^\circ, 2\theta = 10^\circ$

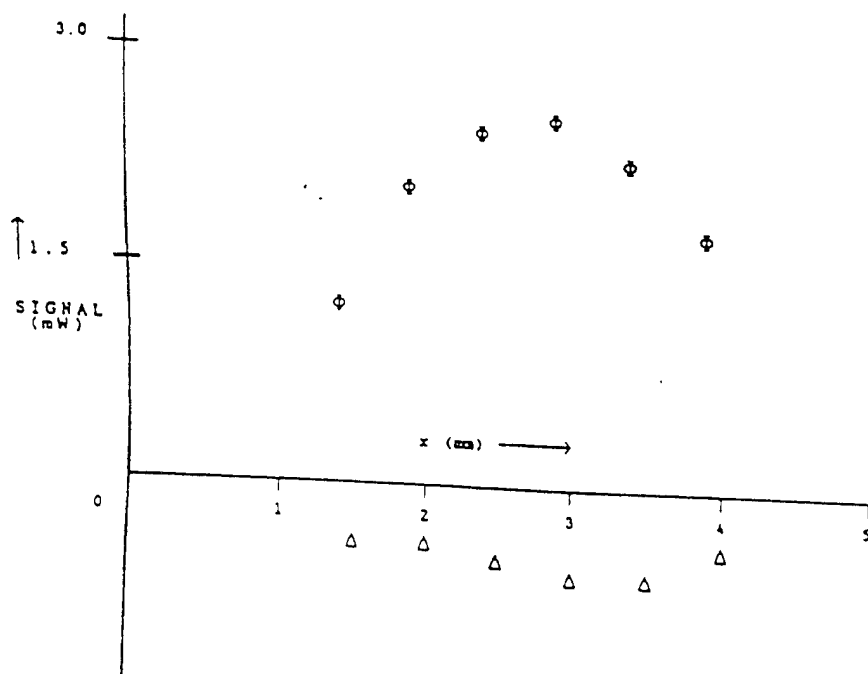
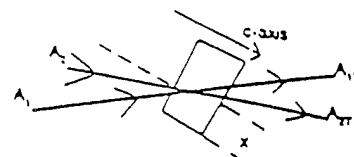


Fig. 4.6a Change in transmitted intensities in BaTiO_3 crystal before γ -irradiation in two beam coupling as the point of entry is changed. Here A_{1i} and A_{2i} are transmitted intensities of individual beams, while A_{1s} and A_{2s} are transmitted intensities under two beam coupling.

Δ - Corresponds to $\Delta A_{1t} = A_{1ts} - A_{1ti}$

ϕ - Corresponds to $\Delta A_{2t} = A_{2ts} - A_{2ti}$

$\phi = 10^\circ$, $2\theta = 10^\circ$

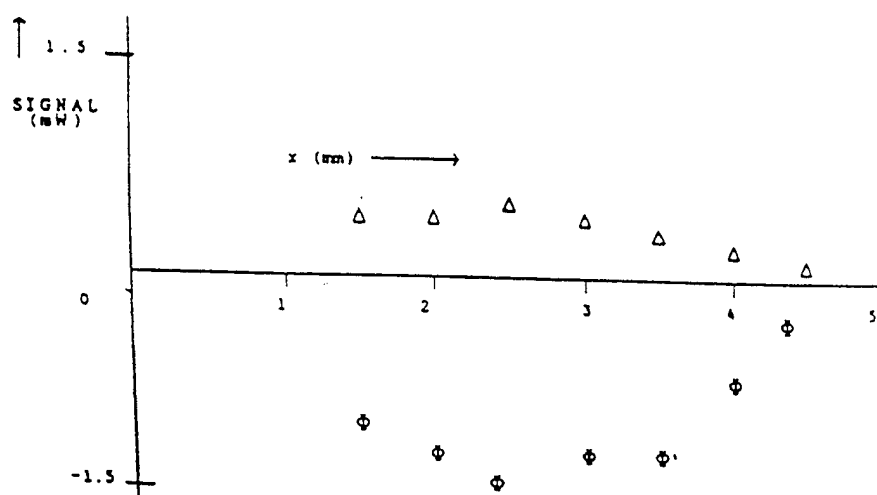
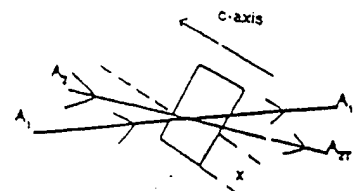


Fig. 4.6b Change in transmitted intensities in BaTiO_3 crystal before γ -irradiation in two beam coupling as the point of entry is changed. Here A_{1i} and A_{2i} are transmitted intensities of individual beams, while A_{1s} and A_{2s} are transmitted intensities under two beam coupling. Here the orientation of the c axis is changed by 180° .

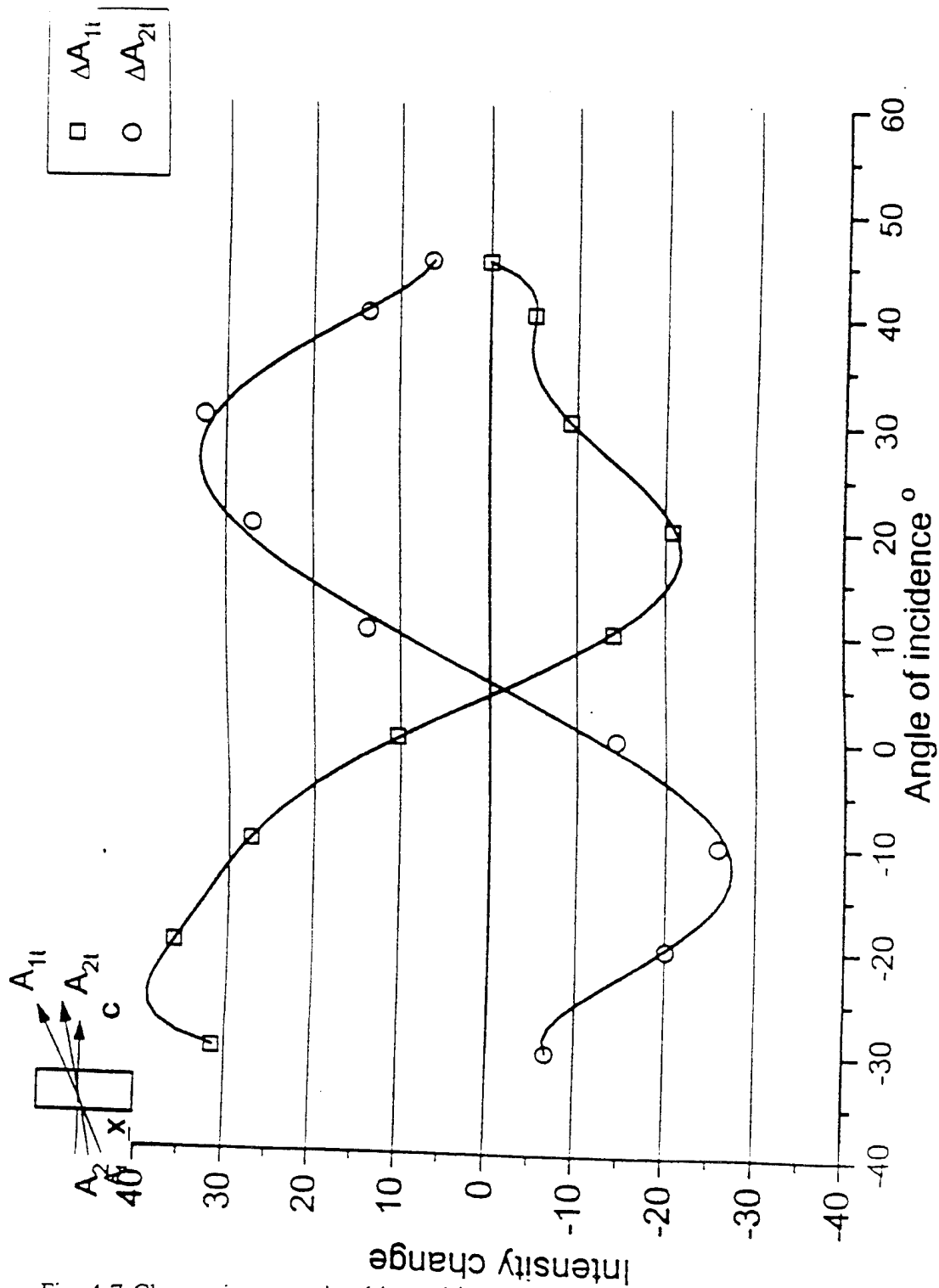


Fig. 4.7 Change in transmitted intensities $\Delta A_{1t} = A_{1s} - A_{1i}$ and $\Delta A_{2t} = A_{2s} - A_{2i}$ in γ -irradiated BaTiO_3 crystal in two beam coupling as the angle of incidence at the point of entry is changed. Here A_{1i} and A_{2i} are transmitted intensities of individual beams, while A_{1s} and A_{2s} are transmitted intensities under two beam coupling. The point of entry is 2.5mm.

Δ - Corresponds to $\Delta A_{1t} = A_{1ts} - A_{1ti}$
 ϕ - Corresponds to $\Delta A_{2t} = A_{2ts} - A_{2ti}$
 $x = 2.5 \text{ mm}$

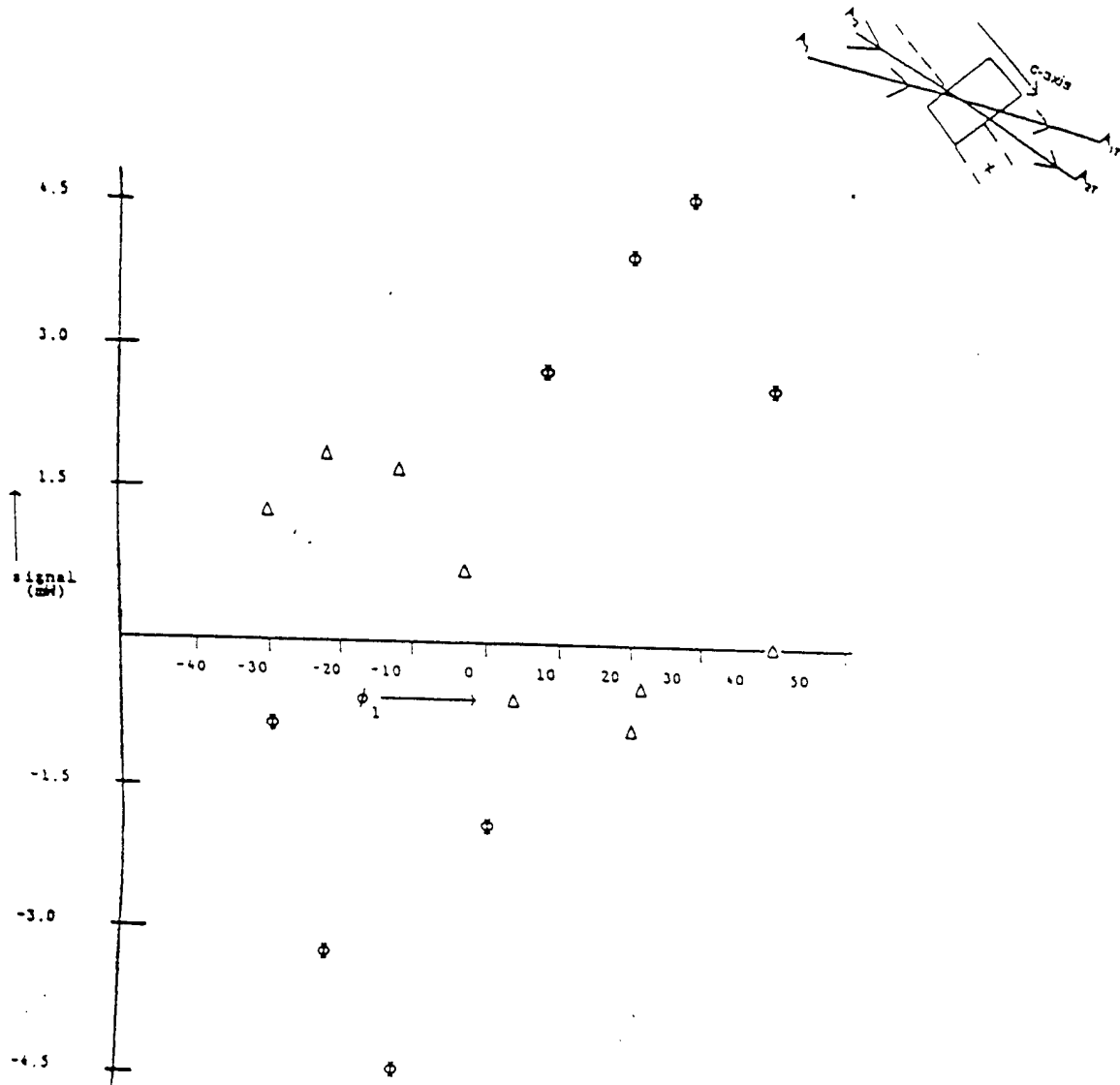


Fig. 4.7a Change in transmitted intensities in BaTiO₃ crystal in two beam coupling as the angle of incidence at the point of entry is changed. Here A_{1i} and A_{2i} are transmitted intensities of individual beams, while A_{1s} and A_{2s} are transmitted intensities under two beam coupling.

CHAPTER 5

NEW BEAM COUPLING IN BaTiO₃

5.1 Introduction

We discussed in the earlier chapter the beam couplings of two coherent beams in transmission and in self-pumped phase conjugation wherever observed. The diffraction, exchange of energy in the transmission and phase conjugation were discussed in detail. In this chapter we discuss the experiments where a new type of beam coupling and corresponding phase conjugation have been observed. The results obtained are presented and discussed.

5.2 Experiment

Two coherent beams 1 and 2 from a He-Ne laser (6328 Å), horizontally polarized in the same plane with the c axis of an electrically poled BaTiO₃ crystal (10 x 10 x 10 mm³) are incident on a face of the crystal in the configuration shown in Figure 5.1. The beams meet at the center of the surface of the crystal with the angles of incidence $\phi_1 = 60.5^\circ$ and $\phi_2 = 61.5^\circ$ shown in more detail in Figure 5.2, and it was made sure that the specular reflections do not interfere in the experiment. This configuration is not convenient for individual CAT phase conjugation and no individual phase conjugation could be detected. However when the two beams are on simultaneously pumping, fanning gets developed. The development of the fanned beam inside the crystal looks like a pincushion. Detectors D₁ and D₂ (Fig. 5.2) record the phase conjugates 1* and 2* of the beams 1 and 2 respectively. We discuss below the results obtained in this new beam coupling experiment.

5.3 Results and Discussion

When the beams are coherent, the growth of 1^* and 2^* show random fluctuations (Fig. 5.3). If the beams are incoherent, the growths are smooth and reach saturated maximum values (Fig. 5.4). The simultaneous growth of the phase conjugate beams 1^* and 2^* can be seen separately in these Figures: The right portion of these Figures (region B) show the signals at the detectors D_1 and D_2 when one of the beams 1 or 2 is put off.

If we start with the two coherent beams being on for a few minutes and then put off 1, then beam 2^* at D_2 decays fast while the beam 1^* at D_1 goes up for a while and then decays. Similar is the situation when beam 2 is put off. Then 2^* shows an increase first and then a decay while 1^* decays with out showing any increase though the decay shows a kink in its decay. At the beginning one can see the sudden rise of 2^* in the region B of Figure 5.3 which shows an increase and then decay there is a sharp decay for 1^* with out a raise. Figure 5.4 shows the same with a slower speed. However when two incoherent beams are on for a few minutes till the phase conjugates 1^* and 2^* get well developed and then one of the beams say 2 is put off, 2^* does not show an increase but decays slowly, while 1^* shows a sharp decay. This can be seen in Figure 5.4.

5.31 Coherent Beams

The following analysis will explain the above results when coherent beams are used. The regions marked A_1 , A_2 , A_3 and A_4 shown in Figure 5.2 around the points PQRS respectively are those where the beams meet from two different directions. Here in these regions the beams develop gratings, say of type α , as in the experiments of earlier workers [1.2] which give rise to mutual phase conjugation. For instance the gratings in the region A_1

responsible to send a part of the beam 2 to detector D_1 (in the backward direction of 1 as its phase conjugate 1^*) and similarly to send part of beam 1 to detector D_2 as 2^* (in the backward direction of beam 2). In addition, the region marked A_1 includes gratings of type β formed by two beam coupling where a part of the beam 1 goes in the forward direction (PQ) of beam 2, and a part of the beam 2 goes in the forward direction PS of beam 1. Further one can see that the beam 1 and similarly 2 will travel in opposite directions in the regions PQ, QR, RS and SP giving rise to gratings of type γ responsible for normal reflection. The γ type gratings are formed in the above regions by $[1 \rightarrow \leftarrow 1]$, $[2 \rightarrow \leftarrow 2]$ and $[1 \rightarrow \leftarrow 2]$ of which the first two can be seen to be weaker. Thus when the beams 1 and 2 are simultaneously on, detector D_1 will record:

$$1^* = 2(1\alpha) + 2(3\alpha - 4\gamma - 1\beta) + 1(3\alpha - 4\gamma + 1\beta) + 2(1\beta + 3\alpha + 1\beta - 4\gamma) + 1(1\beta + 3\alpha - 4\gamma - 1\beta) \text{ at } D_1. \quad 5.1$$

and the detector D_2 will record :

$$2^* = 1(1\alpha) + 1(3\alpha - 4\gamma - 1\beta) + 2(3\alpha - 4\gamma + 1\beta) + 1(1\beta + 3\alpha + 1\beta - 4\gamma) + 2(1\beta + 3\alpha - 4\gamma - 1\beta). \quad 5.2$$

Here $2(1\alpha)$ means that beam 2 after one effect of type α grating goes to detector D_1 , $2(3\alpha - 4\gamma - 1\beta)$ means beam 2 before reaching D_1 undergoes 3 diffractions by type α gratings (mutual phase conjugation), and 4 of type γ and 1 of β type. Negative sign indicates loss of intensity because of the particular diffraction.

When both the beams are on, the phase conjugates 1^* and 2^* at D_1 and D_2 reach their maximum values though coupled with fluctuations. If then the beam 1 is put off, the detectors record 1^* at D_1 as:

$$1^* = 2(1\alpha) + 2(3\alpha - 4\gamma - 1\beta) + 2(1\beta + 3\alpha + 1\beta - 4\gamma) \quad 5.3$$

and 2^* at D_2 as:

$$2^* = 2(3\alpha - 4\gamma + 1\beta) + 2(1\beta + 3\alpha - 4\gamma - 1\beta) \quad 5.4$$

Similarly if beam 2 is put off 2^* at D_2 will be as

$$2^* = 1(1\alpha) + 1(3\alpha - 4\gamma - 1\beta) + 1(1\beta + 3\alpha + 1\beta - 4\gamma) \quad 5.5$$

and 1^* at D_1 as

$$1^* = 1(3\alpha - 4\gamma + 1\beta) + 1(1\beta + 3\alpha - 4\gamma - 1\beta) \quad 5.6$$

The major contribution at D_1 in 5.3 (and similarly at D_2 in (5.5)) will be due to the first term and then the second term, the least contribution being due to the third term. The first term in the eqn. 5.4 will give more contribution than the second at D_2 . Similarly the first term in eq. 5.6 will give more contribution from the second at D_1 than the second one.

When the beam 2 is put off all the gratings decay. The signal 2^* at D_2 decays because of the first term and also because of the first parameter in the second term and the first 3 parameters in the third term all in 5.5. However the two parameters (-4γ) and (-1β) indicate that their decay will give a growth to the signal at D_2 . Then one sees the resultant effect of growth and decay of the signal. As shown in Figures 5.5 to 5.8, the resultant signal at D_2 first grows and then decays. These Figures represent the results from four different, but similar, experiments. The gratings β and γ are probably short-lived compared to α grating.

The signal 1^* when the beam 2 is blocked does not show a prominent growth as the signal 2^* . However it shows a kink. The time taken for the maximum growth point m in 2^* is the same as for the kink m' in 1^* (Figures 5.5 - 5.8). The temporal behavior of the phase conjugate $2^*(I^*_2)$ at D_2 can be represented by

$$I^*_2(t) = K_1(1 - K_2 \exp(-t/\tau_1)) \exp(-t/\tau_2) \quad 5.7$$

In the above equation K_1 and K_2 are constants and are related to the diffraction efficiencies of the above mentioned gratings. τ_1 and τ_2 are respectively the growth and decay rates of the conjugate signal I^*_2 when beam 2 is blocked. It can be noticed in the above equation that when the beam 2 is blocked the phase conjugate I^*_2 will first grow and then decay. Also the

result can be seen for decays of the signal at D_1 . The temporal behavior of the phase conjugate $I^*_1(I^*_1)$ at D_1 when beam 2 is blocked can be represented by the equation

$$I^*_1(t) = K'_1(1 - K'_2 \exp(-t/\tau'_1)) \exp(-t/\tau'_2) \quad 5.8$$

In equation 5.8 K'_1 and K'_2 are constants which are related to different gratings mentioned above. τ'_1 and τ'_2 are respectively the growth and decay times of the phase conjugate signal $I^*_1(I^*_1)$ at D_1 when beam 2 is blocked.

When we tried to fit the above equations in our observed temporal response of both the phase conjugate signals in different conditions, we found that in our temporal curves the decay was probably not a single exponential. Therefore we tried to fit a function with one exponential growth and two exponential decays such that the temporal behavior of the I^*_1 and I^*_2 will be given by the following expressions. Here in the following expressions τ_1 , τ_2 and τ_3 represent one growth and two decays respectively in equation 5.9 while the expressions τ'_1 , τ'_2 and τ'_3 represent one growth and two decays respectively in equation 5.10.

$$I^*_2(t) = K_1(1 - \exp(-t/\tau_1))[\exp(-t/\tau_2) + K_2 \exp(-t/\tau_3)] \quad 5.9$$

and

$$I^*_1(t) = K'_1(1 - \exp(-t/\tau'_1))[\exp(-t/\tau'_2) + K'_2 \exp(-t/\tau'_3)] \quad 5.10$$

Figures 5.5 and 5.6 show the temporal behavior of I^*_1 and I^*_2 when the beam 2 was blocked. Figures 5.5a, 5.5b, 5.6a, and 5.6b show correspondingly the fitting of the above mentioned equations to the observed curves shown in Figures 5.5 - 5.6. Equations 5.9 and 5.10 fitted in good agreement with our data. The time constants and the amplitudes are given in Tables 5.1 and 5.2 in which the data from two other sets of similar experiments are included. The decays when beam 1 is put off are shown in Figure 5.7 while the decay constants for this set and another similar set are shown in Tables 5.3 and 5.4.

5.3.2 Incoherent Beams

Fig. 5.8 shows a typical temporal behavior of the decay of the conjugate signals when one of the two incoherent beams beam 1 was blocked. The prominent growth in 1^* and the kink in 2^* observed when the beams were coherent (Figure 5.7) are absent in Fig. 5.8. The initial small growth of 1^* in Figure 5.8 is because of the decay of the terms -4γ and -1β in eqn. 5.3 due to the decay of the gratings β and γ . When the beams are coherent, β gratings do not exist. Further as pointed out earlier γ gratings are reflection gratings due to $[1 \rightarrow \leftarrow 1]$, $[2 \rightarrow \leftarrow 2]$ and $[1 \rightarrow \leftarrow 2]$ of which the third one will be more prominent. When the beams are coherent all the three varieties of γ gratings are present, but when the beams are incoherent the interaction $[1 \rightarrow \leftarrow 2]$ will not give γ gratings. Therefore, the effect of γ gratings will be less pronounced and will show a minimal rise in 1^* as indicated in 1^* in Figure 5.8. Ding in our laboratory observed slightly more prominent rises for 1^* for slightly different angles of ϕ_1 and ϕ_2 . The decay time constants and magnitudes for incoherent beam coupling are given in Tables 5.5 and 5.6.

5.3.3 Growth of Phase Conjugates When the Beams 1 and 2 are Incoherent

The typical growth of the phase conjugates 1^* and 2^* when the beams 1 and 2 are incoherent is shown in Figure 5.4 (called set I). The growths 1^* or 2^* could be respectively represented by the equation:

$$I^* = k(1 - \exp(-t/\tau))^2 \quad 5.11$$

$$I^* = k'(1 - \exp(-t/\tau'))^2 \quad 5.12$$

The fittings of the growths of 1^* and 2^* to equations 5.11 and 5.12 are in Figs. 5.9a and 5.9b and the agreement is quite good. The time constants and amplitudes for three sets of experiments (including set I) are given in Tables 5.7 - 5.8 for signals 1^* and 2^* .

5.3.4 Growth of Phase Conjugates 1^* and 2^* for Coherent Beams

As seen in Fig 5.3, the growths of the phase conjugate beams 1^* and 2^* show strong fluctuations when the beams 1 and 2 are coherent. When the two beams are coherent equations 5.1 and 5.2 represent the signals 1^* and 2^* at the detectors D_1 and D_2 due to the combined effect the three types of gratings α , β and γ . Of these the effect of the normal reflection gratings of γ is to reduce the signal strength of 1^* and 2^* creating strong fluctuations in the growth curves. These fluctuations also indicate that the τ values of γ are very likely shorter than those of α and β . In spite of these fluctuations, parts of three different growth curves for 1^* are used to get approximate values of the growth constants and are given in Table 5.9. The larger values of τ_1 in Table 5.9 compared to those in Table 5.7 are because of the effect of the fluctuations due to γ -type gratings.

These experiments on growths of 1^* and 2^* have been repeated by vibrating the optical table. The growth of 1^* and 2^* are shown in Fig 5.10 and the fluctuations are absent confirming that the γ -gratings die out fast with vibrations without showing their effect on the growth. The growth constants for 1^* from two sets of experiments including the one of Fig. 5.10 are given in Table 5.10. The τ values obtained are nearer to those obtained when the beams are incoherent (Table 5.7) where the effect of γ type gratings is minimal.

Table 5.1 Decay time constants and magnitudes of equations 5.10 for signal 1* at D1 for coherent two beam coupling in BaTiO₃ when beam 2 is put off.

Parameters	τ'_1	τ'_2	τ'_3	k'_1	k'_2
Set I	0.9481	0.1991	2.092	0.4842	29.81
Set II	1.957	0.1311	2.382	0.6145	35.13
Set III	3.762	0.1291	1.881	0.6313	49.64
Set IV	2.171	0.1271	1.881	0.6251	33.81
Average	2.21	0.15	2.06	0.59	37.1

Table 5.2 Decay time constants and magnitudes from equation 5.9 for signal 2* at D₂ in BaTiO₃ when beam 2 is off.

Parameters	τ_1	τ_2	τ_3	k_1	k_2
Set I	0.2761	8.701	5.201	1.038	0.3501
Set II	0.3551	14.85	4.251	0.8211	0.2251
Set III	0.2771	4.651	4.751	0.6121	0.3701
Set IV	0.3251	4.451	4.301	0.8261	0.4101
Average	0.3084	8.163	4.626	0.8243	0.3389

Table 5.3 Decay time constants and magnitudes from equation 5.10 for signal 1* at D₁ in BaTiO₃ when beam 1 is off

Parameters	τ_1	τ_2	τ_3	k_1	k_2
Set I	1.259	2.925	4.089	0.6787	1.139
Set II	1.555	2.516	4.211	0.6515	1.331
Average	1.407	2.721	4.15	0.6651	1.235

Table 5.4 Decay time constants and magnitudes from equation 5.9 for signal 2* at D₂ in BaTiO₃ when beam 1 is off.

Parameters	τ'_1	τ'_2	τ'_3	k'_1	k'_2
Set I	0.0	0.3411	18.76	0.0195	49.65
Set II	0.0	0.2684	4.395	0.0219	2.703
Average	0.0	0.30425	11.57	0.0207	26.18

Table 5.5 Decay time constants and magnitudes for incoherent beam coupling from equation 5.10 for signal 1* at D₁ in BaTiO₃ when beam 1 is off.

Parameters	τ_1	τ_2	τ_3	k_1	k_2
Set I	6.019	3.087	2.726	0.8409	
Set II	1.779	4.141	3.762	0.8473	
Set III	2.381	3.423	3.406	0.8729	
Average	3.393	3.550	3.298	0.8537	

Table 5.6 Decay time constants and magnitudes for incoherent beam coupling from equation 5.10 for signal 1* at D₁ in BaTiO₃ when beam 1 is off.

Parameters	τ_1	τ_2	τ_3	k_1	k_2
Set I	9.699	3.592	3.662	0.3189	
Set II	2.575	1.143	1.144	2.726	
Average	6.14	2.37	2.4	1.5225	

Table 5.7 shows growth constants and magnitudes for incoherent beams for signal 1* when two beam coupling takes place.

Parameter	k	τ
Set I	0.7271	0.4657
Set II	0.6521	0.4128
Set III	0.2305	0.4873
Average	0.53	0.39

Table 5.8 shows growth constants and magnitudes for incoherent beams for signal 2* when two beam coupling takes place.

Parameter	k	τ
Set I	0.3304	0.4832
Set II	0.2604	0.4562
Set III	0.2751	0.4871
Average	0.45	0.47

Table 5.9 shows growth constants and magnitudes for coherent beams for signal 1* when two beam coupling takes place.

Parameter	k	τ
Set I	0.8323	2.3442
Set II	1.528	5.219
Set III	1.437	2.841
Average	1.27	3.47

Table 5.10 shows growth constants and magnitudes for coherent beams for signal 1* when two beam coupling takes place when Table is vibrated.

Parameter	k	τ
Set I	0.1472	0.9302
Set II	0.1462	0.4933
Average	0.1465	0.7119

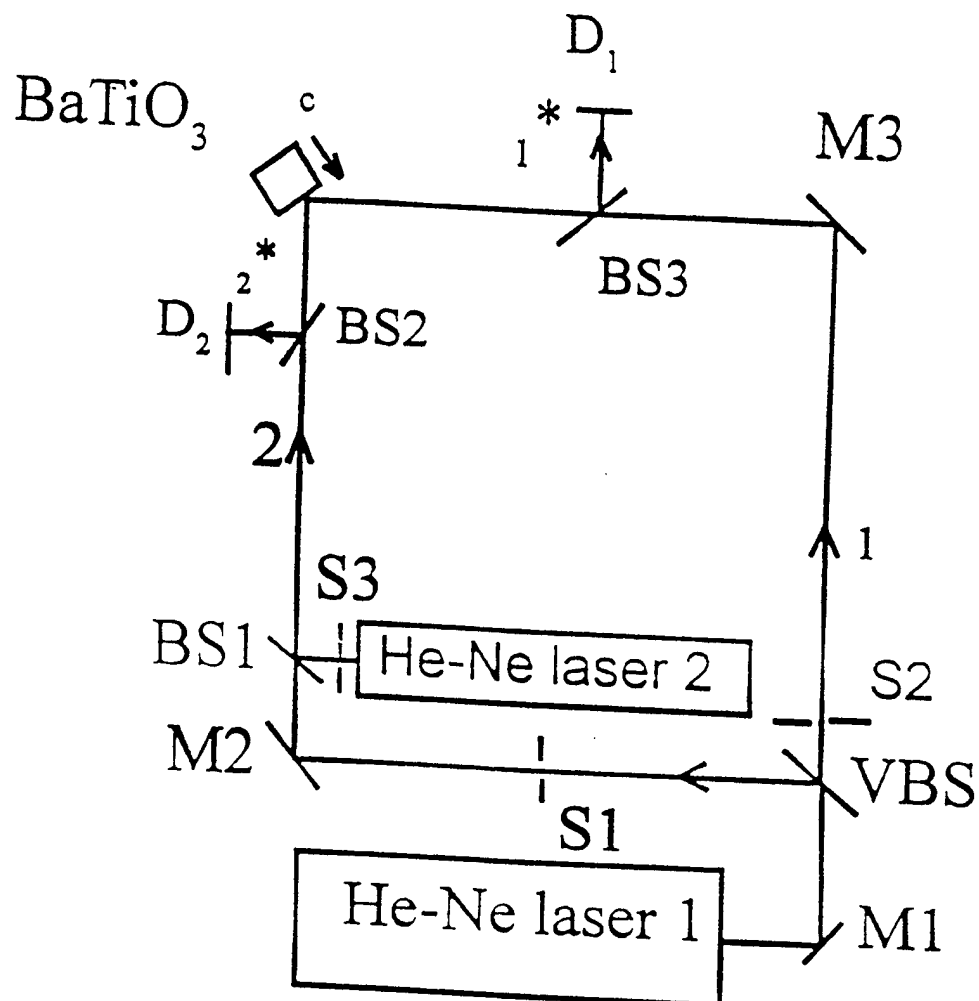


Fig. 5.1 Schematic of experimental setup for the pincushion effect using both coherent and incoherent light. M represents mirrors. VBS represents variable beam splitters. BS represents beam splitter. S represents shutter. C represents BaTiO₃ crystal. For the coherent beam coupling studies, laser 1 only is used to give two coherent beams. For incoherent beam coupling studies, lasers 1 and 2 are used to give incoherent beams.

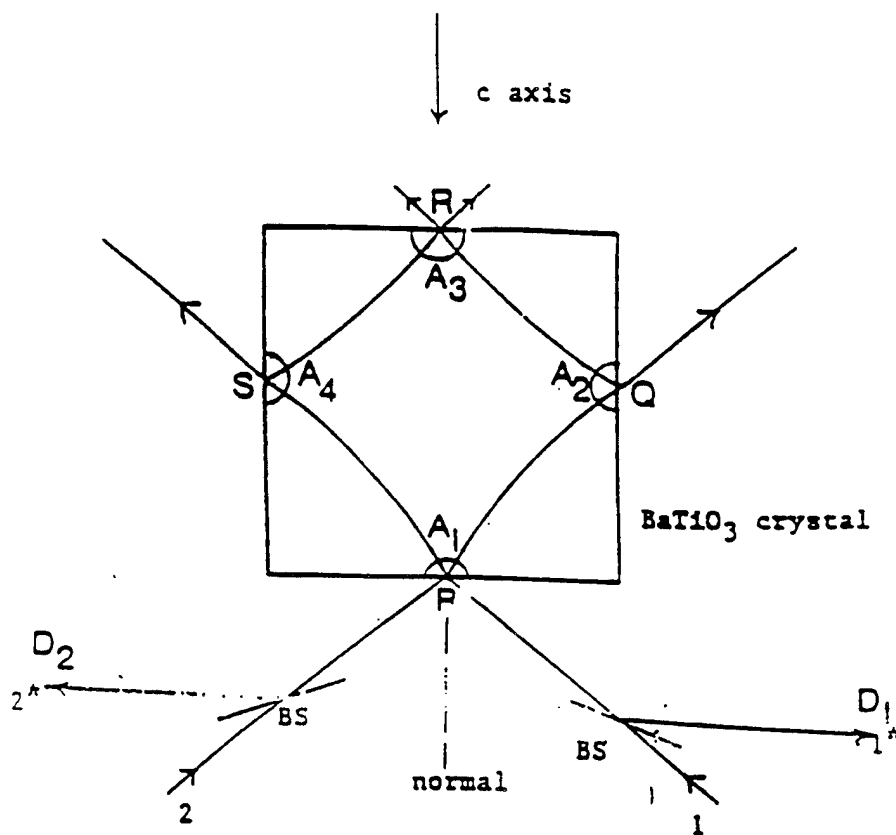


Fig. 5.2 Two beam coupling showing development of the fanned beam inside the crystal when two beams 1 and 2 are incident at the surface.

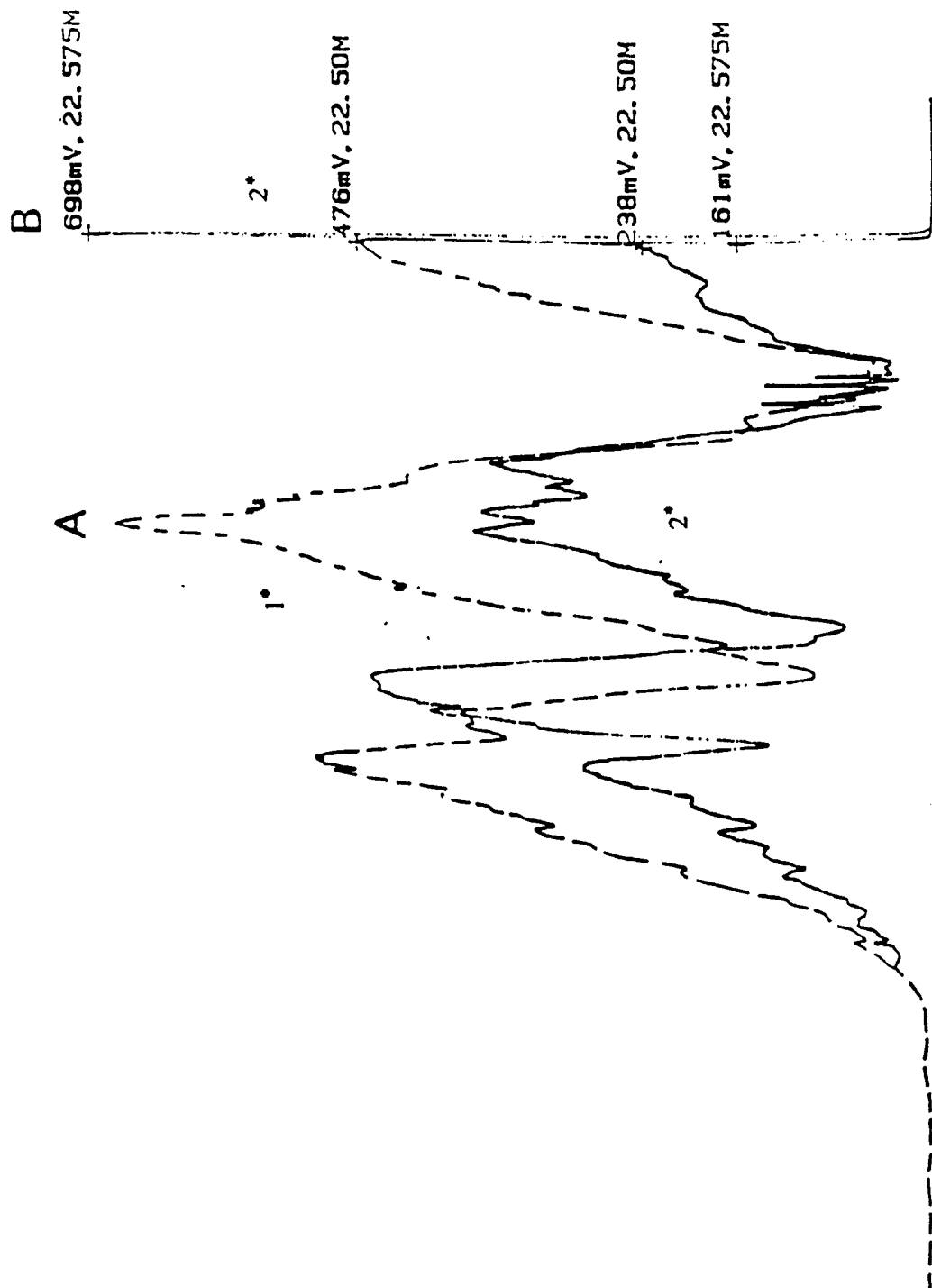


Fig. 5.3 The simultaneous growth of the phase conjugates 1^* and 2^* of the coherent beams 1 and 2. Because of reflection gratings of the growth curves show many fluctuations. Total time of recording is 25 minutes.

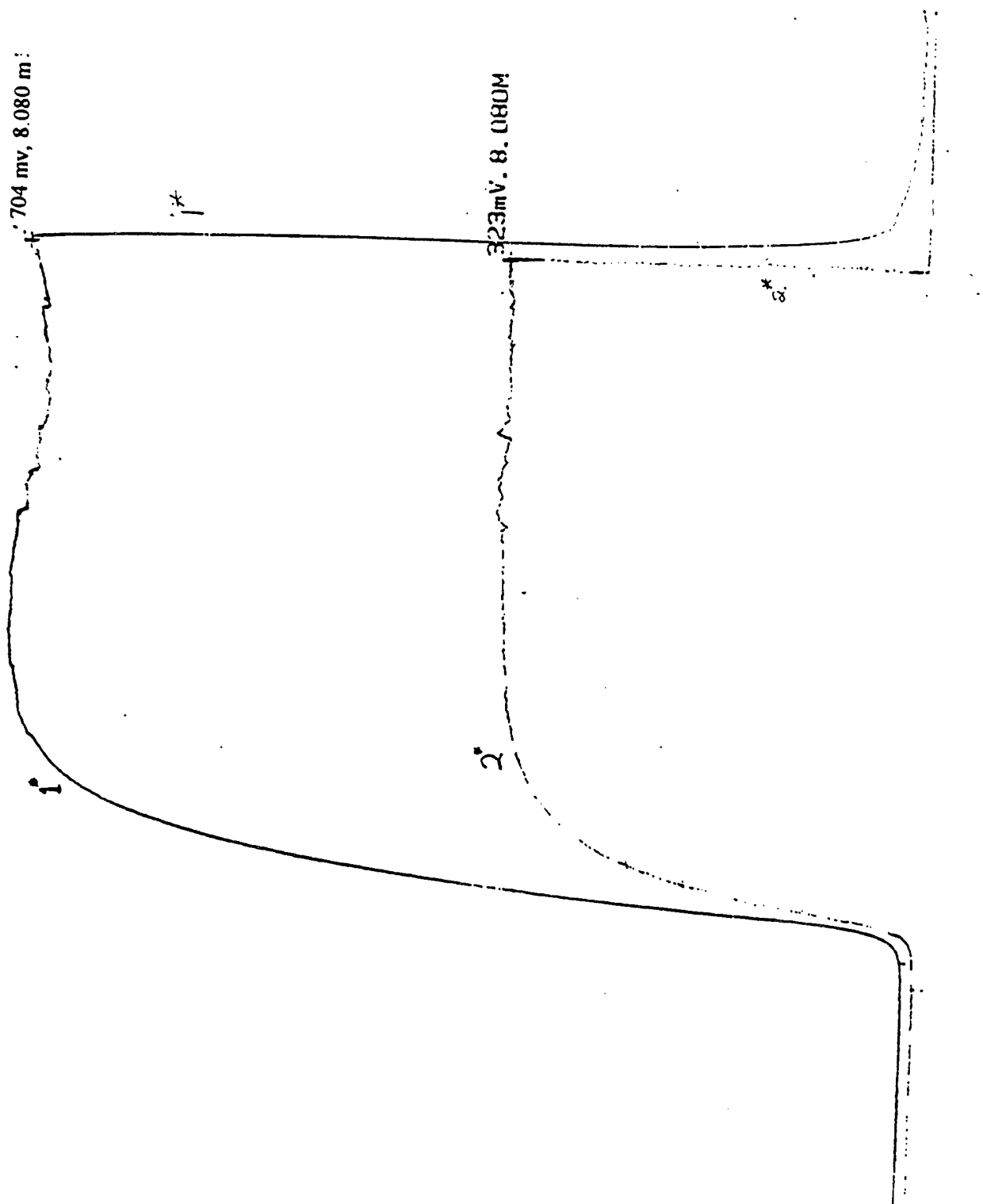


Fig. 5.4 Phase conjugate signal 1* (dashed line) and 2* (solid line) of two incoherent beams under two beam coupling. (Set I)

RANGES: 900.0mV 900.0mV
 OFFSETS: 0.0V 0.0V
 TOTAL TIME: 25.0S
 POST-TRIG: 0.0S

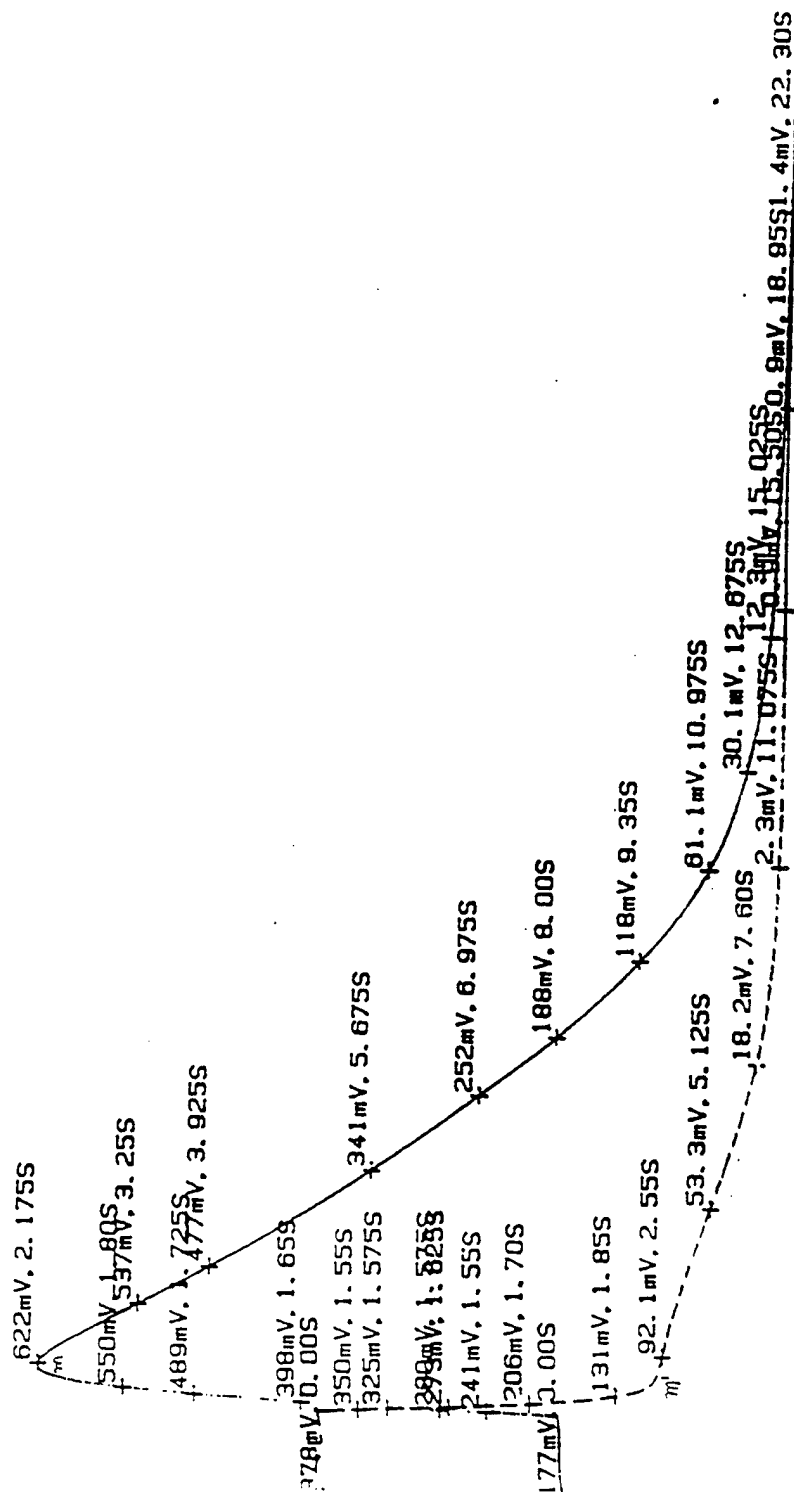


Fig. 5.5 Phase conjugate signal 1* (dashed line) and 2* (solid line) of two coherent beams when beam 2 is put off, (set I).

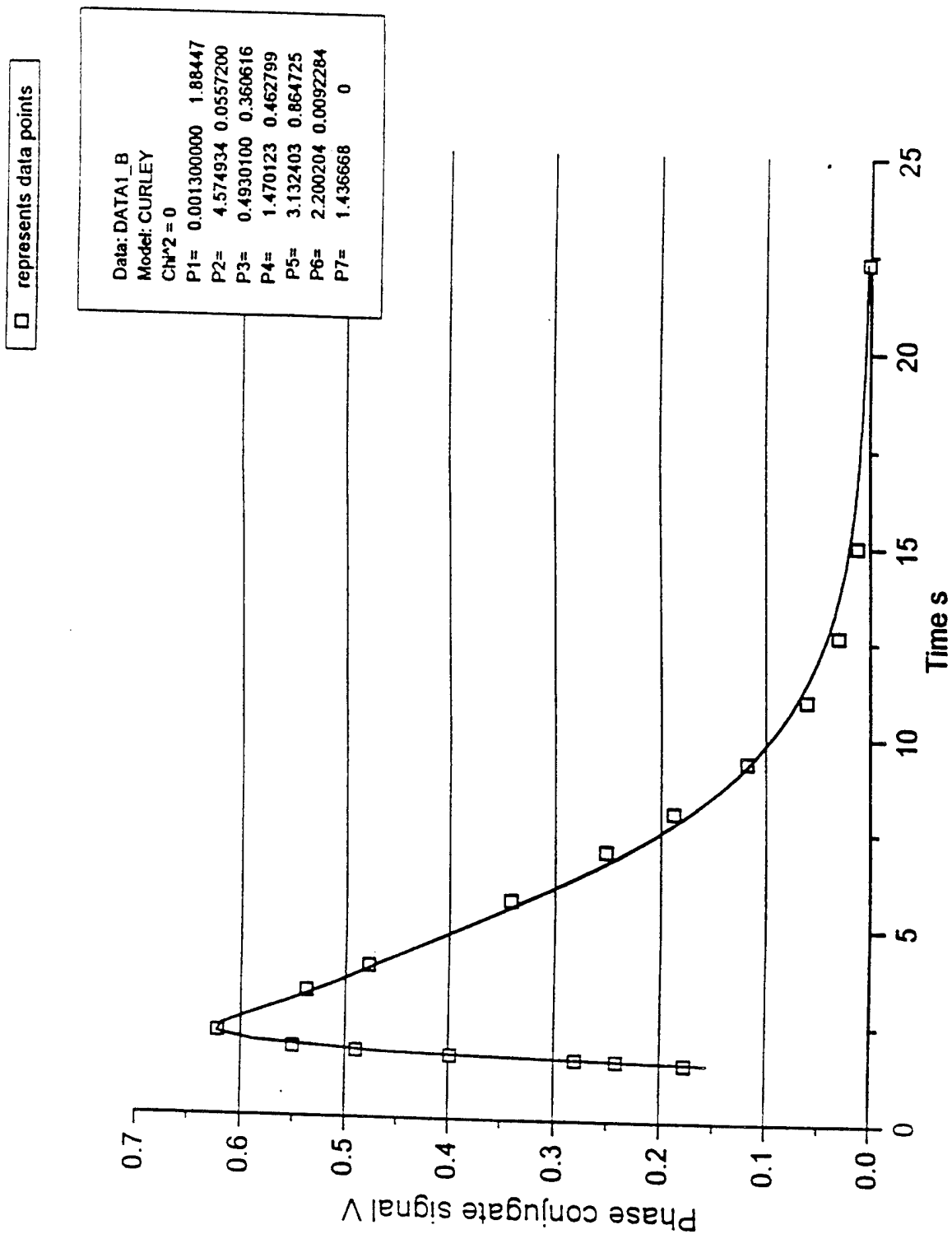


Fig. 5.5a Fitted curve of phase conjugate signal 2* using equation 5.9 involving two exponential decays and one growth when beam 2 is put off, (set I).

□ represents data points

Data:	Data1_D
Model:	CURLEY
Chi^2 =	6.08E-6
P1=	0.0009
P2=	141.3371
P3=	0.1195950
P4=	2.932538
P5=	1.565742
P6=	17.14098
P7=	1.359544
	0.0082401

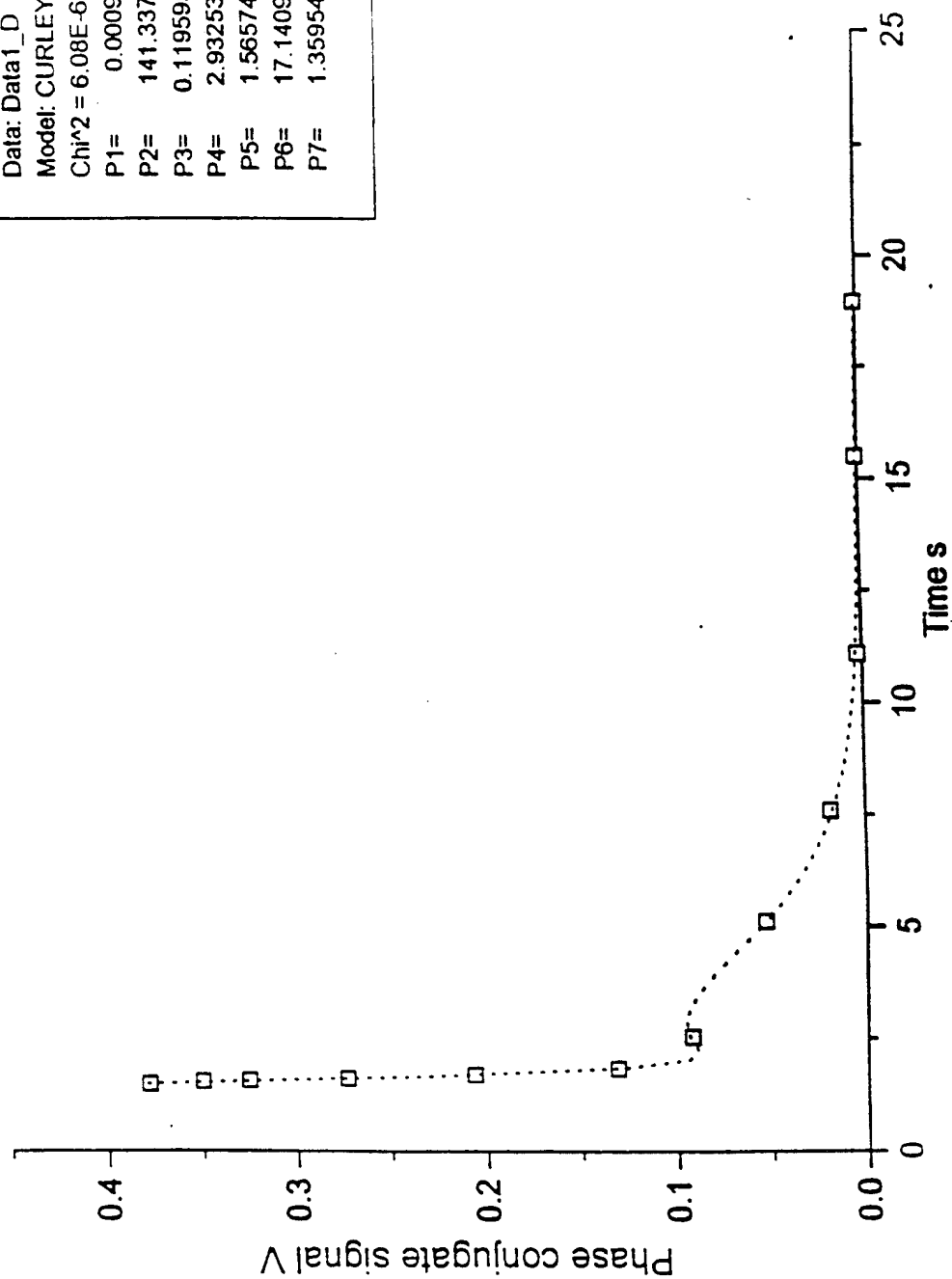


Fig. 5.5b Fitted curve of phase conjugate signal 1* using equation 5.10 involving two exponential decays and one growth when beam 2 is put off, (set I).

RANGES: 900.0mV 900.0mV
 OFFSETS: 0.0V 0.0V
 TOTAL TIME: 25.0S
 POST-TRIG: 0.0S

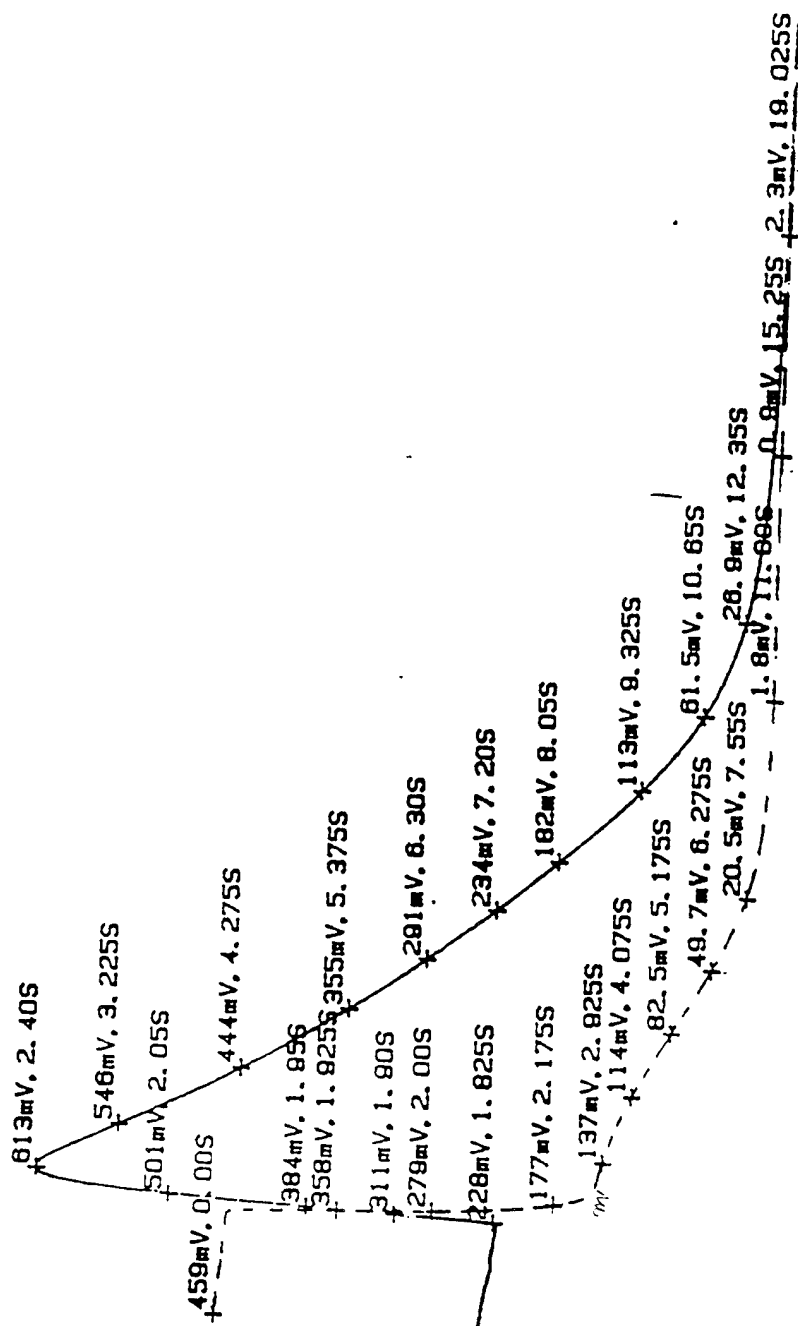


Fig. 5.6 Phase conjugate singal 1* (dashed line) and 2* (solid line) of two coherent beams when beam 2 is put off, (set II).

□ represents data points

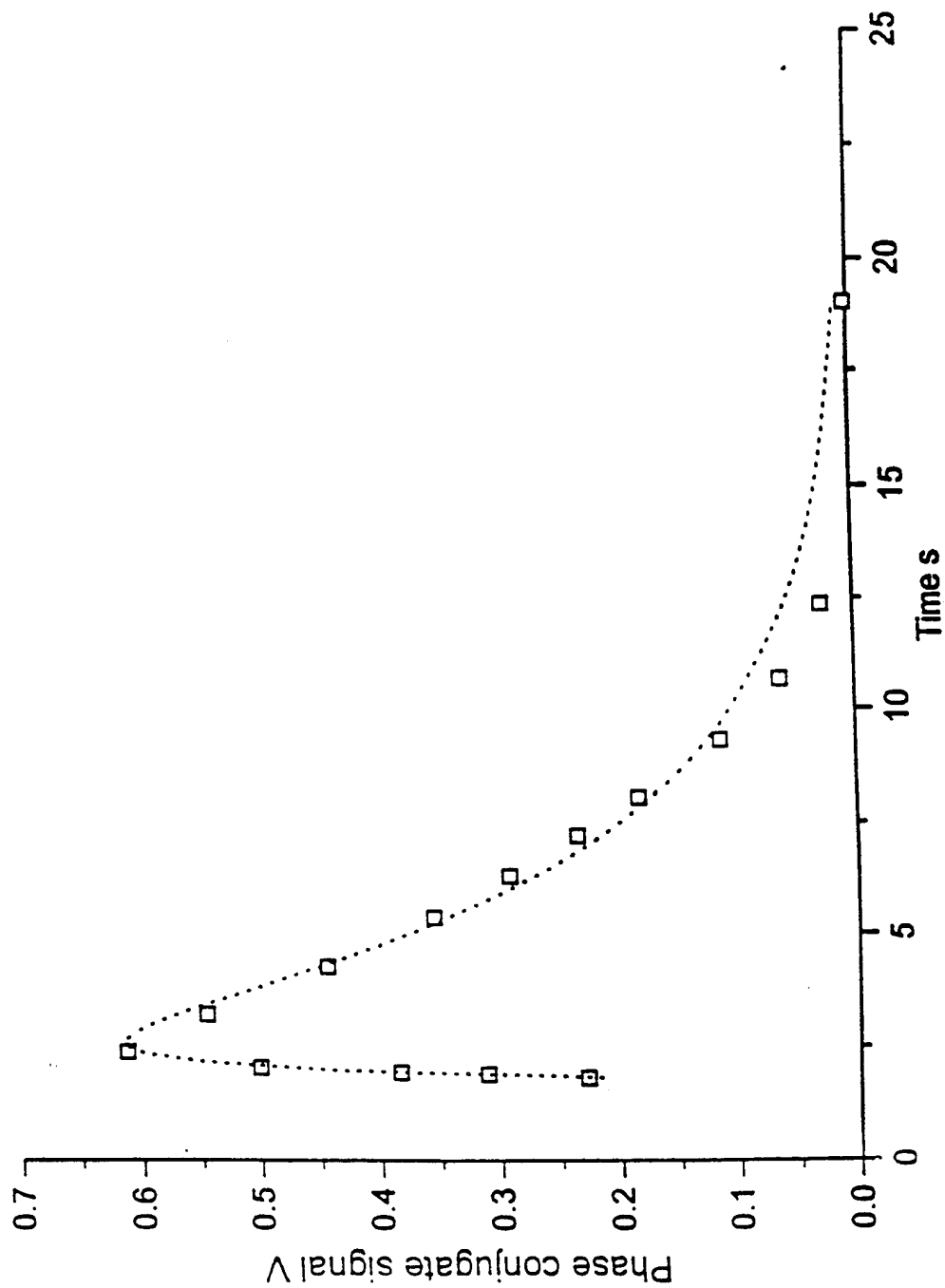


Fig. 5.6a Fitted curve of phase conjugate signal 2* using equation 5.9 involving two exponential decays and one growth when beam 2 is put off, (set II).

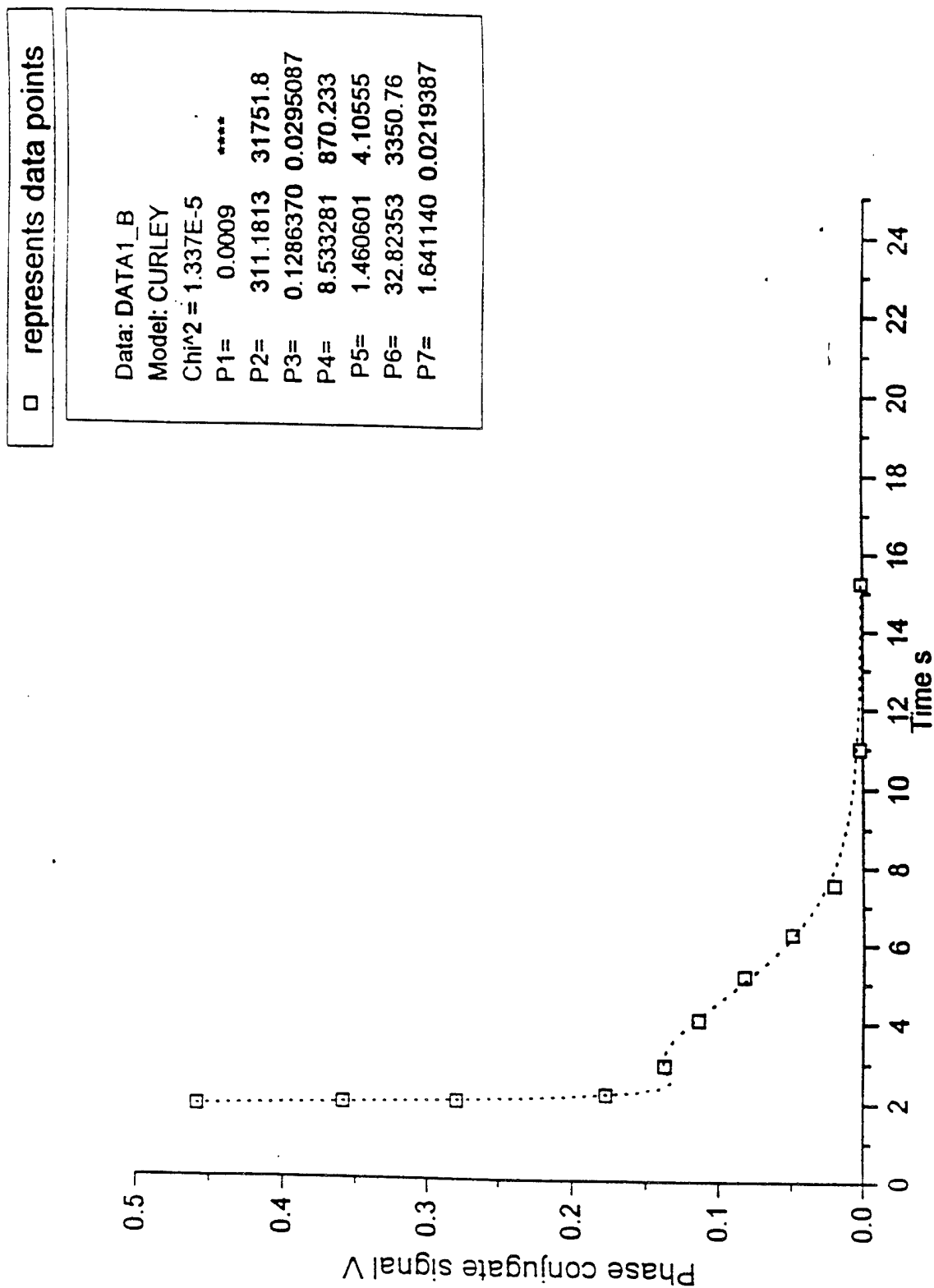


Fig. 5.6b Fitted curve of phase conjugate signal 1* using equation 5.10 involving two exponential decays and one growth when beam 2 is put off, (set II).

RANGES: 800.0mV 500.0mV :
 OFFSETS: 0.0V 0.0V
 TOTAL TIME: 20.0S
 POST-TRIG: 0.0S

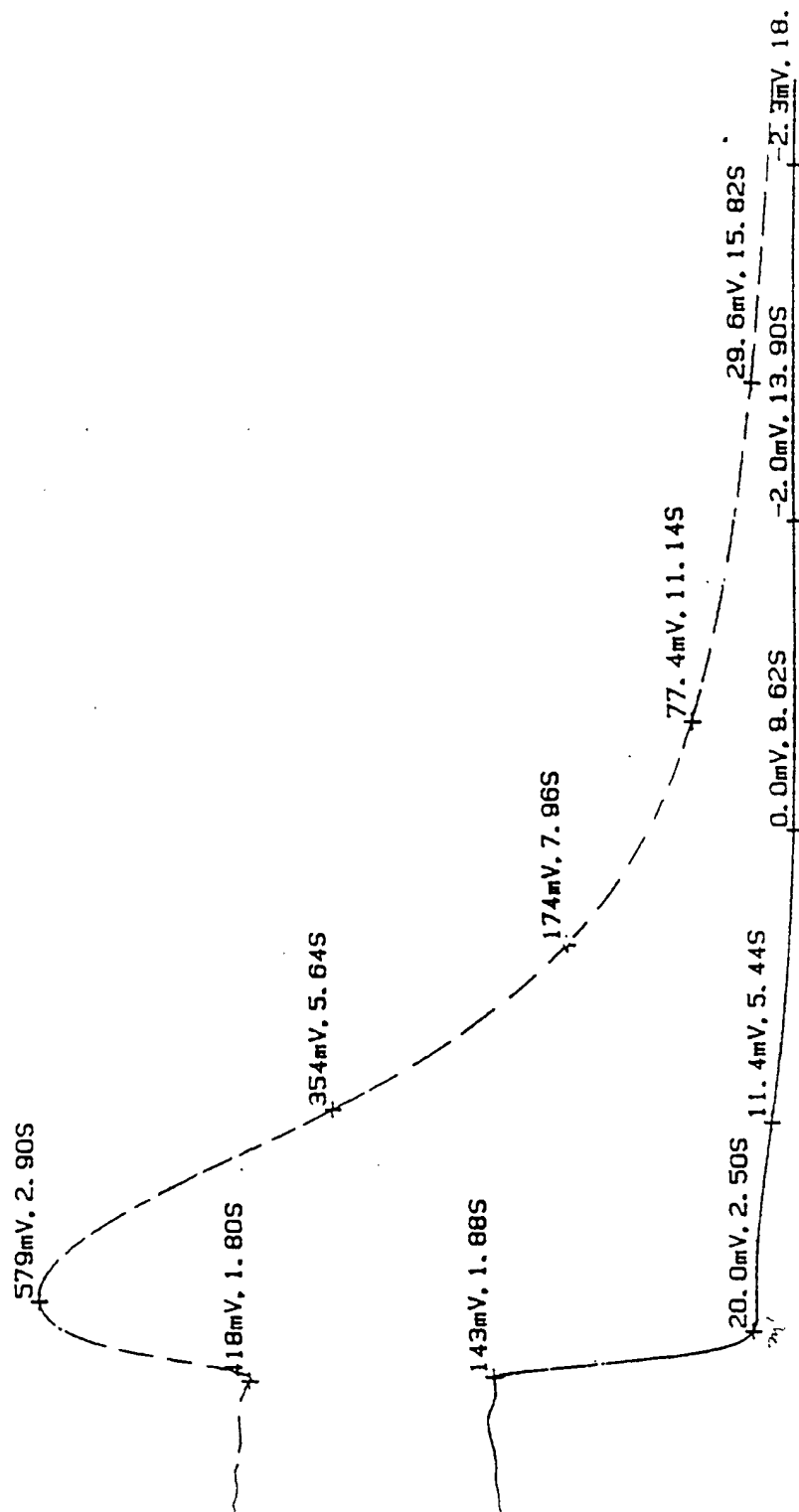


Fig. 5.7 Phase conjugate singal 1* (dashed line) and 2* (solid line) of two coherent beams when beam 1 is put off, (set III).

RANGES: 800.0mV 800.0mV
 OFFSETS: 0.0V 0.0V
 TOTAL TIME: 25.0S
 POST-IRIG: 0.0S

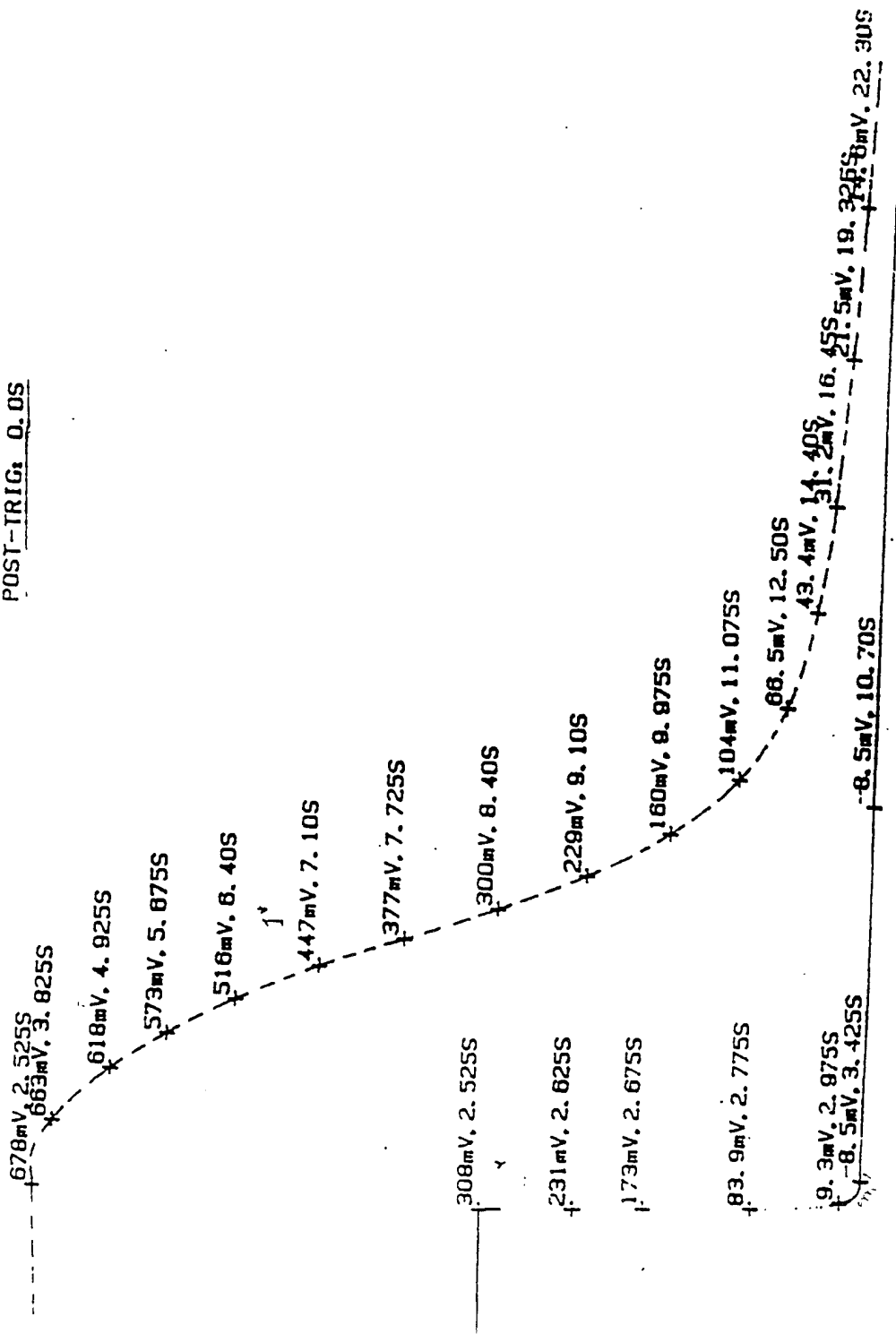


Fig. 5.8 Phase conjugate singal 1* (dashed line) and 2* (solid line) of two incoherent beams when beam 1 is put off, (set IV).

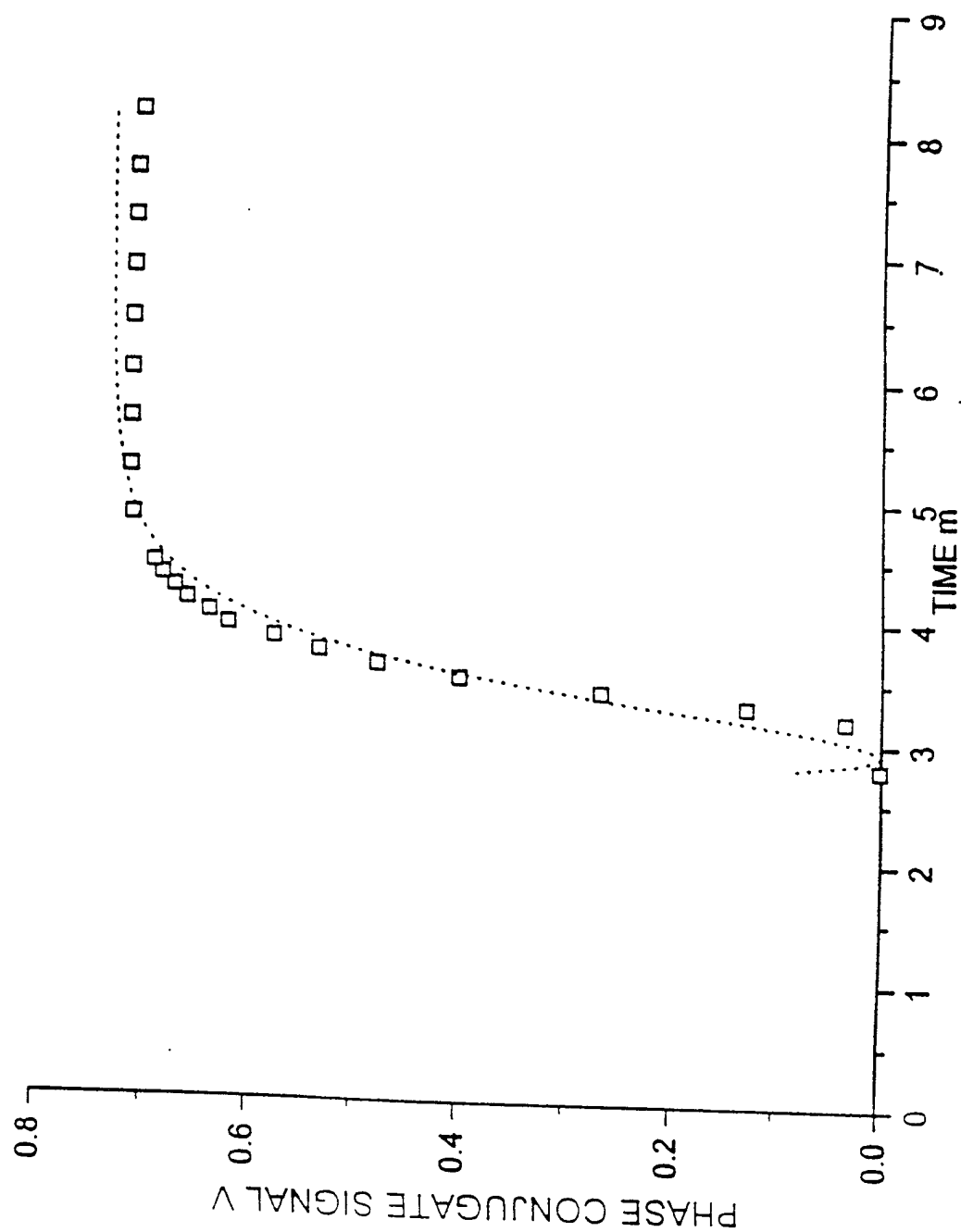


Fig. 5.9a Fitted curve of phase conjugate signal 1^* using equation 5.11 involving one exponential growth when incoherent two beam coupling takes place. (Set I)

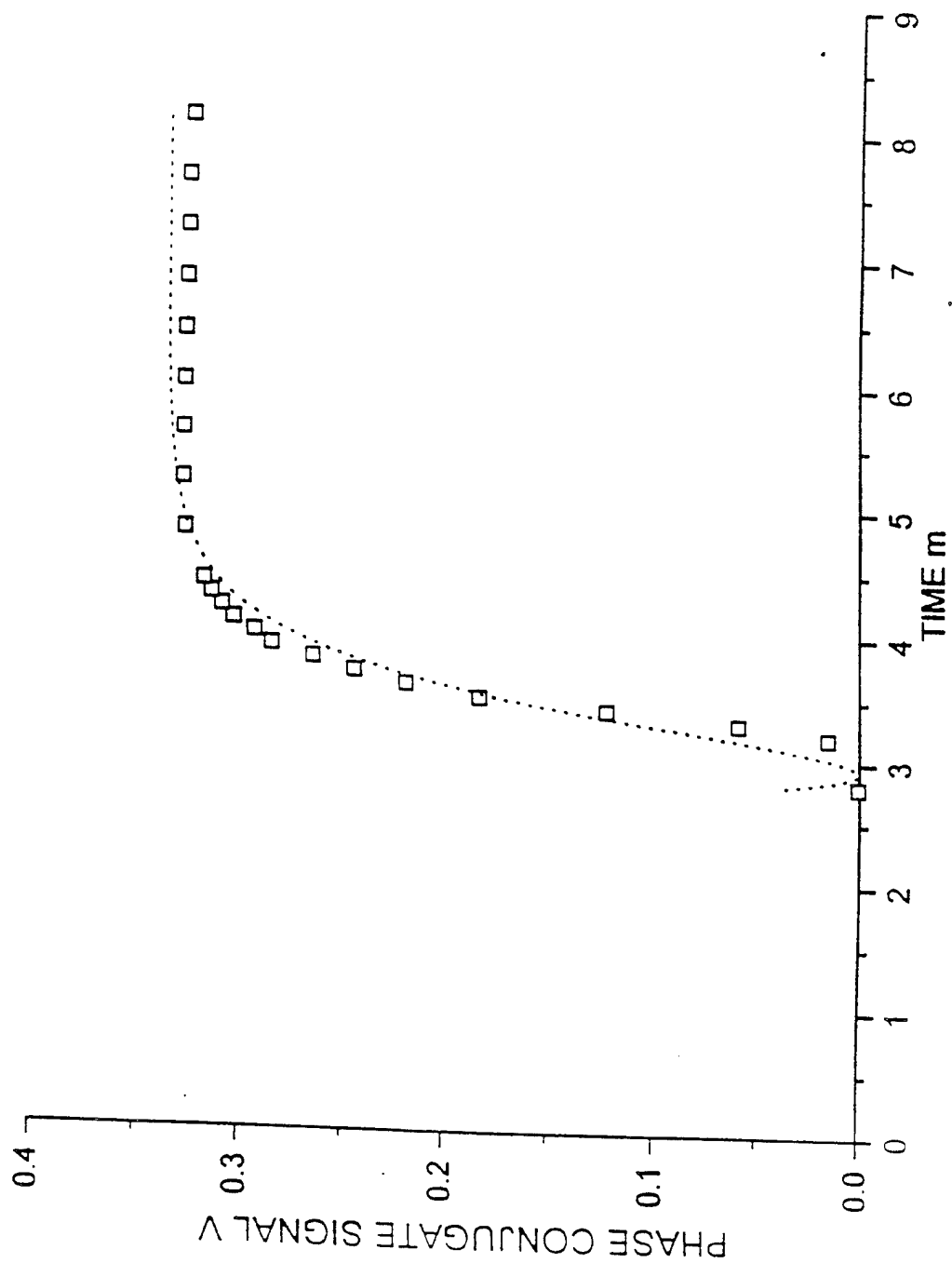


Fig. 5.9b Fitted curve of phase conjugate signal 2* using equation 5.12 involving one exponential growth when incoherent two beam coupling takes place. (Set I)

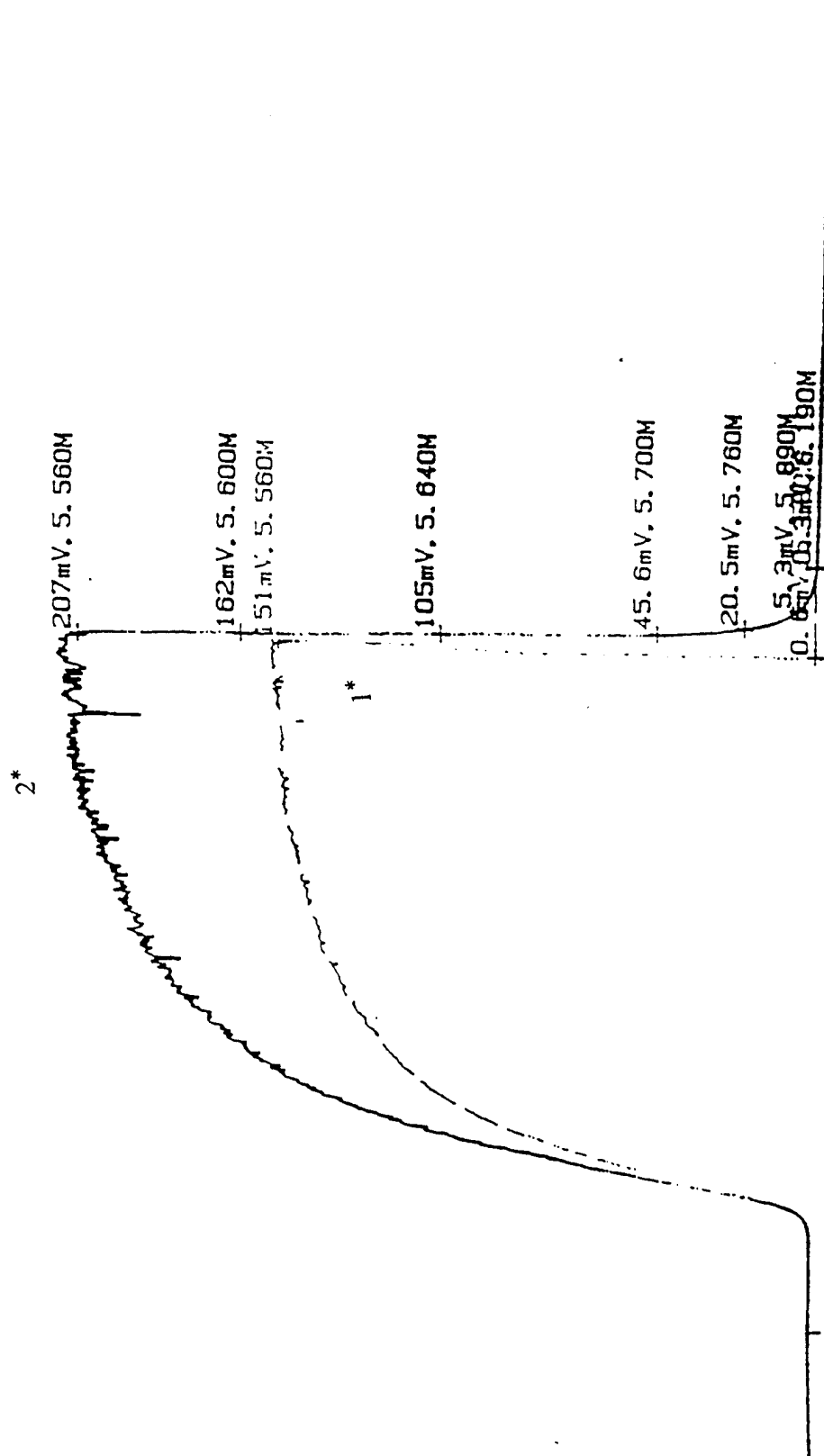


Fig. 5.10 The simultaneous growth of the phase conjugates 1* and 2* of the coherent beams 1 and 2. Because of vibrations, the growth curves do not show any fluctuations.

Chapter 6

Role of Iron Group Impurities in the Microscopic Origin of Photorefractive Effects in BaTiO₃: EPR Investigations on Fe³⁺ and Cu²⁺ Under Laser Illumination

6.1 Introduction

It is generally accepted that impurities of iron group exhibiting multivalence play a crucial role in the occurrence of photorefractive effect in crystal such as BaTiO₃, LiNbO₃, etc.[6.1]. This is attributed to photoinduced charge transfer which brings in charge modulation when two coherent light beams interfere within the body of the crystal. However, the exact mechanism has not yet been completely understood. Among all the dopants of iron group the most dominant role has been identified so far as due to iron impurity [6.2]. It was also suggested that presence of Cu²⁺ might enhance the photorefractive effect [6.2].

R. N. Schwartz and coworkers [6.2-6.5] have conducted the EPR investigations of BaTiO₃ with a view to elucidating the role of paramagnetic centers in the photorefractive effect. In a recent study [6.5] they have obtained a clear evidence of charge transfer from the paramagnetic Co²⁺, Fe³⁺ and O⁻ by conducting "in situ" EPR studies during laser illumination. These measurements were carried out at 45 and 25 K, in the rhombohedral phase of the host lattice, BaTiO₃. Even though the ambient temperature in these experiments was far below the room temperature where photorefractivity experiments are usually conducted, the experiment below 45 K helped in identifying the role of Fe³⁺, Co²⁺ and O⁻ (whose EPR can be best observed mostly at low temperatures due to relaxation

and/or thermal stability reasons), in the photo induced charge transfer processes. It may be pointed out that the work of Schwartz et al [6.5], has shown an interesting temperature dependence of photo induced changes in 45 - 25 K range. Whereas at 25 K, the photo induced effects enhanced Co^{2+} concentration, the opposite effect was observed at 45 K. These results highlight the complexities of photo induced ionization and hopping in BaTiO_3 suggesting that it may be worthwhile to conduct these experiments closer to room temperature, to probe the photo induced electron transfer relevant to photorefractive at room temperature. Furthermore, in crystals undergoing successive phase transitions, the low temperature phase is not expected to be of single [6.6] domain and the defects at the domain boundaries are expected to contribute to the complex behavior. With a view to minimizing the role of such unavoidable defects, and also to understand the processes that happen at room temperature, we have conducted "in situ" EPR investigations under He-Ne laser illuminations on mechanically poled and electrically poled BaTiO_3 crystal in which Fe^{3+} and Cu^{2+} were found to be paramagnetic impurities.

These experiments have given evidence to suggest that Fe^{3+} ions do take part in photo induced charge transfer at room temperature, and also show a marked variation in its behavior in a narrow temperature range around the ambient. These experiments also gave evidence for the possible role of domain boundaries and of nonuniform illumination on charge transfer specially in mechanically poled crystals.

6.2 Experimental Procedure

Experiments were conducted on two commercially available BaTiO₃ crystals (supplied by M/S Sanders Associates, New Hampshire, USA), one mechanically poled and another electrically poled. These crystals were designated M1 and E1.

The EPR studies were conducted on a Bruker ESP-300e X-band spectrometer operating around 9.3-9.5 GHz, equipped with an optical transmission cavity. Some of the preliminary experiments were conducted on a Varian century x-band spectrometer, at the Department of Chemistry, University of Alabama at Tuscaloosa, using a homemade optical transmission cavity. The optical illumination was done using a 35 mW He-Ne laser.

6.3 Characterization of Impurity Centers in Barium Titanate

The investigated crystals, were nominally pure with no intentionally doped impurities. The EPR experiments have however shown that the crystal contained iron impurity, and the mechanically poled crystal which was purchased a couple of years earlier contained additional copper (2+) impurity.

Unlike the EPR of Fe³⁺ in BaTiO₃, where very exhaustive work has been reported [6.6-6.10]. EPR studies of Cu²⁺ have not been reported except for a brief mention of the EPR detection of Cu²⁺ in one of the crystals (BW1) used by Klein and Schwartz [6.2]. In this report we describe the results of our EPR investigations of Fe³⁺ in two crystals and Cu²⁺ in a mechanically poled BaTiO₃ crystal. It was more difficult to tune the spectrometer, obtaining a good AFC lock, for

mechanically poled crystals compared to electrically poled ones, and further the line shapes were more asymmetric for the mechanically poled sample.

6.3.1 Fe^{3+} Center in BaTiO_3 :

Figures 6.1(a and b), 6.2 and 6.3 show the EPR spectrum obtained for crystals M1 and E1 for the magnetic field parallel to c-axis and a or b axis respectively. The lines marked a1 to a5 are the five fine structure transitions of Fe^{3+} which agree with those reported by Klein and Schwartz [6.2] for Fe^{3+} at Ti^{4+} site with no nearby charge compensating defects. In addition to Fe^{3+} , Cu^{2+} impurity was detected in M1 and this spectrum will be discussed in the next subsection.

From these figures it may be noticed that the electrically poled crystal E1 is of single domain. The angular variation of the Fe^{3+} spectrum in the (a,c) plane agrees satisfactorily with that reported by earlier workers [6.2-6.6] shown in Fig. 6.4. The spectrum can be fit to the axial spin Hamiltonian, with the usual notation:

$$H = g\beta\mathbf{H} \cdot \mathbf{s} + D[3s_z^2 - s(s-1)] + a[s_x^4 + s_y^4 + s_z^4 - 1/5s(s+1)(3s^2 + 3s - 1)] \quad (1)$$

The Spin Hamiltonian constants were obtained by using the field values for $\mathbf{H} \parallel \mathbf{c}$ and $\mathbf{H} \perp \mathbf{c}$. The values obtained are:

$$g_{\parallel} = g_{\perp} = 2.003 \pm 0.001$$

$$D = 1055 \pm 5\text{G}$$

$$a = 96 \pm 2\text{G}$$

These values compared very satisfactorily with those reported in the literature [6.6]. The central $-1/2 \rightarrow 1/2$ transition which is expected to be nearly angular independent for Fe^{3+} ions at axial sites has showed strong angular dependence, particularly for the direction of H close to $\langle 110 \rangle$ axis as in the work of Klein and Schwartz [6.11]. This arises due to relatively large value of "D" and obeyed the expression,

$$H_{1/2 \rightarrow -1/2} = H_0 + 2D^2 / (g\beta)^2 H_0 [8\sin^2\theta \cos^2\theta - \sin^4\theta] \quad (2)$$

where θ is the angle, the direction of the magnetic field makes with the c-axis. However, another anomalous feature of $+1/2 \rightarrow -1/2$ transition is its apparently large intensity compared to the expected intensity ratio of 5: 8: 9: 8: 5 with other fine structure transitions which can partly be accounted for by the larger linewidths of other transitions. This suggests that there exist inherent crystal field inhomogeneities even in optical quality, electrically poled crystals.

When Fe^{3+} entered the lattice substitutionally at Ti^{4+} site, some of the Fe^{3+} ions may be associated with oxygen vacancies for charge compensation. Such centers are designated as $[\text{Fe}^{3+} - \text{V}_\text{O}]$ center. It was most exhaustively studied in Fe^{3+} doped SrTiO_3 [6.11,6.12], but there were no reports of this center in BaTiO_3 . When Fe^{3+} is associated with an oxygen vacancy in the first coordination sphere, the ion will be subjected to a very strong axial distortion and the three Kramers' doublets arising from the ground ^6S state will have a separation significantly larger than the microwave energy (0.3 cm^{-1}) used. EPR in such cases will be observable only if $|\pm 1/2\rangle$ state lies lowest. In this state g-values will have the form $g_{\parallel}=g_j$ and $g_{\perp}=3g_j$. The line marked "V" in this spectrum (Fig. 6.1b) has exhibited typical behavior of resonance arising from effective spins $s'=1/2$ and has g

values $g_{||} = 2.00$ and $g_{\perp} = 5.98$ and this therefore assigned to the $(\text{Fe}^{3+}\text{-Vo})$ center in BaTiO_3 . In addition to this, an extra resonance around 650 G also was observed. This cannot be attributed to either paramagnetic oxygen center $(\text{O}^{\cdot}, \text{O}^{2\cdot})$ or to $(\text{Fe}^{3+}\text{-Vo})$ center due to its very large effective g-value. It is most likely a forbidden transition of the type $\Delta M_S = \pm 2$ in Fe^{3+} at Ti^{4+} site without a nearby oxygen vacancy.

6.3.2 EPR of Cu^{2+} in BaTiO_3

In addition to the intense spectrum due to Fe^{3+} a weaker but sharper spectrum due to Cu^{2+} ion was detected. It has the characteristic quartet hyperfine structure with unresolved isotope structure expected due to ^{63}Cu and ^{65}Cu (both have $I=3/2$). The g and hyperfine coupling constants were found to be isotropic in [a,b] plane, but highly anisotropic in [a/b, c] plane. The site symmetry of the Cu^{2+} ion is found to be tetragonal with the principal axis along the c-axis. The spectrum of Cu^{2+} can be seen in Fig. 6.1a for M1 sample with the magnetic field parallel to c-axis. Free Cu^{2+} ion has the outer electronic configuration of $3d^9$ and when placed in an octahedral crystal field it takes the form $t_{2g}^6 e_g^3$. When the octahedral symmetry is lowered due to an axial distortion, the lowest electronic state is an orbital singlet, and it facilitates the observation of EPR over a wide temperature range. Electronic wave function would either be $(x^2 - y^2)$ or $(3z^2 - r^2)$ depending upon whether the octahedron is elongated or compressed respectively. These two cases can be distinguished using EPR studies from the relative values of the principal component of g-tensor. In the case of $|x^2 - y^2\rangle$ state, i.e. when the octahedron is elongated in one direction the principal g-values follow, the pattern

$g_{||} > g_{\perp} > 2$. On the other hand, in the case of $13z^2 - r^2$ state, i.e. when the octahedron is compressed is in one direction the principal component of g-values follow the pattern $g_{\perp} > 2 > g_{||}$ [6.13].

The spectrum of Cu^{2+} is shown in Fig. 6.5 for different angles with the magnetic field with c-axis in [a,c] plane. The Spin Hamiltonian constants of the Cu^{2+} sites are :

$$g_{||} = 2.383 \pm 0.001$$

$$g_{\perp} = 2.066 \pm 0.0001$$

$$A_{||} = 97 \pm 1 \text{ Gauss}$$

$$A_{\perp} \sim 5 \text{ Gauss}$$

The line positions and hyperfine coupling constants at any angle can be satisfactorily predicted using the principal values of g and A tensors. It is important to note that the principal axis system of g and D tensors of Fe^{3+} at the octahedral site coincide with those of g and A tensors of Cu^{2+} .

The hyperfine coupling constants $K(\theta)$, and $g(\theta)$ in their respective principal axis systems are given by the expressions [13]:

$$K^2 g^2 = A_{||}^2 g_{||}^2 \cos^2 \theta + A_{\perp}^2 g_{\perp}^2 \sin^2 \theta \quad (3)$$

and

$$g^2 = g_{||}^2 \cos^2 \theta + g_{\perp}^2 \sin^2 \theta \quad (4)$$

The fitting between observed and expected values of $K(\theta)$ and also of $g(\theta)$ were quite satisfactory. The angular variation of $g(\theta)$ is shown in Figure 6.6. The

points shown are experimental points and the curve is the calculated one using $g_{||}$ and g_{\perp} values given above.

The experimentally obtained values of $g_{||}$ and g_{\perp} are 2.383 and 2.066, respectively suggest that $[\text{CuO}_6]^{10-}$ is elongated along the z-axis (or compressed along the x and y axis). This clearly suggests that substitution of Cu^{2+} at Ti^{4+} site brought in a local distortion of what was a regular $[\text{TiO}_6]^{9-}$ octahedron.

6.4 Effect of "In Situ" Laser Illumination

EPR investigations were carried out under He-Ne laser illumination. This work was carried to examine "in situ" the photoinduced charge transfer from Fe^{3+} in BaTiO_3 crystal lattice, as this was supposed to be a key step in inducing photorefractive behavior of BaTiO_3 crystal. These experiments were carried out using an optical transmission cavity (Bruker model, EI4104 or) on samples M1 and E1.

The measurements were carried out under the following two experimental conditions:

(i) Sample loaded in an optical transmission cavity was uniformly illuminated by light from a He-Ne laser with Gaussian profile of the laser beam, and also after beam expansion and collimation.

(ii) The sample was half covered by black paper and illuminated by laser light, essentially to simulate the condition of an interference pattern with a large fringe width (or grating period). This will be referred to as nonuniform illumination.

These measurements were also done at temperatures slightly higher and lower compared to the ambient and some interesting results were obtained when room temperature changed from 25° to 18° C.

6.4.1 Mechanically Poled Crystal M1

Figure 6.7(a), (b) and (c) represent the EPR of M1 crystal with H_{LL}c, with no laser illumination, with uniform illumination and nonuniform illumination (half bright and half dark), respectively. The drastic change in line shape when only half the crystal was illuminated can be seen in Figure 6.7c. Under the condition of half bright and half dark illumination condition, the detector current showed prominent time dependent increase, and it was found to be reversible, reverting back to its original value after the laser was switched off. The changes were highly reproducible. Figure 6.8 shows time dependence of detector current during non-uniform (half bright and half dark) illumination.

The time dependence of changes in intensity of the Fe³⁺ spectrum during uniform illumination was also investigated, by locking the magnetic field on the peak position of one of the fine structure transitions of Fe³⁺. Figure 6.9 shows the recovery and decay of Fe³⁺ signal with laser off and laser on condition. An interesting observation in these measurements is a small but definite surge in the intensity of Fe³⁺, soon after the laser was on, and it will be commented upon later in this chapter. The EPR spectrum of Cu²⁺ also showed changes in intensity with laser illumination. Figs. 6.10(a) and 6.10(b) show the decay and growth characteristics of Cu²⁺ spectrum with light on and off conditions respectively.

6.4.2 Electrically Poled Crystal E1

Experiments similar to those described above on M1 were conducted with the crystal E1. When the illumination was made highly nonuniform, with bright and dark regions as in the case of M1, the line shape was found to become asymmetric, but the difference was much less drastic compared to that in the case of M1. This can be seen in Figure 6.11. Figure 6.12 shows the time dependence of the decay and growth of Fe^{3+} with and without laser illumination respectively. In a significant number of cases it was observed that a surge in the Fe^{3+} intensity occurs when the laser was switched on before it started decaying. This was not observed in a few cases but we believe that the observed surge was genuine.

In the course of extensive investigations on the effect of light on both M1 and E1, it was observed a few times that the laser illumination resulted in an opposite effect viz an increase in intensity of Fe^{3+} with laser illumination. A careful examination of the experimental conditions revealed that it was a temperature effect. When the room temperature was more than 24 to 26° C, the laser illumination resulted in the decrease of intensity of Fe^{3+} signals. To confirm this thermal effect the crystal was heated in the cavity to 28° C using a hot air blower (the room temperature was kept at 18° C by extra cooling) and the effect of laser illumination was monitored as the crystal was progressively cooled to 18° C. This is shown in Figure 6.15, which shows the reversal in the behavior of Fe^{3+} intensity under laser illumination as the sample cooled. This appeared to be analogous to the effect observed by Stewards et al [6.5] on Co^{2+} resonance in the 45 - 25K region. It may be mentioned that Cronin-Golomb [6.14] reported drastic increases in the phase conjugation properties of BaTiO_3 when the sample temperature was less than

18° C. Similar effects were observed with M1 also. In view of the large size of the crystals used, it was not feasible to load them in standard cryostats for working at different temperatures.

6.4.3 Analysis of Time Dependence of Growth and Decay of Fe³⁺

The time dependence of intensity of the EPR spectrum with and without laser illumination was fitted using standard expressions characterizing the single and/or double exponential decay and growth (Fig.6.12) respectively. Best fits were observed for single exponential in case of the decay of the signal, and a double exponential in case of the growth of the signal.

$$I_{\text{decay}} = I_0 + A \exp [- (t-t_0) / \tau_1] \quad (5)$$

$$I_{\text{growth}} = B + C \{ 1 - \exp [- (t-t_0) / \tau_2] \} + D \{ 1 - \exp [- (t-t_0) / \tau_3] \} \quad (6)$$

where A, B, C and D are constants: and τ_1 , τ_2 and τ_3 are time constants characterizing the respective time dependencies. The values of τ_1 , τ_2 and τ_3 are the parameters that characterize the decay and two growth times. The values of these parameters obtained in different conditions are given in Table 6.1. As mentioned earlier optical induced change of EPR showed interesting temperature dependence close to room temperature. The conditions under which the growth and decay showed contrasting behavior are described as "high temperature" and "low temperature" regions. It may be mentioned that this description is rather qualitative. In the high temperature region ($T > 24^\circ - 28^\circ \text{ C}$) the intensity of Fe³⁺ went down

with laser illumination and recovered after the illumination was cut off. In low temperature region ($T \leq 18^\circ \text{C}$, typically 18 to 15°) reverse effect viz. an increase in intensity of Fe^{3+} with laser illumination, was observed.

6.5 Discussion

From the experimental results described above the most important observations, in the present work may be summarized as:

(a) Charge transfer on photoexcitation does result in the valence change of iron impurity, which gives direct evidence about the photorefractive nature of the Fe center.

(b) There is a distinct difference in the behavior of mechanically and electrically poled crystals with regard to change in line shape on laser illumination. In a mechanically poled crystal, the change of line shape to Dysonian form is very prominent compared to that in a single domain electrically poled crystal.

(c) The decay time constant τ 's data, observed under different conditions, suggest that predominantly there are two charge transfer processes in BaTiO_3 illuminated with 633 nm light, with characteristic time constants around 100 ± 10 sec and 26 ± 2 sec. These time scales are significantly greater than those reported in the case of optical experiments.

(d) In a number of growth and decay characteristics, a "surge" (a sharp but small rise) in the concentration of Fe^{3+} was observed before the onset of decay of the Fe^{3+} signal, during laser illumination.

(e) The effect of laser illumination on the EPR lines of Cu^{2+} indicates clearly that there is charge transfer on Cu^{2+} also like on Fe^{3+} and Cu^{2+} plays a similar role like Fe^{3+} on the photorefractive characterization of BaTiO_3 .

6.5.1 Photo-Induced Valence Change and its Temperature Dependence

It has been accepted for quite some time that iron impurity does play an important role as a photorefractive center in barium titanate crystal. The first direct experimental evidence, however, was obtained recently in the EPR study of Schwartz et al. [6.3], where it was shown that laser illumination at 25 K results in valence change of Fe. The observations "(a) and (e)" mentioned above gives direct evidence of a photo-induced valence change of Fe^{3+} and Cu^{2+} in BaTiO_3 right at room temperature and, more interestingly, this has shown temperature dependence on Fe^{3+} even in a narrow range around room temperature.

6.5.2 Decay and Growth Behavior

Table 6.1 gives the values of τ_1 , τ_2 and τ_3 characterizing the decay and growth of Fe^{3+} signal (see equations 5 and 6) in M1 and E1 crystals. In case of E1 crystal, the growth and decay measurements were carried out at " low temperature" and the data are included in Table 6.1. Under "half bright-half dark" illumination condition the detector current change was prominent and measurable only with M1. Under these conditions, in case of sample E1, the line shape changed slightly (not as

prominent as that for M1), and so the dependence measurements done by locking the field to a peak position were not considered meaningful.

From Table 6.1 the charge transfer process on illumination with He-Ne laser, resulting in the valence change of Fe^{3+} has a characteristic time of around 98 sec in M1, whereas it was nearly double that in the case of E1. The shorter time in the case of M1, appears to be due to the presence of multidomains and therefore defects at domain walls, which quickly trapped the electrons or holes.

In general, it appears that the net charge transfer process, as viewed from the change of Fe^{3+} concentration, had two characteristic time constants. One was around 100 sec, and the other was around 25 sec. The slower process characterized the charge relaxation within half bright - half dark illumination, which brought an extra mechanism of nonresonant dissipation. It is known [6.15] that under the condition of infinitely large fringe width, the grating erasure rate becomes equal to the dielectric relaxation rate. Under the present experimental conditions, $\tau = 98$ sec, may be identified with dielectric relaxation rate " τ_d " which for BaTiO_3 sets the slowest limit of grating erasure time.

The charge transfer process with time constant ~ 25 sec may be due to charge transfer between different Fe sites and/or static O^- sites, without mediation from the conduction band.

6.5.3 Surge in Fe^{3+} Under Depleted Pump Condition and Mechanism of Growth of Transient Grating

One interesting observation in these experiments is the sudden surge in the intensity of Fe^{3+} , in the high temperature range, immediately after the laser was

switched on, before subsequent decay of Fe^{3+} (see Fig. 6.9 and 6.12). One possible mechanism can be understood as follows. When the crystal was exposed to He-Ne laser light it produced electron and hole pair. The "hole" has the chemical identity equivalent to a mobile O^- , which becomes static O^- , close to a lattice defect. Initially after switching on the light, the holes essentially "populate" static O^- , whereas electrons are free to get trapped or react with impurity transition metal ions. In principle, conduction electrons can reduce Fe^{3+} , to Fe^{2+} or Fe^{4+} to Fe^{3+} . In view of half filled stability of Fe^{3+} , reduction of Fe^{4+} to Fe^{3+} will be a more probable reaction as far as the involvement of Fe impurity is concerned. After the formation of O^- gets saturated, holes will be available for the oxidation of Fe^{2+} to Fe^{3+} though to a lower degree in view of the expected low concentration of Fe^{2+} . Therefore, the initial surge in Fe^{3+} , is attributed to $\text{Fe}^{4+} + e^- \rightarrow \text{Fe}^{3+}$ reaction, before the holes start oxidation Fe^{3+} to Fe^{4+} , and to $\text{Fe}^{3+} + h\nu \rightarrow \text{Fe}^{2+} + e^-$. These reactions give the net effect and note that net concentration of Fe^{3+} went down on illumination with laser light. The sudden surge of Fe^{3+} , soon after switching on the light has certain interesting consequences on the grating formation. Applications in the investigation of two beam coupling and the model suggested above can be tested in such a beam coupling experiment. In a two beam coupling experiment, when one of the beams is shut off, the interference pattern disappears bringing in uniform illumination. The regions which formed the "dark" part of the interference pattern, should therefore experience the same "surge" in the concentration of Fe^{3+} which essentially should make the contrast in the phase grating more prominent despite switching off the writing beam. This was tested with E1 crystal. Figure 6.13 shows a typical result of a beam coupling experiment with \mathbf{k} (grating vector) parallel to the c-axis. When the beam A2 was off, sudden jump in

the intensity of A1t after the crystal was seen as there is no cause for energy transfer in the absence of A2. The transmitted part of A1 i.e. A1t has shown a clear reduction in intensity due to diffraction characteristic of grating formation, for the first few seconds, before the grating started to decay. This result is quite consistent with the EPR observation. The large timescale in EPR decay was due to the effect of large differences in \mathbf{k} vector in these experiments. Horowitz et al. [6.16] have reported a similar growth of a grating after the input signal was turned off in a two wave mixing experiment. They attributed it due to the formation of new grating in regions of the crystal where they could not grow earlier due to the relative weakness of the pump beam. In our model, the "new grating" is essentially the same "old grating" with greater contrast and thereby large diffraction efficiency. It continued to have the same \mathbf{k} vector and hence the position of the diffraction signal does not change. We found that the appearance of "new grating" is prominent when the index of interference $m=I_1/I_2=1$.

6.6 Conclusions

We have obtained direct EPR evidence for photo-induced charge transfer from Fe^{3+} in BaTiO_3 at room temperature and also the involvement of defect at domain walls as sources/traps for charge carriers. The investigation of growth and decay of Fe^{3+} has lead to the determination of dielectric relaxation time τ_d , and also for a possible explanation for the formation of transient grating after one of the beams was switched off in a two beam coupling experiment.

REFERENCES:

- 6.1. E. Kratzig and O. F. Schirmer chapter v. "Photorefractive Materials and their Applications" Ed. P. Gunter and J. P. Huignard, Springer-Verlag, (1988).
- 6.2. M. B. Klein and R. N. Schwartz, J. Opt. Soc. Am. B, 3, 293 (1986).
- 6.3. R. N. Schwartz, B. A. Wechsler and D. Rytz, J. Opt. Soc. Am. B, 3 2245 (1990).
- 6.4. B. A. Wechsler, D. Rytz, M. B. Klein and R. N. Schwartz, Proceedings of American Chemical Soc. (ACS) Series No. 445 "Materials for Nonlinear Optics: Chemical Perspectives" Chapter 26, ACAS (1991).
- 6.5. R. N. Schwartz, B. A. Wechsler and R. A. McFarlane Phys. Rev. B, 46, 3263 (1992).
- 6.6. T. Sakudo, J. Phys. Soc. Japan, 18, 1626 (1963).
- 6.7. A. W. Horning, R. C. Remple and H. E. Weaver, J. Phys. Chem. Solids, 10, 1 (1959).
- 6.8. T. Sakudo and H. Unoki, J. Phys. Chem. Solids, 19, 2109 (1964).
- 6.9. K. A. Muller and W. Berlinger, Phys. Rev., 34, 6130 (1986).
- 6.10. K. A. Muller, Helvetica Physica Acta, 59, 874 (1986).
- 6.11. E. S. Kirkpatrick, K. A. Muller and R. S. Rubins Phys. Rev., A 86 135 (1964).
- 6.12. Th. Von Waldkirch, K. A. Muller and W. Berlinger Phys. Rev., B, 5, 4324 (1972).
- 6.13. A. Abragam and B. Bleaney " Paramagnetic Resonance of Transition Ions" Clarendon Press (1970).

- 6.14. M. Cronin-Golomb, Paper ThT3, CLEO' 85, Baltimore, Maryland.
- 6.15. R. A. Mullen, "Photorefractive Materials and their Applications " Ed.
by P. Gunter and J.P. Huignard, p.178, Springer-Verlag (1988).
- 6.16. M. Horowitz, D. Kligler and B. Fisher, J. Opt. Soc. Am. B, 8, 2204
(1991).

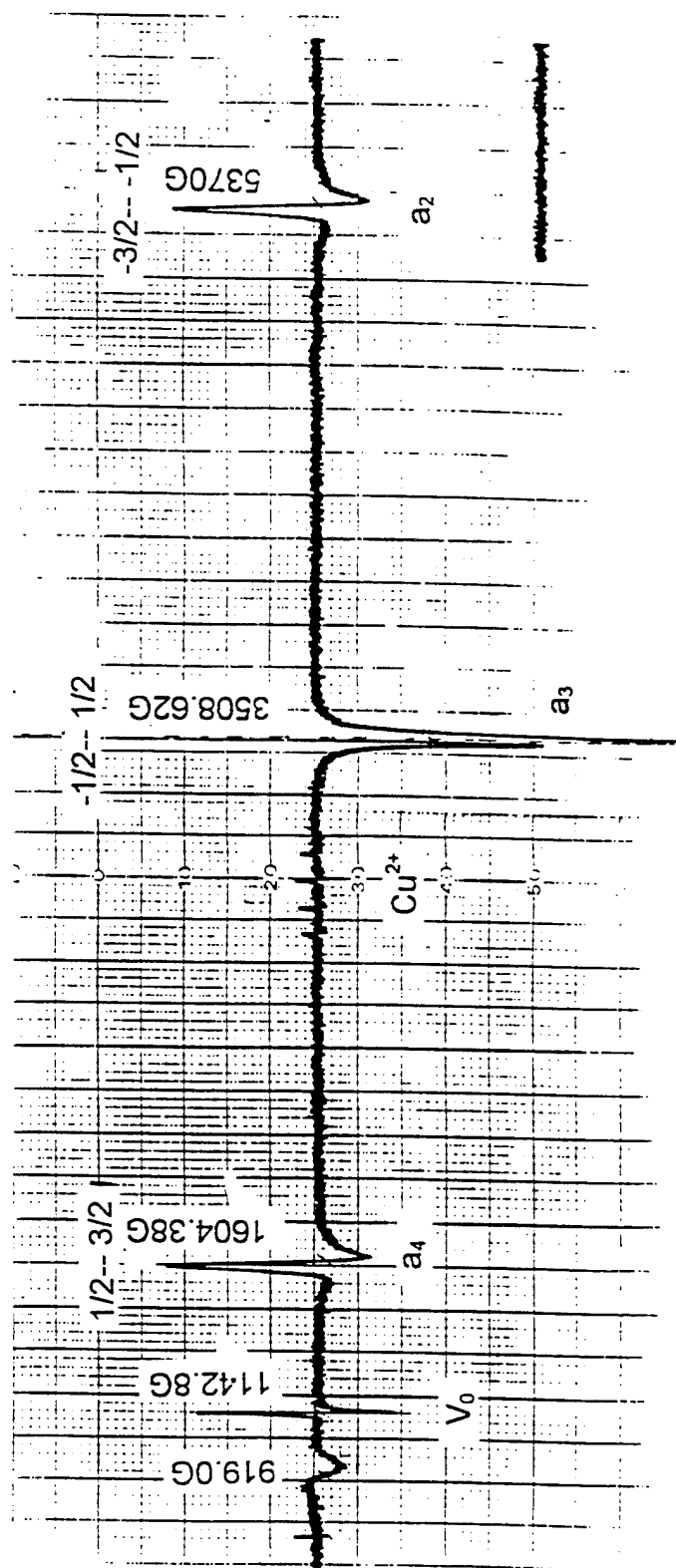


Figure 6.1(a). EPR of mechanically poled BaTiO₃ crystal (M1), when H || c-axis.

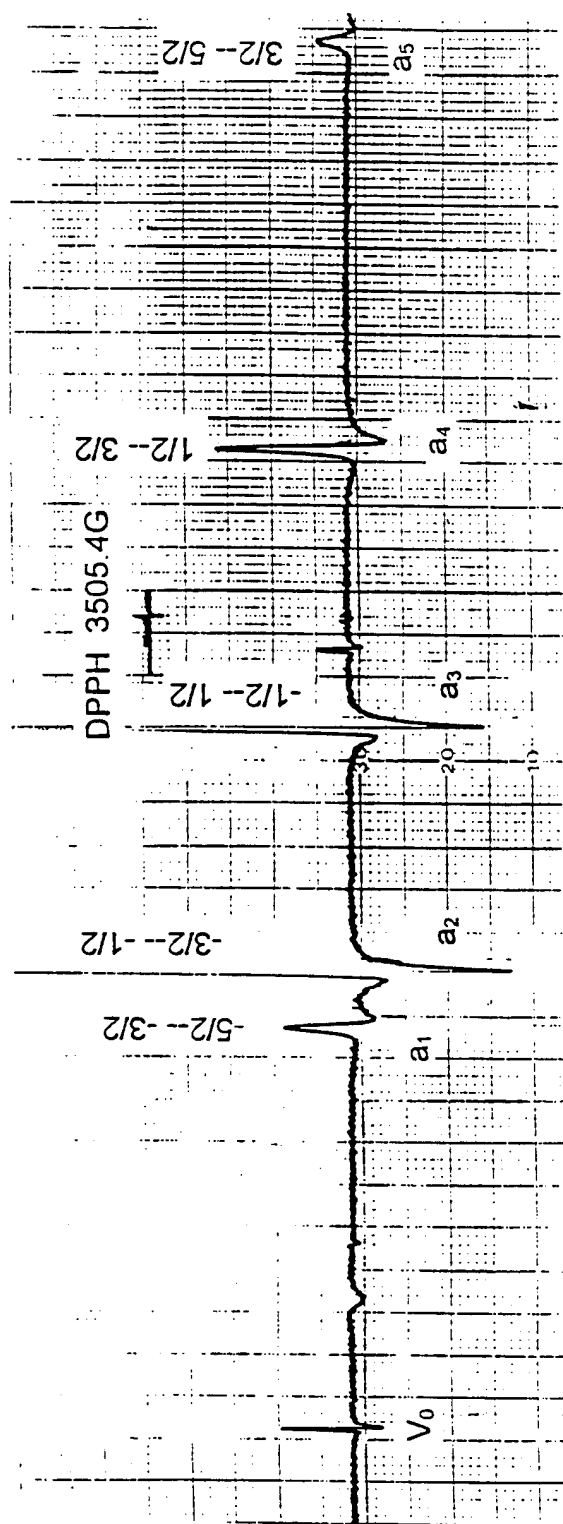


Figure 6.1(b). EPR of mechanically poled BaTiO₃ crystal (M1), when

H \perp c-axis.

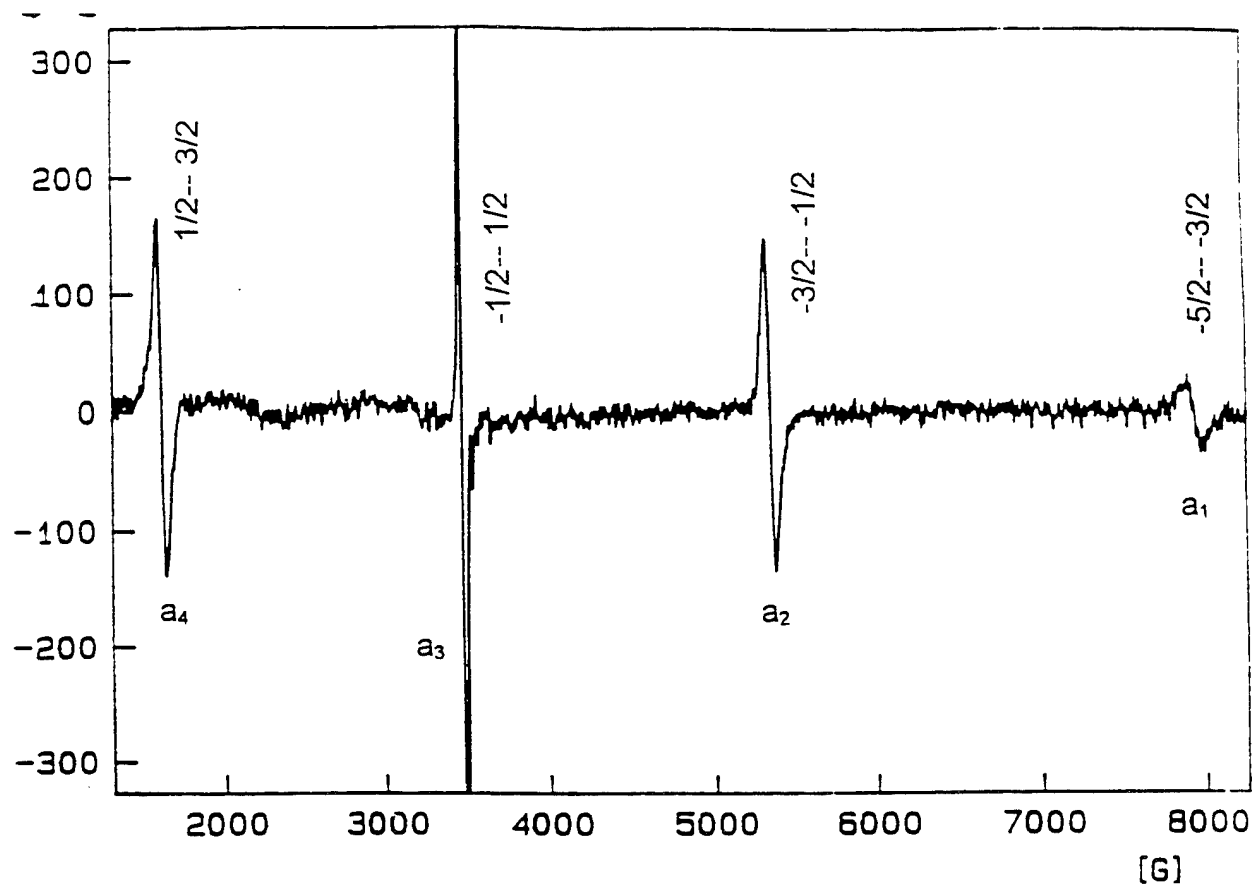


Figure 6.2. EPR of E1-BaTiO₃ crystal, when H || c-axis.

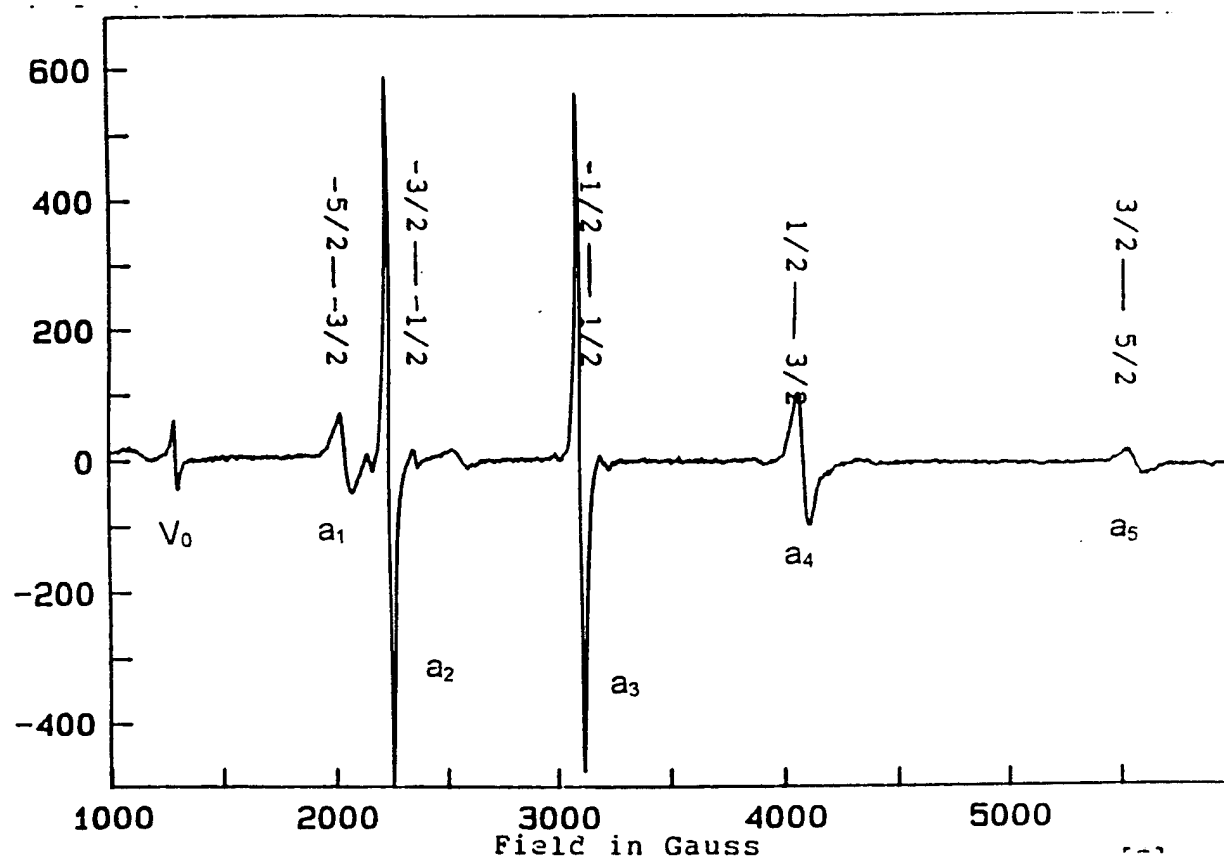


Figure 6.3. EPR of E1-BaTiO₃ crystal, when $H \perp c$ -axis.

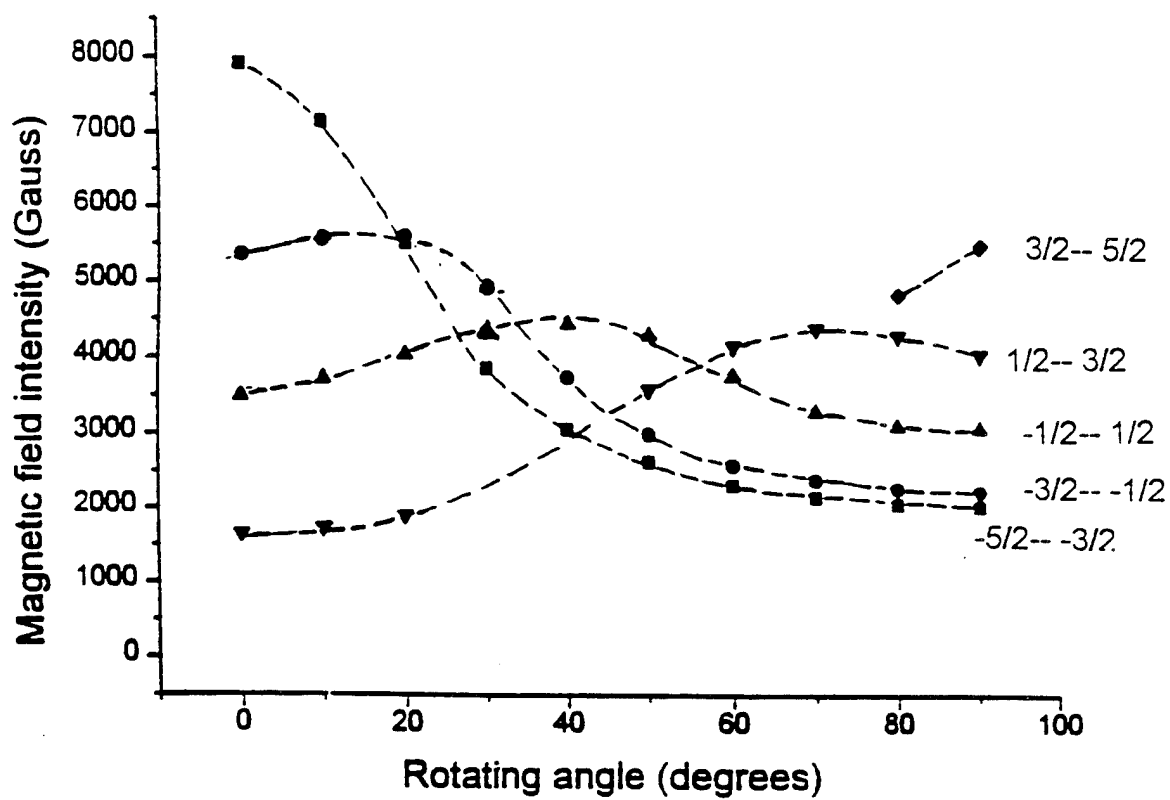


Figure 6.4. Angular variation of the EPR spectrum of Fe^{3+} in (a,c) plane of barium titanate (E1).

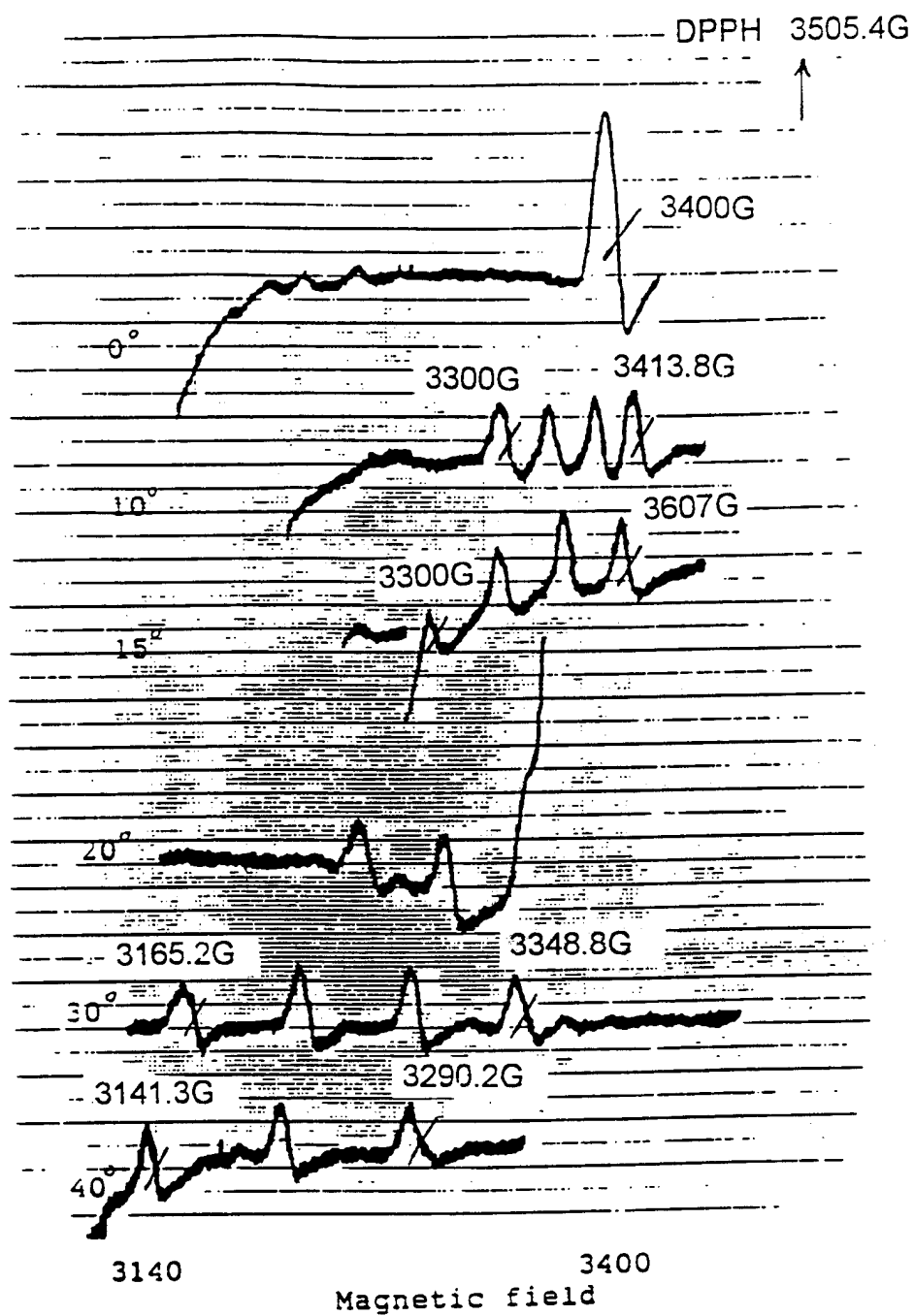


Figure 6.5. Angular variation of the EPR spectrum of Cu^{2+} in (a,b) plane of barium titanate (M1).

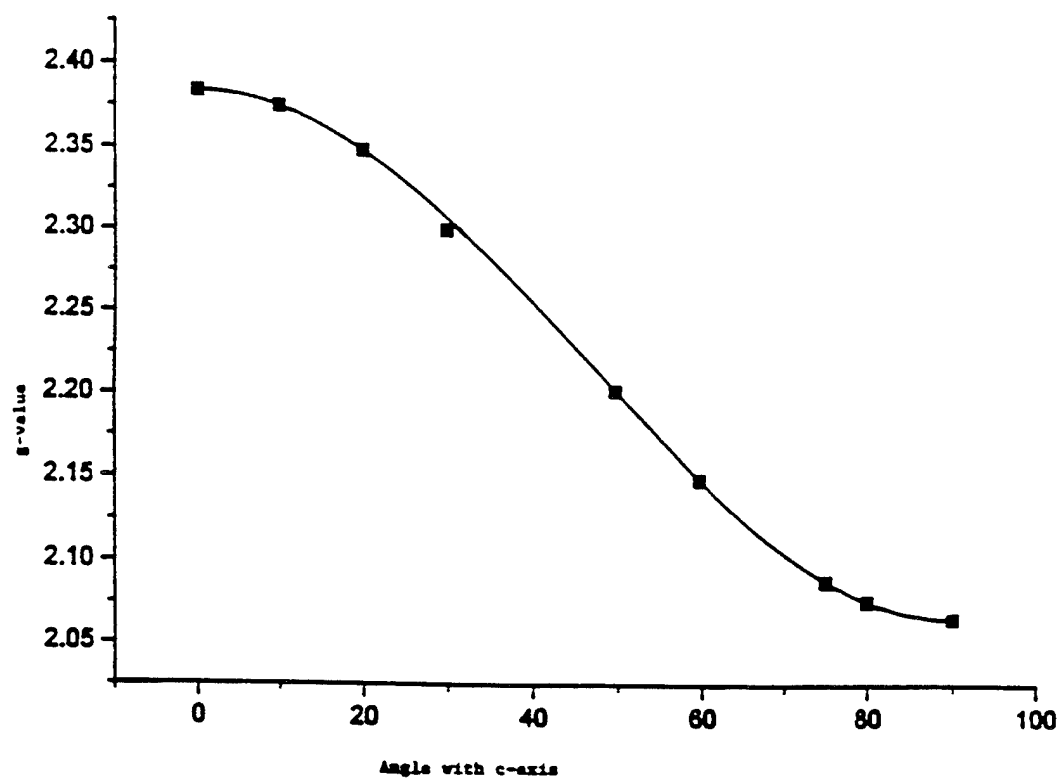


Figure 6.6. Angular dependence of g value in (a,c) plane. The curve is a theoretical curve and the points are experimental.

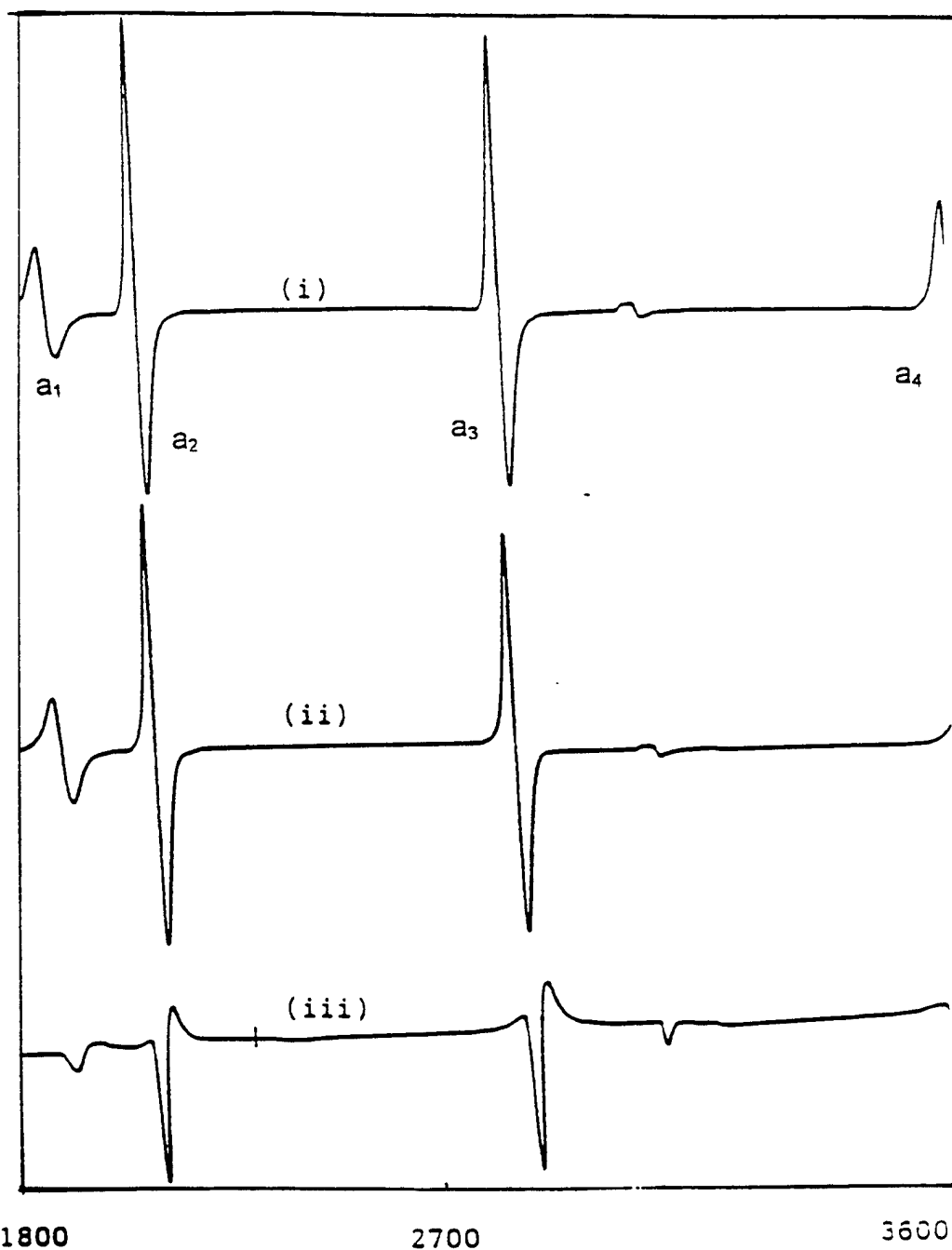


Figure 6.7. The effect of laser light on the EPR spectrum of Fe^{3+} in M1 for $H \perp c$ -axis (i) without illumination, (ii) with uniform illumination and (iii) with nonuniform illumination. Half of the crystal was blocked by a piece of black paper. This simulated a bright and dark pattern of an interference pattern, with a very large fringe width.

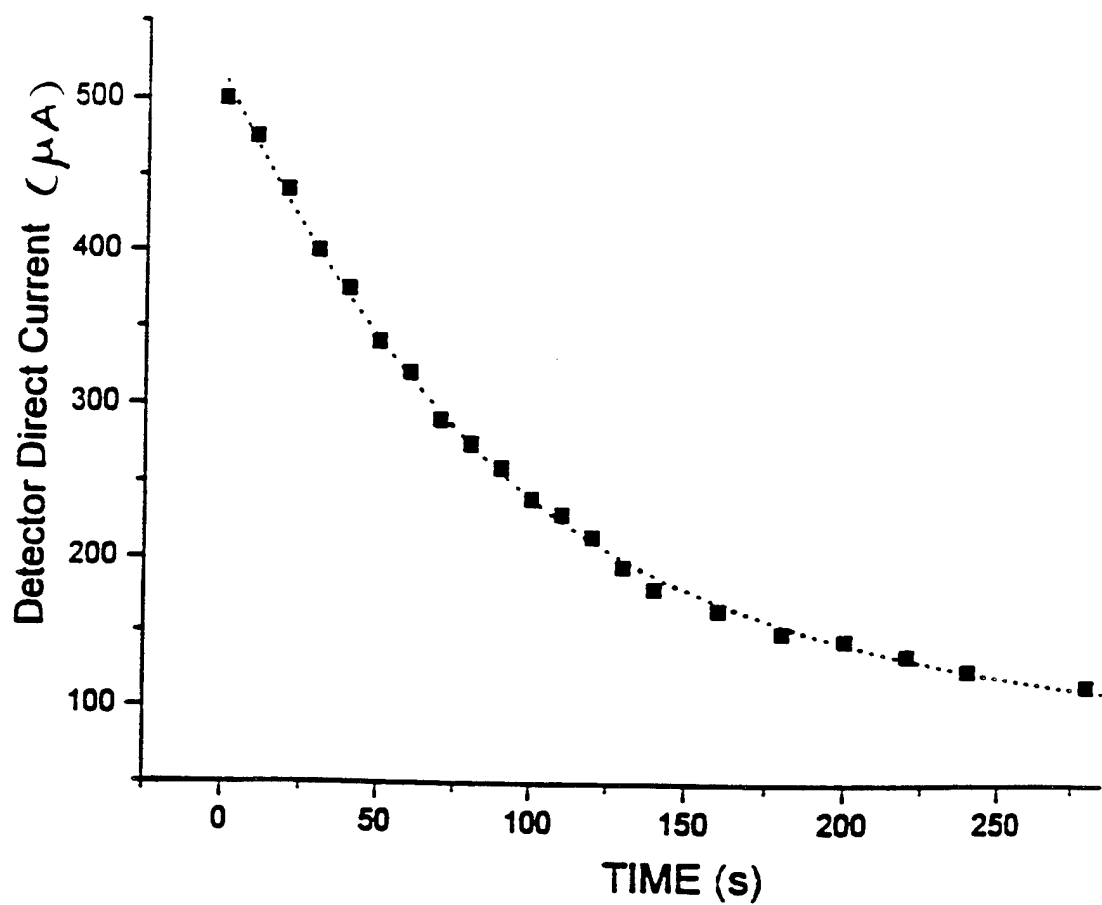


Figure 6.8. Time dependence of the detector current under the condition of half bright and half dark illumination of mechanically poled crystal (M1).

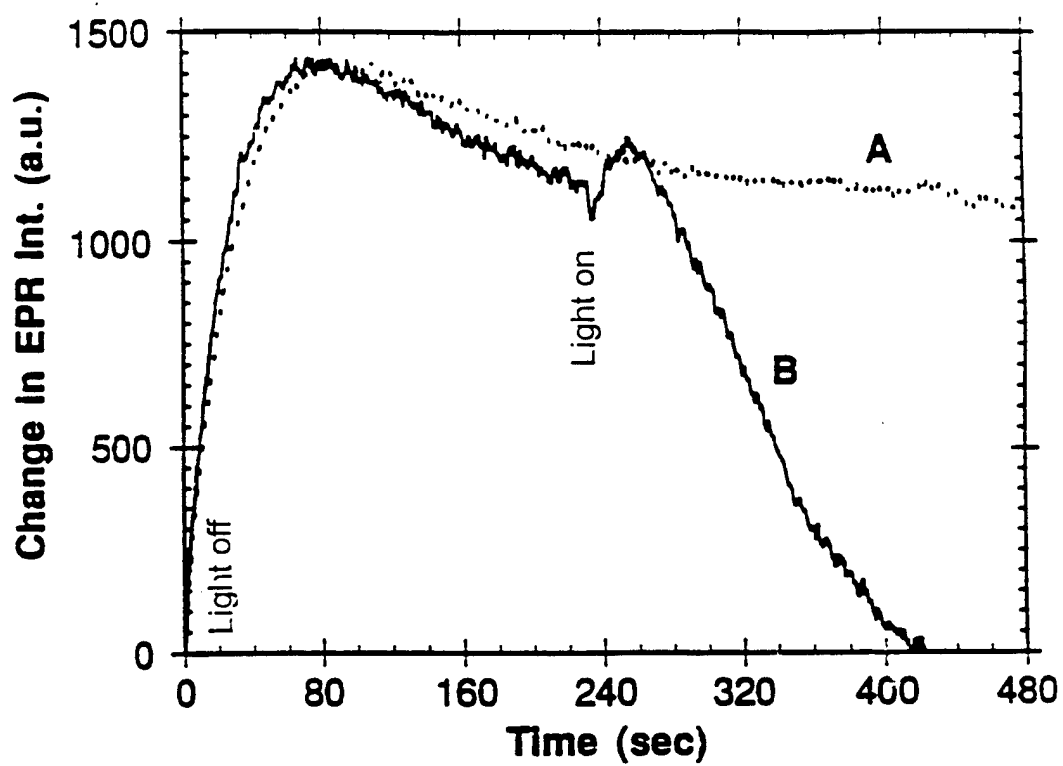


Figure 6.9. Recovery and decay of Fe^{3+} signal under the condition of laser OFF and laser ON for M1-BaTiO_3 .

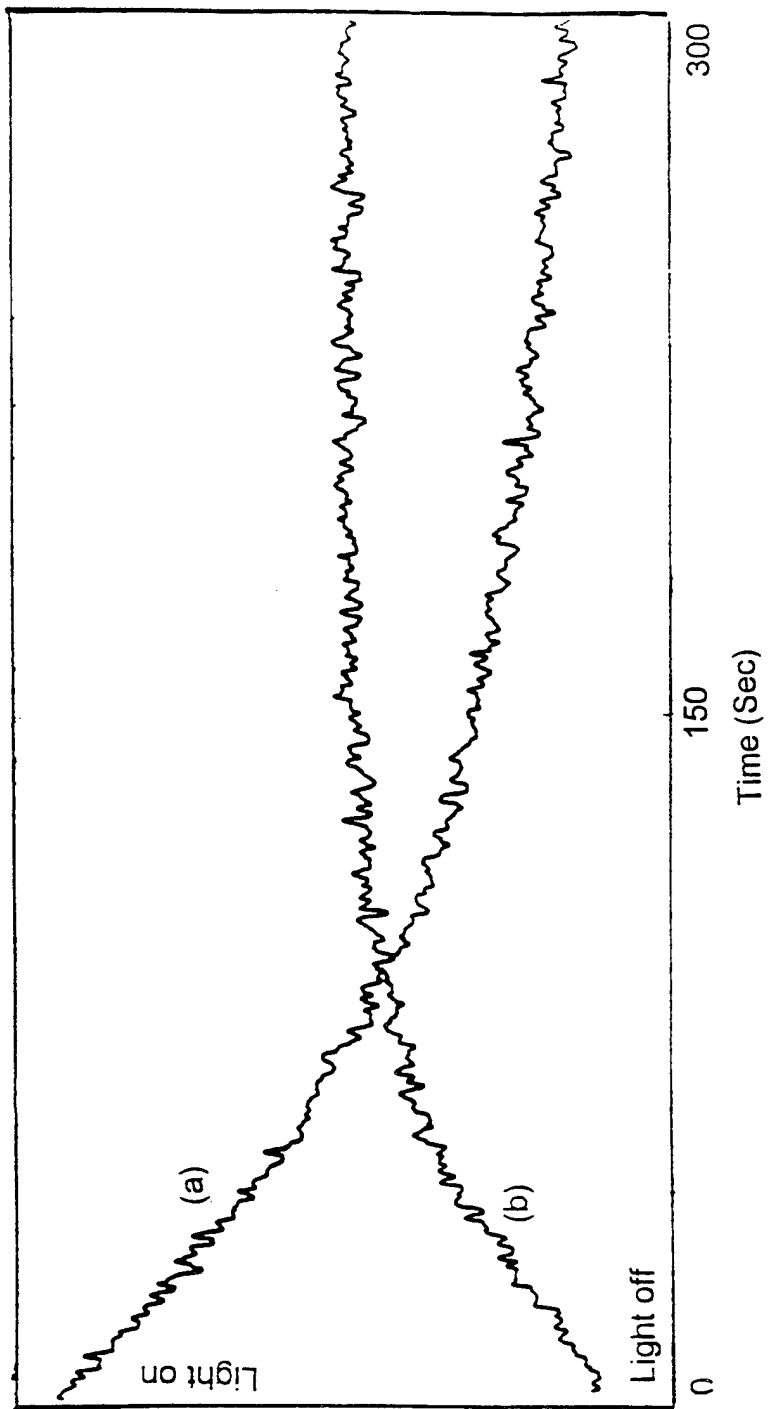


Figure 6.10. (a) Decay and (b) growth characteristic of Cu^{2+} signal in M1-BaTiO₃ when HLLc -axis.

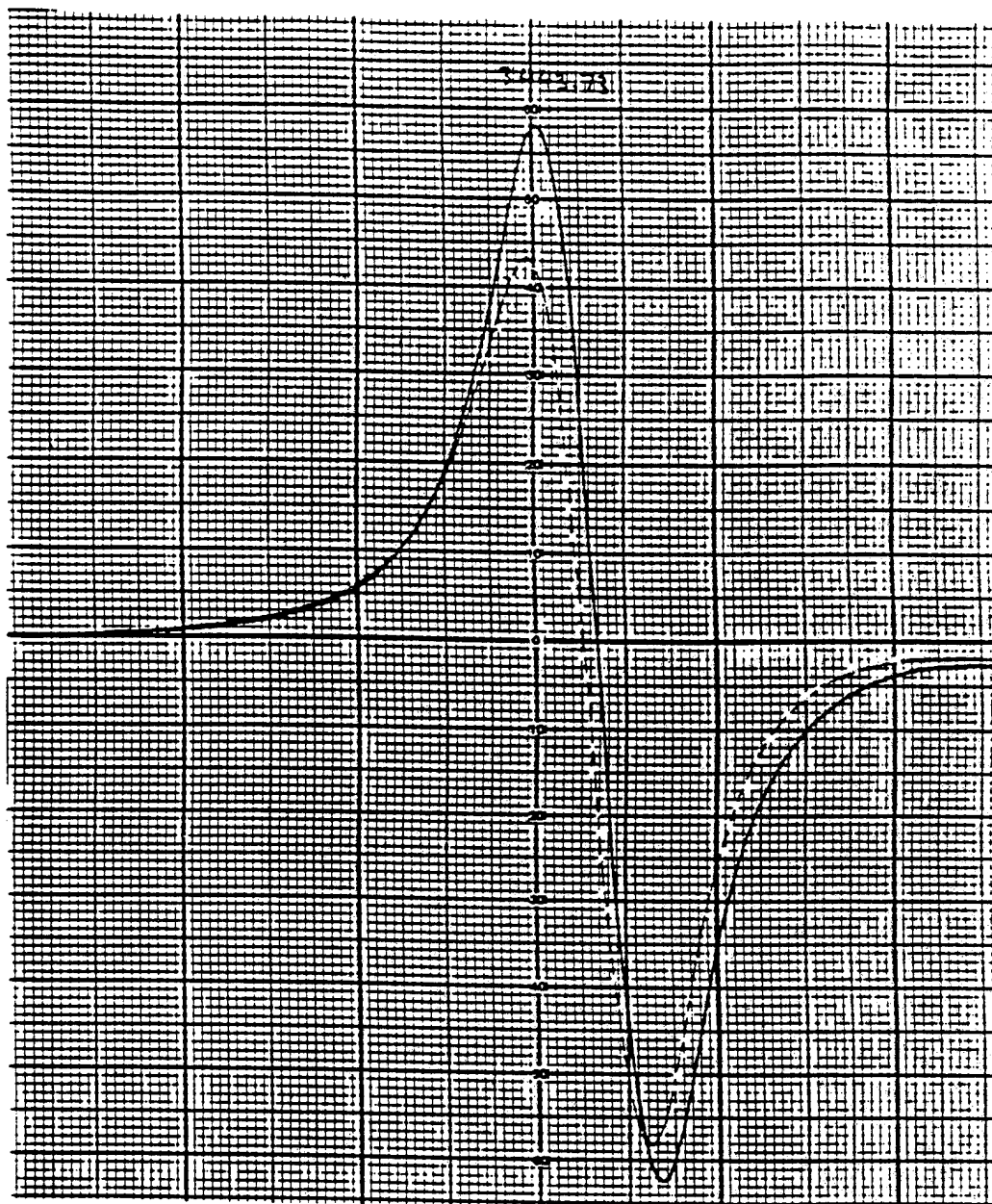


Figure 6.11. The effect of half bright half-dark illumination on the line shape of $1/2 \rightarrow -1/2$ transition of Fe^{3+} in E1-BaTiO₃ crystal. Despite the nonuniform illumination, the shape change are not as drastic as in the case of M1-BaTiO₃.

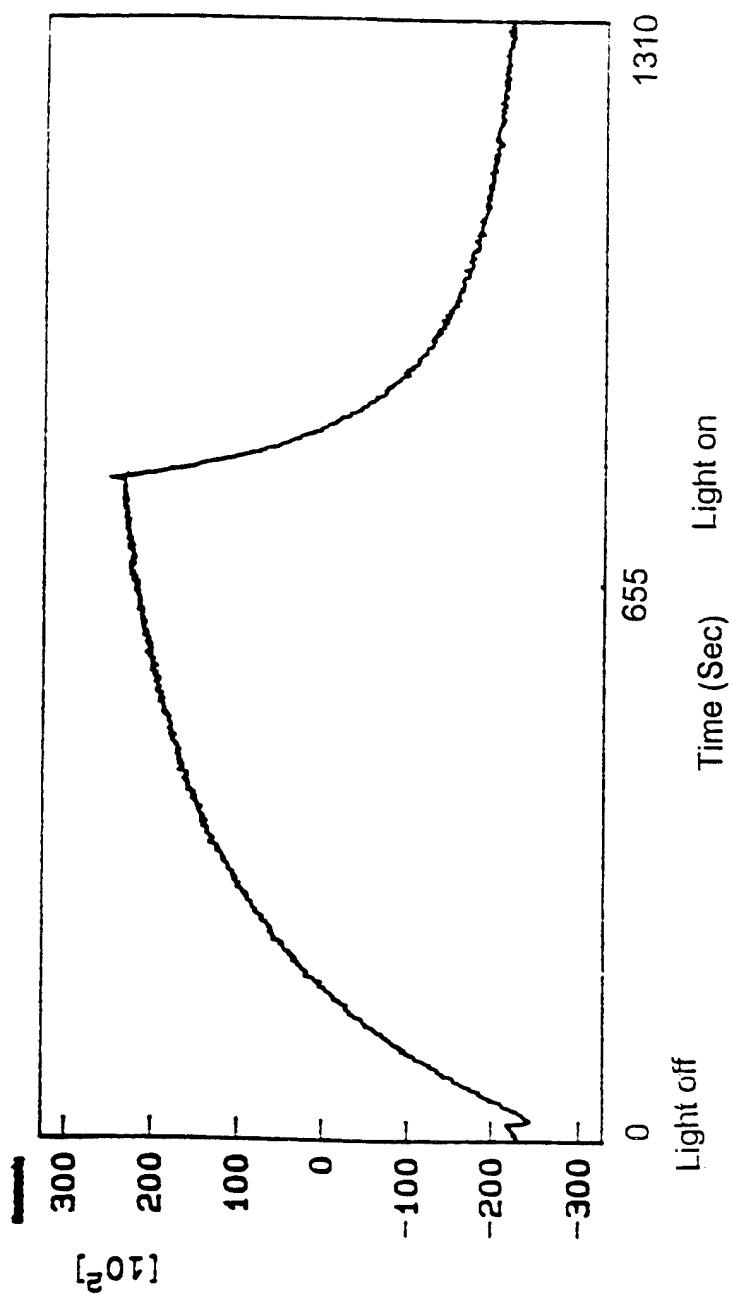


Figure 6.12. Decay and growth of Fe^{3+} intensity ($1/2 \rightarrow 1/2$ line) in E1-BaTiO_3 at room temperature with and without laser illumination respectively.

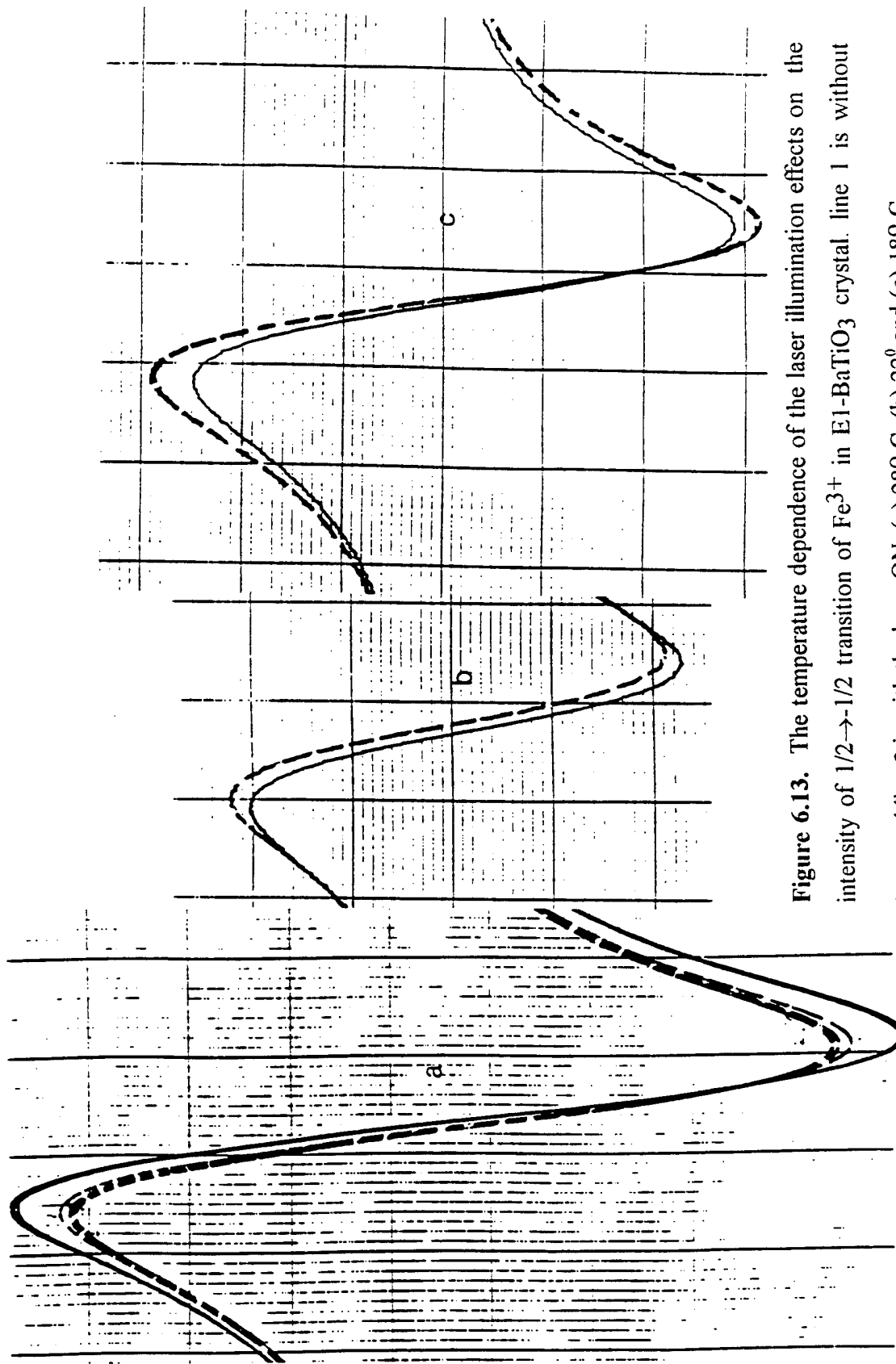
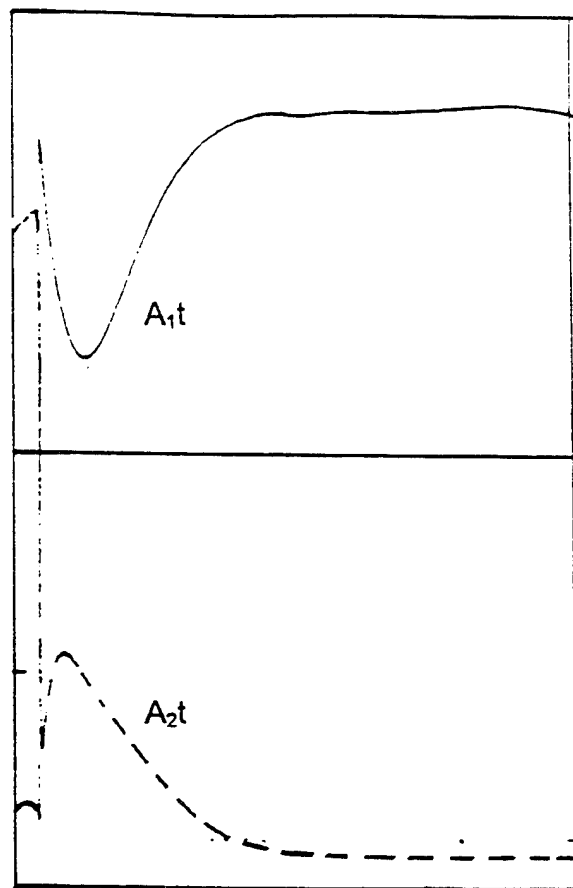


Figure 6.13. The temperature dependence of the laser illumination effects on the intensity of $1/2 \rightarrow -1/2$ transition of Fe^{3+} in E1-BaTiO₃ crystal. line 1 is without laser and line 2 is with the laser ON. (a) 280°C, (b) 22°C and (c) 180°C.



Beam A_2 off

Figure 6.14. Time dependence of the transmitted beam intensity of writing beam A_{1t} , after the second beam was switched OFF. The initial decay of A_{1t} and associated increase of the diffraction signal clearly show the grating formation after the second beam A_2 was switched OFF.

Table 6.1: Time Constant Characterizing the Decay and Growth of Fe^{3+}
Signal on Switching ON/OFF Laser Light.

TIME CONSTANT			
Details of the sample.	Experimental conditions and observations	Decay of Fe^{3+} signal / Bulk microwave loss	Growth of Fe^{3+} signal / Bulk microwave loss
Mechanically poled crystal (M1).	High temperature region, uniform illumination-beam expanded and collimated	(light on) 85.5 sec	(light off) 97.6 sec 27 sec
Mechanically poled crystal (M1)	High tamperature region, non uniform-illumination-(half bright and half dark)	(light on) (detector current) 97.6 sec	(light off) (detector current) 97.6 sec
Electrically poled crystal (E1)	High temperature-uniform illumination	(light on) 166 sec.	(light off) 100 sec. 24 sec.
Electrically poled crystal (E1)	Low temperature uniform illumination	(light off) 113 sec.	(light on) 192 sec. 28 sec.

Chapter 7

Study of Photorefraction and EPR experiments in BSO single crystals and photoinduced charge transfer.

7.1 Introduction

Bismuth silicon oxide, $\text{Bi}_{12}\text{SiO}_{20}$ (BSO) is an important photorefractive crystal because of its good photorefractive nature. It is known that the photorefractive sensitivity could be increased by doping the photorefractive crystals with elements of the iron group. Usually the BaTiO_3 , SBN and LiNbO_3 are known to have inherent Fe^{3+} or other iron group element impurities and the photorefractive nature is attributed to the presence of Fe^{3+} . The doped or the inherently present impurities may have resonant absorption which will enhance the photorefractive sensitivity. Work has been taken up to study the variation of photorefractive characteristics with wavelength and also to study the effect of iron impurity by the use of optical experiments and electron paramagnetic resonance experiments. The color centers whether impurity center or those created by γ -ray irradiation have significant effects on photorefractive characteristics. Work on SBN and BaTiO_3 has been presented in the earlier chapters. Results on the work on BSO are discussed in this chapter.

7.2 Optical Work and Phase Conjugation

Three different BSO crystals have been used. Two were home grown crystals C_1 and C_2 of which C_1 was grown without adding iron and C_2 was grown adding iron as impurity. These crystals were grown by Czochralski technique by Dr. M. D. Aggarawal and Dr. W. S. Wang in the Minority Research Center of Excellence in our university. The third crystal C_3 was a commercial crystal bought from crystal technology, Palo Alto, Ca.

EPR experiments have shown that the undoped crystals C_1 and C_3 have the presence of a very small amount of inherent Fe^{3+} as impurity.

7.2.1 Absorption

The absorption spectrum of the crystal C_1 has been recorded using a Perkin-Elmer Prism Spectrograph model 323 UV VIS NIR and the spectrum in the region 350-700 nm is shown in Fig. 7.1 while that in the region 700-2,600 nm is shown in Fig. 7.2. There are two peaks observed at 1,408 nm and 2,245 nm. These peaks are common to those obtained in the SBN crystal indicating that both the crystals have a common impurity yet to be identified. The crystal shows complete absorption in the region 350-437 nm (Fig. 7.1). There is good transmission in the region 525-700 nm.

7.2.2 Optical Phase Conjugation

The apparatus used for obtaining phase conjugate signals by using degenerate four wave mixing is shown in Fig. 7.3. The intensities of the phase conjugate signals with crystal C_1 in arbitrary units at different wavelengths of the Ar^+ laser lines are shown in Table 7.1, and the variation of the phase conjugate signal intensity versus wavelengths is shown in Fig. 7.4. The phase conjugate signal intensities at different wavelengths of the Ar^+ lines for the iron doped BSO crystal C_2 are given in Table 7.2 and their variation with wavelengths is shown in Fig. 7.5. Comparing the results on the crystal C_1 and C_2 , one sees a regular increase of phase conjugation with wavelengths in the undoped crystals C_1 . The variation in crystal C_2 is irregular, the minimum being at 476.5 nm and the maximum at 496.5 nm. The difference is probably because of the doped iron impurity. Fe^{2+} and Fe^{3+} ions are known to have absorption in the visible region. These absorptions may give wavelength dependent resonant effects on phase conjugation. The variation of the phase

conjugate signal on wavelengths in the undoped crystal C_1 in Fig. 7.3 did not show irregularities.

Table 7.1 Variation of phase conjugate signal intensity with wavelength in the undoped crystal C_1 .

number	wavelength of Ar^+ lines nm	Phase conjugate signal (a.u.)
1	514.5	878
2	501.7	730
3	496.5	518
4	488.0	420
5	476.5	132
6	472.7	$97 + 15$
7	465.8	$72 + 15$
8	457.9	$54 + 15$

The growth and decay of phase conjugation have been recorded at different wavelengths of Ar^+ lines for the doped home grown BSO crystal C_2 and the undoped commercial crystal C_3 . The variation of decay times τ with λ is shown in Figs. 7.6 and 7.7 for crystals C_3 and C_2 respectively. The results are tabulated in Tables 7.3 and 7.4 for crystals C_3 and C_2 respectively. τ increased with wavelength in both the cases though the curve for crystal C_2 is slightly more irregular. The τ values are slightly higher for the crystal C_2 .

The irregularities in the variation of phase conjugate signal intensity on wavelength and variation of decay times of phase conjugation on wavelengths in the iron doped BSO crystal are probably because of the doped iron in the form of Fe^{3+} , Fe^{2+} and Fe^{4+} and the respective charge transfers on laser illumination.

7.3 Study of the EPR of BSO:Fe^{3+} under the He-Ne Laser Illumination and Photoinduced Charge Transfer.

7.3.1 Background

We observed in separate EPR experiments that the homegrown BSO:Fe^{3+} showed a cubic spectrum of Fe^{3+} which is not sensitive to the angular orientation of the crystal with respect to the magnetic field direction and a weak axial spectrum which is angular dependent. We discussed the EPR experimental results on Fe and Cu inherently present in BaTiO_3 crystal in the earlier chapter. We studied the effect of He-Ne illumination on the EPR lines of Fe^{3+} and Cu^{2+} described in the earlier chapter and obtained interesting information. In this section we describe similar work on BSO:Fe^{3+} . Jani and Halliburton [7.1] have investigated the effect of photoillumination on the EPR of Fe^{3+} in BSO. They found that excitation with 350 nm light indeed changed the valence of Fe^{3+} at 77K, and it

recovered to its original site only on warming the crystal to room temperature. They did not, however, find any photoinduced valence change of Fe^{3+} at room temperature. In view of the role of Fe^{3+} as a trapping site for electrons in subroom temperature region, they suggested that Fe^{3+} ions might be playing an important role in the photorefractive effect. Baquedano et al. [7.2] have investigated the EPR of BSO by illuminating with He/Cd (442 nm) laser, and also Xe arc lamp. We report here direct detection of photoinduced charge transfer by EPR for the first time in BSO at room temperature with 632.8 nm light. We can observe this only under special conditions in view of the fast dielectric relaxation time in the case of BSO. The effect of He-Ne laser illumination was observed more easily at 77K consistent with the earlier reports. The kinetics of charge transfer on laser illumination is also investigated.

7.3.2. Experimental

EPR measurements were carried out on a Bruker ESP - 300E, X-band spectrometer equipped with an optical transmission cavity. The optical transmission cavity facilitates selective illumination of the crystal (without illuminating the walls of the cavity) giving unambiguous evidence for any photoinduced changes occurring in the crystal. DPPH, with $g=2.0036$ is used as a g -marker. A 35-mW He-Ne laser was used for illuminating the crystal. The spectra at 77K were taken by immersing the crystal in a standard quartz dewar (liquid nitrogen insert).

7.3.3 He-Ne Laser Illumination on EPR Lines and Charge Transfer on Fe^{3+}

With an aim to understand the possible role of Fe^{3+} impurity in BSO on its photorefractive properties, we have monitored the changes in the intensities of Fe^{3+} EPR

lines, both at cubic and noncubic sites. The measurements were done in situ at room temperature by loading the sample in an optical transmission cavity. When the crystal was uniformly illuminated, no detectable changes were observed in the signal intensity. This is shown in Figure 7.8. Jani and Halliburton [7.1] also have not reported any photoinduced changes in the intensity of the Fe^{3+} signal at room temperature despite using shorter wavelength (350 nm) radiation. Baquedano et al [7.2] monitored the intensity changes of a broad EPR line at $g=2$, as a function of optical illumination at different temperatures. This EPR line was attributed to a mobile trapped hole center. However, the contribution of cubic Fe^{3+} center at that field position cannot be ruled out. Baquedano et al. [7.2] also have not reported any intensity changes in the EPR of the "trapped hole center" at room temperature. Our observation is, therefore, consistent with that reported by these workers [7.1,7.2] clearly suggesting that either there is no optically induced charge transfer involving Fe^{3+} , or the charge transfer and relaxation takes place in a time much shorter compared to the time constant of the EPR detection system (which is 10ms in the present experiment). The former observation, i.e. the absence of photoinduced valence change of Fe in BSO, leads to a trivial conclusion, which may not be physically consistent as Fe^{3+} at Si^{4+} should act as a "hole" trap on electrostatic arguments. The temporal behavior of charge relaxation, after photoexcitation, as monitored in EPR comes closest to the situation of very large fringe width or zero grating wave vector, and it will be equal to the dielectric relaxation time τ_d [7.3], where

$$\tau_d = \epsilon \epsilon_0 / n_0 \mu e$$

where $n_0 = n_d + n_l$, n_l is the free carrier concentration due to the incident illumination I_0 , n_d is the thermally excited free carrier concentration, μ is the charge mobility of the photocarriers, ϵ is the dielectric constant of BaTiO_3 and ϵ_0 is the permittivity of free space. We [7.3] have deduced τ_d in BaTiO_3 by illumination at room temperature. In contrast to BaTiO_3 , in BSO the charge transport mechanism is of long range, and the dielectric relaxation rate is faster than the photo-excitation rate [7.3], and τ_d sets the

fastest limit for grating erasure rate. Therefore, the long range nature of the Coulomb force in BSO helps to decrease the erasure rate of gratings with smaller fringe spacing. This suggests that if BSO is illuminated nonuniformly, simulating a grating formation, the probability of detection of photoinduced charge transfer should enhance. To examine this qualitatively, a grid of black lines 1 mm in width separated by 1 mm were drawn using a marker on the BSO crystal and was illuminated by He-Ne laser at room temperature. The results are shown in Figures 7.9 and 7.10 for cubic and noncubic Fe^{3+} centers respectively. These figures show that the concentration of Fe^{3+} goes down with non-uniform illumination. By locking the field to the peak positions, the decay and growth of respective Fe^{3+} centers are monitored.

As the changes in the intensity in the Figures 7.9 and 7.10 are not very substantial at the laser power used (35 mW), it is important to ascertain that these are not artifact of possible change in Q-factor of the cavity where the crystal with "grid formation" was illuminated. Experiments were done by keeping a DPPH marker on the top of a crystal. The crystal was not kept at the center of the cavity to avoid the intense cubic spectrum. The intensity of DPPH signal did not show any changes on laser illumination. This gives a reasonable assurance that the observed changes are not artifact of changes of the bulk properties of the crystal. It would have been more certain in case the overlap of DPPH and that of cubic spectrum did not exist. It may be further mentioned that the decay characteristics of cubic and noncubic spectra are different (Figures 7.9 and 7.10) suggesting that the observed changes are not due to changes in the temperature of the sample. The results, therefore, give considerable insight into the photoinduced charge transfer involving Fe^{3+} and its relaxation. To the best of our knowledge, this is the first direct observation of charge transfer involving Fe - impurity at room temperature, where the photorefractive experiments are normally conducted. The growth and decay of cubic and noncubic Fe^{3+} signals, with light off and on respectively were analyzed and the decay constants were found to be 182s and 236s as seen in Figures 7.11, 7.12 and 7.13. It may

be noted that the decay time constant obtained using noncubic sites is much larger than the one obtained with cubic sites. This is physically consistent, as the cubic sites act as much better hole traps, due to electrostatic reasons, compared to noncubic sites. Fe^{3+} at Si^{4+} site, with no local charge compensation creates an attractive potential for "holes" whereas this is much less probable in the case of Fe^{3+} at Si^{4+} site associated with oxygen vacancy. When Fe^{3+} takes the place of Bi^{3+} , it does not act as a trap either for electrons or holes.

In view of the earlier reports of photoinduced changes in EPR, at low temperatures using 350-nm and 430-nm light, we have uniformly illuminated the crystal, with 632-nm light at 77K, placing the crystal in a liquid nitrogen insert. The EPR intensity reduced as a function of time. This is shown in Figure 7.14. The intensity was not regained at 77K when the laser was switched off. The spectrum regained its intensity only when the crystal was warmed to room temperature. This suggests that Fe - impurity in BSO, is only acting as a static trap for charge carriers at 77K, and as a recombination center when it is released on thermal stimulation. This highlights the fact that photo-EPR experiments at room temperature can lead to a realistic understanding of the processes involved in "writing" the real-time holograms in photorefractive crystals. EPR can be potentially used for understanding the nature of electron/hole traps, but the presence of very intense and broad cubic spectrum of Fe^{3+} prevented such an investigation.

7.2.4. Conclusion

Irregularities have been observed in the variation of phase conjugation with wavelength which is probably because of the resonant effect of the doped multivalent iron impurity. We have shown for the first time, using a simple method of simulating the grating formation, that photoinduced charge transfer involves Fe^{3+} impurities. This escaped the detection during uniform illumination due to the long range nature of charge transport in BSO resulting in very short dielectric relaxation time, τ_d .

References

- 7.1 M. G. Jani and J. E. Halliburton, J. Appl. Phys., 64, 2022 (1988).
- 7.2 J. A. Baquedano, F. J. Lopez and J. M. Cabrera, Solid State Communications, 72, 233 (1989).
- 7.3 M. D. Sastry, M. Moghbel, A. Darwish and P. Venkateswarlu (To be published).

Table 7.2 OPC signal in (a.u.) of "home grown iron doped BSO crystal C₂ at different wavelengths.

	Wavelength nm	Intensity
1	514.5	25.8
2	496.5	46.6
3	488.0	19.4
4	476.5	10.6
5	457.9	27.2

Table 7.3 Decay time constant (in seconds) of OPC signal for a commercial BSO at different wavelengths.

	Wavelength nm	Decay time τ (s)
1	457	0.114
2	488	0.1535
3	496	0.1571
4	514	0.1832

Table 7.4 Decay time constant (in seconds) of OPC signal for a "home grown " iron doped BSO crystal C₂ at different wavelengths.

	Wavelength nm	Decay time τ (s)
1	457	0.145
2	488	0.155
3	496	0.161
4	514	0.177

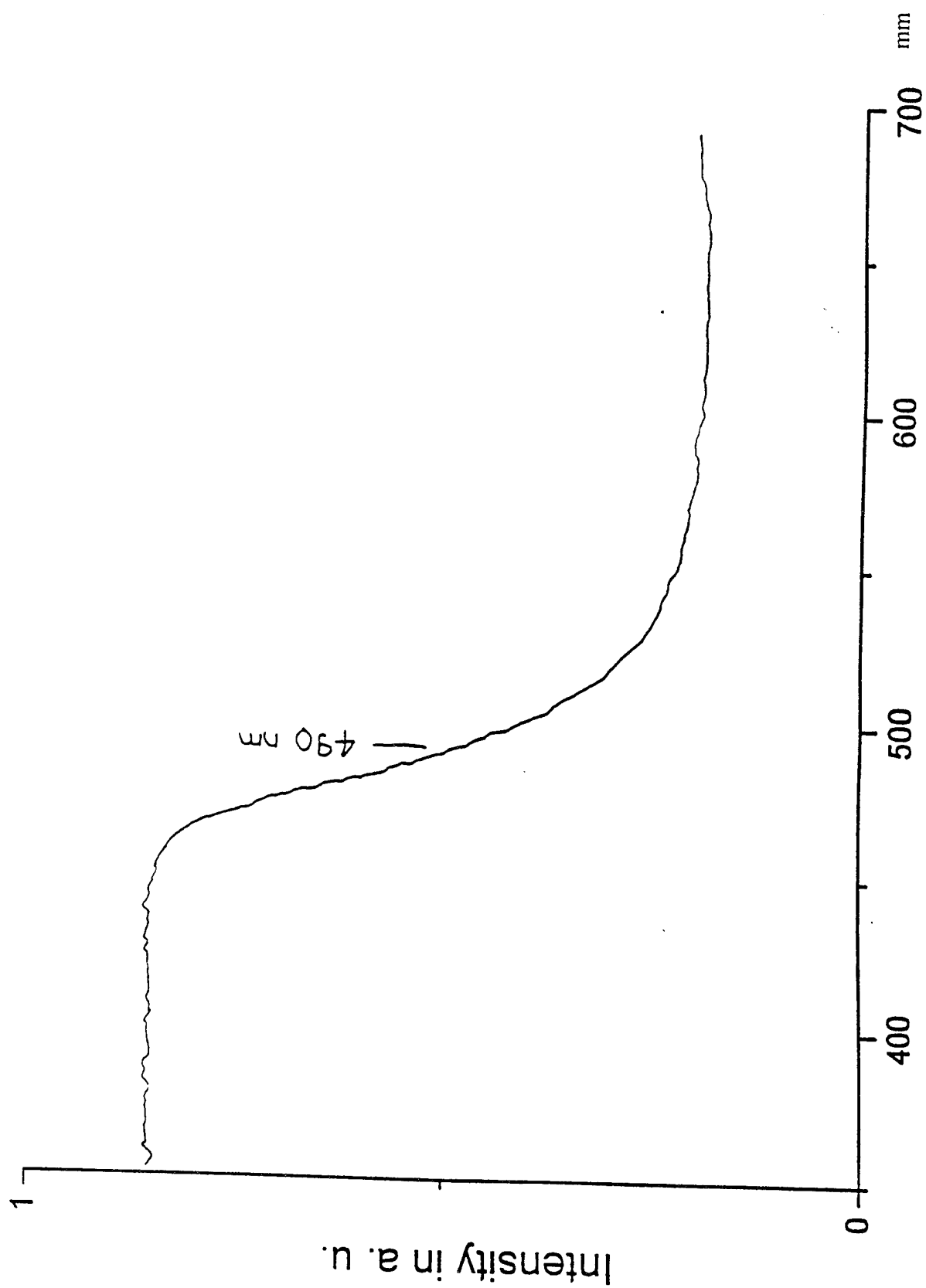


Fig. 7.1 Absorption Spectrum of crystal C₁ in region 350 - 700 nm.

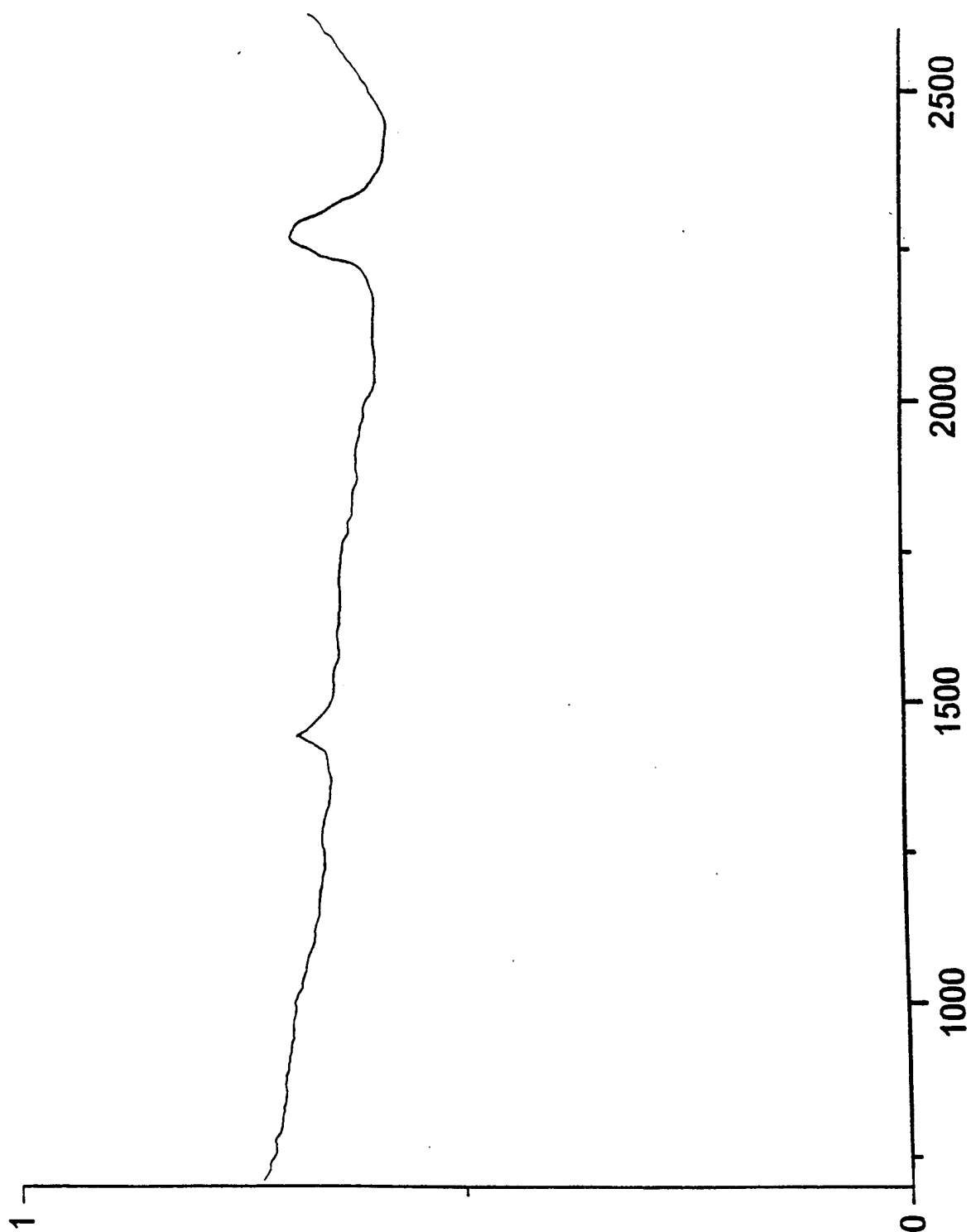


Fig. 7.2 Absorption Spectrum of crystal C₁ in region 700 - 2600 nm.

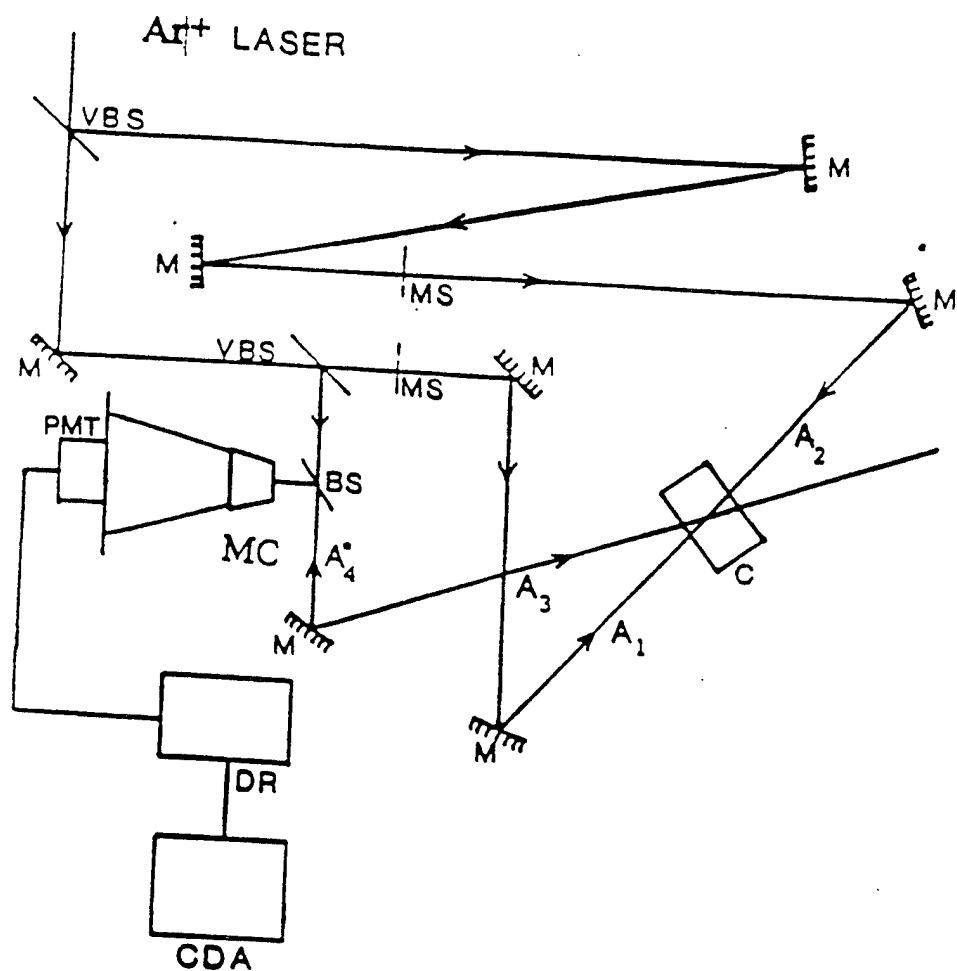


Fig. 7.3 Schematic experimental setup of four wave mixing in BSO. PMT; photomultiplier tube, M; mirror, VBS; variable beam splitter, MS; mechanical shutter, c; crystal, MC monochromator, DR; digital recorder, CDA; computer data analyser.

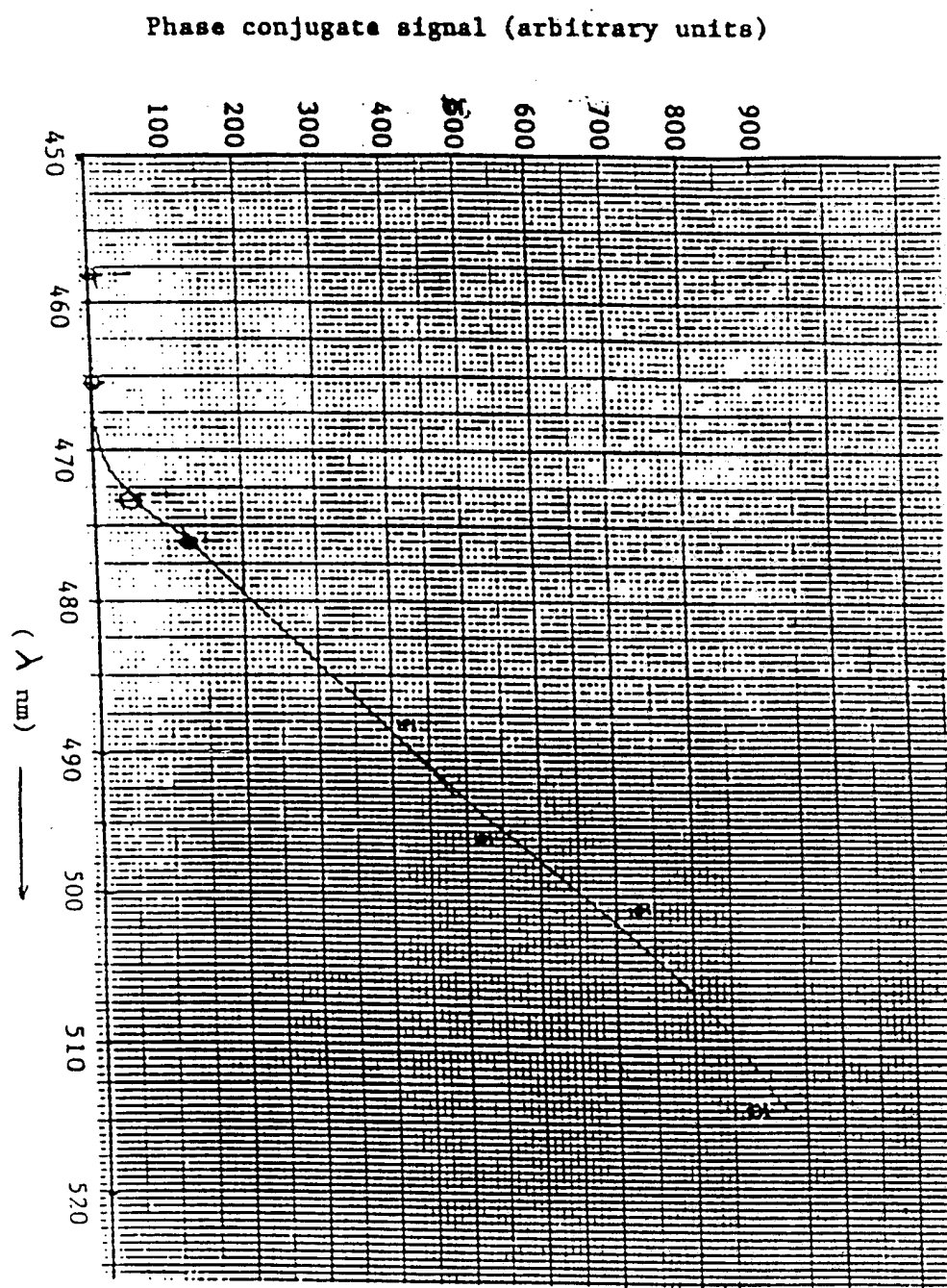


Fig. 7.4 Variation of signal intensity of Optical Phase Conjugation (arbitrary units) with wavelength in crystal C_1 .

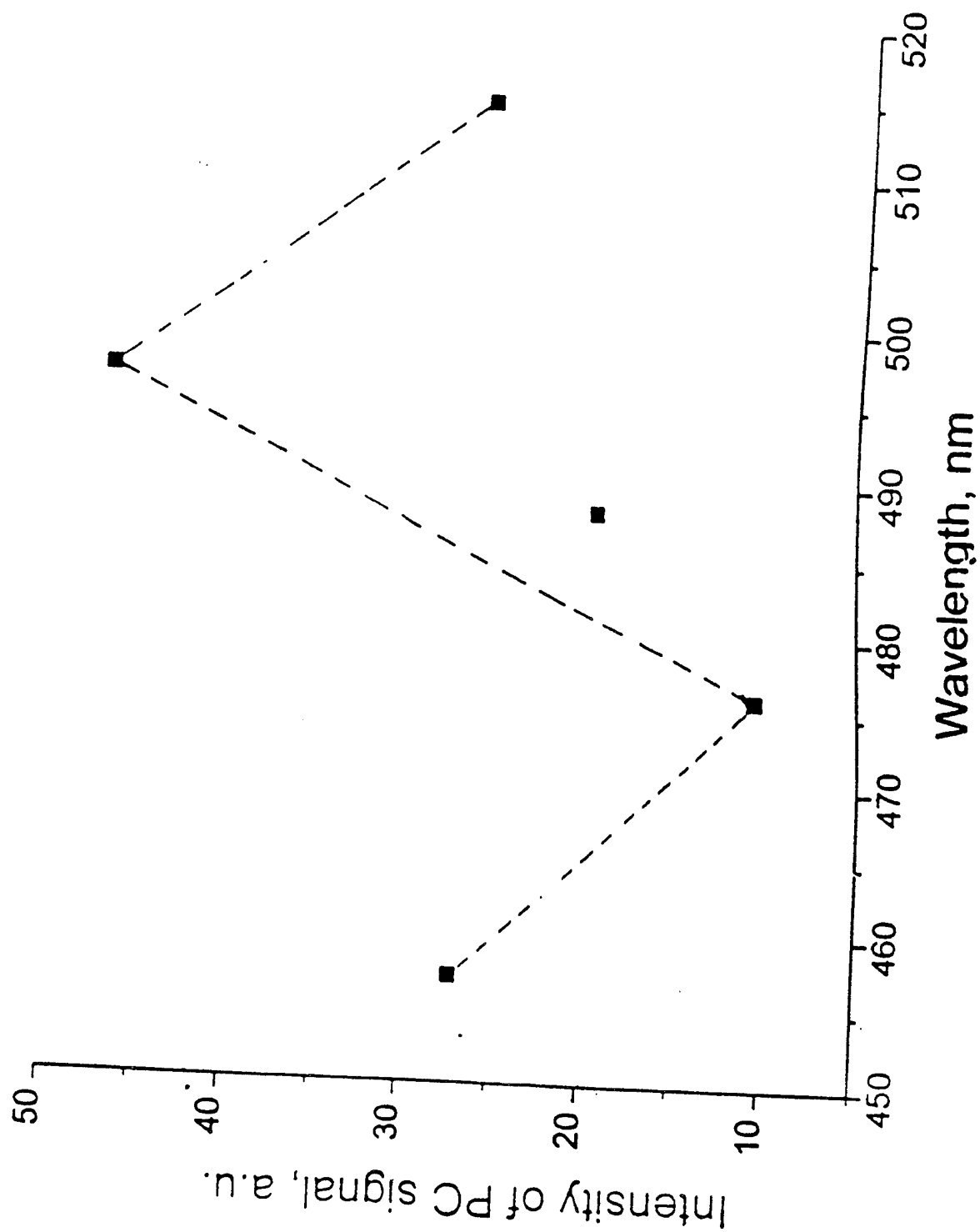


Fig. 7.5 Intensity of OPC signal for a "home grown" Fe doped BSO crystal C_2 at different wavelengths.

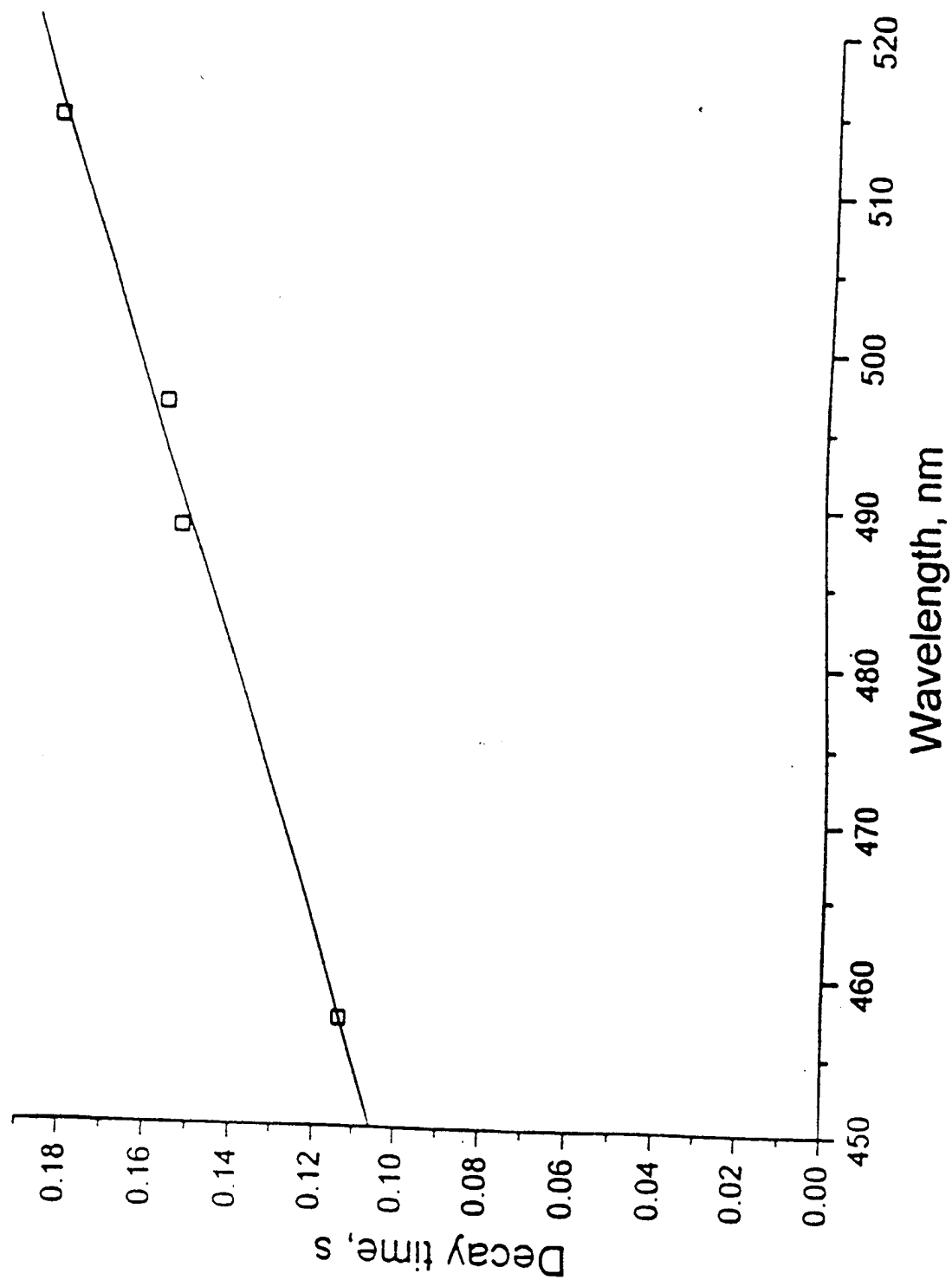


Fig. 7.6 Decay time constants of OPC signal for a commercial BSO crystal C_3 at different wavelengths.

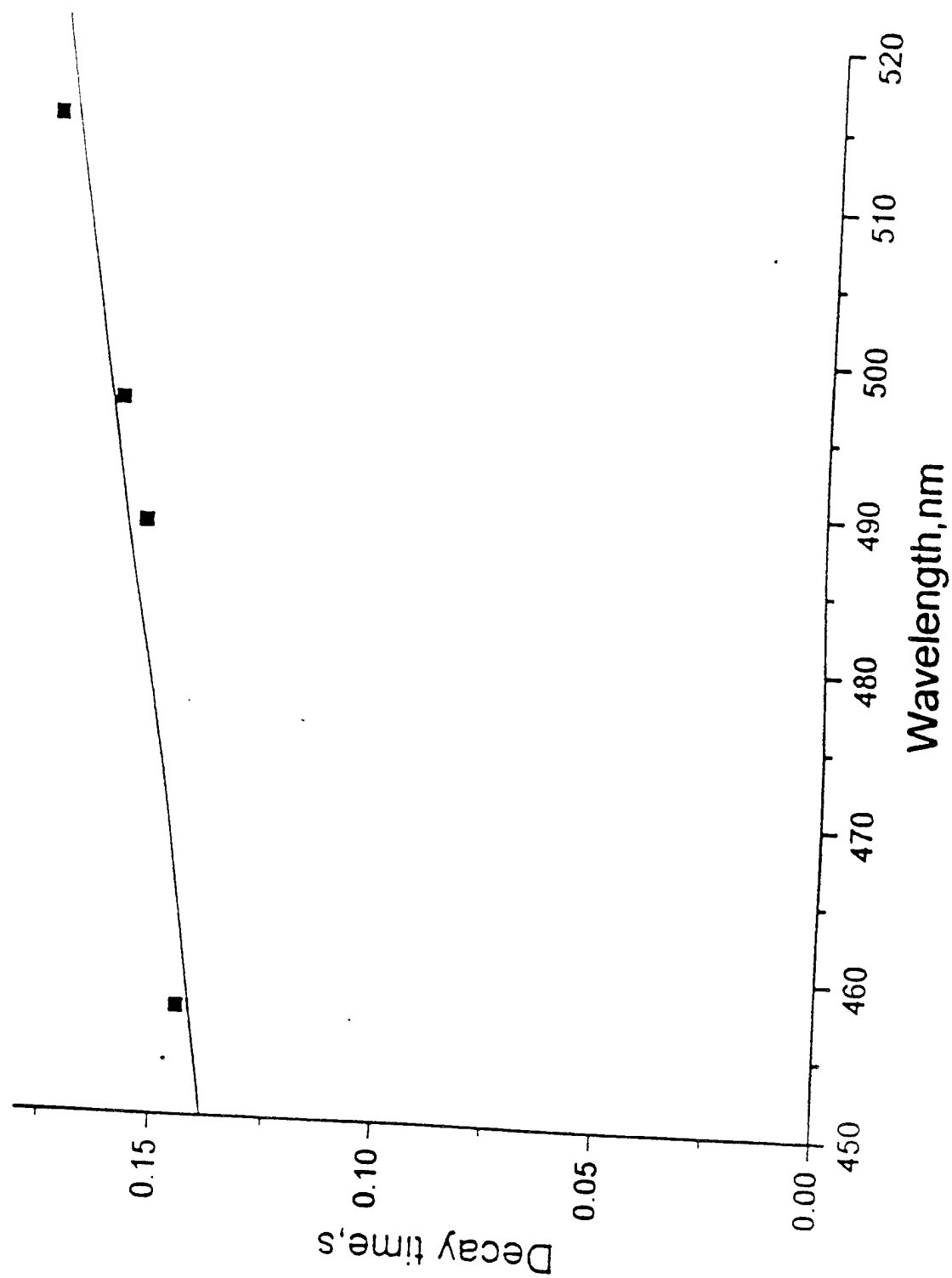


Fig. 7.7 Decay time constants of OPC signal for a "home grown" iron doped BSO crystal C_2 at different wavelengths.

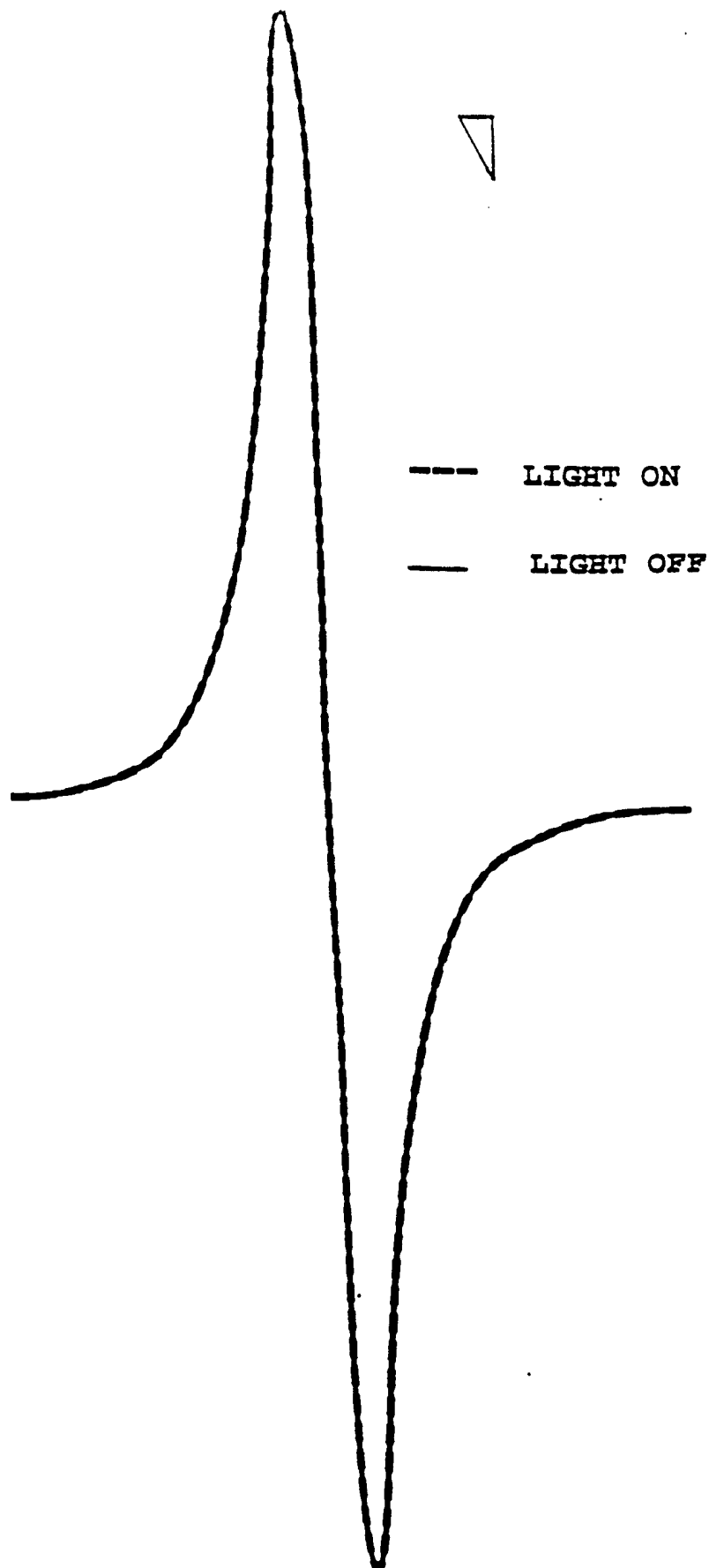


Fig. 7.8 Intensity of Fe^{3+} cubic spectrum at room temperature with uniform laser illumination.

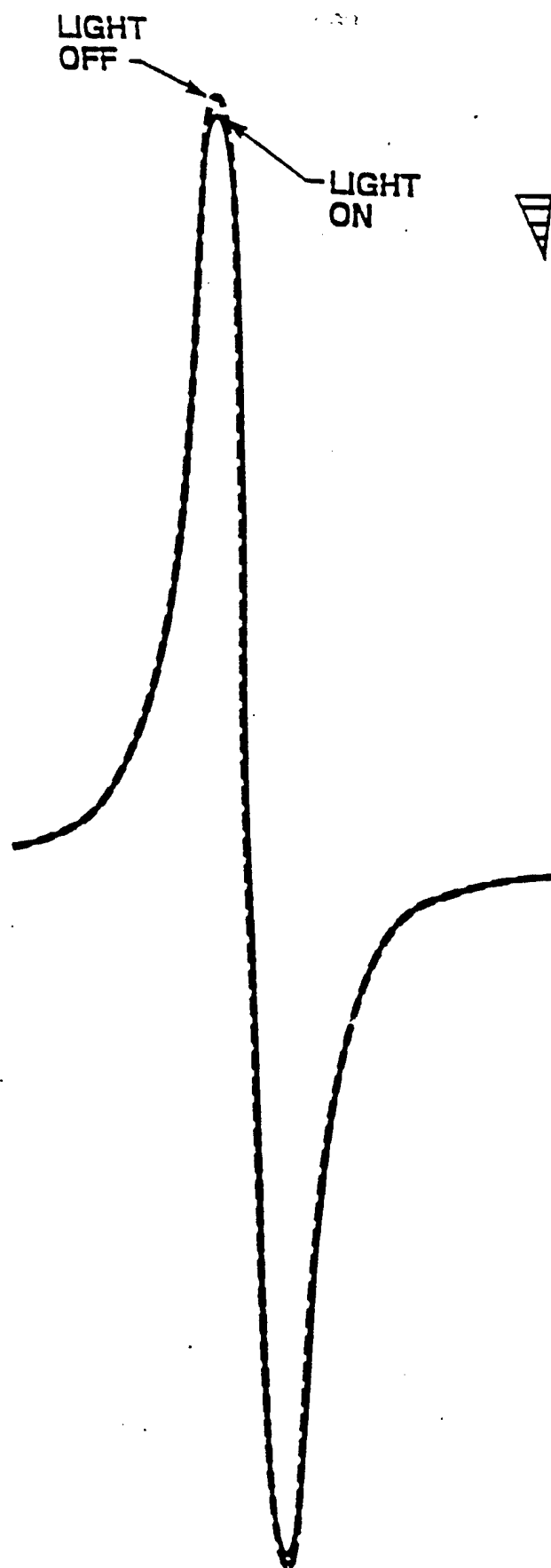


Fig. 7.9 Intensity of Fe^{3+} cubic spectrum at room temperature with nonuniform laser illumination.

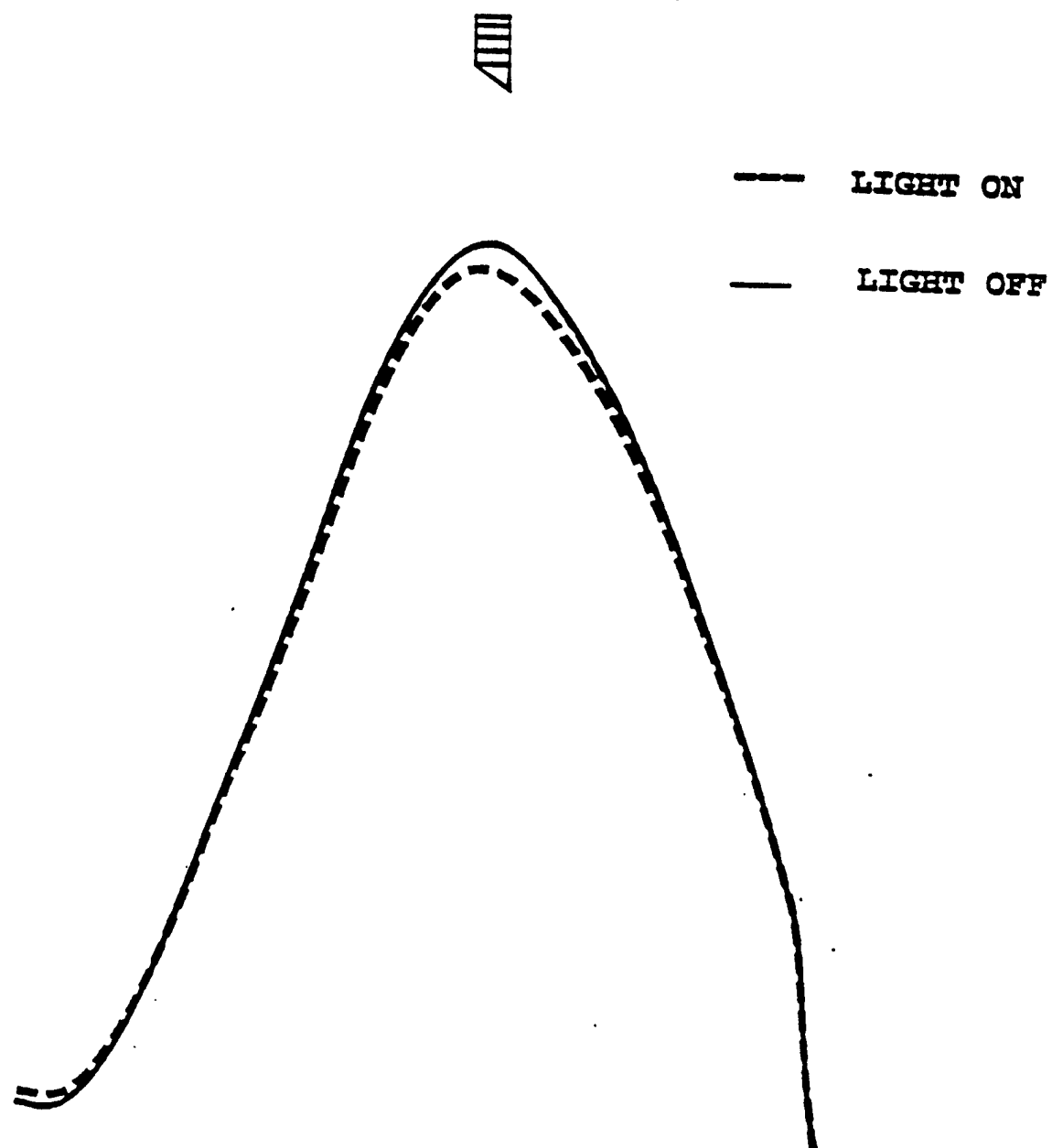


Fig. 7.10 Intensity of Fe^{3+} noncubic spectrum of "home grown" BSO, with nonuniform illumination.

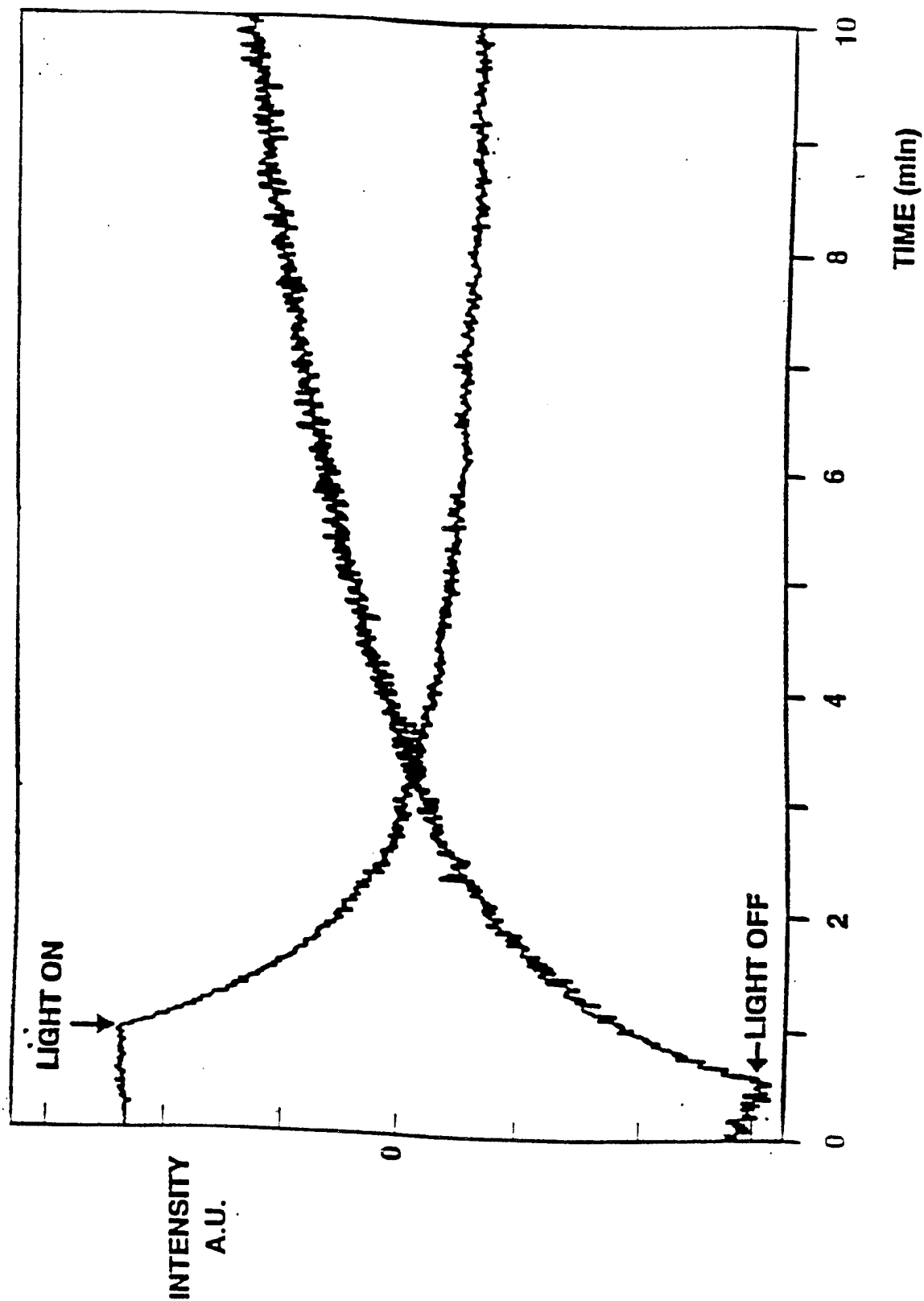


Fig. 7.11 Decay and growth of EPR signal intensity of Fe^{3+} at cubic site.

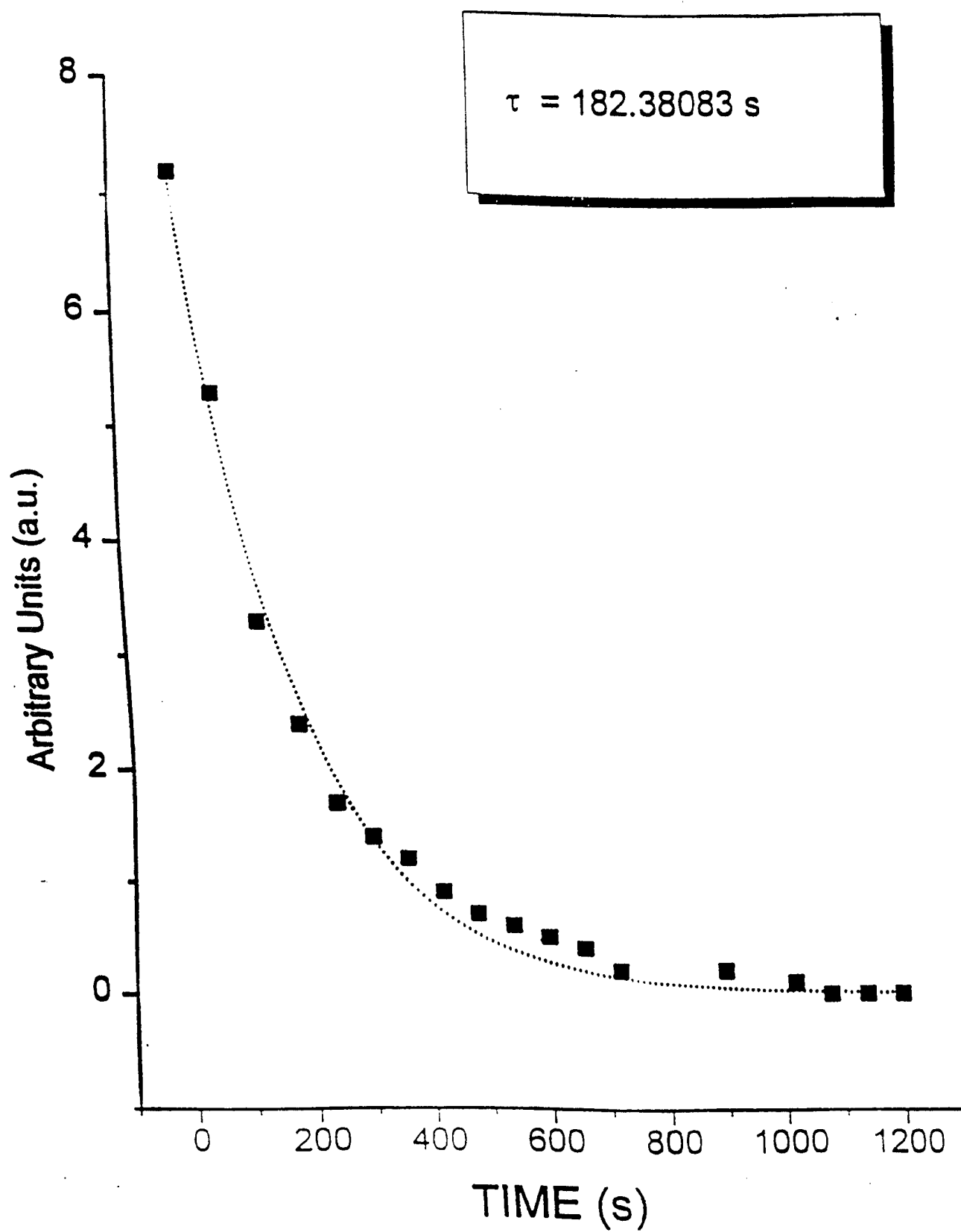


Fig. 7.12 Decay and decay constant of EPR signal intensity at cubic site

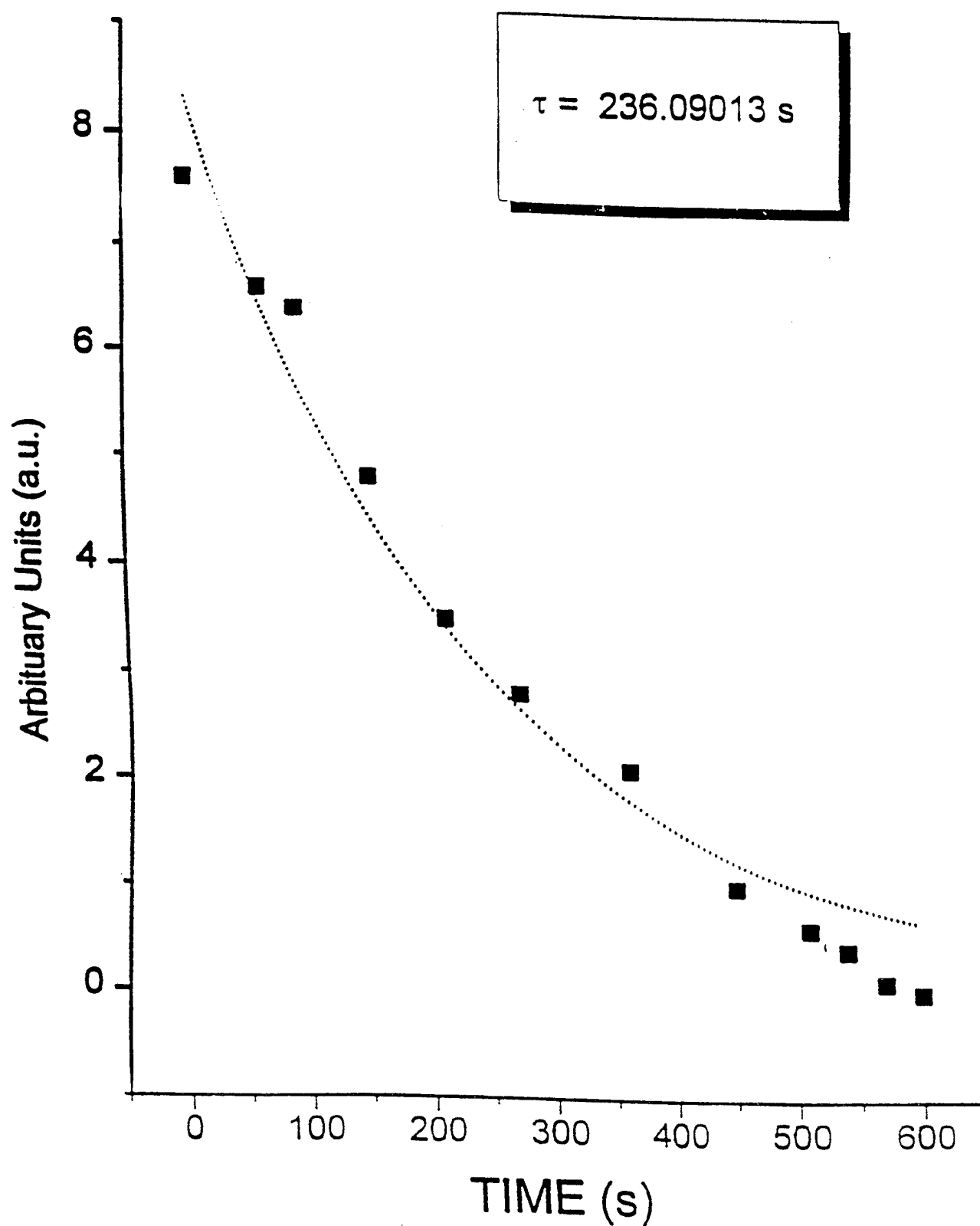


Fig. 7.13 Decay and decay constant of EPR signal intensity at noncubic site

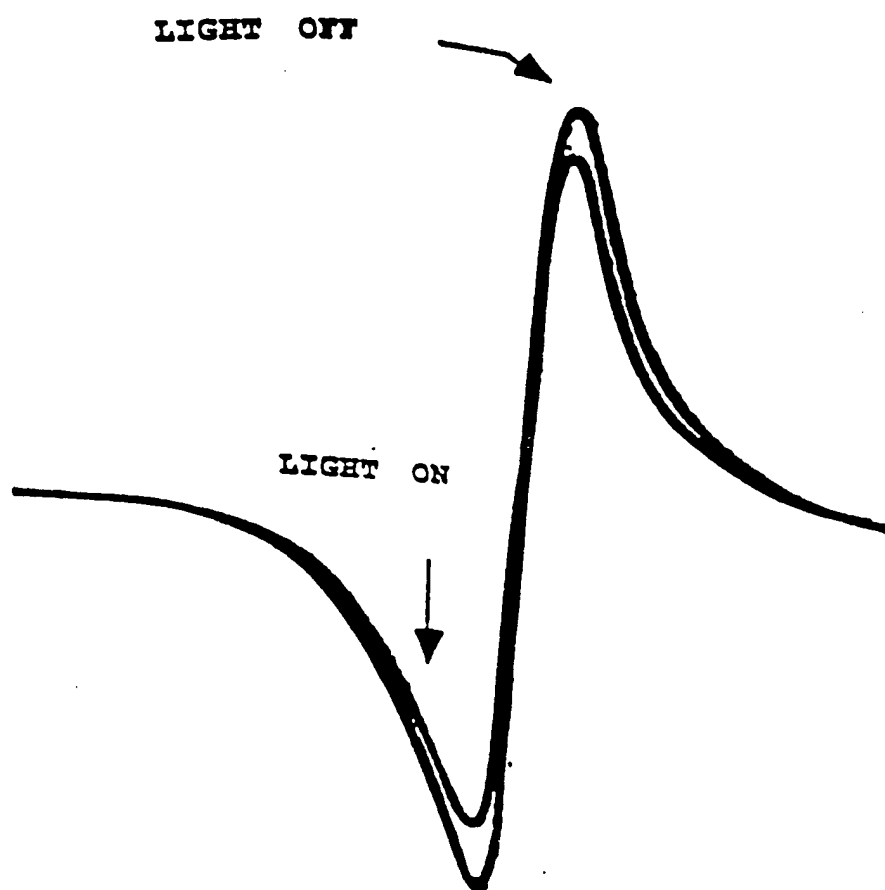


Fig. 7.14 EPR cubic spectrum of "home grown" iron doped BSO crystal C_2 at 77 K, without and with laser illumination.